UNIVERSITY OF CALIFORNIA,
IRVINE

Micromachined Vibratory Gyroscopes Designed for Precision of Measurements and Environmental Robustness

DISSERTATION

submitted in partial satisfaction of the requirements
for the degree of

DOCTOR OF PHILOSOPHY

in Mechanical and Aerospace Engineering

by

Danmeng Wang

Dissertation Committee:
Professor Andrei M. Shkel, Chair
Professor Michael McCarthy
Professor William C. Tang

2022

DEDICATION

To the Lord Jesus Christ, and my beloved parents, Wenju Wang and Shiming Xu.

TABLE OF CONTENTS

LIST OF FIGURES

LIST OF TABLES

ACKNOWLEDGMENTS

Firstly, I would like to express my deepest gratitude to my advisor Professor Andrei M. Shkel for this wonderful research opportunity. This journey would not have been possible without his continuous support, patience, encouragement, and immense knowledge throughout the years. I am also deeply grateful to my dissertation committee, Professor Michael McCarthy and Professor William C. Tang, for taking the time to review this work and provide valuable comments.

Next, I would like to thank the colleagues and friends at UCI Microsystems Lab for the stimulating discussions, for the insightful suggestions, and for the moments we spent together. More specifically, I would like to thank Dr. Yusheng Wang, Dr. Daryosh Vatanparvar, Dr. Sina Askari, Dr. Dogukan Yildirim, Doreen Hii, Yu-Wei Lin, Chi-Shih Jao, Austin Parrish, Eudald Sangenis, Wei Guan, Yi Zhuang, and Daria Shkel for their valuable discussion and help in various aspects of my Ph.D. research, as well as Dr. Alexandra Efimovskaya, Dr. Mohammad H. Asadian, and Dr. Radwan M. Noor for their guidance and support during the first few years of the research.

I would like to thank Professor Solmaz Kia and her research group for their help in my Ph.D. research. In addition, I would like to acknowledge Integrated Nanosystems Research Facility (INRF) staff members, Jake Hes, Dr. Mo Kebaili, Dr. Chuang-Yuan Lee, and Dr. Richard Chang for their assistance on the fabrication process development, and staff members of UCI Irvine Materials Research Institute (IMRI) for technical support over the years.

I also would like to acknowledge the funding, generously provided by Defense Advanced Research Projects Agency (DARPA) and National Institute of Standards and Technology (NIST), without which this work would not have been possible. Specifically, this work was supported by DARPA under Grant N66001-16-1-4021 (PRIGM-AIMS) and NIST grant 70NANB17H192.

Finally, I would like to thank my family and friends, who have been supporting me all the time, both mentally and spiritually. Without them, none of this would be possible.

VITA

Danmeng Wang

EDUCATION

Doctor of Philosophy in Mechanical Engineering **2022**
University of California, Irvine *Irvine, CA, USA*

Master of Science in Electrical Engineering **2018**
University of California, Irvine *Irvine, CA, USA*

Bachelor of Engineering in Electrical Engineering **2013**
Beijing Jiaotong University *Beijing, China*

RESEARCH EXPERIENCE

Graduate Research Assistant **2016–2022**
University of California, Irvine *Irvine, CA, USA*

TEACHING EXPERIENCE

Teaching Assistant **2022**
University of California, Irvine *Irvine, CA, USA*

REFEREED JOURNAL PUBLICATIONS

Danmeng Wang, Mohammad H. Asadian, Wei Guan, Doreen Hii, Austin R. Parrish, and Andrei. M. Shkel, "Effect of metallization on quality factor and noise characteristics in fused silica dual-shell gyroscopes," IEEE Journal of Microelectromechanical Systems (JMEMS), 2022 (to be published).

Danmeng Wang, Mohammad H. Asadian, Doreen Hii, Austin R. Parrish, Wei Guan, and Andrei. M. Shkel, "Modeling and Compensation of Assembly Errors in Fused Silica Dual-Shell Gyroscopes," Sensors and Actuators A: Physical, 2022 (under review).

Danmeng Wang and Andrei M. Shkel, "Effect of EAM on capacitive detection of motion in mems vibratory gyroscopes," IEEE Sensors Journal, vol. 22, no. 3, pp. 2271-2281, 2022.

Daryosh Vatanparvar, **Danmeng Wang**, and Andrei M. Shkel, "Direct Angle Measurement Using Dynamically-Amplified Gyroscopes," IEEE Sensors Journal, vol. 22, no. 7, pp. 6336-6344, 2022.

Mohammad H. Asadian, **Danmeng Wang**, and Andrei M. Shkel, "Fused Quartz Dual-Shell Resonator Gyroscope," IEEE Journal of Microelectromechanical Systems, vol. 31, no. 4, pp. 533-545, 2022.

Alexandra Efimovskaya, **Danmeng Wang**, and Andrei. M. Shkel, "Mechanical Trimming with Focused Ion Beam for Permanent Tuning of MEMS Dual-Mass Gyroscope," Sensors and Actuators A: Physical, vol. 313, pp. 112189, 2020.

Alexandra Efimovskaya, **Danmeng Wang**, Yu-Wei Lin, Andrei M. Shkel, "Electrostatic compensation of structural imperfections in dynamically amplified dual-mass gyroscope," Sensors and Actuators A: Physical, vol. 275, pp. 99–108, 2018.

REFEREED CONFERENCE PUBLICATIONS

Danmeng Wang, Wei Guan, Mohammad H. Asadian, Doreen Hii and Andrei M. Shkel, "Effect of metallization on fused silica dual-shell gyroscopes," IEEE International Symposium on Inertial Sensors and Systems (INERTIAL), Avignon, France, May 8-11, 2022.

Danmeng Wang, Mohammad H. Asadian, Doreen Hii and Andrei M. Shkel, "Fused silica dual-shell gyroscope with in-plane actuation by out-of-plane electrodes realized using glass-blowing and thru-glass-vias fabrication," IEEE International Conference on Micro Electro Mechanical Systems (MEMS), Tokyo, Japan, Jan 10-14, 2022.

Chi-Shih Jao, **Danmeng Wang**, Austin R. Parrish, and Andrei M. Shkel, "A Neural Network Approach to Mitigate Thermal-Induced Errors in ZUPT-aided INS," IEEE International Symposium on Inertial Sensors and Systems (INERTIAL), Avignon, France, May 8-11, 2022.

Wei Guan, **Danmeng Wang**, Mohammad H. Asadian, Yusheng Wang, and Andrei M. Shkel, "Effect of geometry on energy losses in fused silica dual-shell gyroscopes," IEEE International Symposium on Inertial Sensors and Systems (INERTIAL), Avignon, France, May 8-11, 2022.

Danmeng Wang and Andrei M. Shkel, "Electrical Dissipation in MEMS Vibratory Gyroscopes as a Method for Controlling "Effective" Q-factor," IEEE International Symposium on Inertial Sensors and Systems (INERTIAL), Virtual Symposium, Mar 22–25, 2021.

Danmeng Wang, Radwan M. Noor, and Andrei M. Shkel, "Dynamically amplified dual-mass gyroscopes with in-situ shock survival mechanism," IEEE International Symposium on Inertial Sensors and Systems (INERTIAL), Virtual Symposium, March 23-26, 2020.

Mohammad H. Asadian, **Danmeng Wang**, Yusheng Wang, and Andrei M. Shkel, "3D dualshell micro-resonators for harsh environments," in IEEE/ION Position, Location and Navigation Symposium (PLANS), Portland, Oregon, USA, April 20-23, 2020.

Danmeng Wang, Alexandra Efimovskaya, and Andrei M. Shkel, "Amplitude Amplified Dual-Mass Gyroscope: Design Architecture and Noise Mitigation Strategies," IEEE International Symposium on Inertial Sensors and Systems (INERTIAL), Naples, FL, USA, April 1–5, 2019.

Danmeng Wang, Mohammad H. Asadian, Alexandra Efimovskaya, and Andrei M. Shkel, "A Comparative Study of Conventional Single-Mass and Amplitude Amplified Dual-Mass MEMS Vibratory Gyroscopes," IEEE Inertial Sensors 2017, Kauai, HI, USA, March 27–30, 2017.

Alexandra Efimovskaya, Yu-Wei Lin, **Danmeng Wang**, and Andrei M. Shkel, "Electrostatic Compensation of Structural Imperfections in Dynamically Amplified Dual-Mass Gyroscope," IEEE Inertial Sensors 2017, Kauai, HI, USA, March 27–30, 2017.

ABSTRACT OF THE DISSERTATION

Micromachined Vibratory Gyroscopes Designed for Precision of Measurements and Environmental Robustness

By

Danmeng Wang

Doctor of Philosophy in Mechanical and Aerospace Engineering

University of California, Irvine, 2022

Professor Andrei M. Shkel, Chair

This Ph.D. dissertation investigates how precision of measurement and environmental robustness can be addressed simultaneously in designing the Coriolis Vibratory Gyroscopes (CVGs). Toward implementation of such sensors, this thesis focuses on sensor's design and demonstration of functionalities, realizing devices based on Microelectromechanical System (MEMS) manufacturing techniques. This thesis investigated and demonstrated the following two different paradigms:

- Realization of precision sensors that are capable of surviving the extreme events of shock and vibrations while the sensors are not in operation. Toward this objective, we developed and implemented a capacitive Trap-and-Hold (TAH) concept as an add-on feature intended to increase survivability of low-frequency MEMS CVGs by immobilizing the proof-mass of the oscillatory system in the event of shock and vibration and then recovering the sensor's high-sensitivity operation after the extreme events. To demonstrate the mechanism, a design of MEMS Dynamically Amplified dual-mass Gyroscope (DAG) was implemented as the test vehicle. This design was chosen for an increased amplitude of sensing response to enhance the signal-to-noise ratio and thus increase the precision of measurements. To accomplish such measurements, we investigated the effects of resonant mode ordering and energy dissipation with respect to

the geometrical parameters. We demonstrated that the design is capable of achieving the noise characteristics of 0.007 deg/rt-hr of Angular Random Walk and 0.08 deg/hr of in-run bias instability. Two wafer-level fabrication processes using through-wafer-interconnect (TWI) techniques were investigated in order to realize the TAH add-on mechanism to DAGs. The TWI technique was experimentally validated to improve the DAG's shock survivability under 5g shocks while preserving its noise characteristics.

- Realization of precision sensors that are capable of operating through extreme events of shock and vibrations. Toward this objective, we developed Fused Silica MEMS Dual-Shell Gyroscopes (DSGs). A Thru-Glass-Vias (TGVs) planar electrode substrate for electrostatic gyroscope actuation and detection was designed, fabricated, and integrated with DSG in a single microsystem. Effects of fabrication imperfections and assembly errors on structural symmetry and sensor performance were analyzed. An electromechanical tuning model for electrostatic compensation of structural asymmetry in DSGs was developed, taking into account the effect of assembly errors to realize near-mode-matched gyroscope operation with frequency matching on the order of 0.1 Hz for high angular rate measurements, followed by an experimental demonstration of the gyroscope operation with noise characteristics of 0.017 deg/rt-hr of Angular Random Walk and 0.2 deg/hr of in-run bias instability.

Factors that impact the structural symmetry and energy dissipation mechanisms in MEMS resonators were also analyzed and implemented to improve gyroscope performance in the realization of both paradigms. The impact of metallization on quality factor and electrical conductivity in Fused Silica devices was quantified and linked to the in-run noise performance using a developed analytical model. An existing trade-off between metallization and quality factor was investigated. It was concluded that optimization of the metal coating parameters was necessary to achieve optimal gyroscope noise characteristics. Finally, the effects of Electromechanical Amplitude Modulation (EAM) on electrical dissipation, non-

linearity, scale factor instability, and in-run noise performance of CVGs were investigated. Analytical models to predict the impact of EAM effect were developed, followed by experimental validation. Optimization of EAM parameters was demonstrated to achieve improved performance of MEMS CVGs.

Chapter 1

Introduction

We present in this Chapter the background for realization of environmentally robust Micro Electro Mechanical System (MEMS) based Coriolis Vibratory Gyroscopes (CVGs). The bulk of this chapter is the literature review of the prior state of the art. The chapter concludes with an outline of the dissertation.

1.1 Motivation

Global Positioning System (GPS) based navigation systems have been the ubiquitous solution, both in civil and military domains. However, unavailability and susceptibility of GPS signals in complex environments such as indoors, urban canyons, tunnels, and underground areas, and a slow update rate varying from 1 to 10 Hz motivate the development of high accuracy, fast dynamics, self-contained navigation systems [1, 2].

Inertial navigation is based solely on inertial sensor (gyroscopes and accelerometers) readouts that provide an object's rotation and acceleration information enabling motion tracking [3]. Inertial sensors can achieve an update rate of the object's trajectory on the order of a few

kHz. Due to fast accumulating errors, ultra-low noise performance of inertial sensors is demanded to meet the requirements of long-term navigation in many applications. However, such devices typically cost hundreds of thousands of dollars per axis with a large volume (500-2000 cm^3), for example, Safran PRIMUS 400, [4], and Honeywell HG9900, [5].

Among the inertial sensor technologies, MEMS-based inertial sensors provide unique advantages in the cost, size, weight, and power consumption (CSWaP) as compared to more traditional mechanical and optical sensors, making MEMS inertial sensors highly attractive in many fields [6]. However, due to the relatively low precision of the micro-machining process over the macro-level, especially for gyroscopes, there is a challenge for MEMS inertial gyroscopes to simultaneously benefit from miniaturization and achieve high-performance level for the needs of applications due to the complexity in gyroscope development [7].

Over the past years, a number of high-performance MEMS gyroscope designs with increased proof masses, high quality factors, and relatively low operational frequencies, such as tuning fork, disk, ring, and multi-mass resonators, have been realized using MEMS technique and showed a potential for achieving the navigation-grade accuracy. As a result, the resolution and noise characteristics have been enhanced by approximately a factor of ten every two years [8].

Despite the remarkable continuing improvement in gyroscope performance, their relatively poor stability and robustness, due to their weak suspensions, "flat" proof-masses, and temperature sensitivity [9], limit their performance in challenging environments, such as indoor pedestrian navigation for firefighters and first responders and localization for underground mining operations where the sensors are subject to high-g shocks, intense vibrations, and thermal variations. In order to be compatible with such navigation applications, methods for minimizing the impact of environment on MEMS devices have been recently reported in literature and typically involve a sacrifice of tunability and sensitivity through modifying the design parameters, for example, strengthening structures, [10], reducing quality factors,

[11], or employing resilient supporting features, [12]. Strategies utilizing external add-on mechanisms have been demonstrated [13, 14, 15], but they are generally complex to process.

While there have been efforts to develop mitigation strategies for MEMS CVGs, there are potential solutions in large-scale CVGs that could scale well and could be realized using MEMS processes, such as macro-scale Fused Silica (FS) Hemispherical Resonator Gyroscope (HRG). The HRG incorporates a rugged structure and higher out-of-plane stiffness with a better than navigation-grade gyroscope performance and exceptional reliability [16]. Despite the optimistic outlook, the complexity of implementing miniaturized HRGs as a type of CVGs is a primary challenge in achieving high-resolution operations. Imperfections introduced by the fabrication process, including the manufacturing of micro-shells, metal-coating, and assembly between the sensor and electrode substrate, influence the structural symmetry and degrade the gyroscope noise characteristics.

This dissertation presents developments of sensors and addressing the challenges in the realization of environmentally robust MEMS gyroscopes for precision CVGs.

1.2 Background

This section gives a brief overview of the principle of operation of a CVG and the performance parameters. The common terms used throughout the thesis are also given in the section.

1.2.1 MEMS Coriolis Vibratory Gyroscope

MEMS CVGs are based on the principle that the Coriolis forces produced by vibration of the sensing element and rotation of the system result in a transfer of energy between two vibration modes of a gyroscope [17]. The dynamics of a CVG can be modeled as a

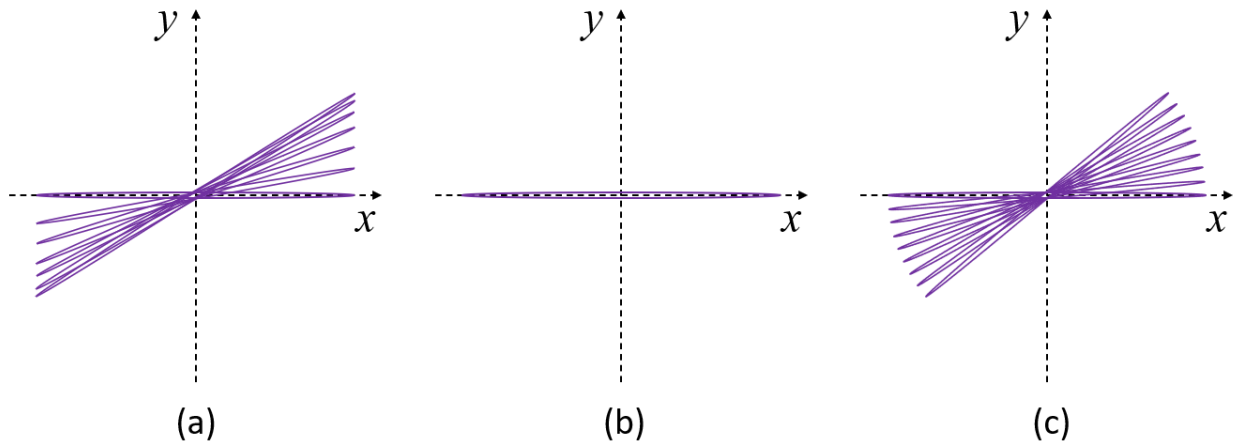

Figure 1.1: Ideal response of a CVG operated in (a) open-loop mode, (b) force-to-rebalance mode, and (c) whole angle mode.

two-degree-of-freedom (DOF) lumped mass-spring-damper model in terms of the primary (drive) and secondary (sense) modes. The equation of motion in the matrix form can be represented as, [18],

$$\begin{bmatrix} \ddot{x} \\ \ddot{y} \end{bmatrix} + \begin{bmatrix} 2\mu_0 & 0 \\ 0 & 2\mu_0 \end{bmatrix} \begin{bmatrix} \dot{x} \\ \dot{y} \end{bmatrix} + \begin{bmatrix} 0 & -2\Omega \\ 2\Omega & 0 \end{bmatrix} \begin{bmatrix} \dot{x} \\ \dot{y} \end{bmatrix} + \begin{bmatrix} \omega_0^2 & 0 \\ 0 & \omega_0^2 \end{bmatrix} \begin{bmatrix} x \\ y \end{bmatrix} = \begin{bmatrix} F_x/m \\ F_y/m \end{bmatrix}, \tag{1.1}$$

where ω_0 is the resonant frequency of the degenerate (or mode-matched) mode of the gyroscope, Ω is the input angular rate, μ_0 is the damping coefficient, and m is the effective mass of the system. F_x, and F_y are the control forces along the orthogonal axes of the resonator.

CVGs are classified into two main categories: rate gyroscopes, which measure the angular velocity, and rate-integrating (or whole angle) gyroscopes, which measure the angle of rotation [17]. In the rate mode of operation, the vibration amplitude along the drive axis is typically actuated at its resonant frequency and stabilized by the Automatic Gain Control (AGC) and Phase-Locked Loop (PLL) control loops to prevent variations in the amplitude and phase. The Coriolis acceleration coupling excites the sense mode oscillation when the rotation occurs. The detection schemes in the rate gyroscopes can be divided into two classes: open-loop and force-to-rebalance (FRB) modes, depending on whether the closed-loop con-

trol is implemented or not, illustrated in Fig. 1.1(a) and (b). In the whole angle mode of operation, the proof-mass oscillates freely, and the orientation of the vibration precesses due to the external input rotation. As a result, the output in the whole angle mode is the angle and has theoretically unlimited mechanical bandwidth. Fig. 1.1(c) schematically illustrates the whole angle mode of operation.

The concept of CVGs utilizing vibrating elements to induce and detect Coriolis force is compatible well with electrostatic actuation and detection mechanisms using either parallel-plates or comb-drives of capacitive electrodes. This configuration scales well and has been proven to be effectively implemented in the batch micro-fabrication, making the capacitive CVGs attractive for applications where low CSWaP and high precision are required.

1.2.2 MEMS CVG Performance Parameters

In this section, the performance parameters of MEMS capacitive CVGs are discussed. The critical design parameters for enhancing performance are pointed out. The general goal is to increase the gyroscope sensitivity and to reduce the noise sources of the devices.

1.2.2.1 Gyroscope Sensitivity

Mechanical scale factor in the rate gyroscope is a parameter describing the ratio between the sense axis displacement, Y, and the input angular rate, Ω. In the presence of asymmetry caused by the fabrication imperfections, i.e., frequency split, in a rate gyroscope, the mechanical scale factor, SF_{mech}, is [19]

$$SF_{mech} = \frac{Y}{\Omega} = \frac{2A_g X_a \omega_x}{\sqrt{({\omega_y}^2 - \omega_x^2)^2 + (\frac{\omega_x \omega_y}{Q_y})^2}}, \tag{1.2}$$

where X_a is the vibration amplitude along the X-axis (drive mode), A_g is the angular gain, and Q_y is the quality factor (Q-factor) of the Y-axis (sense mode). Parameters ω_x and ω_y are the resonance frequency along the X- and Y-axis. In the mode-matched gyroscopes, which $\omega_x = \omega_y = \omega_0$, the mechanical scale factor is maximized and can be described as

$$SF_{max} = \frac{Y}{\Omega} = \frac{2A_g X_a Q_y}{\omega_0}. \tag{1.3}$$

Angular gain in MEMS CVGs describes the mechanical sensitivity to the Coriolis force. It is only determined by the geometry of the sensing element. In the whole angle mode of operation, the precession angle of the oscillation pattern, θ, can be expressed as

$$\theta = \theta_0 - A_g \int_{t_0}^{t} \Omega(\tau) d\tau \tag{1.4}$$

with

$$\dot{\theta} = -A_g \Omega, \tag{1.5}$$

where θ_0 is the initial pattern angle.

1.2.2.2 CVG Noise Characteristics

Reduction of the noise sources is key to achieving the high performance of MEMS CVGs. The noise characteristics of rate gyroscopes are typically represented by Angle Random Walk and in-run Bias Instability, which can be calculated by the Zero-Rate Output (ZRO) noise estimation through Allan Deviations and Power Spectral Density (PSD) analysis methods, illustrated in Fig. 1.2.

Angle Random Walk (ARW) is a kind of noise caused by white mechanical-thermal noise (MTN) and thermo-electrical noise and describes the random walk of angle estimation

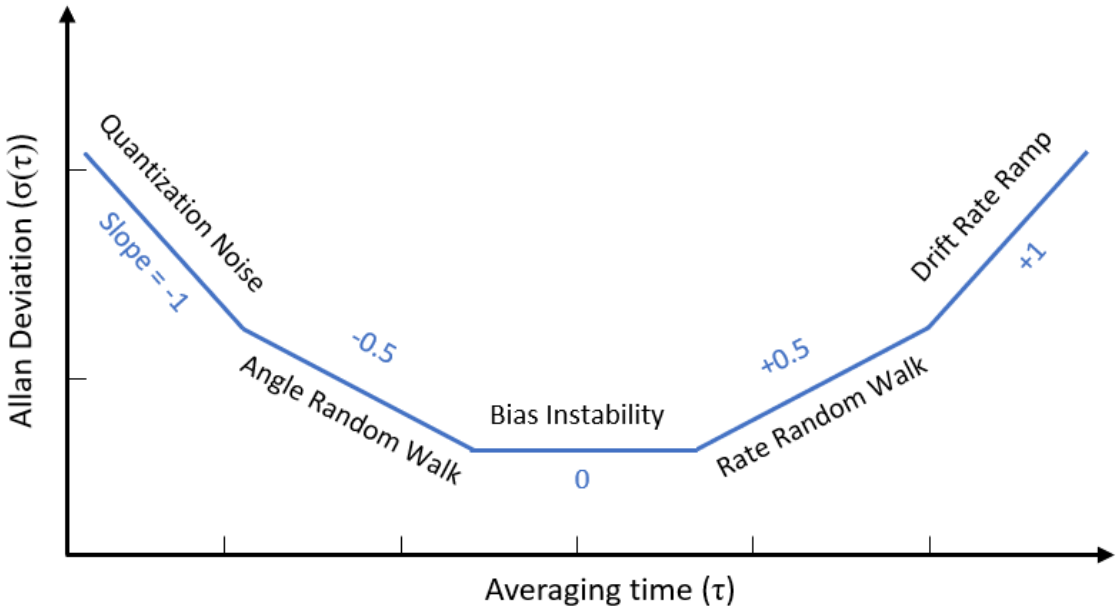

Figure 1.2: A schematic illustrated of Allan Deviations in log-log scale.

during navigation. It shows a slope of $\tau^{0.5}$ in the log-log scale Allan Deviations plot (see Fig. 1.2). Power Spectral Density (PSD) provides information of the signal in the frequency domain; hence, ARW is characterized by the flat part (slope 0 in the log-log plot) of the characteristic around the sensor's mechanical bandwidth (see Fig. 1.3). ARW caused by MTN typically indicates the theoretical limit of the noise performance of a rate gyroscope, which can be approximate as the MTN equivalent rate in the form of, [20],

$$\Omega_{rw} = \sqrt{\frac{k_B T \omega_y}{m X_a^2 \omega_x^2 Q_y}}, \tag{1.6}$$

where k_B is the Boltzmann's constant, m is the proof-mass, and T is the operating temperature.

Bias Instability (BI) indicates a gyroscope bias fluctuation in the data and shows a curve on the Allan Deviations plot with a zero slope (see Fig. 1.2). It is usually considered to be originating from electronics susceptible to random flickering. In the PSD plot (see Fig. 1.3), the in-run bias instability occurs at a slope of -1.

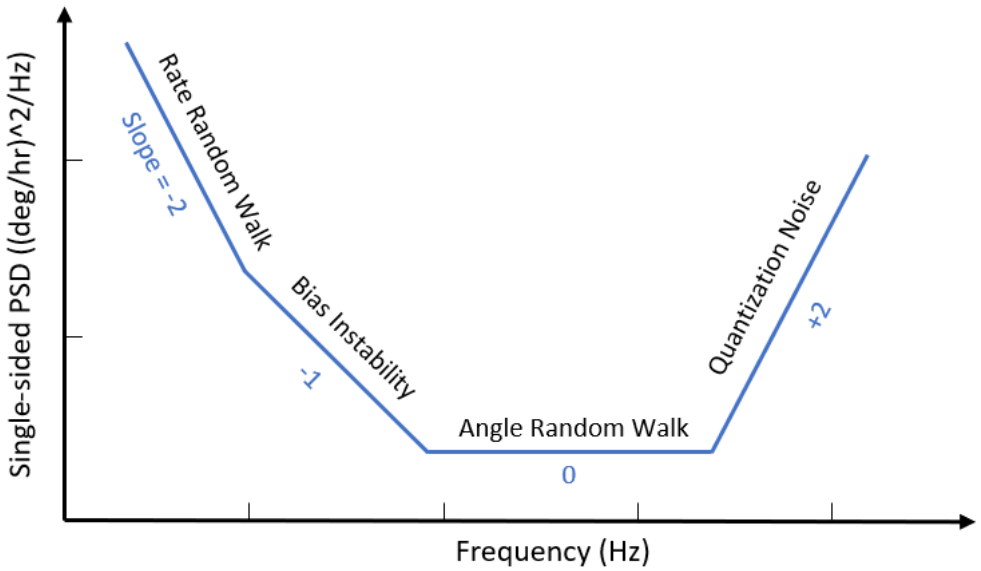

Figure 1.3: A schematic illustrated of Power Spectral Density in log-log scale.

Angle drift in the output of a whole angle gyroscope is a parameter describing the accuracy of gyroscope measurement. The rate of precession can be expressed as, [21],

$$\dot{\theta} = -A_g\Omega + \frac{1}{2}\Delta(\frac{1}{\tau})\sin 2(\theta - \theta_\tau) + \frac{1}{2}\Delta\omega\cos 2(\theta - \theta_\omega)\frac{Q}{E}, \tag{1.7}$$

where θ_τ, θ_ω, E, and Q denote the principal axes of damping and elasticity, and the energy and quadrature error, respectively. Parameters $\Delta\omega$ and $\Delta(\frac{1}{\tau})$ are the frequency mismatch and damping mismatch caused by the fabrication imperfections, where $\Delta\omega = \omega_x - \omega_y$ and $\Delta(\frac{1}{\tau}) = \frac{1}{\tau_x} - \frac{1}{\tau_y}$. Thus, the anisodamping and anisoelasticity need to be minimized in order to reduce the quadrature effect and drift of the output measurement.

In conclusion, mass, quality factor, vibration amplitude, angular gain, operational frequency, and structural symmetry, including damping and stiffness symmetries, are the critical characteristics related to the gyroscope's sensitivity and noise that contribute to the performance of both rate and whole angle MEMS CVGs. However, such gyroscopes are typically susceptible to environmental variations, including shocks, vibrations, temperature, etc., due to their heavy proof-masses, delicate suspensions, and temperature sensitivity.

1.2.3 Energy Dissipation Mechanisms in MEMS

The quality factor (Q-factor) is a critical parameter that describes the rate of energy loss in resonating structures and is directly related to sensitivity, power consumption, and noise characteristics [22]. The Q-factor in MEMS resonators is typically limited by mechanical losses, including viscous air damping, thermoelastic dissipation (TED), anchor loss, surface loss, electrical damping, internal loss, losses due to mode coupling, and other losses such as the Akhiezer damping [23, 24]. The overall Q-factor can be expressed in the form as,

$$\frac{1}{Q_{all}} = \frac{1}{Q_{viscous}} + \frac{1}{Q_{TED}} + \frac{1}{Q_{anchor}} + \frac{1}{Q_{surface}} + \frac{1}{Q_{ele}} + \frac{1}{Q_{internal}} + \frac{1}{Q_{mode}} + \frac{1}{Q_{other}}. \quad (1.8)$$

Viscous Air Damping is one of the major sources of energy dissipation in the micro-scale level due to the large surface-to-volume ratio and small spacing between the anchored and movable structures. It is generally classified into two categories in MEMS resonators: squeeze film damping [25] and lateral damping [26]. It arises the requirement to operate the devices in an ultra-high vacuum on the order of a few tens of micro-Torr to eliminate the air damping [27].

Thermoelastic Dissipation is related to the material's Coefficient of Thermal Expansion (CTE) [28, 29] and typically defines an upper bound on achievable Q-factors of MEMS devices in the kHz range [30]. The theoretical Q-factor caused by the TED can be expressed by the Zener's standard model in the form of, [31],

$$Q_{TED} = \frac{C_v}{\alpha^2 E T_0} \frac{1 + (\omega_0/\omega_R)^2}{\omega_0/\omega_R} \quad (1.9)$$

with

$$\omega_0/\omega_R = \frac{\chi \pi^2}{b^2}, \quad (1.10)$$

where α, E, C_v, T_0, ω_0, and ω_R denote the CTE, heat capacity of the solid, Young's mod-

ulus, nominal average temperature, resonant frequency, and the thermal relaxation rate, respectively. Parameter χ is the thermal diffusivity of the solid and b is the width of the strained beam. Thus, approaches to minimizing the TED are optimizing the design [32], adding slots to block heat flow [33], reducing the operation frequency, and building devices using materials with lower CTE, such as Fused Silica (FS) [34] and Ultra-Low Expansion (ULE) glass [35].

Anchor Loss is the acoustic energy of a resonator dissipated into the supporting substrate by transmission through its anchor [22]. It is related to the location and geometry of the anchor, as well as the vibrational mode shape. Thus, anchors are usually placed at the node of the mode shape to minimize the energy dissipation through the anchor point.

Surface Loss refers to the energy losses due to surface imperfections of a resonator. Many factors, including surface roughness, surface oxidation, metal coating, dust, moisture absorption, and sub-surface damage, influence surface condition and reduce the quality factor of the resonator [36, 37].

Electrical Damping arises from electrical interactions, especially, for capacitive and magnetomotive detection of MEMS resonators [38], in which the induced charge flow dissipates in the resonator body, nearby grounded electrodes, and the measurement circuit.

Internal Loss denotes the energy losses of the devices caused by the imperfections inside the material, such as defects, impurities, and grain boundaries. Therefore, high material purity is needed to achieve the high quality factor [39].

Mechanical Mode Coupling in a MEMS resonator would result in energy distribution from the actuated operational mode to all the nearby parasitic modes [40]. An increase in the frequency separation between modes is needed to maintain the desired quality factor.

Akhiezer Damping arises from phonon scattering processes within the devices, which is

independent of structural geometry and more dominant in the resonators of high frequencies [41]. For silicon, the product of the resonant frequency and quality factor due to Akhiezer damping has an estimated order of magnitude of 10^{13}.

1.3 Literature Review

This section reviews the state-of-the-art in realization of high-performance MEMS CVGs and mitigation strategies for robustness and stability against environmental variations.

1.3.1 Improvement of Robustness of MEMS Gyroscopes

One active research area in the field of environmentally robust MEMS gyroscopes is to increase the shock survivability of high resolution gyroscopes for operation in extreme environments. This is necessary in military [42] and aerospace [43] applications, which typically require devices to withstand high amplitudes of vibration and shock. However, conventional planar high performance MEMS devices fall short of these demands due to their delicate suspensions, heavy proof-masses, and amplified gyroscope sensitivity. Typical failures include mechanical wear, stiction, fracture in structures, and material fatigue [10]. In this section, we review different approaches for improvement of shock survivability reported in literature.

1.3.1.1 Structural Approaches

To address shortcoming of gyroscopes of being susceptible to shocks, multiple compensation strategies with varying levels of complexity have been proposed. The most straightforward design modification aims to strengthen released structures or increase spring stiffness. One strategy is to push the operational frequencies of the sensor above 100kHz [44]. The drawback

of this implementation is that gyroscope amplitude of response is sacrificed, compromising its sensitivity and tunability. Alternatively, one may opt to preserve and even improve mechanical properties of gyroscopes by using extremely hard materials (e.g. silicon carbide [45]). However, the technique not only sacrifices sensitivity and tunability but is also generally expensive and difficult to process.

Another approach pursued in literature is to increase the degree-of-freedom of an oscillatory system for achieving wide-bandwidth frequency responses of the vibratory gyroscopes, such as the wide-bandwidth robust gyroscope, [46] and [47], Fig. 1.4(a), including two interconnected masses with 2-DOF sense-mode. By designing the drive-mode operating frequency to match the flat region of its sense-mode response curve, robustness against environmental variations was realized. As a result, the requirement of mode-matching between the drive and sense modes was spontaneously met. A similar design concept was presented in [48]. The distributed-mass gyroscope, Fig. 1.4(b), utilizes multiple drive-mode oscillators with incrementally spaced resonance frequencies to enhance mode-decoupling in a drive-mode to form a wide-bandwidth response in the gyroscope drive mode. Although those approaches improve sensors' robustness by relaxing the need for mode-matching during the event of external variations, a reduction of environmental sensitivity would also decrease the precision of gyroscope measurements.

Three-Dimensional (3D) Fused Silica (FS) hemispherical resonator gyroscopes (HRGs) are also good candidates for operation in extreme environments by incorporating a rugged structure, higher out-of-plane stiffness, and a relatively low operational frequency [16]. This not only improves the sensor's integrity and survivability during the events of high-g shocks or intense vibrations, but it also permits the use of a lower stiffness in-plane mode, such as the n = 2 and the n = 3 wineglass modes, for high sensitivity angular rate measurements. This configuration also scales well to the micro-level and has been implemented in MEMS CVGs, making the sensors potentially robust for operation in harsh environments [49, 50].

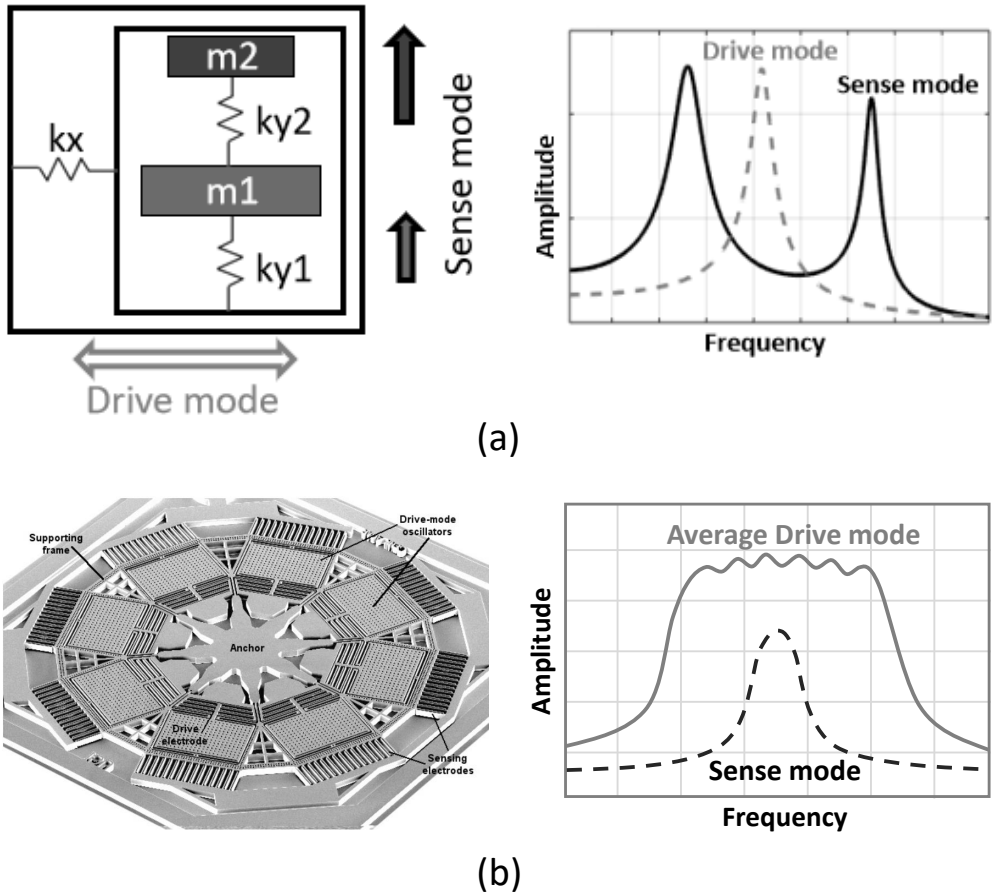

Figure 1.4: Examples of wide-bandwidth robust gyroscopes: (a) dual-mass system with a 2-DOF sense-mode oscillator, [46], and (b) distributed-mass system with up to 8 drive-mode oscillators, [48].

The fabrication technology was developed at the University of California, Irvine [51, 52, 53]. However, due to limitations in accuracy of micro-machining, achieving a high structural symmetry, i.e. low frequency mismatch, for realization of navigational-grade performance in miniaturized HRGs is an ongoing research topic.

1.3.1.2 Shock Survival Mechanisms

Moving away from variations in gyroscope design, several studies approached the challenge by integrating external add-ons. For example, an active cancellation of vibrations has been explored as an environmental isolation strategy [13]. The limitation, however, is that the

technique only works on some specific structures and may not be well suited for high-g shocks sensors. Some proposed the concepts of micro-machined integrated shock protection for MEMS devices [14], using either a soft material coating or nonlinear springs as shock stoppers, to reduce the impact between the proof-mass and stoppers. Nevertheless, the approach is very difficult to realize: it is a challenge to fabricate these devices.

A high performance MEMS CVG typically has a carefully designed structure with specific geometry and performance parameters, such as a relatively low operational frequency on the order of 10 kHz, [54], or demand for special implementation of a certain architecture. Therefore, even though those shock mitigation strategies mentioned above had their respective strengths and applications, they are likely incompatible with high-performance low resonant frequency CVGs.

In addition to the complex and design-dependent add-on mechanisms described above, 3D encapsulation of the planar MEMS gyroscopes with the aid of the additional out-of-plane stoppers could be a flexible solution to enhance shock survivability of gyroscopes while preserving their high sensitivity since the modification of design is eliminated [55, 56, 57]. The method utilizes the out-of-plane stoppers and the added stationary mode, contrary to the normal gyroscope operational mode, to limit motion amplitude or freeze the proof-mass during the event of shocks, and can be applicable to a broad class of gyroscope designs.

Fabrication of the 3D encapsulation stage typically involves electrically isolated stoppers and Through-Wafer-Interconnects (TWI). Various methods for realizing high density and low parasitic TWIs were widely explored in recent years, such as electroplated copper vias, [58], magnetically assembled nickel wires [59], and Thru-Glass-Si vias [60]. Instead of filling the vias using either metal or silicon materials, depositing or electroplating conductive metal layers on the sidewall of the vias created on a glass substrate wafer as the electrical paths can significantly simplify the fabrication process and minimize parasitics of interconnects [61].

1.3.2 Thermal Compensation Techniques

Temperature sensitivity of MEMS CVGs is one of the critical factors limiting the gyroscope's performance. Temperature variations due to temperature dependence of Young's Modulus and thermal-induced stresses, [9], result in noise, long-term bias, and scale-factor drifts. Different thermal compensation techniques have been demonstrated in order to improve the sensor's long-term stability. In general, the approaches could be classified into two main categories: temperature control methods and post-processing compensation methods.

The approaches of temperature control techniques have been experimentally implemented during the phase of MEMS sensor characterization to actively compensate for thermal variations in the environment, for example by attaching a heater element and a temperature sensor to the outside of a packaged MEMS sensor, [62], or utilizing a micro-oven co-fabricated with inertial sensors, [63]. The methods are typically sufficient to eliminate the thermal-induced drifts at the cost of power consumption and rely on the accuracy of the additional control tools to execute the action.

The post-processing compensation methods conducted on MEMS resonators were also investigated to ease the thermal effect. For example, the temperature compensation was demonstrated by utilizing the drive-mode frequency as a built-in thermometer for temperature self-sensing and the pre-calibrated algorithm for real-time compensation [64]. The accuracy depends on the repeatability and linearity of the sensors' temperature dependence of thermal-induced drifts.

1.3.3 Multi-Mass Gyroscopes

Conceptually, a single-lumped mass-spring structure is required for a single-axis gyroscope to measure the Coriolis acceleration induced by the input angular rate. Since the 1990s,

several types of capacitive MEMS CVGs, such as tuning fork and resonant ring gyroscopes [65, 66], have been produced and have become highly popular designs of their kinds to date. Recently, a variety of multi-mass designs emerged to seek further improvements, each offering different advantages with the intention to enhance various aspects of performance, such as dynamical balance and dynamic amplification.

- Examples of successful dynamically balanced systems, the Dual Foucault Pendulum gyroscope (DFP) [70] and Quadruple Mass Gyroscope (QMG) [68], Fig. 1.5(a) and (b), utilize two or more equivalent and mechanically coupled proof-masses. Oscillation of these masses in the anti-phase motion improves the vibration immunity, and the dynamically balanced forces and moments in the anchor for both the drive and sense modes minimize the energy dissipation through the substrate, resulting in ultra-high quality factor ($>$ 9M) under cryogenic temperature conditions [67] and high quality factor ($>$ 2M) under room temperature conditions [71, 27].

- As for multi-mass solution utilizing dynamically amplified dual-mass system, gyroscope performance was improved when an increased gyroscope amplitude of response led to an increased signal-to-noise ratio, [72] and [73], Fig. 1.5(d). The dual-mass system consists of a drive mass attached to an anchor and structurally coupled to a sense mass. The frequency of the driving force is at the first resonant frequency of the coupled dual-mass system, satisfying the dynamic amplification condition, resulting in an increased amplitude of the gyroscope. Nevertheless, a Dynamically amplified dual-mass gyroscope demonstrated an effective angular gain of 0.99 [74], close to an ideal angular gain of 1, to further increase Coriolis acceleration sensitivity.

However, environmental variations are important factors to consider for a high-performance multi-mass gyroscope since the impacts of external stimulations can be different for different masses. Generally, the complex and dedicated suspensions connecting these masses can be

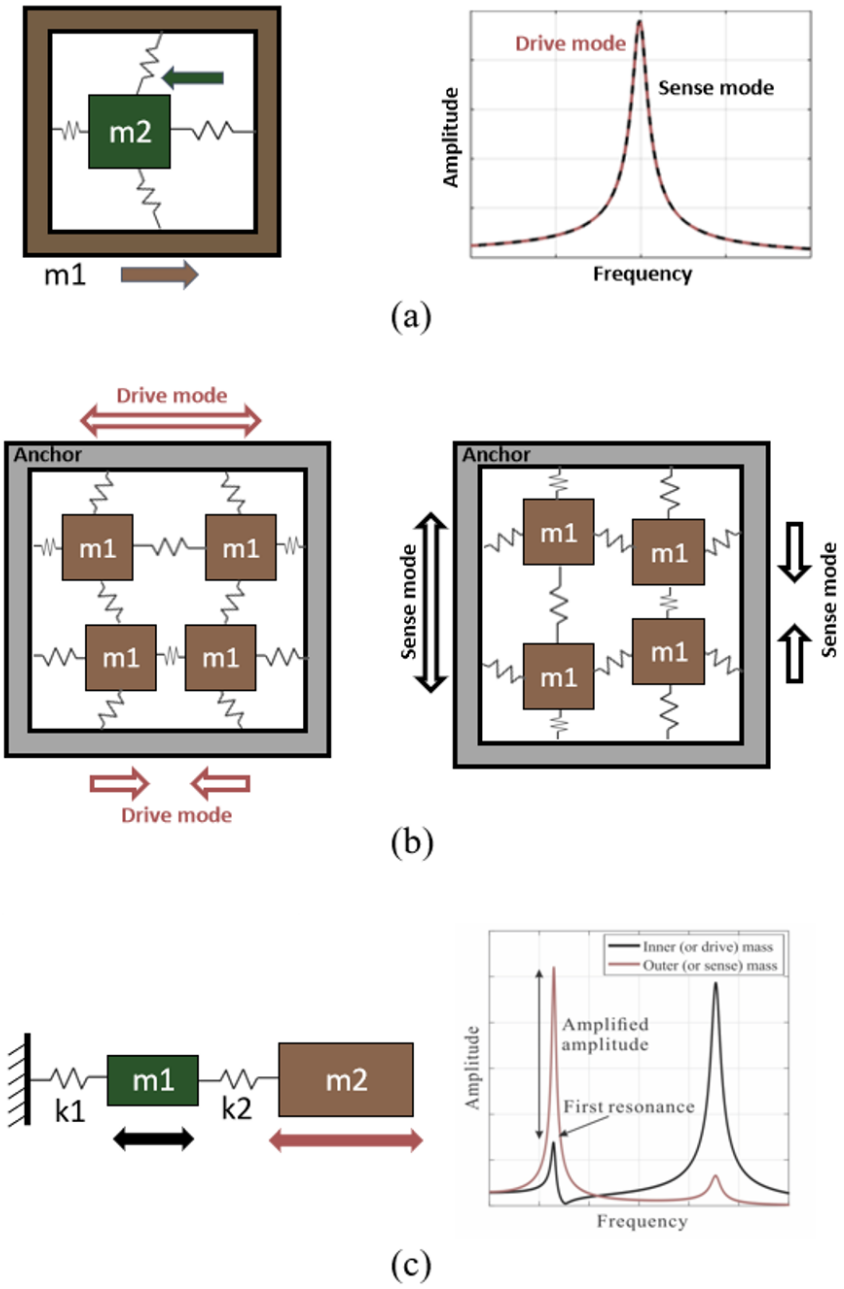

Figure 1.5: Examples of multi-mass gyroscopes: (a) dynamically balanced two-mass system, [67], (b) dynamically balanced quad-mass system, [68], and (c) dynamically amplified system, [69].

susceptible to high-g shocks and intense vibrations. The different effects of the temperature-induced stresses and frequency shifts on the multi-mass can lead to long-term bias and scale-factor drifts to degrade the gyroscope performance. Thus, the mitigation strategies are needed.

1.3.4 Compensation of Structural Imperfections of Micro-HRGs

Development of miniaturized FS HRGs with high stiffness symmetry, low energy dissipation, and inherent structural robustness for implementation of precision rate and rate-integrating MEMS CVGs has been of high interest in recent years. This section presents the challenges and efforts in the realization of high resolution FS micro-HRGs.

1.3.4.1 Methods for Frequency Mismatch Reduction

Fabrication of FS micro-shells typically starts with a thermo-elastic "blowing" of FS device layer, such as a high-temperature micro-glassblowing process [75, 76, 49] or blow-torch molding process [77, 78], followed by a subsequent mechanical release procedure, such as mechanical lapping, chemical–mechanical polishing (CMP) [34, 79], or a laser-assisted cutting process [80, 81]. Conventionally, structural symmetry is essential to achieve a high precision CVG. Imperfections during the fabrication of the micro-shell structure can introduce axial asymmetry and change the mode shapes. These imperfections are caused by the non-uniform temperature distribution during the glassblowing process, misalignment between the ideal and actual lapping planes during the release step, and variation of the device layer thickness created during the hydrogen fluoride (HF) wet etching [82]. The imperfections induced by processing would result in frequency and damping mismatches and quadrature coupling between the operational mode pairs, which not only degrade the gyroscope sensitivity, but also contribute significantly to the noise sources of a micro-HRG, thus impacting the random noise errors, bias instability, and dynamic range. In this section, we review various methods reported in literature to reduce the frequency split of the device.

Electrostatic tuning is a common active-tuning method to compensate for frequency splits in MEMS gyroscopes by employing non-linear electrostatic forces to selectively modify the effective stiffness of a certain operational mode [83, 84, 85]. The compensation accuracy de-

pends on the precision of control of the tuning voltages. It is challenging for control electrics to provide a large magnitude of tuning voltage with the required precision. Increasing the tuning voltage amplitude would also introduce non-linear dynamics in the device and result in an amplitude-frequency coupling which would degrade the gyroscope's noise performance [86].

Therefore, to enable reduction of tuning voltages and achieve high accuracy electrostatic compensation, permanent modifications of HRGs are first engaged for reducing large as-fabricated frequency splits, followed by relatively low tuning voltages to achieve a mode-matched operation desirable for high angular rate sensitivity and whole angle mode of operation.

Methods of passive mechanical trimming techniques of the micro-shell structure are generally based on a permanent modification of the structure by means of selectively removing material from the vibrational element, such as using a high resolution micro-ultrasonic machining [87], ion-beam etching [88], chemical etching [89], or directional lapping [82]. Frequency split reduction from a few tens of Hz to sub-Hz have been demonstrated in many applications using these techniques.

1.3.4.2 Quality Factor Improvement of Micro-HRGs

In addition to structural symmetry, the quality factor is another key parameter in micro-machined HRGs. For example, increasing the Q-factor reduces the energy consumption, increases the thermomechanical signal-to-noise ratio (SNR), and improves in-run noise performance, such as lowering the threshold of bias instability and Angle Random Walk (ARW) [21, 90]. Utilizing the ultra-low CTE of FS structural material and the dynamically balanced degenerate mode pair, such as the n = 2 or n = 3 mode, Q_{TED} and Q_{anchor} of FS HRGs are typically on the order of few millions or few tens of millions, to the point where the

contribution of surface loss becomes dominant [34, 91].

Methods for surface loss reduction tend to improve surface quality using different post-processing treatments. Thermal-related polishing, such as flame polishing using either natural gas [37] or forming gas [36], was reported to increase the quality factor of FS structures by removing the surface contaminants and defects. The quality factor of FS Cylindrical Resonator Gyroscope (CRG) was improved significantly by six times to the order of 25 million using NH4HF2 chemical etching for 1h at the cost of increased surface roughness and reduced resonant frequency [92]. The reason was the removal of sub-surface damage and micro-cracks introduced during the lapping and polishing of the surface [93]. Annealing in nitrogen for 9h at 950°C was reported to increase the quality factor by two times [94]. The increase in quality factor was believed to be the result of the improved surface roughness and reduced thermal stresses originated from nonisothermal fast cooling after micro-glassblowing of HRGs.

Due to electrically non-conductive property of the FS structural material, a thin-film metal coating is deposited onto the sensing element to bias the proof-mass and electrostatically excite and detect the motion of a FS micro-shell resonators. Typically, a few tens of nanometers of the metal layer thin films – or a combination of metals, such as Ir, Cr, Cr/Au, or Ti/Au – are coated onto the FS resonators using a sputter or an e-beam evaporator, [94, 95]. Metallization of the FS results in an increase in surface dissipation and a reduction in the quality factor [96]. Efforts to minimize mechanical losses by reducing the metal coating thickness in FS resonators can lead to a significant increase in electrical resistivity of the coated layer [97] and result in a large electrical resistance in the gyroscope's signal path. Metal annealing at 300°C has been experimentally demonstrated to change the stress and roughness of the metal layers of FS birdbath resonators, but both quality factor improvement and deterioration were reported [98].

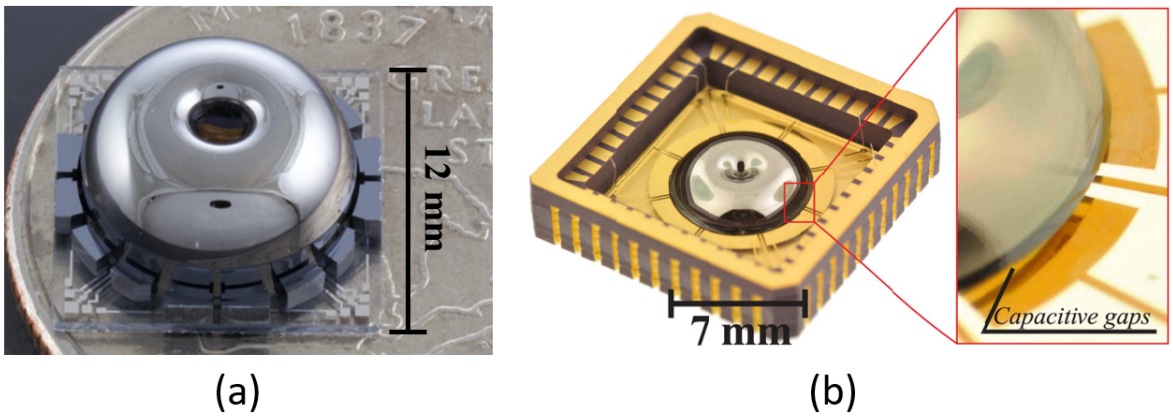

Figure 1.6: Illustration of (a) a FS micro-machined Precision Shell Integrating (PSI) gyroscope [103] and (b) a FS Microglassblown Wineglass gyroscope [76].

1.3.4.3 Control of Capacitive Gaps of Micro-HRGs

To implement the 3D FS micro-shell structures to operate as a CVG, an assembly procedure is also needed to rigidly bond the resonator to a substrate for capacitive actuation and detection using either in-plane peripherally distributed electrodes [99] or out-of-plane planar electrodes [76], as illustrated in Fig. 1.6. Due to limitations in accuracy of the integration step, assembly misalignment at any of the six-DOF of the sensor position and orientation would lead to uneven capacitances of the shell sensors and form a more complex electromechanical system compared to a 2D MEMS sensor [100, 101]. The nonuniform capacitive gaps caused by the assembly errors impact the electrostatic actuation efficiency, motion detection sensitivity, and stiffness adjustment flexibility, thereby influencing the structural symmetry, electrical noise, and overall gyroscope performance [86, 102].

Approaches of controlled capacitive gaps could be achieved with the aid of a uniform sacrificial layer between the movable proof-mass and anchored electrode pads or spacer shims during the bonding step. In [104], the uniform $<5\mu$m capacitive gaps between the rim of the micro-shell and the planar electrodes were demonstrated using the electroplated Nickel layer as the sacrificial layer, which was selectively formed on the planar substrate prior to shell attachment. The ratchet mechanisms and rack gears were used to achieve the movable

electrode mechanism on the substrate [105]. It demonstrated a positioning resolution of 10 μm of the capacitive gap. Various methods have been reported in [106] to control the capacitive gaps of micro-shell resonators. The growth of the seed layer deposited onto the in-plane discrete electrodes to fill the gaps between the sacrificial layer coated onto the micro-shell resonator and the electrode pads was disclosed. The method of using movable jigs and latch mechanisms to align the micro-shell with respect to the center of the electrode substrate was also reported in [106]. However, the limitations of those approaches are that the techniques are typically restricted to some specific micro-shell resonators or very difficult to realize.

1.4 Research Objective

A technological gap exists in the MEMS inertial sensors between the high-performance low operational frequency gyroscopes and structural robustness against the environmental variations. For the high resolution MEMS CVGs, the multi-mass structures with outstanding performances in various aspects motivate the development of new designs with enhanced sensitivity, low noise characteristics, as well as environmental immunity to satisfy the requirements in a broad range of applications. This dissertation aims to develop new MEMS planar high-resolution CVGs with add-on mechanisms to achieve low energy dissipation, high sensitivity, long-term bias stability, and shock and vibration tolerance.

To achieve high-resolution inertial navigation, the development of planar MEMS gyroscopes that achieve a high quality factor, large signal-to-noise ratio, and high sensitivity is the key. Implementation and realization of dynamical amplification concept in designing such gyroscope is a good candidate to increase the amplitude of vibration, hence, improving sensitivity and reducing noise. A development of evaluation electronics and analysis of detection schemes are also studied to further improve the gyroscope's noise characteristics. To increase the environmental immunity of the low-frequency MEMS inertial gyroscopes

against mechanical shocks and vibrations, a shock survival mechanism is developed based on a wafer-level fabricated TWI cap stage and a developed trap-an-hold strategy.

Another objective of this thesis is the development and realization of micro-machined FS HRGs for precision operation through environmental variations. The dual hemispherical shell gyroscope is a good candidate as a potential solution to achieve high quality factor and low noise performance while providing the high-shock tolerance. However, challenges of realizing a high accuracy gyroscope performance using the sensor have not yet been addressed. In this dissertation, the fabrication process of implementing the capacitive actuation and detection in the gyroscope is first designed and demonstrated. Then, the impacts of metallization and assembly errors on performance of micro-scale HRG implementations are explored and addressed to realize a mode-matched gyroscope operation desirable for high angular rate sensitivity and environmental robustness.

1.5 Dissertation Outline

In Chapter 2, we report on development of a Trap-and-Hold (TAH) concept intended to increase survivability of high-performance low-frequency MEMS CVGs against mechanical shocks and vibrations. The TAH concept utilizes out-of-plane electrodes to electrostatically excite the gyroscope's proof-mass at resonance in the direction perpendicular to the substrate, trap the proof-mass electrostatically, and then keep the sensor structure locked to the substrate during the events of shock. To demonstrate the mechanism, a Dynamically Amplified dual-mass MEMS Gyroscope (DAG) is used as a test vehicle. The design architecture and optimization are presented for selecting geometry parameters to increase the modal frequency separation and mitigate energy dissipation through TED and anchor loss to achieve the desired gyroscope performance. The scaling of the resonant frequency of operational and parasitic vibrations modes with respect to the device layer thickness, concentric

ring suspension radius, dual masses, and anchor radius are analyzed using the finite element parametric modal analysis. We discuss the effects of frequency mismatches and quadrature errors on gyroscope performance. A noise characteristics of 0.8 deg/hr in-run bias stability and 0.007 deg/rt-hr ARW are experimentally demonstrated. Based on the development of DAGs, we discuss our fabrication process to realize the TAH mechanism on DAGs and present the initial experimental results to improve the gyroscope's shock survivability while preserving its noise characteristics. Additionally, a process for dust-proof cap stage with both in- and out-of-plane Through-Glass-Vias created by an in-house glass re-flow process is proposed. The cap stage is compatible with both the in-plane operation of MEMS resonators and out-of-plane TAH mechanism.

In Chapter 3, we report on development and realization of precision measurements of Fused Silica (FS) MEMS Dual-Shell Gyroscopes (DSGs). The FS DSG architecture with a fixed-fixed anchor for double-sided support of the sensing element and an increased bonding area is capable of providing continuous high-precision gyroscope operation through extreme events of shock and vibration. To allow for accurate capacitive actuation and detection of motion, a Thru-Glass-Vias (TGVs) planar electrode substrate is designed and fabricated. We study the assembly errors introduced by the misalignment of the integration step and propose an identification method based on static capacitance measurements. We develop an electromechanical model for electrostatic frequency tuning of DSGs taking into account the effect of assembly errors to realize the mode-matched gyroscope operation for high angular rate measurements. Algorithms for asynchronous and synchronous compensations of the n = 2 and n = 3 mode pairs are theoretically derived using the proposed model and experimentally validated on a DSG prototype, followed by the demonstrations of gyroscope operation.

In Chapter 4, we report the effect of metallization on performance of FS Micro-machined capacitive vibratory gyroscopes. Metal coating provides electrical conductivity to enable electrostatic actuation and detection of motion, but reduces the quality factor of FS res-

onators. To achieve high-performance CVG operation, we study the effect of the metallization material and its thickness on the quality factor and electrical resistance in FS devices. We establish a link to the in-run noise performance using a developed analytical electromechanical model. A clear influence of varying coating materials and thicknesses on the quality factor and electrical resistance is observed. We demonstrate an existing trade-off between metallization and quality factor to achieve the optimal gyroscope's noise performance. This study concludes that it is necessary to optimize metal coating parameters of FS resonators to achieve optimal gyroscope noise characteristics.

In Chapter 5, a study on the contribution of EAM to the performance of capacitive MEMS CVGs is presented. The EAM is frequently used to eliminate feed-through signals between forcer and pick-off electrodes of resonant microstructures. We study the effect of EAM on dissipation of energy and non-linear dynamics in MEMS CVGs. We present an analytical model, capturing the effect of AC carrier signal on amplitude-frequency coupling, scale factor instability, and in-run noise performance of CVGs. We experimentally conclude that the AC carrier signal in EAM influences the amplitude-frequency couplings along both the drive and sense modes of the gyroscope through modifying the non-linear electrostatic stiffnesses, which is also proven to be one of the dominant sources of both scale factor nonlinearity and frequency instability in the near-mode-matched gyroscope, operating in the open-loop rate mode.

Finally, Chapter 6 concludes the dissertation with a summary of contributions and future research directions.

Chapter 2

Trap-and-Hold Shock Survival Mechanism

In this chapter, we propose an approach to the realization of precision MEMS CVGs capable of surviving the extreme events of shock and vibrations while the sensors are not in operation. In Section 2.1, a Trap-and-Hold (TAH) shock survivability strategy intended for low frequency inertial devices is developed. We first present the shock survival mechanism by engaging a modification in sensor fabrication to allow switching from Mode (1), high performance gyroscope operational mode, to Mode (2), high shock stability mode. To demonstrate the TAH concept, a design of MEMS Dynamically Amplified dual-mass Gyroscope (DAG) as the test vehicle is introduced and implemented, followed by a design optimization and an electrostatic tuning algorithm for compensating the fabrication imperfections in Section 2.2. The high sensitivity angular rate measurement with low noise characteristics is also demonstrated in the same section. In Section 2.3, the high-performance DAGs are chosen for illustration purposes. We present two thru-wafer-interconnects (TWIs) fabrication processes with out-of-plane electrodes per the constraints of DAGs to realize the TAH strategy. Section 2.4 then evaluates the mechanism by applying multiple shocks to the gyroscope.

Fundamental characteristics of the device are validated before and after shocks. Finally, the chapter is concluded with Section 2.5.

2.1 Shock Survival Mechanism

MEMS inertial sensors are good candidates for operation in extreme environments due to their relatively small size and mass. However, it is a challenge for high performance gyroscopes to be immune to shocks while preserving sensitivity. In general, high precision MEMS CVGs are designed for operating at a relatively low operational frequency, on the level of 5 kHz, for effective electrostatic tunability and high signal-to-noise ratio. The devices are therefore susceptible to mechanical shock due to their increased proof-mass and weak suspension. For shock survivability, gyroscope structures need to be stiffened. Devices having high operational frequencies (>200 kHz) may capable of withstanding large magnitude shocks without any protection, [10]. For example in [107], operational frequencies of the device was increased to >100kHz in an attempt to increase shock resistance, with the cost of sacrificing the SNR. An increase in stiffness limits gyroscope's amplitude of response, thus affecting sensitivity and tunability. The increased stiffness is also a hindrance to implement the multi-mass structures for precision of measurements [108, 68].

The Trap-and-Hold (TAH) architecture is an add-on mechanism to such architectures to improve shock resistance of the low frequency devices. It utilizes out-of-plane electrodes along the non-operational mode to selectively trap the proof-mass before the events of shock, effectively immobilizing the device in preparation for shocks. The proposed implementation is similar to the dynamic switching idea used in bistable mechanisms, [109], where the two stable modes of a device are: a high sensitivity operational mode and a Shock-Lock mode for shock survival. It should be noted, the shock survival approach presented in this chapter is intended for switching to the Shock-Lock mode before the events of shock and is not intended

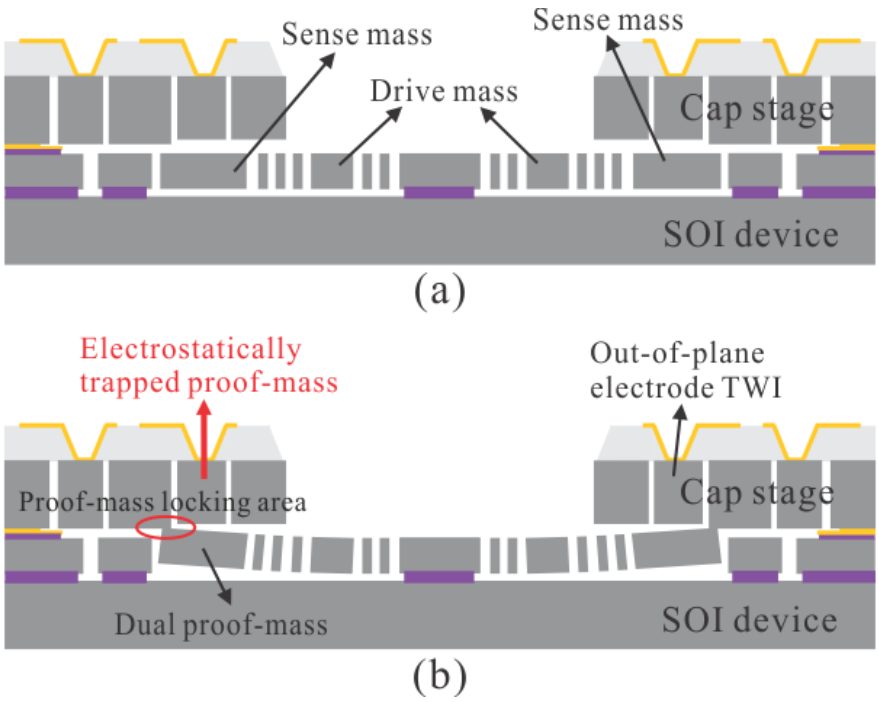

Figure 2.1: Schematic diagram of TAH concept. (a) Normal position of the dual-mass gyroscope before and after TAH (Normal Operation). (b) TAH engaged, immobilizing the sensor throughout the duration of shock (Shock-Lock).

for operation-through-shock.

A typical TAH-engaged operation is demonstrated in Fig. 2.1. At the beginning, the device is in its neutral position or in the Normal Operation mode, Fig. 2.1(a). Right before the event of shock, the device is transitioned from the Normal Operation mode to the Shock-Lock mode. A DC voltage is applied to the out-of-plane electrodes to actuate the proof-mass perpendicular to the substrate at the out-of-plane resonance frequency, driving the edge of the proof-mass to make a contact and temporary immobilizing the structure. The device remains at its Shock-Lock mode throughout the event of shock, Fig. 2.1(b). After the shock, the electrostatic DC voltage is removed to allow a transition of the proof-mass from the Shock-Lock mode back to the Normal Operation mode. As the proof-mass is released to return to its neutral position, the device restores its normal operation of the angular rate sensing.

2.2 Dynamically Amplified Dual-mass Gyroscopes

To demonstrate the proposed TAH concept on high performance CVGs, we designed a dual-mass vibratory gyroscope as the test vehicle. This sensor was chosen for a low operational frequency, an increased amplitude of sensing response to enhance sensitivity and signal-to-noise ratio, and thus a capability of precision gyroscope measurement. Toward this goal, a MEMS Dynamically Amplified dual-mass vibratory Gyroscope (DAG) with a dynamic amplification concept is introduced, and the design optimization is discussed in this section.

2.2.1 Design of DAG

A dual mass-spring structure of a dynamically amplified system is shown in Fig. 2.2(a). The structure is comprised of two mechanically coupled proof-masses: a drive mass (m_1) and a sense mass (m_2). It utilizes an increased number of degrees of freedom (DOF) to achieve amplitude amplification between the drive and sense masses. The equations of motion are derived using a dual mass-spring-damper model [72]:

$$m_1\ddot{x}_1 + c_1\dot{x}_1 + (k_1 + k_2)x_1 - k_2x_2 = F_x, \tag{2.1}$$

$$m_2\ddot{x}_2 + c_2\dot{x}_2 + k_2x_2 = k_2x_1, \tag{2.2}$$

where m_1 and m_2 represent the drive and sense masses, k_1 and k_2 are the respective stiffness of the first and the second suspension elements, and c_1 and c_2 are damping coefficients associated with each mass. The parameter x_1 is the displacement of the drive mass and x_2 is the displacement of the sense mass, both along the x-axis. F_x is the sinusoidal driving force applied to the drive mass along the x-axis. The frequency of the driving force is at the resonant frequency of the coupled dual-mass system, Fig. 2.2(b), where the dynamic

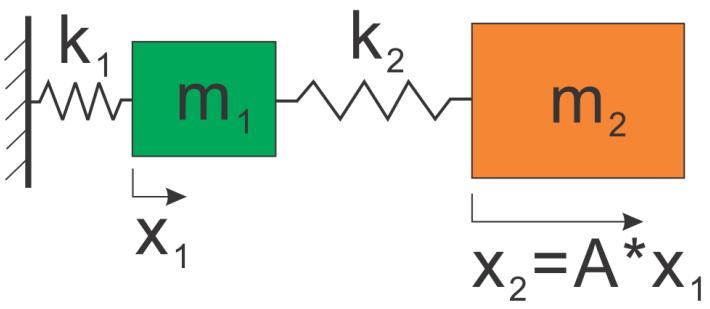

(a)

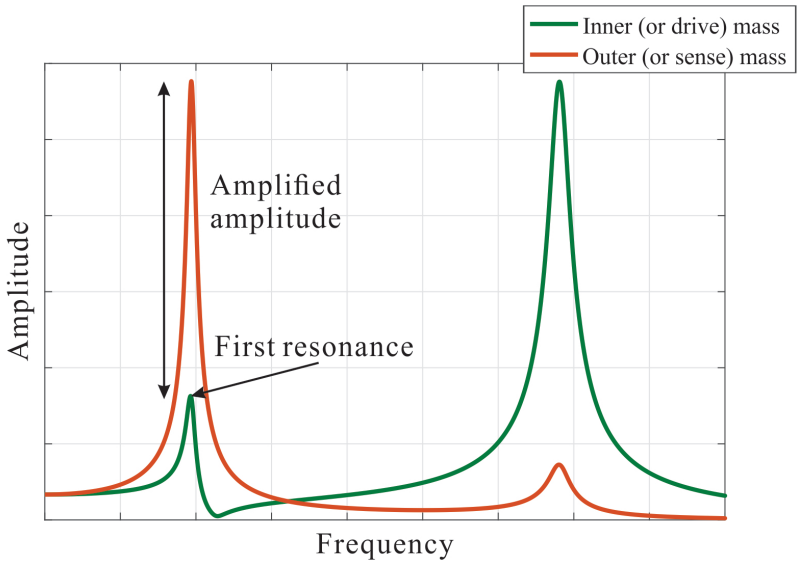

(b)

Figure 2.2: (a) Dual mass-spring structure. By actuating the drive mass, m_1, a large amplitude of the sense mass, m_2, is achieved. (b) Frequency response of the architecture with amplitude amplification.

amplification condition is satisfied. The amplitude amplification factor, A, is expressed as

$$A = \frac{x_2}{x_1} = \frac{\omega_2^2}{\omega_2^2 - \omega^2 + j\omega\frac{c_2}{m_2}}. \tag{2.3}$$

Utilizing the amplitude amplified concept in the dual-mass design, we increase the number of DOF of the system from two to four. In our implementation, the device comprises an inner drive-mass attached to a central anchor and connected to an outer sense-mass by concentric ring suspensions, Fig. 2.3. For the dual-mass structure, the equations of motion along the

drive axes (x_1 and x_2) and sense axes (y_1 and y_2) are given as [72]:

$$\ddot{x}_1 + \frac{c_1}{m_1}\dot{x}_1 + \frac{k_1 + k_2}{m_1}x_1 - \frac{k_2}{m_1}x_2 = \frac{F_x}{m_1} + 2\Omega\dot{y}_1, \tag{2.4}$$

$$\ddot{x}_2 + \frac{c_2}{m_2}\dot{x}_2 + \frac{k_2}{m_2}x_2 = \frac{k_2}{m_2}x_1 + 2\Omega\dot{y}_2, \tag{2.5}$$

$$\ddot{y}_1 + \frac{c_1}{m_1}\dot{y}_1 + \frac{k_1 + k_2}{m_1}y_1 - \frac{k_2}{m_1}y_2 = \frac{F_y}{m_1} - 2\Omega\dot{x}_1, \tag{2.6}$$

$$\ddot{y}_2 + \frac{c_2}{m_2}\dot{y}_2 + \frac{k_2}{m_2}y_2 = \frac{k_2}{m_2}y_1 - 2\Omega\dot{x}_2. \tag{2.7}$$

In those equations, F_x and F_y are the sinusoidal driving forces applied to the inner mass and Ω is a constant input angular rotation along the z-axis. Parameters x_1 and y_1 are displacements of the inner mass (or "drive mass") and x_2 and y_2 are displacements of the outer mass (or "sense mass"). In the primary and secondary modes, m_1 and m_2 represent the masses of the inner and outer masses, k_1 and k_2 are the respective stiffness of the inner and outer ring suspensions, and c_1 and c_2 are damping coefficients associated with each mass.

The drive frequency of interest is the first resonant frequency of the dual-mass system, as depicted in Fig. 2.2(b). The two resonant peaks in Fig. 2.2 of the dual-mass system, $\omega_1^{'}$ and $\omega_2^{'}$, are [72]:

$$\omega_1^{'2}, \omega_2^{'2} = \frac{1}{2}\left[{\omega_1}^2 + {\omega_2}^2 + \frac{k_2}{m_1}\right] \mp \frac{1}{2}\sqrt{\left({\omega_1}^2 - {\omega_2}^2 + \frac{k_2}{m_1}\right)^2 + 4\frac{k_2}{m_1}{\omega_2}^2}, \tag{2.8}$$

where $\omega_1 = \sqrt{k_1/m_1}$ and $\omega_2 = \sqrt{k_2/m_2}$.

The drive mass oscillates at the first resonance frequency in response to a drive voltage provided by the electrodes, and the sense mass follows the drive mass, but responds with an amplified amplitude. That means the dual-mass system operates in the translational mode with amplitude amplification at the first resonant frequency along both x- and y-axis,

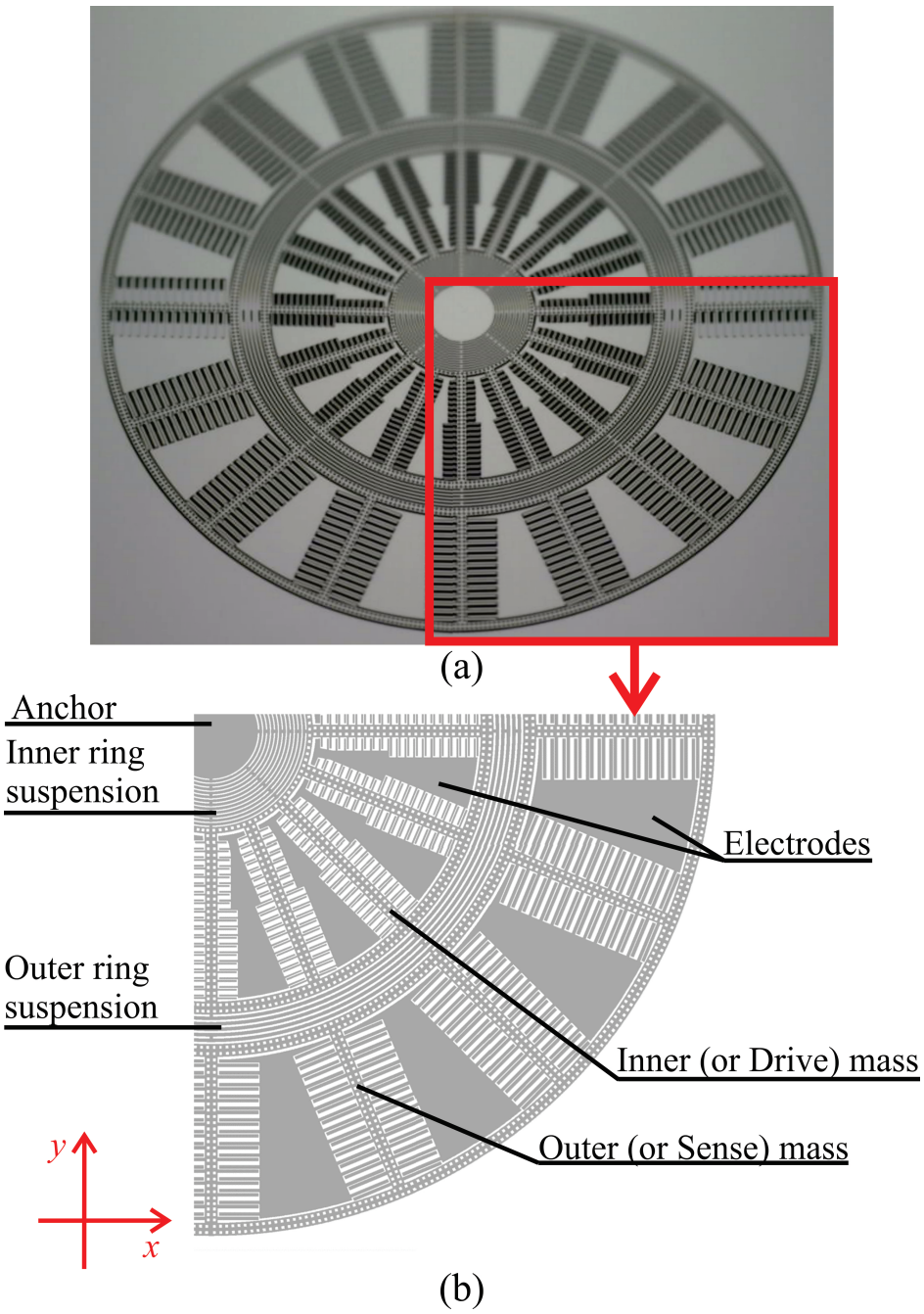

Figure 2.3: (a) A dynamically amplified dual-mass vibratory gyroscope fabricated using an in-house 100 μm SOI process; (b) Nomenclature of a close-up of the quarter of the device.

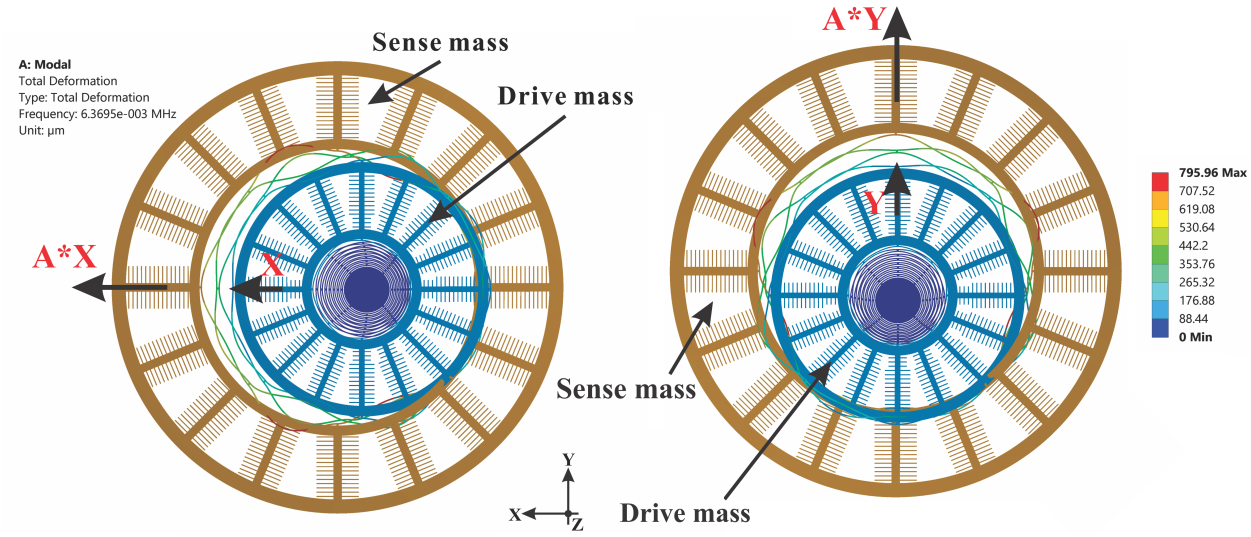

Figure 2.4: FEA model of the amplitude amplified dual-mass structure, showing operational modes along (left) drive-mode direction (x-axis) and (right) sense-mode direction (y-axis).

Fig. 2.4. Thanks to the amplitude amplification, the dual-mass architecture possesses larger amplitude of response, smaller (more linear) amplitude of actuation, and higher sensitivity. However, the increase in DOF increases the footprint of the device and therefore its susceptibility to shock and vibrations.

2.2.2 Design space exploration

Improvement of noise characteristics of DAGs through enhancing the quality factor (Q-factor) is essential to realize a high-resolution performance. Q-factor is directly related to sensitivity, power consumption, and noise characteristics [22] that depends on the design parameters. Scaling of modal resonant frequencies and energy dissipations through Thermoelastic Damping (TED) and substrate loss with respect to the operational frequency and geometry parameters are analyzed using the Finite Element (FE) parametric modal analysis and presented in this section.

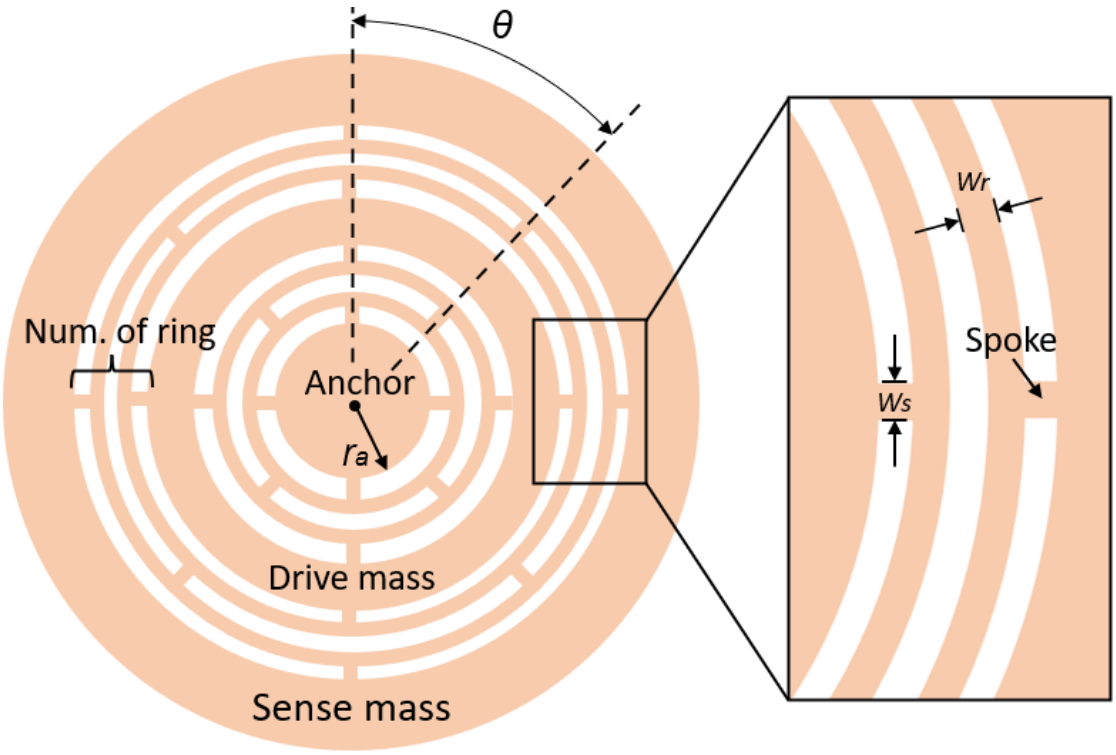

Figure 2.5: Schematics of geometry parameters of a DAG architecture. The number and thickness of the ring suspensions, n_{out} and W_r, width of the interconnecting spokes, W_s, angle between the interconnecting spokes, θ, and anchor radius, r_a are indicated on the top view of the DAG.

2.2.2.1 Effect of DAG Geometry on Modal Frequency Separation

The DAG typically comprises an inner drive-mass attached to a central anchor and connected to an outer sense-mass by concentric ring suspensions. The main geometry parameters in the DAG design are illustrated in Fig. 2.5, including the number of outer ring suspensions, n_{out}, thickness of the ring suspensions, W_r, width of the interconnecting spokes, W_s, angle between the interconnecting spokes, θ, anchor radius, r_a, and device thickness, W.

Modal frequency separation between the resonant frequency of operational and parasitic vibrations modes has to be considered during the design of MEMS resonators. A small frequency separation would result in energy dissipation via nearby spurious modes to reduce the Q-factor of a MEMS resonator [40]. Fig. 2.6 shows the first six vibration modes of

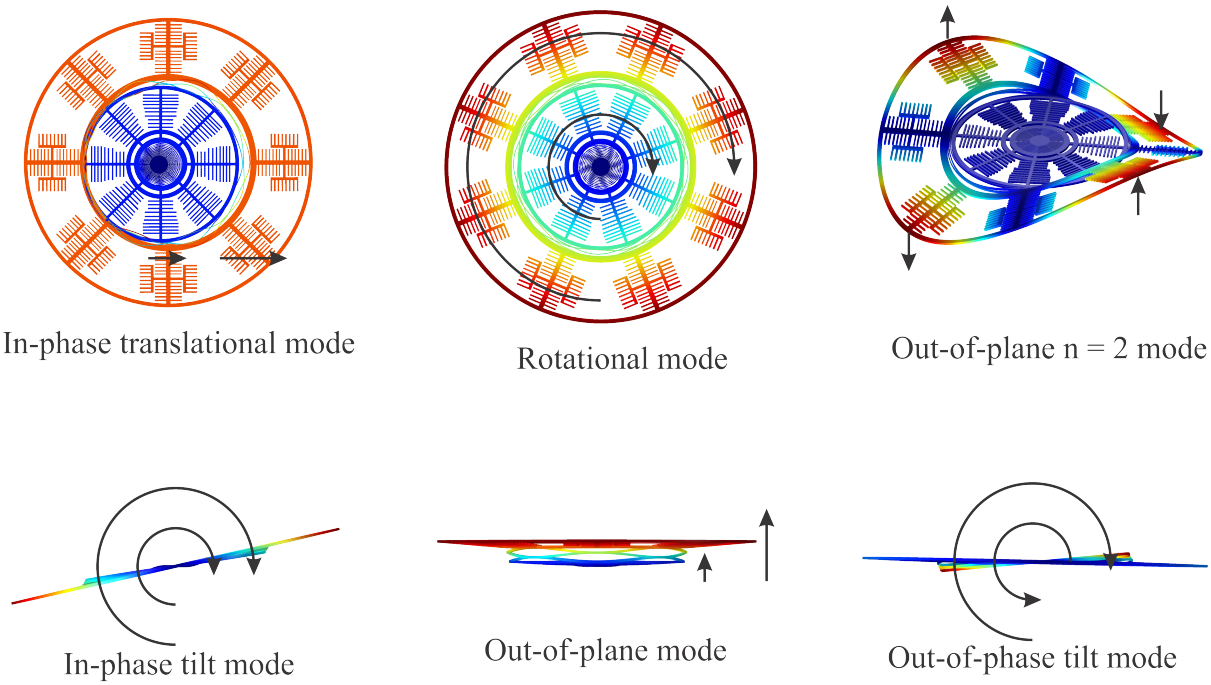

Figure 2.6: FEA model of the first six resonance modes of a typical DAG structure. The in-phase translational degenerate mode, satisfying the dynamical amplification concept, is preferable to use for rotation sensing due to a higher gain [74].

typical DAG structures anchored at the central stem. For an in-phase translational frequency of interest, a dual-mass resonator can be obtained from a different combination of design parameters. The mode separation depends on selection of the geometric parameters. A parametric FE modal analysis was performed to study the frequency scaling of the spurious and operational resonant modes, as shown in Fig. 2.7. The result demonstrated a possibility of achieving a large frequency separation and ordering the resonance modes of a DAG, with parasitic modes far away from the frequency of the operational mode, to avoid the dissipation of energy through mode coupling.

2.2.2.2 Effect of DAG Geometry on Thermoelastic Damping

The Q-factor due to Thermoelastic Damping, Q_{TED}, in Silicon MEMS resonators is mainly related to the resonant frequency. The Q_{TED} of Silicon DAGs were calculated for the in-

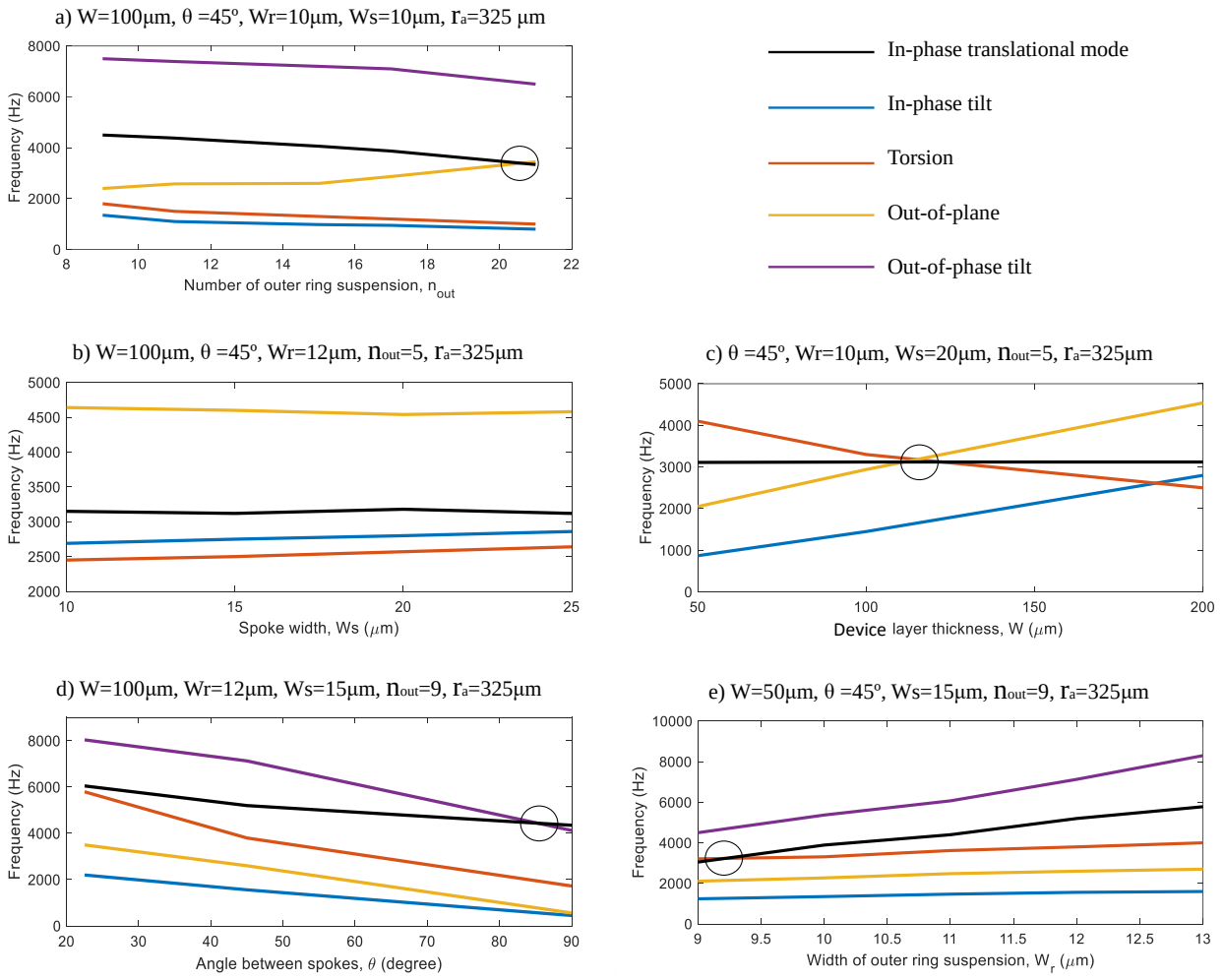

Figure 2.7: Scaling of the resonance frequencies with respect to the geometry of dual-mass resonators. The order of vibrational modes can switch at certain geometries marked by the circles. It indicates that the mode order of the operational mode and its closest parasitic modes changes.

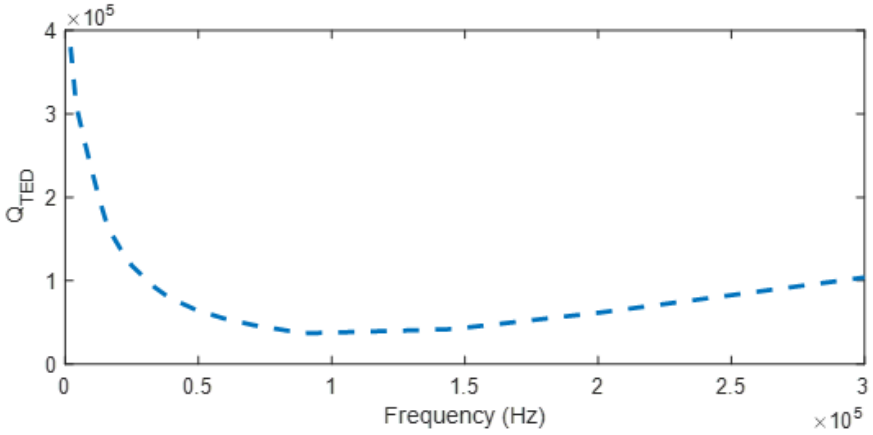

Figure 2.8: Simulated TED quality factor limit, Q_{TED}, as a function of operational frequency, for Silicon DAGs.

phase translational mode from FE simulations using COMSOL Multiphysics. The Q_{TED} is plotted as a function of the in-phase translational mode frequency in Fig. 2.8, for a constant anchor radius of 500 μm, spoke width of 10 μm, spoke angle of 45°, ring width of 30 μm, and the device thickness of 100 μm. It was also assumed that the numbers of the inner and outer concentric rings were both five during the simulation.

The scaling of Q_{TED} caused by the geometrical parameters is plotted in Fig. 2.9. For a constant resonant frequency, ring width, anchor radius, and device thickness, Fig. 2.9(a), the Q_{TED} increases slightly with increasing the number of concentric ring suspension. Fig. 2.9(b), (c), and (d) show the impacts of the ring width, spoke width, and angle between spokes on the Q_{TED} while other parameters were kept constant. The effect of the device layer thickness on the Q_{TED} was observed and shown in Fig. 2.9(e). The anchor radius had a minor impact on the Q_{TED}, and the results are plotted in Fig. 2.9(f).

2.2.2.3 Effect of DAG Geometry on Anchor Loss

In addition to Q_{TED}, reduction of the anchor loss is an effective method to increase the quality factor in the DAGs. Because of the unbalanced force applied to the anchor of the

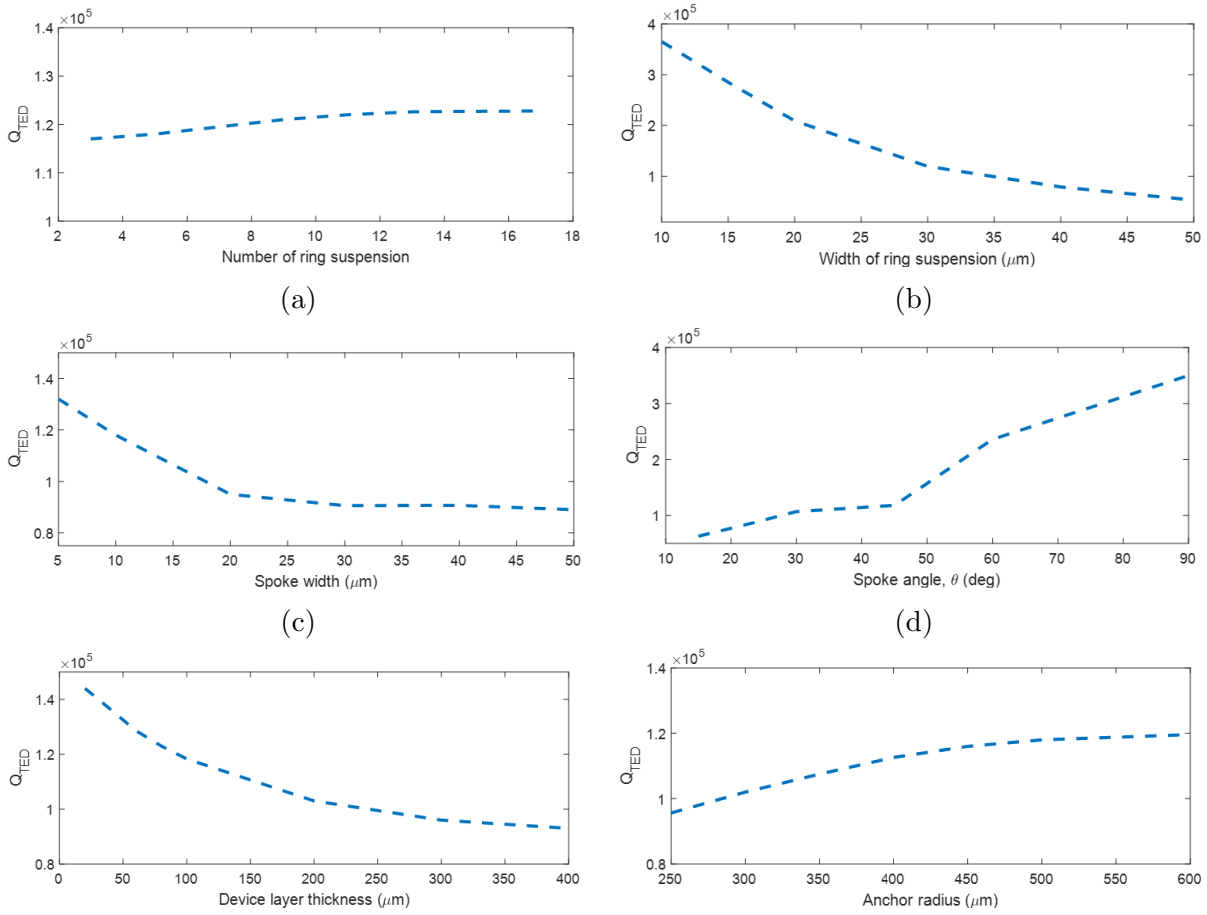

Figure 2.9: Scaling of the Q_{TED} with respect to the geometrical parameters of DAGs.

in-plane translational mode DAG, the anchor loss is highly related to the anchor geometry and usually smaller than their Q_{TED} limit, which becomes the main limitation of the quality factor. Fig. 2.10 shows the effect of anchor radius on the Q_{anchor} with a constant operational frequency and all geometric parameters, including the number of the outer ring suspension, spoke width and angle, ring width, and the device thickness.

To mitigate the downside and to reduce the anchor loss, we studied the designs with stress contained both inside of the DAG suspensions and applied to the center anchor. The large displacement of the mass would create a stress concentration contained inside of the suspension. The stress would relieve from outer to inner concentric rings and finally reach or apply to the center anchor. A simulation result of a single mass resonator with 43 concentric rings

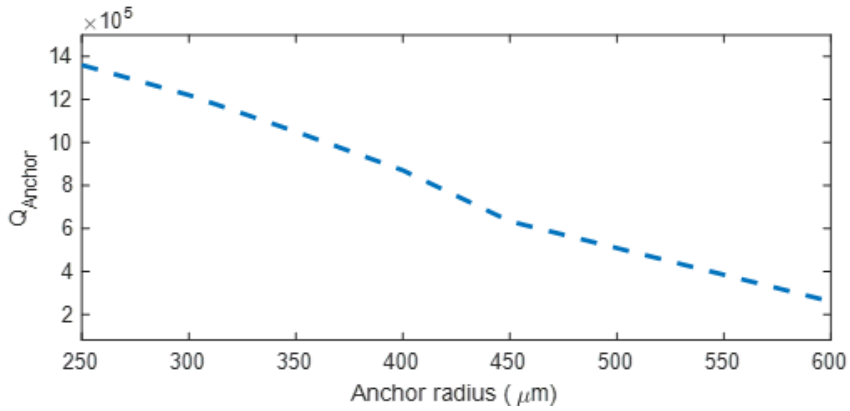

Figure 2.10: Simulated Anchor loss quality factor limit, Q_{Anchor}, as a function of the anchor radius of DAGs.

as its suspension is illustrated in Fig. 2.11(a). The stress contained in each concentric ring of the suspension decreased from the outer ring to the center ring, as intended by design. The maximum stress of each ring is concentrated at the area closed to each spoke, which is the mechanical connection between the rings. Under the 0.5 μm displacement condition, the maximum stress and the average displacement of each ring are shown in Fig. 2.11(b). The effect of the gradually decreased stress from the outer to the center rings in the concentric ring suspension indicates that the minimized stress applied to the anchor could be achieved by utilizing a large number of rings in the inner suspension design and a small anchor radius.

2.2.2.4 Design Parameters of DAGs

The explored design space in previous subsections provides a set of parameters for the DAG geometry at the high quality factor and large modal frequency separation of interest. The analysis of the FE modal simulation results reveals that:

- The modal frequency separation, Q_{TED}, and Q_{anchor} scale differently with respect to resonant frequency and geometrical parameters of the DAG;

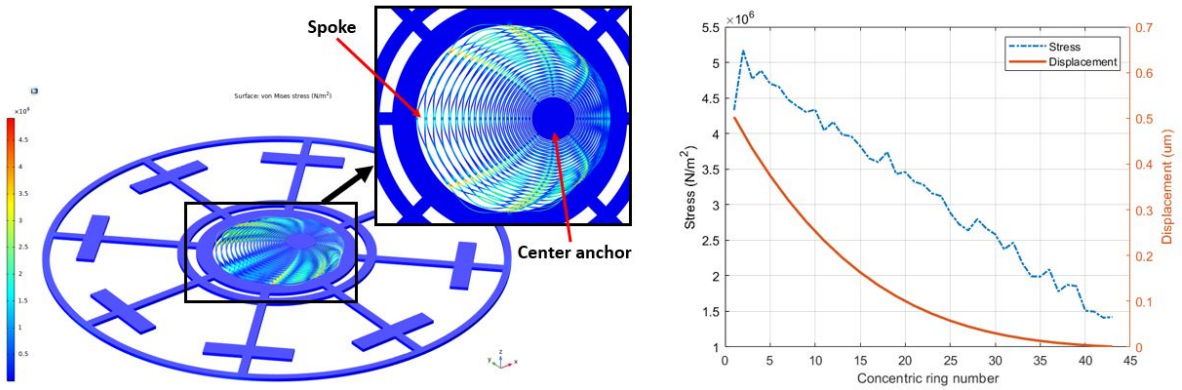

(a) (b)

Figure 2.11: (a) Stress contained in a single mass resonator under 0.5 μm displacement condition with a zoomed-in view on the concentric ring suspension. (b) The maximum stress and displacement of each ring. The ring number is counted from the outer ring (the largest ring in diameter) to the center ring (the smallest ring in diameter).

- The number and width of the outer ring suspension, spoke angle, and device thickness are the main factors impacting the mode ordering of the operational and parasitic modes and have to be considered during the DAG design;
- The resonant frequency, width of the ring suspension, and spoke angle are the main factors impacting the Q_{TED} and have to be optimized during the DAG design;
- Among all geometric parameters listed above, anchor radius and number of inner ring suspension show a dominant effect on the Q_{anchor}.

Based on the above observations, the different scaling of geometric parameters would allow achieving a desired Q-factor and operational frequency to mitigate the noise sources in DAGs. Two optimized Silicon designs of DAGs were presented in this subsection.

The optimized design parameters for increased Q-factor and modal frequency split are designed in coordination with the optimal fabrication parameters to improve yield and reduce frequency mismatch between drive and sense modes. The parasitic modes, such as tilt and out-of-plane modes, are all naturally closed to the operational mode. Increasing the mode splits between operational and parasitic modes to $>$ 1 kHz is first necessary to keep the

Table 2.1: Design parameters of DAG#1 and DAG#2 prototypes

Parameter	DAG#1	DAG#2
Operational frequency, f	4.67 kHz	4.68 kHz
Mode split	1.5 kHz	1.3 kHz
Q_{TED}	528,000	564,000
Q_{anchor}	1,120,000	1,650,000
Number of outer ring suspension, n_{out}	3	5
Number of inner ring suspension, n_{in}	17	22
Ring suspension width, W_r	13 μm	13 μm
Angle between spokes, θ	45 °	45 °
Spoke width (outer ring suspension), W_s	25 μm	25 μm
Anchor radius, r_a	225 μm	225 μm
Device layer thickness, W	50 μm	50 μm
Amplification factor	11.6x	21.5x
Total sensing capacitance	13.1 pF	14.8 pF

energy contained in the operational mode and to reduce the energy loss through parasitic modes. The Q_{TED} and Q_{anchor} are also optimized to reach levels on the order of >500,000 and >1,000,000, respectively.

To fulfill the above requirements in the DAG designs, the design space was reduced to a relatively small region. We completed designs and layouts of two DAGs designs, DAG#1 and DAG#2, shown in Fig. 2.12. The geometric and performance parameters are summarized in Table 2.1. Both DAGs were designed to have more than 0.5M Q_{TED} and were projected to operate at the Q_{anchor} limit, assuming > 1.3 kHz mode split. Besides, the 7 mm footprint of the devices with carefully designed geometric parameters of the drive and sense masses were projected to lead to high total capacitances. The parametric drive electrodes were also included in the designs, which surrounded the sense mass in both sensors, illustrated in Fig. 2.12(a) and (b), enabling the parametric drive capability to further increase the effective quality factor.

The phenomenon of the stress concentration of the dual concentric ring suspensions can be

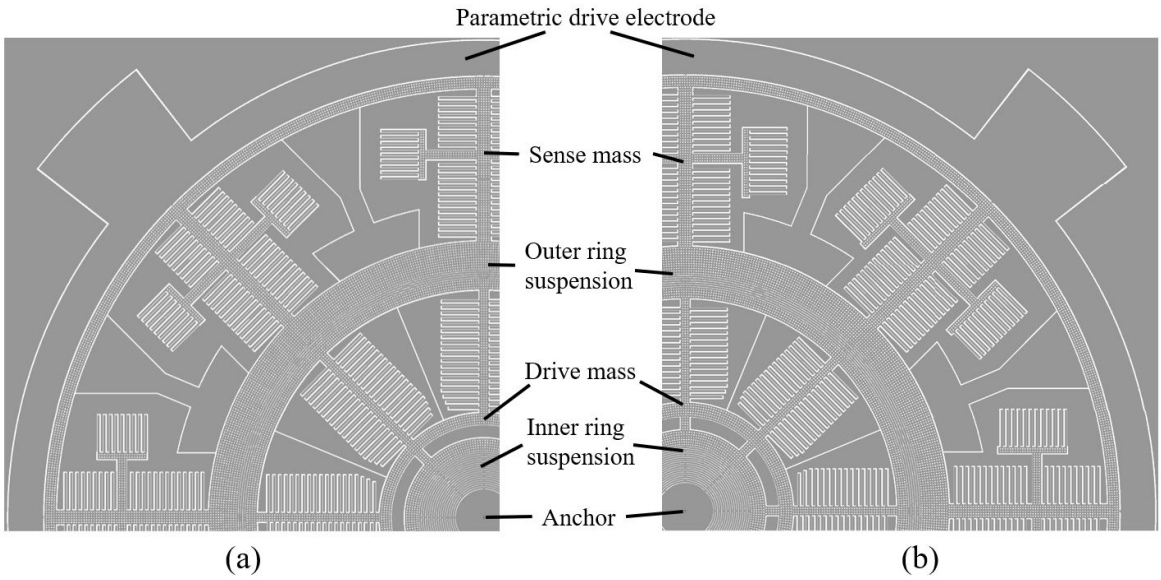

Figure 2.12: Optimized DAG designs for high Q-factor, large mode split, and large capacitance. (a) Design DAG#1 with 11.6 times and (b) design DAG#2 with 21.5 times amplification factors.

also demonstrated in the DAGs. Due to the dynamic amplification of displacement between the two masses, the inner mass will only vibrate in a small amplitude while the outer sense mass remains in a large amplitude. Hence, the stress of a large displacement of the outer sense mass will be mainly concentrated in the outer spring and applied to the inner drive mass instead of spreading the stress into the inner ring suspension and applying it to the center anchor. The stress concentration of the DAG#2 with amplitude amplified by 21.5x under 0.5 μm displacement condition is illustrated in Fig. 2.13(a). The simulated comparison results of the stress concentration in the DAG and the single mass gyroscope are shown in Fig. 2.13(b). There is a sharp decline of the stress between the last ring of the outer suspension and the first ring of the inner suspension in the DAG. The final stress of the DAG with a total of 22 rings in the dual-suspension (orange line) is projected to reduce to 50% with the help of 21.5x amplitude amplification compared to the single mass gyroscope with a 43 ring suspension (blue line). It supports the benefit of stress reduction by utilizing the dynamically amplified dual-mass structure while avoiding the downside of using a large number of ring suspensions.

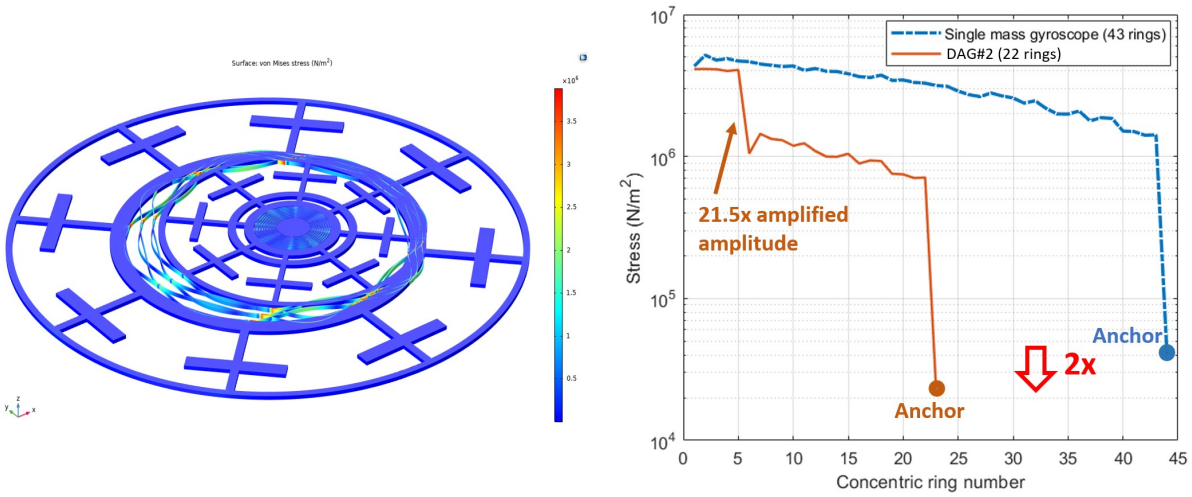

(a) (b)

Figure 2.13: (a) Stress contained in the DAG#2 under 0.5 μm displacement condition. (b) The maximum stress of each ring of the single mass gyroscope (43 rings), presented in Fig. 2.11, and the DAG#2 (22 rings) under 0.5 μm displacement conditions. The average element qualities of meshing are all on the level of 0.65 for precise simulation in COMSOL Multiphysics®. The ring number is counted from the outer ring (the largest ring in diameter) to the center ring (the smallest ring in diameter).

2.2.3 Fabrication of MEMS SOI DAGs

The designed DAG devices were fabricated using the SOI process, presented in Section 2.3, with a footprint of 7mm×7mm on a 8.7mm × 8.7mm die, shown in Fig. 2.14. The process used a 4-inch SOI wafer with a device layer of 50 μm, a buried oxide layer of 5 μm, and a top oxide layer of 1.5 μm. After DRIE and dicing, individual dies were attached to 44-pin ceramic LCC packages and wirebonded for initial gyroscope characterization, as test vehicles for subsequent evaluation of the TAH concept.

2.2.4 Front-end Electronics

A low-outgassing ceramic PCB was designed and used for front-end electronics, as shown in Fig. 2.15. The two-stage ultra-low noise transimpedance amplifier circuits were designed for each sensing channel. The first stage amplification of the gyroscope pick-off signals was

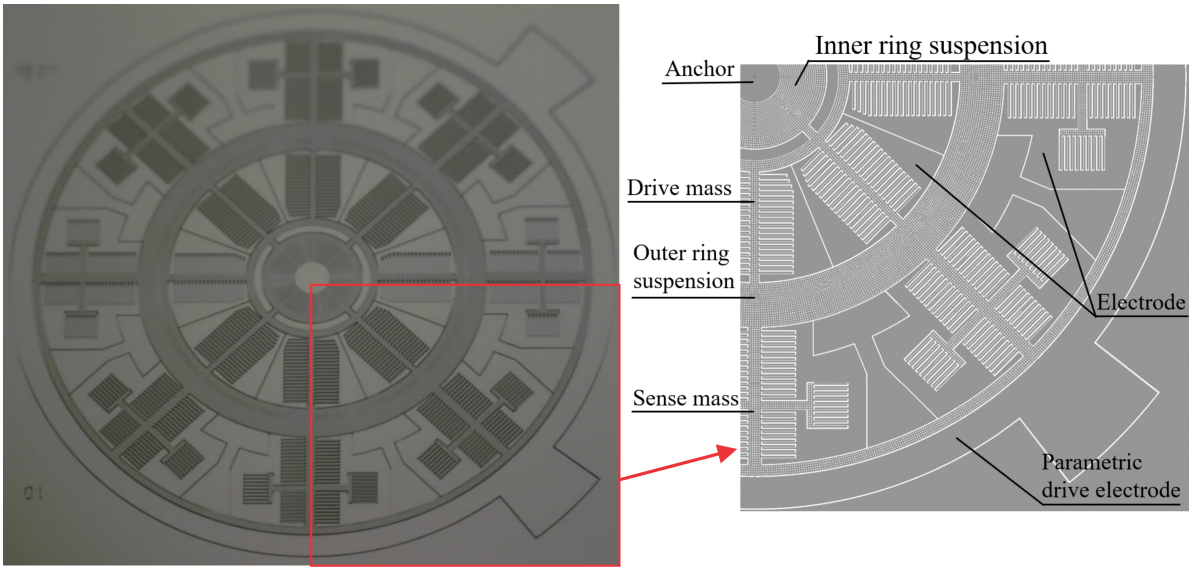

Figure 2.14: An image of the DAG#1 prototype and a close-up view of a quarter of the DAG showing the central anchor, dual-mass architecture, concentric ring suspensions, as well as inner, outer, and parametric electrodes.

executed by dual trans-impedance amplifiers (AD8066) with 200 kΩ gain resistors and 2.2 pF capacitors. The outputs of the first stage transimpedance amplifiers were cascaded into the second stage instrumentation amplifier (AD8429) for differential amplification with a gain of six. The same instrumentation amplifiers (AD8429) were also used for differential actuation electronics with a gain of six. AC carrier signal was applied to the DAGs with up to 4 channels DC tuning voltages to compensate for fabrication imperfections. The electrical noise was reduced by rejecting a large portion of the power supply noise using low dropout voltage regulators (TPS7A3001 and TPS7A4901).

2.2.5 Electrostatic compensation of DAG

Unbalanced suspension springs due to fabrication imperfections are a dominant source of degrading gyroscope performance and introduce quadrature errors resulting in a frequency split between operational modes and misalignment of the principal axes of elasticity [110]. The amplitude amplified architecture has a dual-spring suspension system, which is intrinsi-

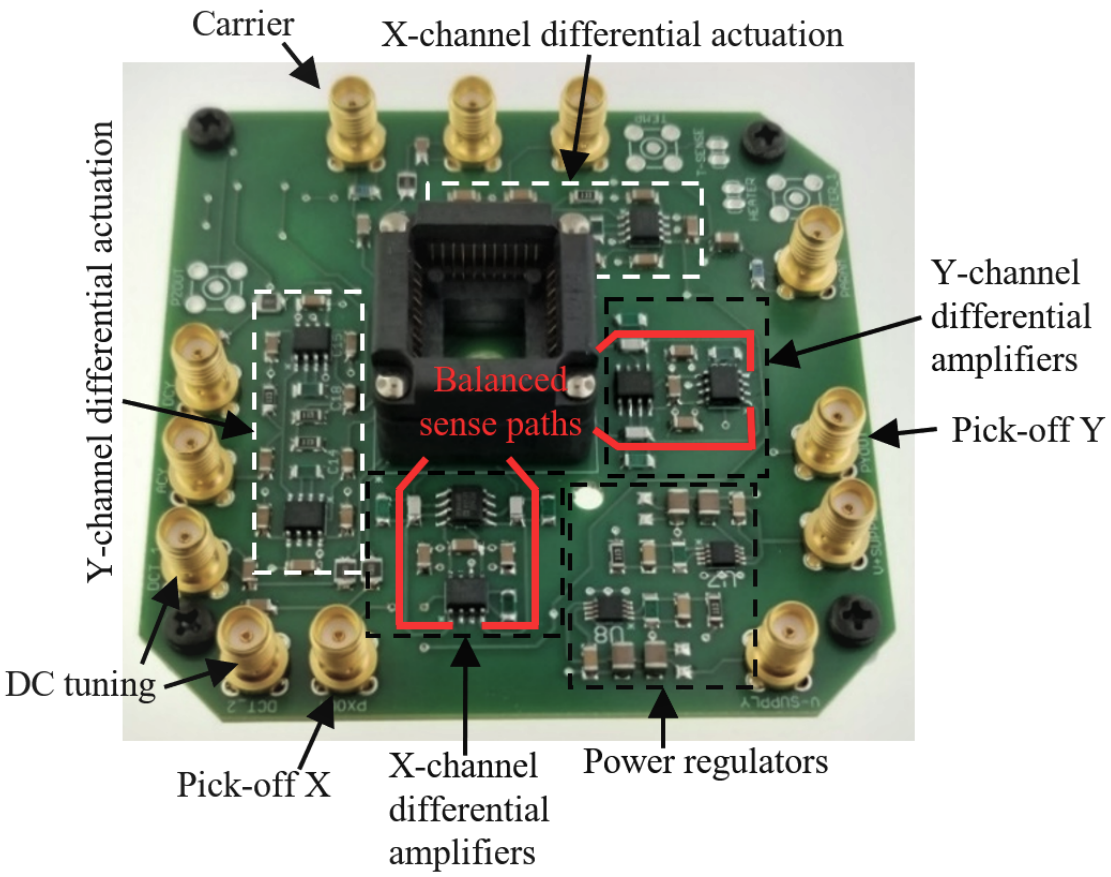

Figure 2.15: The balanced low-noise front-end circuit with 2-channel differential drive and 2-channel differential pick-off.

cally challenging to compensate for quadrature errors due to an increased degree of freedom of the system from two to four. In this section, we implemented a precision electrostatic frequency tuning method for our dual-mass gyroscope, reported in [111], which involved an off-diagonal tuning to decouple the operational modes and an on-diagonal tuning to soften the stiffer mode electrostatically.

The DAG tested had an as-fabricated frequency split (Δf) of 17 Hz. To mitigate the frequency split, an electrostatic compensation was applied along the x-axis, Fig. 5.8. A DC voltage difference of 7.4 V between TODs1 and TODs2 electrodes, TOD, was first applied for off-diagonal tuning, followed by a DC voltage of 13.5 V applied on TDs electrodes for on-diagonal tuning. The frequency mismatch was electrostatically tuned down to <0.1 Hz, Fig.

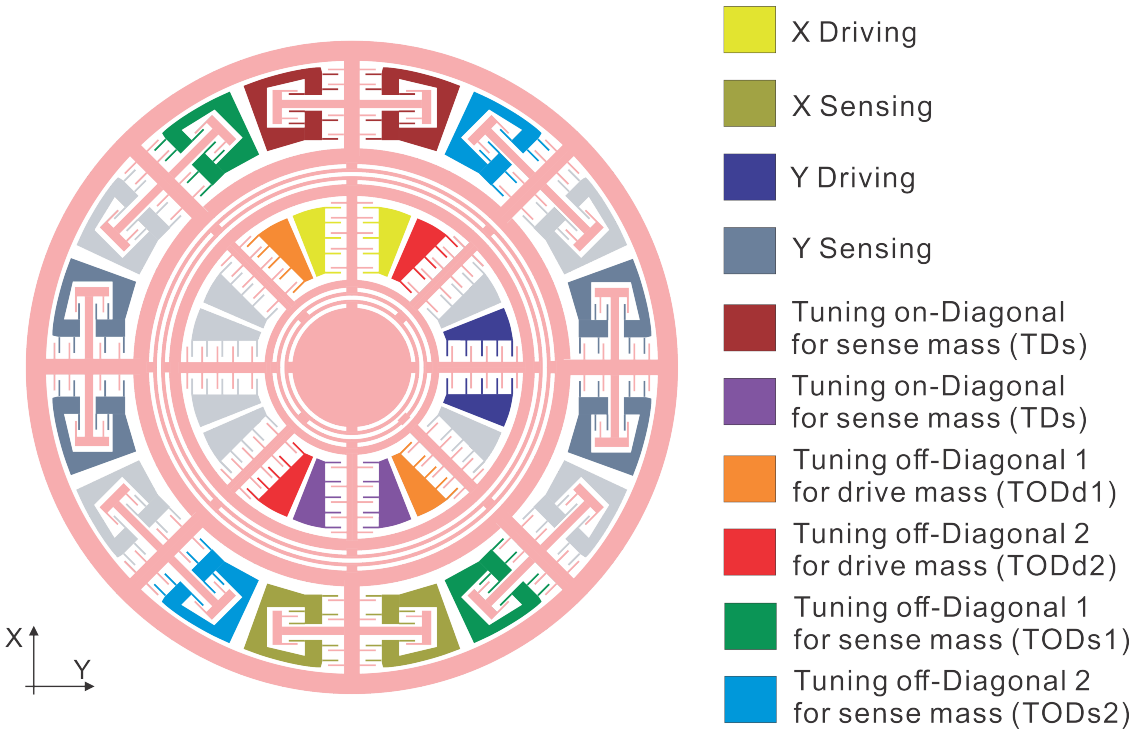

Figure 2.16: Configuration of driving, sensing, and tuning electrodes of both the drive and sense masses of the DAG sensor.

2.17, and the coupling between operational modes was also minimized to reduce quadrature errors.

2.2.5.1 Characterization of DAG

Noises in MEMS gyroscopes have intrinsic and extrinsic origins. The main internal noise sources in bulk micro-machined gyroscopes with capacitance detection include mechanical-thermal noise (MTN), electronic thermal noise (ETN), flicker noise (FN), quadrature error, and parasitic capacitance [112]. MTN and ETN are functions of temperature. FN is a function of frequency of a feed-through signal from the drive to the sense port. The external noise signals coupled to MEMS gyroscopes are diverse, and they vary with temperature, ambient vibration, and pressure within the package. Precision thermal control and vacuum packaging reduce the external noise sources. The well-designed and balanced front-end circuit

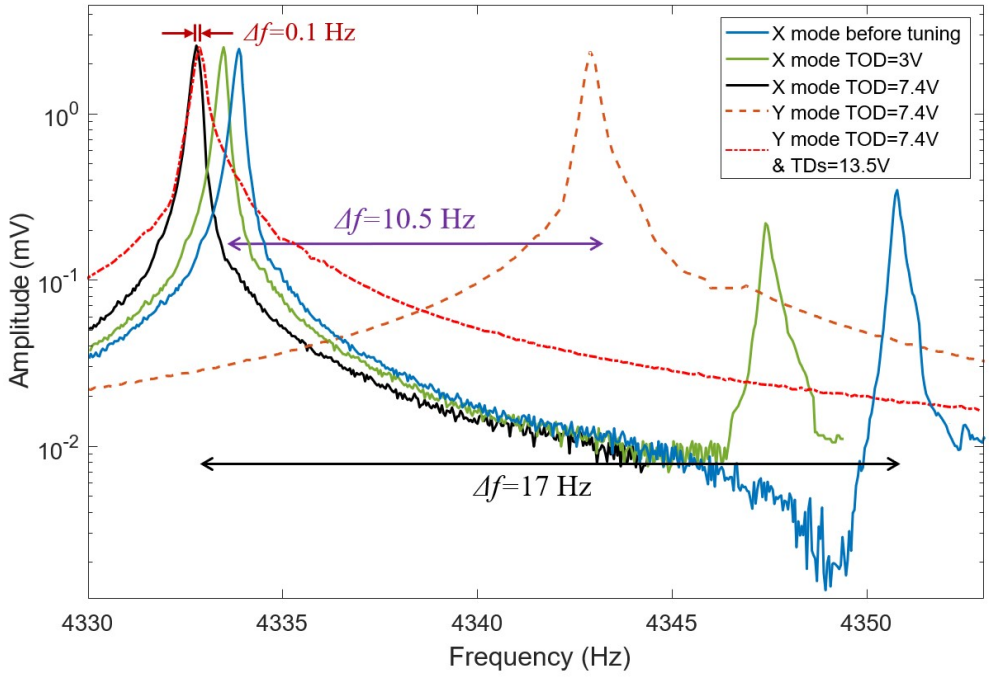

Figure 2.17: Frequency response showing an off-diagonal tuning of stiffness, minimizing the coupling between modes (Δf reduced from 17 to 10.5 Hz), and the on-diagonal tuning of the stiffness, reducing the frequency mismatch to <0.1 Hz.

presented above with low-noise components help to reduce the electronic noise.

The DAG was vacuum packaged with the ultra-high vacuum level on the order of 1e-7 Torr, [27]. The packaged DAG was assembled on the front-end circuit and tested in a temperature control chamber mounted on the rate table (Ideal Aerosmith 2102). The employed thermal chamber with temperature (<0.05 deg fluctuation for 10 hours of recording). Phase-Locked Loop and Amplitude Gain Control were utilized in the control circuit. The frequency split was electrostatically tuned down to 0.1 Hz, and 1.2 V_{pp} AC signal carrier with a frequency of 225 kHz was applied to the proof-mass. Utilizing advantages of the dual-mass structure and the parameter optimization, 0.08 deg/hr in bias stability and 0.007 deg/rt-hr in ARW were experimentally demonstrated for the open-loop angular rate mode of operation. The root-PSD of the noise characterization is shown in Fig. 2.29.

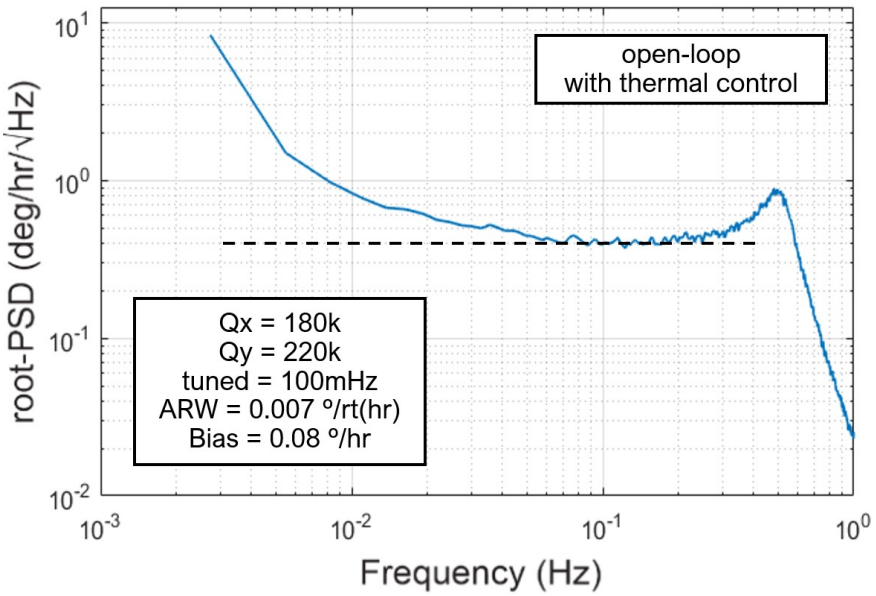

Figure 2.18: The PSD of Zero-rate output of the vacuum packaged DAG operated in the open-loop rate mode.

2.3 Fabrication Process

Based on the TAH shock survival concept and sensor development in the previous sections, the two fabrication processes are presented in this section. The processes utilize the in-house developed TWI and glass-reflow techniques to actualize the TAH concept, which includes: (1) fabrication of a cap stage with out-of-plane electrodes; (2) a modified in-house SOI sensor fabrication process; and (3) integration of the cap stage onto the gyroscope devices.

2.3.1 Fabrication of TWI Cap Stage

The fabrication process for the TWI cap wafer, shown in Fig. 2.19, includes the following steps: Step (1): anodic bonding of an 100 μm thick Pyrex wafer to a 500 μm Si wafer; Step (2): 10% HF wet etching for thru-wafer interconnects (TWI) with 200 nm Au layer as a hard mask; Step (3): E-beam metalization and patterning of Cr/Au on both sides of the cap wafer, which serves as top wire-bonding paths and bottom bonding pads; Step (4) and Step

(5): Deep Reactive Ion Etching (DRIE) of Si on the cap wafer to create out-of-plane gaps (3 μm) and to insulate electrodes. The resulting TWI cap wafer contains the out-of-plane electrodes to trap and hold the device's proof-mass against shocks and at the same time to provide the electrically insulated locking area.

The fabrication process of MEMS sensors wafer is basd on our standard in-house SOI process, Step (II-IV) in Fig. 2.19. An additional step, Step (I), in the process is required for bonding of the cap stage to the device: deposition of a Cr/Au layer as bonding pads. The SOI wafer, which was used for fabrication of devices, consisted of a 50 μm thick Si device layer, a 500 μm thick handle wafer, and a 5 μm thick buried oxide layer between them. In Step II, the positive Shipley 1827 photoresist and conventional contact lithography were used to define the sensor features on the top oxide layer. In Step III, DRIE etching of the device layer was then performed in a STS DRIE system with the top oxide layer as the hard mask, followed by a HF release step using an Idonus Vapor Phase Etcher at 49°C, in Step IV.

The cap wafer was bonded to the SOI wafer using Au-to-Au thermo-compression bonding process in a AML-AWB 4" wafer bonder allowing less than 20 μm between-wafer misalignment in the horizontal direction, Fig. 2.1. The wafer-level bonding process is presented in Appendix A.5. A prototype of TAH integrated with a DAG contains a total of 8 out-of-plane electrodes for TAH and a central opening to access in-plane electrodes on the device layer, necessary for the gyroscope operation, Fig. 2.20(a).

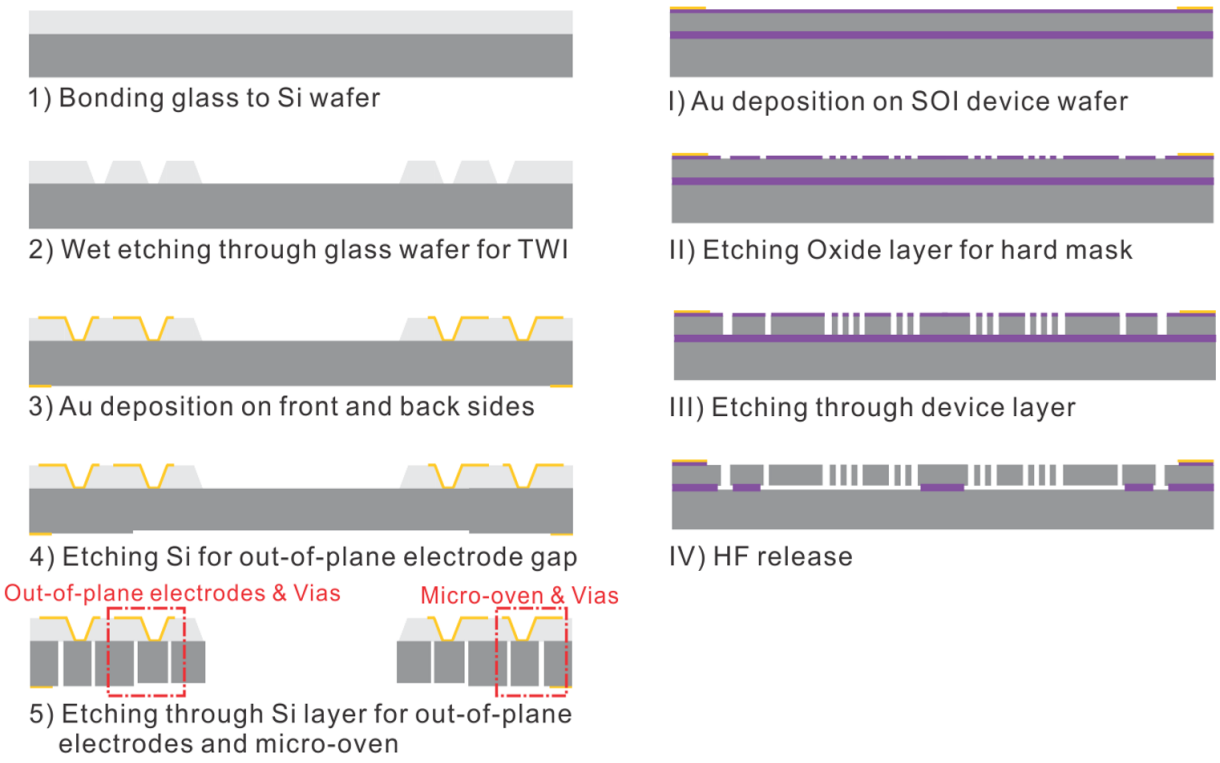

Figure 2.19: The reported fabrication process for implementation of a gyroscope with TWI out-of-plane TAH electrodes.

2.3.2 Fabrication of TGV Cap Stage

An improved fabrication process for the cap stage is also demonstrated in this section, illustrated in Fig. 2.22. The process forms a cap wafer defining Through-Glass-Vias (TGVs) intended for both in- and out-of-plane electrodes and vacuum packaging of the device wafer on the wafer-level. The in-house glass reflow process is developed and presented in Appendix A.5. The demonstration shows a full gap glass filling in 300 um depth Si trench, illustrated in Fig.2.21.

The process starts with DRIE Si etching of 500 μm thick silicon wafer to a depth of 250 μm, which is a 100 mm in diameter, <1-0-0> orientation, and 1-5 Ohm-cm resistivity, in Step (a); Step (b): anodic bonding of the etched Si wafer to a 250 μm thick Borofloat® 33 glass wafer with AML-AWB 4" wafer bonder under pressure <1 mTorr to create vacuum in

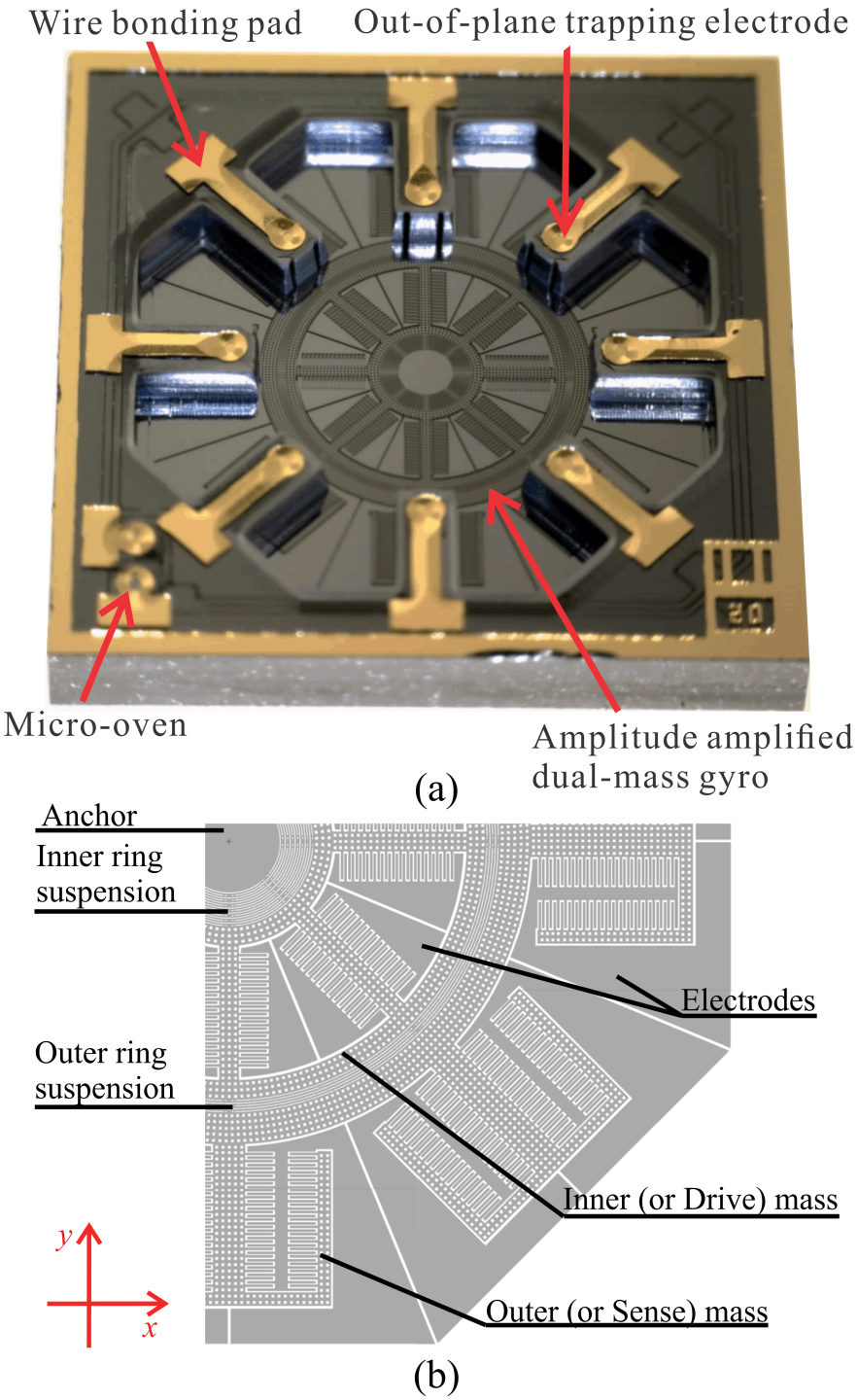

Figure 2.20: (a) A prototype of the dual-mass gyroscope bonded to the cap stage with thru-wafer interconnects serving as in-situ shock survival mechanism. (b) Close-up of a quarter of the amplitude amplified dual-mass device.

the encapsulated cavities; Step (c): 4 hours long glass reflow in a 850 °C annealing furnace; Step (d): lapping of the bonded wafer from the glass side until Si surface is exposed; Step

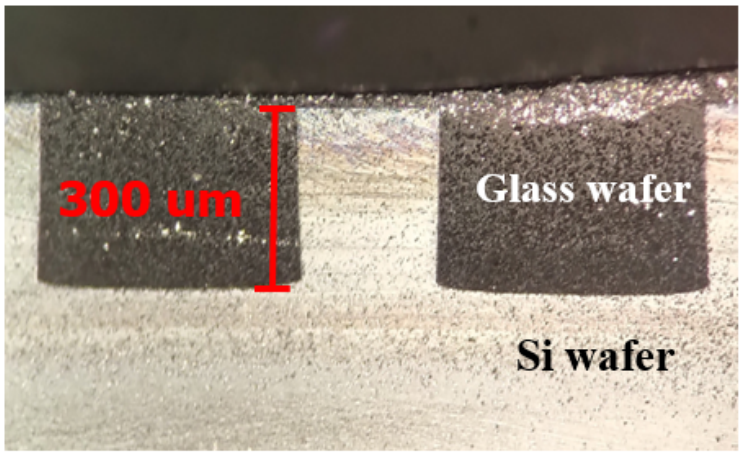

Figure 2.21: The cross section of 300um deep vertical glass reflowing in Si wafer.

(e-g): top and bottom metallization and patterning (500 nm Au with 50 nm Cr) for wire bonding pads (top) and Au-to-Au bonding pads for thermal compression bonding (bottom); Step (f): DRIE of backside Si to create out-of-plane gap of 3 μm; Step (h): etch through the remaining 250 μm Si to insulate TGVs. The fabrication process of SOI device wafer with Au bonding area for encapsulated device and the results of SOI wafer are shown in Fig.2.23.

The process was successfully implemented for forming the cap wafer, shown in Fig. 2.24(a) and (b), allowing for a dust-free and ultimately for an in-vacuum operating condition, in addition to providing electrical interconnects. Fig. 2.24(c) illustrates the assembly of the cap stage to a metallized DAG, Fig. 2.24(a) bottom, using Au-to-Au thermal compression bonding. Initial characterization of the cap stage with a DAG was performed on a probe station under atmospheric pressure. Frequency sweeps of inner and outer masses were characterized using a Zurich lock-in amplifier, Fig. 2.25. The experimental test verified an operation of the 4 DOFs structure with 16 functional in-plane TGV electrodes.

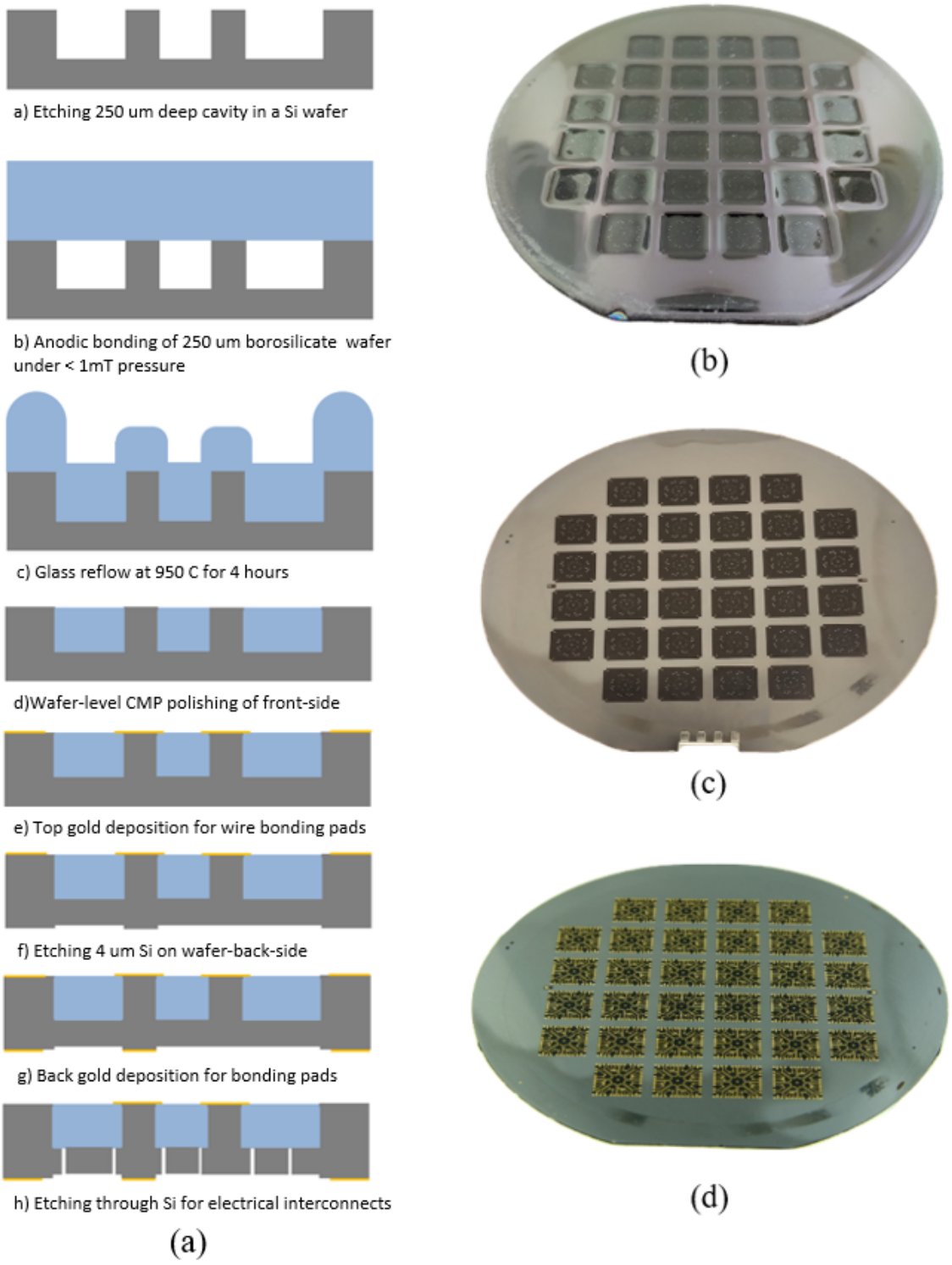

Figure 2.22: The improved fabrication process for dust-free cap wafer with integrated in- and out-of-plane Through-Glass-Via electrodes.

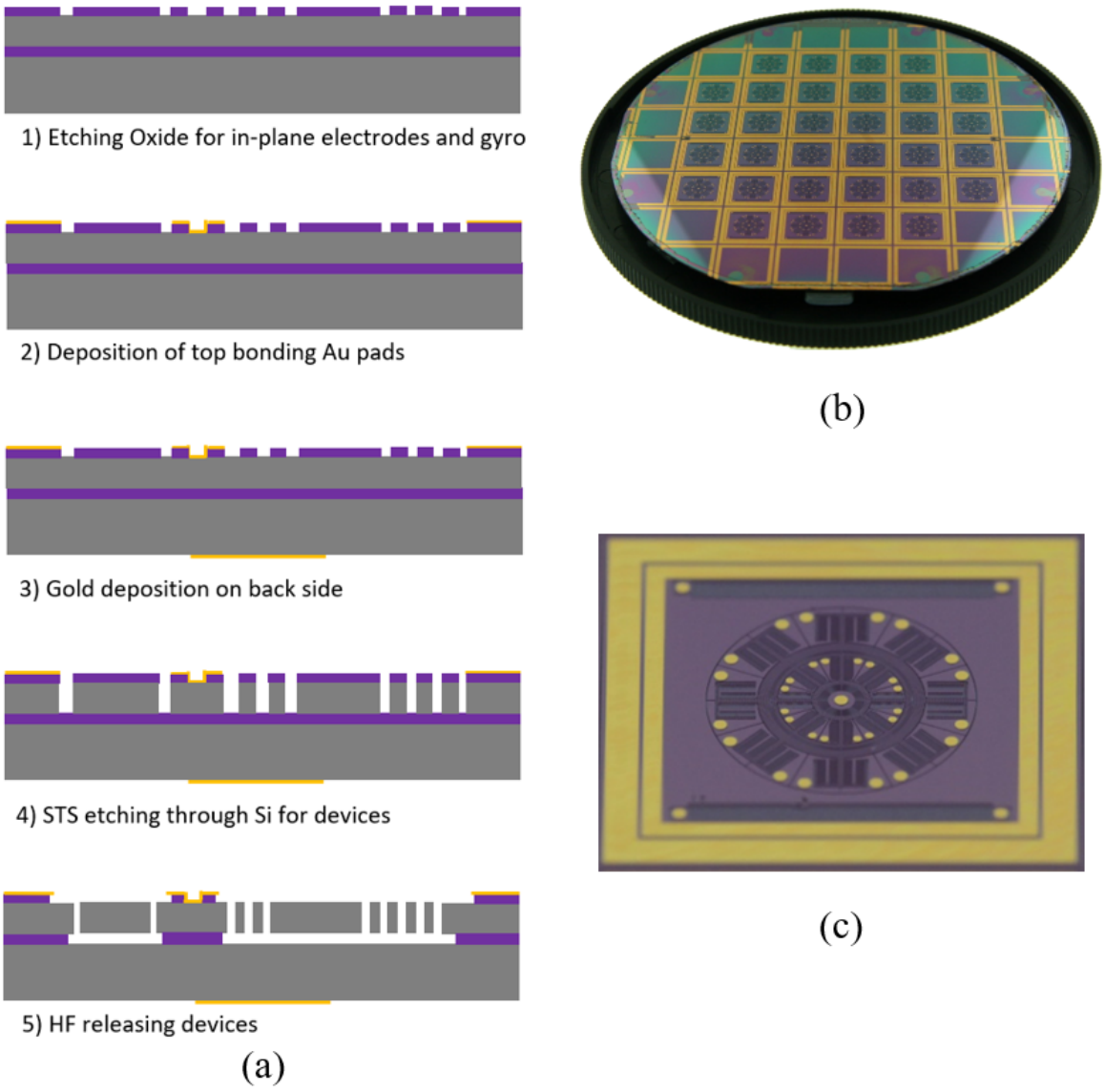

Figure 2.23: (a) SOI wafer in-house fabrication process for encapsulated device; (b) a SOI wafer after DRIE etching, Step (4), with the top bonding Au; (c) a zoomed-in view of a SOI device with Au bonding pads for in-plane electrodes and vacuum sealing.

2.3.2.1 Improvement of TGV Cap Wafer Fabrication

Based on the proposed TGV fabrication process, a simplified process utilizing Au-to-Si eutectic bonding instead of Au-to-Au thermocompression bonding is presented. This new approach is expected to improve the yield of the wafer-level vacuum packaging. The steps of the new silicon-in-glass process are shown in Fig. 2.26.

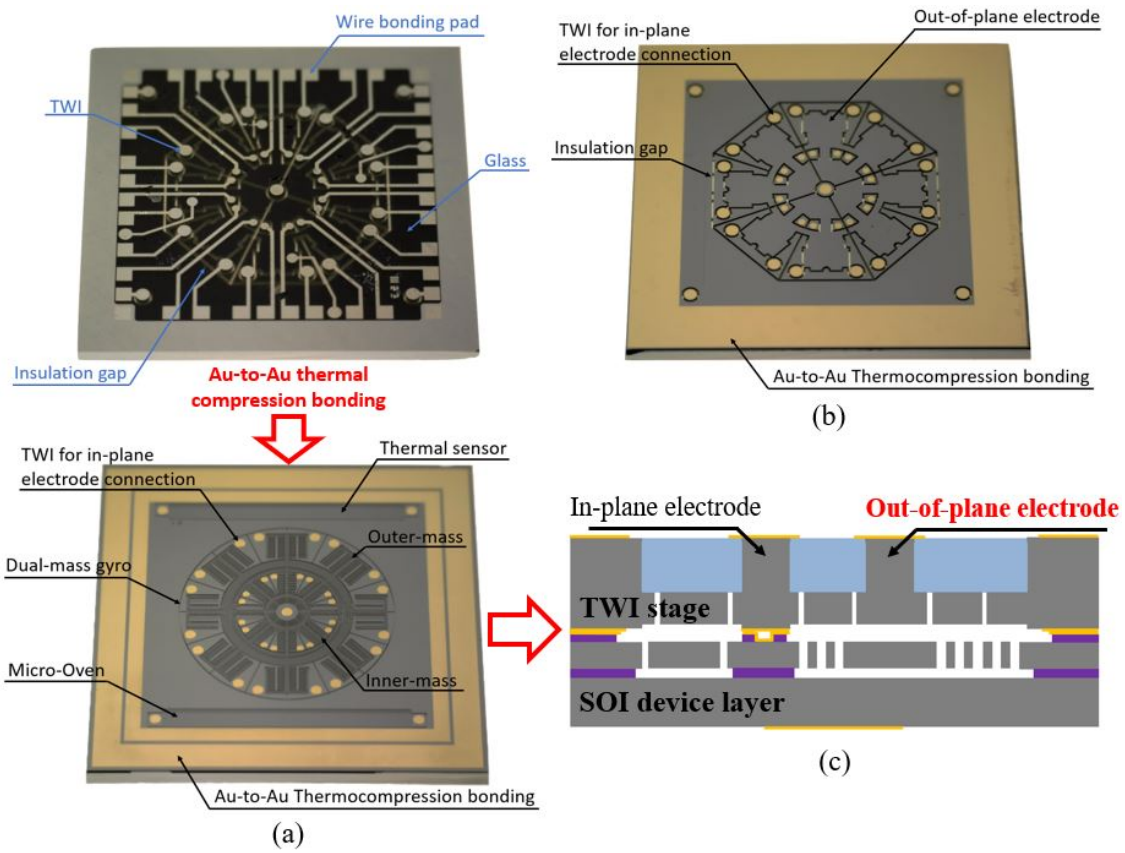

Figure 2.24: (a) Thermal compression bonding of the cap stage (top) to a metallized DAG (bottom). (b) The back side of the cap stage. Glass on the front side, (a) top, provides mechanical integrity to the structure and the 500 nm Au layer on the back side defines as the bonding pads. (c) Schematic diagram of the packaging process for device encapsulation.

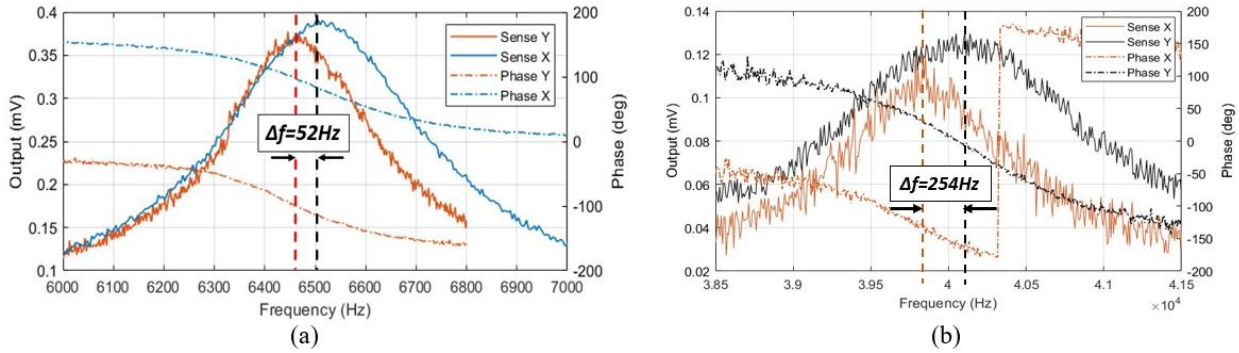

Figure 2.25: Frequency sweeps of (a) outer sense mass and (b) inner drive mass of the DAG prototype in X and Y directions, tested under atmospheric pressure. The device was encapsulated using the process described in Fig. 2.22

In Fig. 2.26 Step (d), the cap wafer was lapped until about 20 μm glass layer remained, which protects Si bonding area from scratching, followed by HF etching of glass. The thin

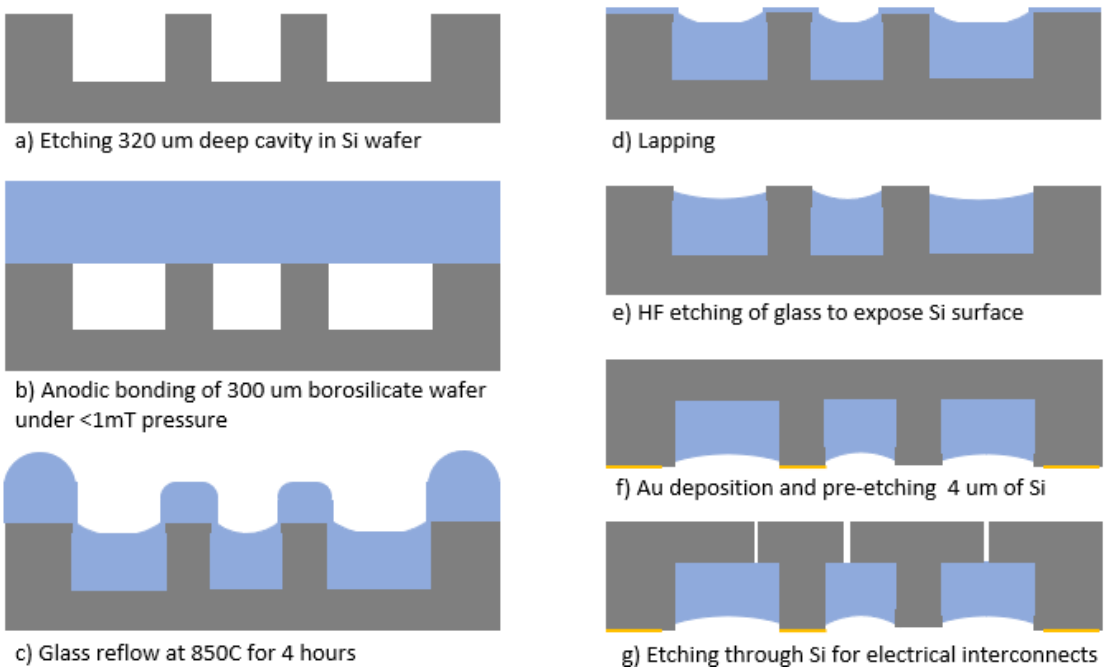

Figure 2.26: The new TGV cap wafer fabrication process for wafer-level encapsulation of devices.

glass layer was removed until the Si surface was exposed, in Fig. 2.26 Step (e).

The new TGV cap wafer fabrication process is compatible with our standard in-house SOI sensor fabrication process, Fig. 2.27(a). Fig. 2.27(b) shows the final step of the wafer-level Au-to-Si eutectic bonding of the new cap wafer to the SOI device wafer in the AML wafer bonder under low pressure. The side with metalization will be facing the SOI sensor, creating a spacer for protecting sensor's proof-mass.

2.4 Evaluation of TAH Mechanism

2.4.1 Experimental Setup

A prototype with bonded DAG to the cap stage, Fig. 2.20(a), was attached to a LCC package and mounted on the front-end circuit board presented in Section 2.2. An accelerometer,

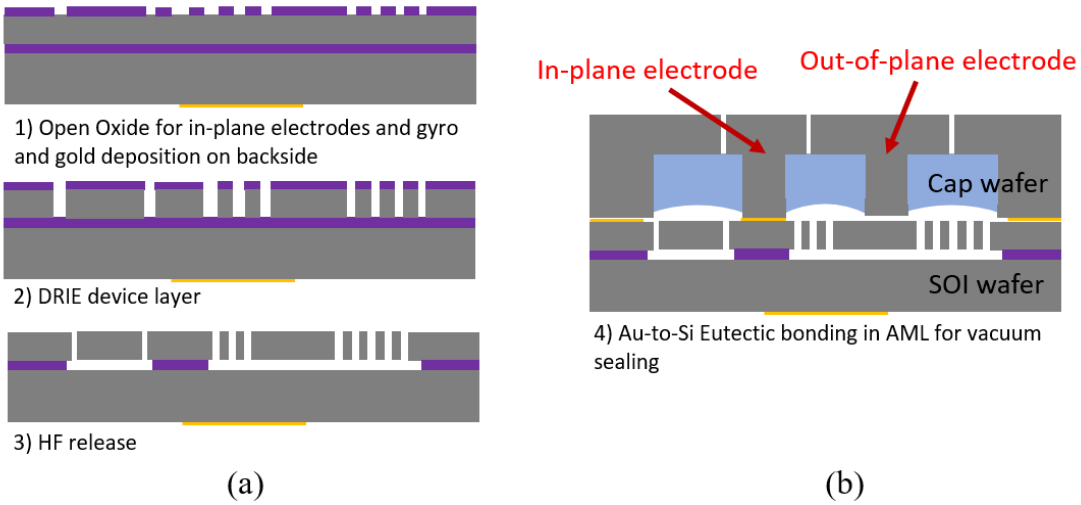

Figure 2.27: (a) In-house SOI sensor fabrication process. (b) Schematic diagram of the final step in device encapsulation.

ADXL356, was affixed on the backside of the front-end circuit to measure the shock applied to the board, and thus the tested gyroscope. The configuration was tested in a vacuum chamber assembled on a rate table, which was harmonically driven at an amplitude of 3.75 deg/s. The gyroscope was operated in an open-loop rate mode along the sense axis with Phase-Locked Loop and Amplitude Gain Control Loop stabilization along the drive axis. The device was excited at its 3.6 kHz in-plane operational frequency, defined as the gyroscope's Normal Operation mode. The gyroscope had an as-fabricated frequency split of 14 Hz, which was tuned down to 1 Hz using the electrostatic compensation method described in [111]. The quality factor of the device was 110k with 11x amplitude amplification.

As a preliminary demonstration of the concept, shocks were applied from outside of the vacuum chamber by a lightweight shock inducing hammer. The shock was transferred from outside to inside of the chamber reaching the front-end circuit with some energy loss, and the transferred shock was measured by the accelerometer attached to the circuit board. Due to safety concerns and for protection of the experimental equipment, the maximum within-chamber shock was limited to about 5g. Nonetheless, 5g shock was sufficient to induce sensor drifts and alter the fundamental characteristics to the degree where re-calibration of

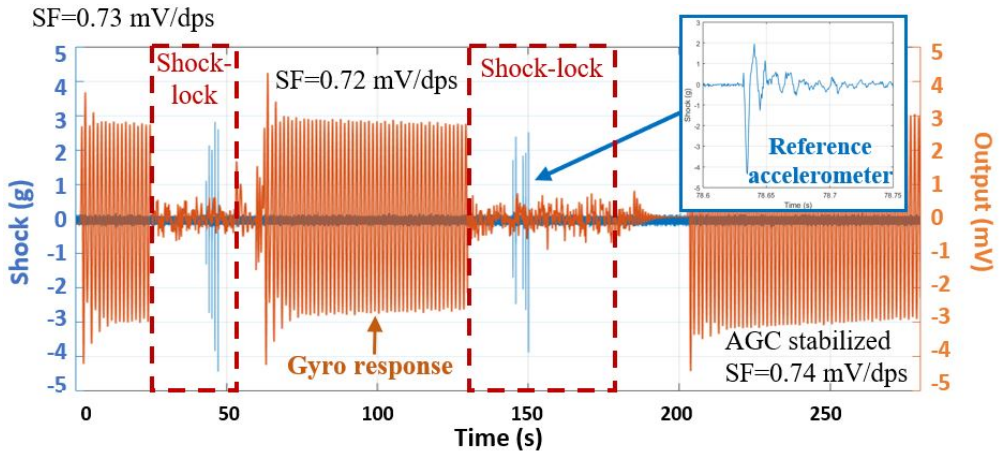

Figure 2.28: Initial demonstration of the TAH strategy on a DAG prototype. Orange line is the measured response from the gyroscope; blue line represents read-outs from the reference accelerometer monitoring the events of shock.

the sensor would be required. Notably, during our experiments, detrimental collisions of electrode structures occurred due to shocks as low as 3g, since the design utilized a larger proof-mass and low operational frequency to achieve a high sensitivity of operation.

2.4.2 Experimental Results

The prototype was in the Normal Operation mode with an initial measured sensitivity to rotation of 0.73 mV/dps (Fig. 2.28, from 0 to 25 sec). At 25 sec, an out-of-plane electrostatic trapping force was applied, driving the proof mass at its out-of-plane resonance of 1.91 kHz to lock and immobilize the structure, activating the Shock-Lock mode. Then, the rotation stimulus was removed (Fig. 2.28, from 30 to 50 sec), followed by few in-plane shocks up to 4.5g with 8 msec half-sine duration (Fig. 2.28, from 40 to 45 sec). After releasing the proof-mass (Fig. 2.28, from 53 to 60 sec), the device returned gradually to its neutral position and continued its normal operation with the sensitivity of 0.72 mV/dps, until the end of the duration of 130 sec. The process was repeated multiple times. The Angle Random Walk (ARW) and in-run bias instability (IrBS) characteristics, before TAH and after repeated TAH operations, are shown in Fig. 2.29. The measured ARW before the shock was 0.048

deg/rt-hr and IrBS was 0.6 deg/hr. The after-shock measured ARW was 0.0483 deg/rt-hr and the measured IrBS was 0.69 deg/hr. A slight deviation in bias instability is explained by uncompensated variations in temperature during experiments.

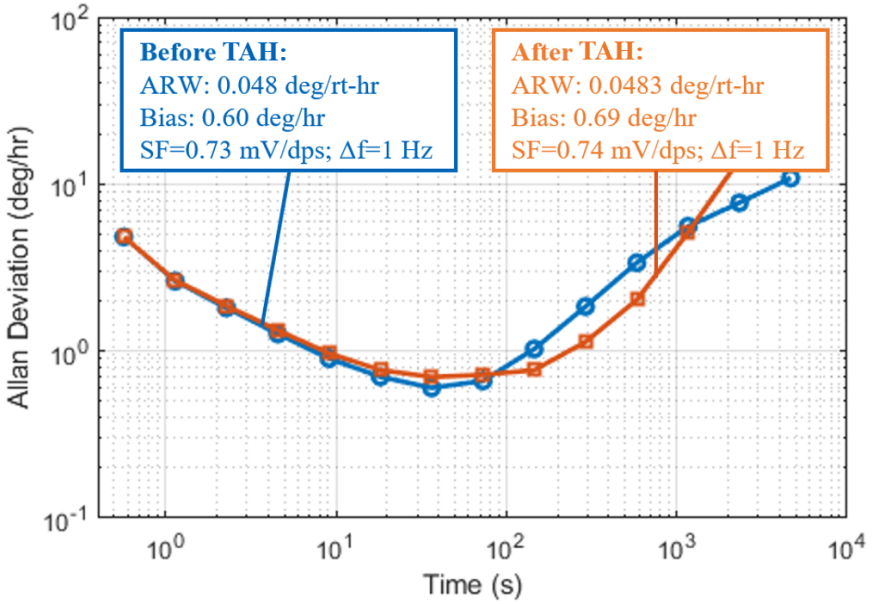

Figure 2.29: The Allan Deviation of the DAG prototype (tested in a vacuum chamber) in the open-loop operational mode before and after TAH.

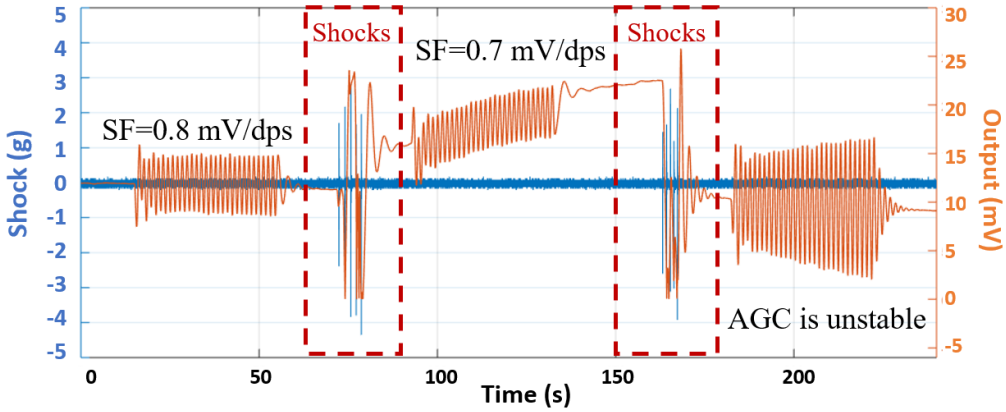

Figure 2.30: The experimental illustration of the gyroscope response to a harmonic excitation amplitude of 3.75 deg/s before and after in-plane shocks. Orange line is the measurement of gyroscope's response; blue line is the output of the reference accelerometer.

For comparison, the same characterization procedures were repeated on the same gyroscope without switching to Shock-Lock mode before the events of shock, Fig. 2.30. Due to the low operational frequency, the output signal convulsed for the duration of excitation (Fig. 2.30,

from 70 to 85 and from 150 to 170 sec), and the sensor was not able to recover its performance after the events of shock (Fig. 2.30, from 85 to 130 and from 180 to 240 sec), emphasizing the relevance of the TAH concept for augmenting shock performance of gyroscopes.

2.5 Conclusion

The Trap-and-Hold (TAH) mechanism as an add-on shock survival strategy was demonstrated to improve the gyroscope's shock survivability while preserving its noise characteristics. To demonstrate the approach, a new type of MEMS Dynamically amplified dual-mass gyroscope (DAG) is designed for illustration purposes. In designing a DAG, the frequency scaling of the operational and non-operational (parasitic) resonant modes must be taken into account to prevent the energy dissipation through the nearby resonant modes and reduce the noise cross-coupling sensitivity. The effect of the DAG operational frequency and geometry parameters on Q_{TED} and Q_{anchor} was also revealed in the chapter. Thus, geometry optimization is an essential step in the design of DAGs to achieve both high Q-factor and larger mode split to achieve the high resolution CVG operation. The explored design space provided a set of parameters for the DAGs, which were fabricated and experimentally characterized using the in-house developed low-noise front-end circuit. A 0.08 deg/hr in in-run bias stability and a 0.007 deg/rt-hr ARW in the open-loop rate operation mode was then demonstrated. Utilizing a proposed fabrication process with a through-wafer-interconnects, the TAH strategy was then evaluated on a DAG. The Gyroscope switches from its existing operational mode to survival mode and is stabilized by out-of-plane snapping and holding sensors proof-mass during events of shock while preserving its noise characteristics before and after shocks. Additionally, we described a process for dust-proof cap stage with experimentally demonstrated electrical interconnects with both in- and out-of-plane TGVs using an in-house glass re-flow process.

Chapter 3

Fused Silica Dual-Shell Gyroscopes

Three-Dimensional Fused Silica (FS) micro-Hemispherical Resonator Gyroscopes (micro-HRGs) with remarkable structural robustness are good candidates capable of providing continuous high-precision gyroscope operation through extreme environmental variations, such as high-g shock and vibrations [16]. Toward realization of precision gyroscope measurements, this chapter reports on developments of Fused Silica (FS) Dual-Shell Gyroscopes (DSGs), a version of micro-machined HRG, in presence of fabrication imperfections. The technologies of structural asymmetry compensation in micro-HRGs are first discussed in Section 3.1. The FS DSG is then introduced in Section 3.2 and Section 3.3, describing the fabrication processes of the dual-shell structure, followed by a description of the Thru-Glass-Vias (TGVs) interconnects substrate along with the integration procedure. An electromechanical model of an integrated DSG system is presented in Section 3.4, capturing the structural asymmetry of the dual-shell layer, parasitics of interconnects, and assembly errors. An electrostatic frequency compensation algorithm of the n = 2 and n = 3 wineglass modes is also developed in the same section. An assembly error identification method is developed to support the usage of the tuning algorithms and is validated experimentally on a DSG prototype, followed by demonstrations of gyroscope operation in Section 3.5 and Section 3.6. Finally, the chapter

is concluded with Section 3.7.

3.1 Introduction

Three-Dimensional macro-scale Fused Silica (FS) Hemispherical Resonator Gyroscopes (HRGs) have demonstrated high structural symmetry, low mechanical energy losses, and remarkable structural rigidity, [50], with better than the navigation-grade gyroscope performance [16]. The success of FS macro-shell structures has inspired developments of 3D micro-machined HRGs (micro-HRGs) for extreme reduction of size and production cost, while preserving all benefits of HRG, including the environmental robustness and high accuracy operation as MEMS Coriolis Vibratory Gyroscopes (CVGs) [49, 113]. Conventionally, structural symmetry of HRGs is achieved through a combination of high precision macro-machining and post-process trimming [16]. However, for micro-scale devices the conventional approaches are typically not available or restricted due to the nature of lithography-based manufacturing and extremely small size of samples. To achieve a high structural symmetry, i.e. low frequency mismatch, for realization of navigational-grade performance in miniaturized HRGs is an ongoing research topic. Compensation of asymmetry in HRGs is essential for reduction of the frequency split to lower the fundamental noise sources in CVGs, including mechanical thermal noise and electrical noise [20], thus improving the in-run noise characteristics.

Fabrication of 3D FS wineglass resonators typically involves a wafer-level Micro-glassblowing technique. In this process, a FS wafer is first etched by hydrogen fluoride (HF) to create cavities for glassblowing. Then, it is bonded with another FS wafer to seal the cavities. The bonded wafer stack is placed in the high-temperature furnace for glassblowing. This approach takes the advantage of pressure difference and surface tension driven plastic deformation of the FS wafer to form 3D symmetrical micro-shell structures. Finally, a mechanical release procedure, such as mechanical lapping and Chemical–Mechanical Polishing (CMP), [34, 79],

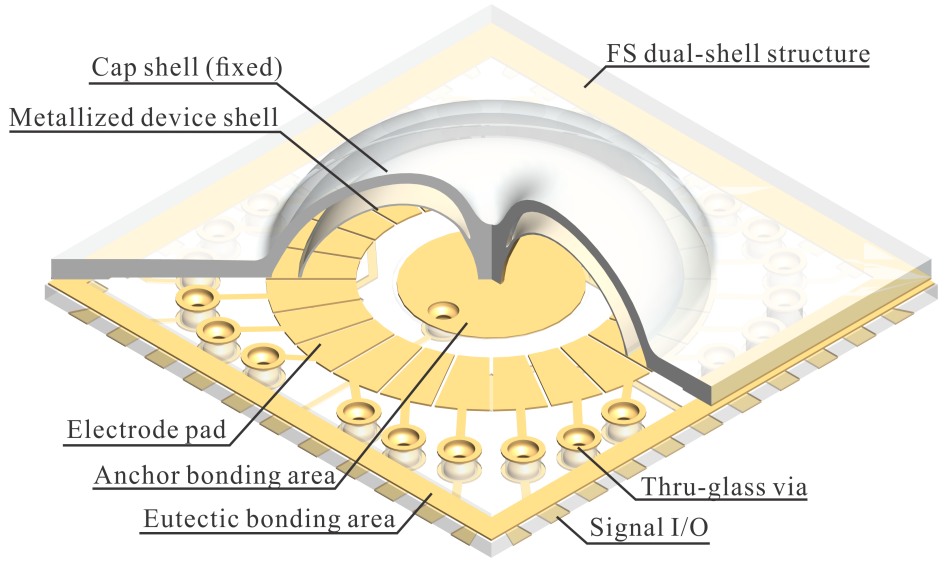

Figure 3.1: Schematics of a 3D Fused Silica Dual-Shell Gyroscope, fabricated using the micro-glassblowing technique and assembled on a FS planar electrode substrate with Thru-Glass-Vias (TGVs). Bonding of the cap shell and the central stem to a substrate is performed in a single bonding step and forms a fixed-fixed double-ended anchor for the inner vibrating shell (the sensing element).

is conducted after the blowing in order to release the devices. However, imperfections during the processes can introduce structural asymmetry, i.e. frequency splits and deformation of mode shapes. These imperfections are caused by a non-uniform temperature distribution during the glassblowing process, misalignment between the ideal and actual lapping planes during the release step, and variation of the device layer thickness created during the HF wet etching [82]. The imperfections induced by processing result in frequency and damping mismatches and quadrature coupling between the operational mode pairs, which not only degrade the gyroscope sensitivity, but also contribute significantly to the noise sources of a micro-HRG, thus impacting the random noise errors, bias instability, and dynamic range.

Most methods of matching the operational modes of micro-shells are based on a post-processing mechanical trimming of the structure by means of selectively removing material from the vibrational element, such as using a high resolution micro-ultrasonic machining [87], ion-beam etching [88], chemical etching [89], or directional lapping [82]. Frequency split re-

duction from a few tens of Hz to sub-Hz have been demonstrated in many applications using these techniques. However, such passive tuning methods are mainly limited by calibration accuracy in a laboratory environment.

To enable operation of a micro-shell as a resonator or a gyroscope, a conductive layer on the sensing element is needed to electrically bias the proof-mass, in cases when electrostatic actuation and detection are used. The micro-hemispherical shell is also required to be rigidly assembled on a substrate for electrostatic operation utilizing either in-plane peripherally distributed electrodes [99] or out-of-plane planar electrodes [76], as illustrated in Fig. 3.1. Unlike in conventional Silicon MEMS devices, in which the electrodes are co-fabricated with the sensing elements and capacitive gaps are defined relatively uniformly on the same plane using photo-lithography and etching, assembly misalignment of micro-HRG at any of the six degrees-of-freedom (DOF) of the position and orientation relative to the substrate would lead to uneven capacitances of the micro-shells and angular mismatches between the principal axes of elasticity of operational modes and directions of electrostatic forcers and pick-offs defined by the electrode substrate [114, 115]. Therefore, in addition to accounting for fabrication imperfections of micro-shells, many other factors, including assembly errors [116], non-uniformity of metallization [117], and parasitics of interconnections [58] may also influence symmetry and result in a more complex electromechanical system compared to a more conventional planar MEMS sensor. The asymmetry impacts sensitivity of motion detection, mechanical energy losses, stiffness adjustment, and the gyroscope's overall noise performance [118]. The asymmetry needs to be compensated to achieve a mode-matched, or near-mode-matched, operation, which is desirable for precision detection of angular rotations and ability to measure rotations in a wide range of angular velocities.

The passive mechanical trimming techniques described above are often not applicable or restricted to three-dimensional (3D) micro-HRG sensors. In [119], a femtosecond laser ablation was used to trim assembled T-masses of micro-HRGs. However, the re-deposition of ablation

debris can potentially cause the proof mass to stick to the substrate or limit the amplitude of vibration. This approach is typically not available for a broad class of micro-HRGs.

In contrast to the mechanical trimming, electrostatic tuning is a common active-tuning method to compensate for frequency splits in MEMS gyroscopes by utilizing non-linear electrostatic forces to selectively modify the effective stiffness of a certain operational mode. In the assembled micro-HRG type of sensors, the non-uniform capacitive gaps caused by misalignments during integration step of the sensor and substrate would lead to uneven electrostatic forces, and thus impact the effectiveness of electrostatic stiffness adjustment and increase the amplitude of tuning voltages necessary to achieve a mode-matched gyroscope operation [116]. Increasing the tuning voltage amplitude would also introduce non-linear dynamics in the device and result in the amplitude-frequency coupling, which would degrade the gyroscope's noise performance [86, 120]. To allow for reduction of tuning voltages and achievement of high accuracy electrostatic compensation, the impact of assembly errors has to be precisely considered in the tuning algorithm, and an error identification method for a micro-HRG system is necessary.

The FS Dual-Shell Gyroscope (DSG) is a version of micro-machined HRG, disclosed in [121], which adopts a two-layer shell structure to form a double-ended anchor architecture to increase the bonding area, reduce the anchor stresses, and improve structural robustness, compared to a single stem HRG-type of shell resonator [94], making the sensors potentially robust for operation in harsh environments, Fig. 3.1. It consists of an inner device shell as the sensing element for rotation measurements, an outer cap shell for the top anchor and packaging, and a central stem for the botom structural support of the sensor shell. In addition to the rugged structure due to the double-sided anchor, the inner device shell utilizes the low stiffness degenerate modes of vibration, such as the n = 2 and n = 3 wineglass modes, allowing to potentially achieve a high sensitivity angular rate or direct angle measurements. A substrate with out-of-plane electrodes as well as inner and outer bonding areas, Fig. 3.1,

are used for integration with the dual-shell structure for capacitive detection and actuation [76].

While isotropic gyroscopes, such as micro-HRG, have many operational advantages, achieving and maintaining structural symmetry is a challenge. The structural asymmetry of an integrated DSG was initially analyzed in our previous study [115]. An algorithm was developed and briefly reported in the chapter on how to electrostatically compensate the fabrication imperfections, capturing the impact of assembly errors. To enable a precise compensation of imperfections in DSGs, the asymmetry caused by the integration has to be identified. The identification procedure was not discussed on our previous studies, to fulfill the gap, this chapter develops a method for identification of assembly errors and presents a frequency tuning algorithm derived from a detailed electromechanical model.

3.2 Dual-Shell Gyroscope Architecture

The triple-stack micro-glassblowing technique has been developed as an approach to fabricate FS dual-shell resonators, reported in [51]. Using this approach, cavities were pre-etched on the cap and device wafers of fused Silica in the isotropic wet etching process using the HF solution. Then, the cap and device wafers were aligned and bonded to the substrate wafer before the glassblowing step. This chapter introduces a modified process, illustrated in Fig. 3.2. The modified process avoids HF etching of the device layer, which is anticipated to improve the surface quality of the device shell. This is accomplished by pre-etching the cap and substrate layers before the device layer is added via plasma-assisted FS to FS bonding.

High-purity FS wafers (Corning HPFS®7980) with the initial thicknesses of 500 μm, 200 μm, and 2 mm were used in fabrication as the cap, device, and substrate layers, respectively. A layer of 2 μm undoped poly-silicon was deposited as a hard mask on the cap wafer,

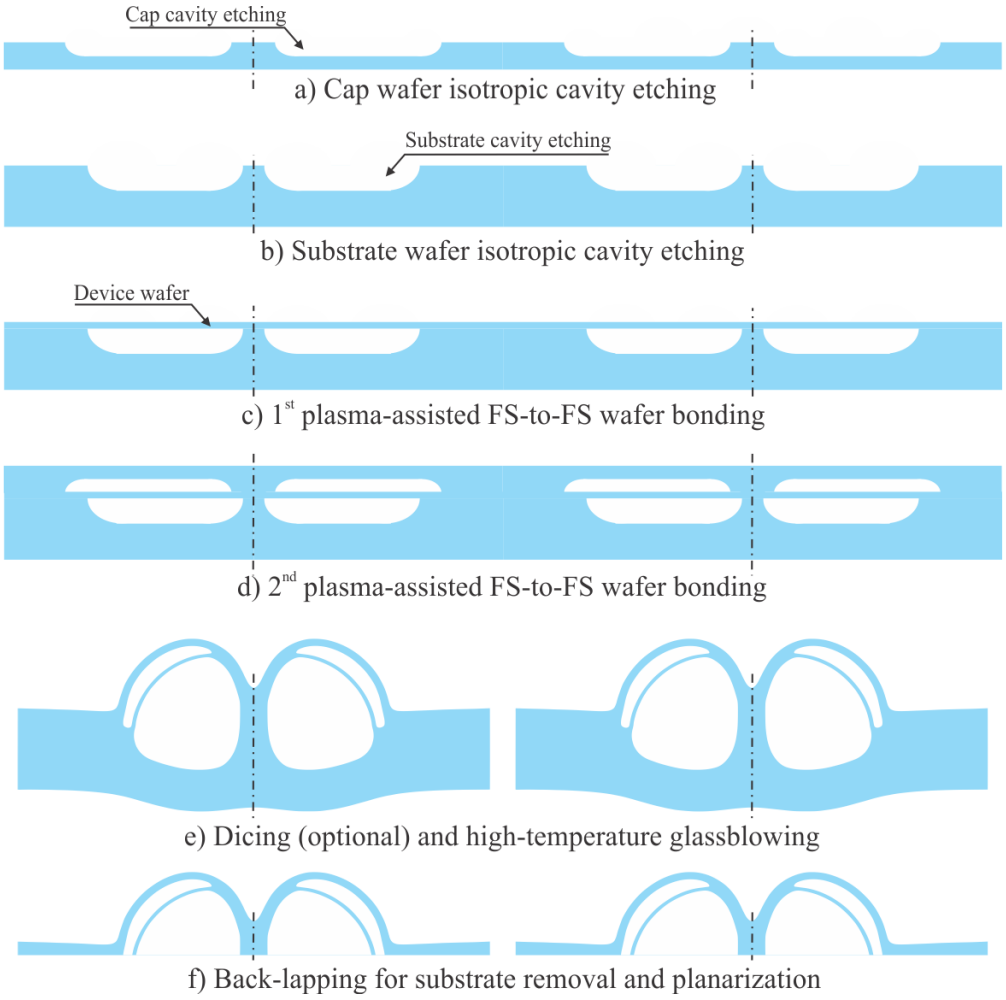

Figure 3.2: Process flow for FS dual-shell architecture fabricated using a glassblowing technology, performed at 1550 °C. The substrate is removed and planarized by lapping and CMP for subsequent characterization. The surface roughness of the polished surfaces is on the order of 0.3 nm [49].

Step (a), and the substrate wafer, Step (b), for wet-etching. The cap and substrate wafers were then time-etched isotropically using HF acid (48 wt.% in water solution) to create cavities. After the poly-silicon hard mask was removed, the triple-stack wafer bonding process was executed using plasma-assisted direct bonding, Steps (c) and (d). An array of aligned cavities were diced, and the glassblowing process was performed individually for each die in a Rapid Thermal Processing (RTP) furnace at 1550 °C. Using the process on the die-level is optional, and the process is compatible with the wafer-level batch fabrication. Without any loss of generality, the subsequent process steps of assembly are described on

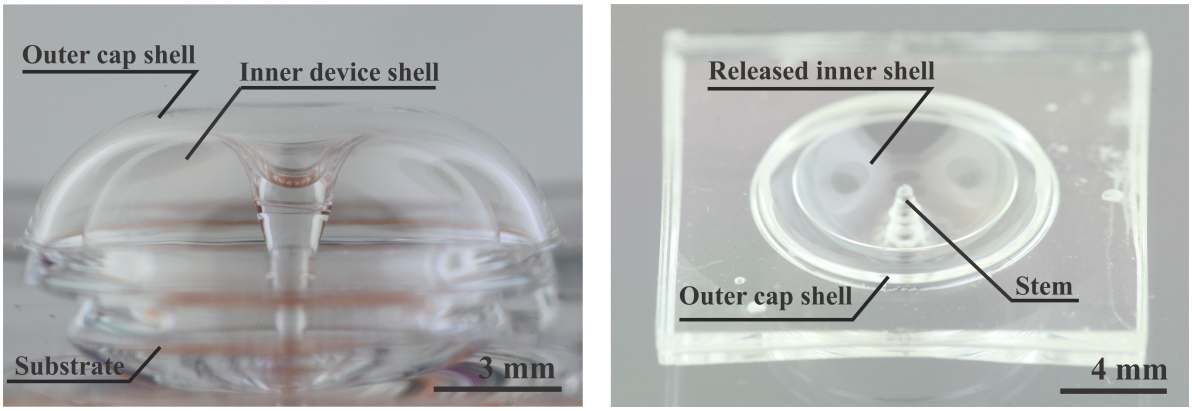

Figure 3.3: (Left) A glassblown dual-shell structure, fabricated using the proposed triple-stack wafer bonding and high temperature glassblowing processes. (Right) An exposed upside-down view of a released dual-shell resonator after the substrate removal showing the central stem, outer cap shell, and movable inner device shell.

the die-level. Fig. 3.3(left) illustrates a FS dual-shell structure after the glassblowing. It consists of an inner shell, an outer cap shell, and a central stem. The inner device shell of the DSG was released as the sensing element using a parallel back-lapping step utilizing the Allied HighTech MultiPrep^{TM} polisher, Step (f). An upside-down view of a dual-shell prototype after completing Step (f) is presented in Fig. 3.3(right).

Ideally, the micro-glassblown dual-shells would be manufactured perfectly symmetric, but this is not realizable in practice. Fabrication imperfections are induced by misalignments between the cap, device, and substrate wafers during the bonding, temperature non-uniformity in the furnace during glassblowing, and the offset between the dual-shell and the lapping plane during the release. These sources of imperfections result in mismatches of operational frequencies and shift in the principal axes of elasticity. The lab methods for identification of structural imperfections of micro-shell sensors before metallization are often conducted using mechanical shakers, such as a piezo-stack shaker, for excitation and optical vibration sensors, such as a laser Doppler Vibrometer (LDV), for detection [98].

For illustration purposes, two DSG prototypes with different geometries and sizes were manufactured and used as test vehicles in this chapter. The DSGs were characterized in a vacuum

Table 3.1: Experimentally measured parameters of DSG prototypes

Design parameter		DSG#1	DSG#2
n = 2 mode	Resonant frequency	7.93kHz	13.4kHz
	Frequency split, Δf	8.2Hz	48Hz
	As-fab. Q-factor, X-axis	760k	< 50k
	As-fab. Q-factor, Y-axis	680k	< 50k
	Metalized Q-factor, X-axis	455k	< 50k
	Metalized Q-factor, Y-axis	372k	< 50k
	Principal axis of elasticity	2°	-5°
n = 3 mode	Resonant frequency	15.7kHz	30.6kHz
	Frequency split, Δf	17.5Hz	30.5 Hz
	As-fab. Q-factor, X-axis	1.61M	1.38M
	As-fab. Q-factor, Y-axis	1.56M	1.45M
	Metalized Q-factor, X-axis	961k	976k
	Metalized Q-factor, Y-axis	836k	985k
	Principal axis of elasticity	-8.3°	-11°
Total height of dual-shell		3.5 mm	4.5 mm
Stem radius		0.31 mm	0.48 mm
Inner shell radius		3.4 mm	4.2 mm
Outer shell radius		3.9 mm	5.2 mm
Rim thickness		70 μm	130 μm
Footprint		13.8 mm	13.8 mm

chamber under pressure on the order of 1 μTorr using the LDV setup with piezoelectric excitation. The frequency splits and orientations of the principal axes of elasticity of the n = 2 and n = 3 modes were identified, Table 3.1. The as-fabricated Q-factors along with other geometric parameters are also listed in Table 3.1.

3.3 Integration with Electrode Substrate

Electrostatic capacitive excitation and detection schemes were implemented in FS DSGs based on the concept of out-of-plane electrodes for excitation of in-plane wineglass modes [91]. To provide a large bonding area and enable electrostatic detection and actuation, a planar electrode substrate with through-wafer-interconnects (TWIs) was designed for integration with release sensor shells (discussed in Section 3.2). Many methods for realizing high density

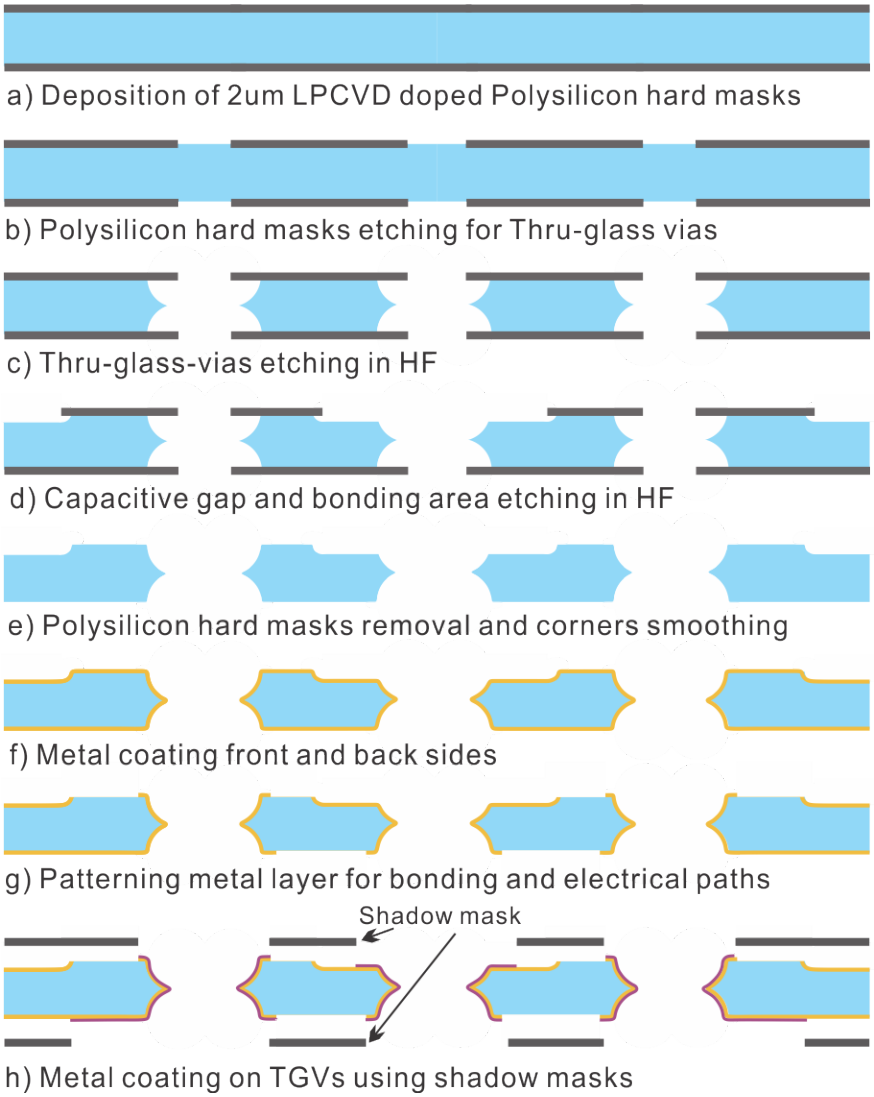

Figure 3.4: Process flow for FS TWIs electrode substrate using Thru-Glass-Vias (TGVs). The TGVs, out-of-plane capacitive gap, and bonding areas were wet-etched in HF solution. The designated electrical paths and bonding areas were coated with Cr/Au for sensor actuation and eutectic bonding.

and low parasitic TWIs were widely explored in recent years, such as electroplated copper vias, [58], magnetically assembled nickel wires [59], and Thru-Glass-Si vias [60]. Instead of filling the vias using either metal or silicon materials, depositing or electroplating conductive metal layers on sidewalls of vias on a glass substrate wafer can significantly simplify the fabrication process and minimize parasitics of interconnects [122, 61]. The technique was adopted in fabrication of planar electrode substrates for DSGs and presented in this section.

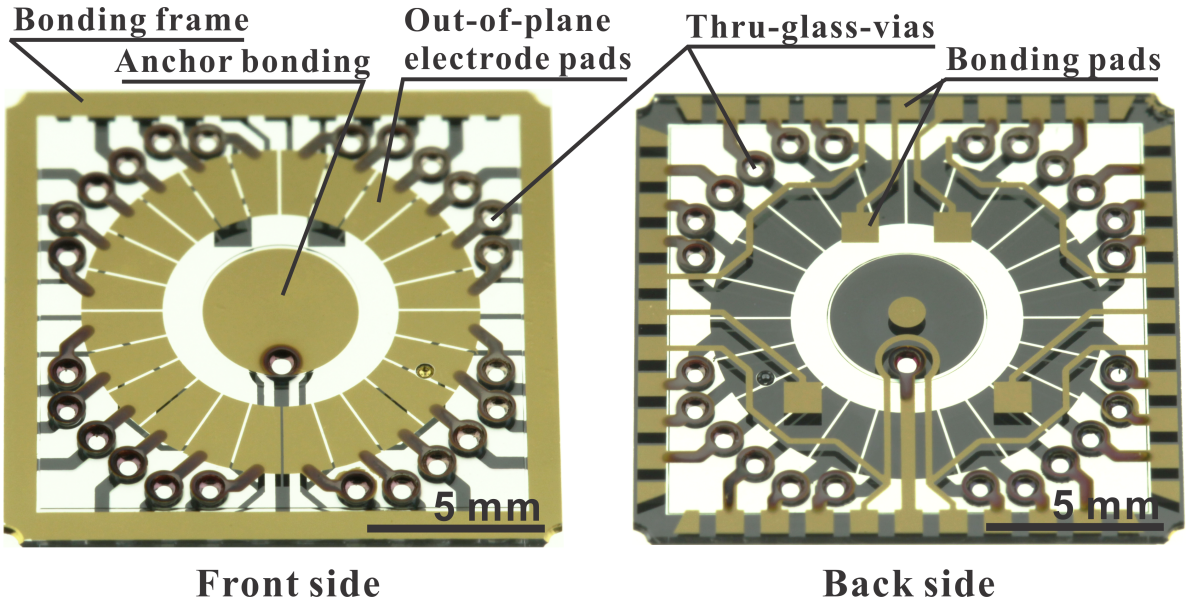

Figure 3.5: Images of the front- and back-side of a TGV planar electrode substrate. The eutectic bonding areas (outer frame and central anchor) and electrical paths are coated with Cr/Au thin films.

3.3.1 Fabrication Process

The TWIs and out-of-plane planar electrodes of the substrate are created by wet-etching TGVs in FS and selectively sputter-coating metal to create conductive layers on both, surface of the substrate and sidewalls of the vias. The simplified wafer-level fabrication process, presented in Fig. 3.4, produces high density, low parasitic interconnects with minimal mismatch of the thermal expansion coefficients between the electrode substrate and the resonator [76].

As shown in Fig. 3.4, the wafer-level fabrication of the TGV electrode substrate started with a 500 μm thick 4-inch diameter FS wafer, coated with 2 μm LPCVD doped poly-silicon layers on both sides in preparation for isotropic wet etching, Step (a). AZ P4620 photoresist layers were spin-coated on both sides of the FS wafer to pattern the poly-silicon hard masks for TGVs. The process was performed in a Surface Technology System (STS) Inductively Coupled Plasma (ICP) system, Step (b). After the photoresist layer was removed, the FS

wafer was time-etched to remove 250 μm from both sides in an HF 48% solution to define the TGVs, Step (c). Using another layer of photoresist, the patterns of the central and outer bonding areas for the fixed-fixed anchor architecture of the dual-shell sensor were defined on the poly-silicon hard mask on the top side of the FS wafer. The FS wafer was then wet-etched to create 40 μm cavities to reduce the capacitive gaps between the rim of the inner device shell and the planar electrodes, Step (d). Using a KOH solution, the poly-silicon hard masks were removed completely, and then the FS wafer was dipped in an HF 48% solution for about 5 minutes with stirring to smooth out all corners and sharp angles prior to the metal coating, Step (e). The conductive layers of 30/300 nm Cr/Au were deposited on both sides of the FS wafer using the Denton DV-502M sputter coater, Step (f). The metal layers were then patterned photo-lithographically for the central and bonding frame areas, out-of-plane electrode pads, and electrical traces, Step (h). Finally, another metallization with 5 nm Cr and 50 nm Au was selectively deposited on each side of TGVs using two shadow masks to improve the yield of TGVs, Step (g). The front and back sides of a TGV electrode substrate are illustrated in Fig. 3.5 with an array of 24 planar electrodes.

3.3.2 Gyroscope Assembly

Metallization of the 3D FS dual-shell resonator is required for electrostatic operation and eutectic bonding, shown in Fig. 4.1. A Cr/Au metal layer with the desired thickness was first used to selectively coat the sensing element, which is the inner sensor shell. The bonding frame and the central anchor were then coated with 50 nm Cr and 500 nm Au for Au-to-Au eutectic bonding with the TGV electrode substrate. The assembly process of the metallized dual-shell structure onto the TGV substrate is illustrated in Fig. 3.7. The eutectic bonding process was performed in a reflow chamber at 375 °C. A graphite fixture was used to center the dual-shell structure and substrate, and spacer shims were aided to control the capacitive gap during the assembly.

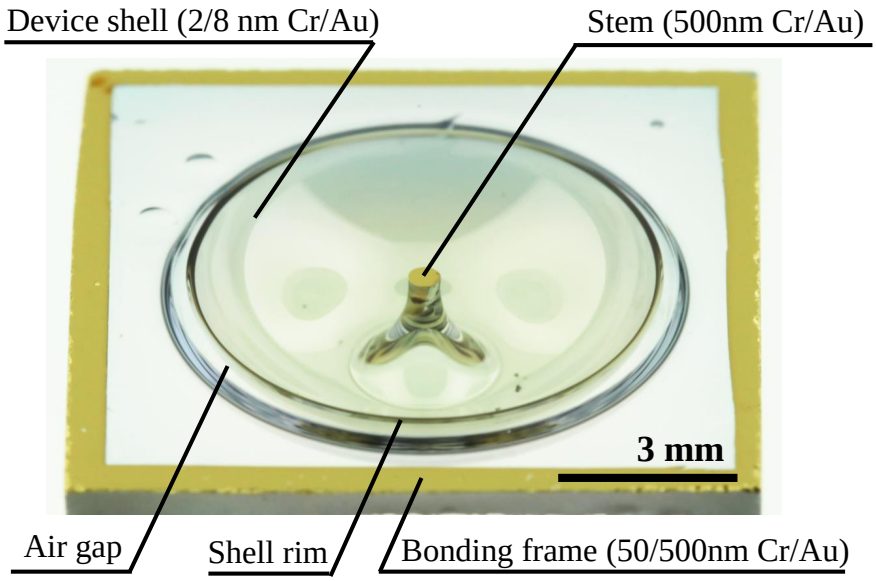

Figure 3.6: Illustration of an upside-down view of a dual-shell resonator metal-coated for conductivity and eutectic bonding before its assembly with an electrode substrate. The resonator was sputter-coated with 2/8 nm Cr/Au, while the bonding frame and the central stem were coated with 50/500 nm Cr/Au layer using a shadow mask.

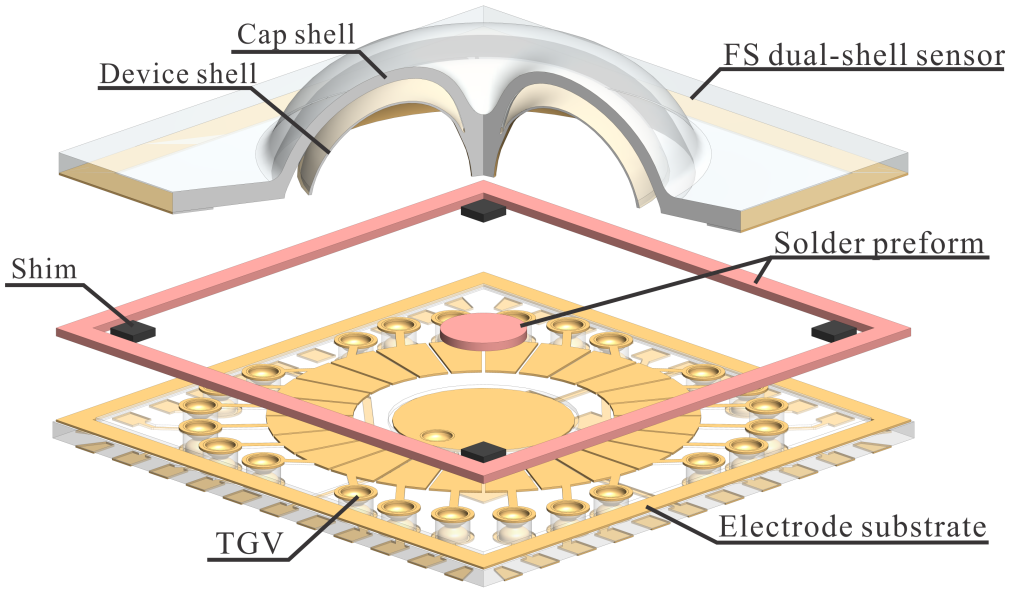

Figure 3.7: Schematic diagram of the assembly process for metallized FS dual-shell gyroscope.

Fig. 3.8 shows the two assembled FS dual shell gyroscope prototypes (DSG#1 and DSG#2) with different geometries, bonded on two TGV electrode substrates using the proposed method and electrostatically characterized. The DSGs were coated with 2 nm Cr and 8

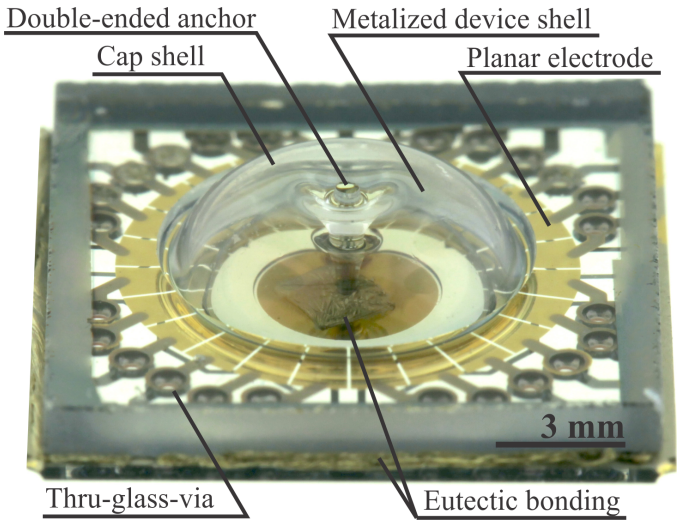

(a) DSG#1

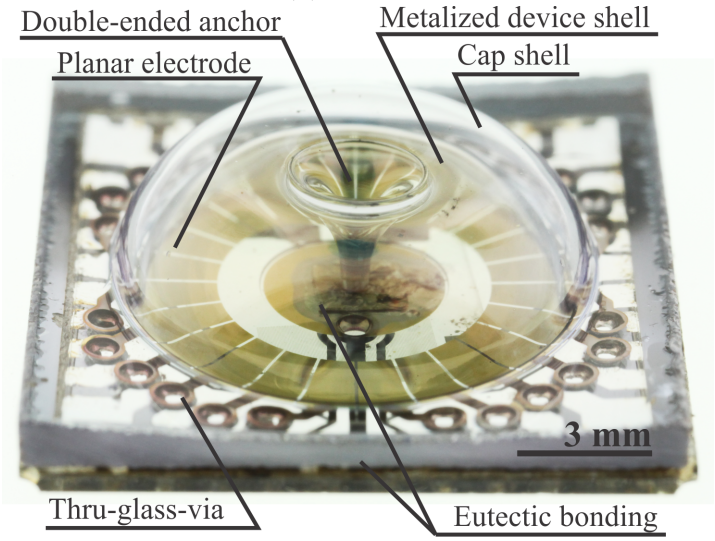

(b) DSG#2

Figure 3.8: The assembled FS Dual-Shell Gyroscope prototypes (DSG#1 and DSG#2 in Table 3.1) with out-of-plane TGV electrode substrates fabricated by the proposed process flow.

nm Au for sufficient conductivity with a minor impact on DSGs' noise performance based on the experimental results on selection of optimal thickness of metallization presented in [118]. The quality factors after metallization were measured and are presented in Table 3.1.

3.4 Electrostatic Compensation

The imperfections and structural asymmetry of DSGs result in a frequency split (Δf) between each mode pair and influence the mode shapes of the resonator [82]. These are the dominant first-order factors that degrade gyroscope performance. These symmetries can be compensated, for example, electrostatically. The assembly misalignment due to the integration step leads to an uneven capacitance gap between the rim of the sensor shell and electrode substrate [102], and has to be considered. In order to fully understand the impact of assembly errors on the electrostatic compensation of DSGs, an electromechanical model is developed in this section.

To simulate dynamics of an asymmetric DSG, a 2-DOF lumped mass-spring-damper model was used. The equation of motion in the matrix form can be represented as

$$\begin{bmatrix} \ddot{x}_n^s \\ \ddot{y}_n^s \end{bmatrix} + \boldsymbol{B}_n^s \begin{bmatrix} \dot{x}_n^s \\ \dot{y}_n^s \end{bmatrix} + \boldsymbol{\Lambda}_{\boldsymbol{n}}^s \begin{bmatrix} x_n^s \\ y_n^s \end{bmatrix} = \begin{bmatrix} f_{xn}^s \\ f_{yn}^s \end{bmatrix}, \tag{3.1}$$

where n denotes, in our case, the operational mode of either $n = 2$ or $n = 3$. x_n^s, y_n^s, f_{xn}^s, and f_{yn}^s are the displacements and forces along the principal axes of elasticity for each mode pair (X- and Y-axis) in the shell coordinate frame, illustrated in Fig. 3.9. Mismatches between the principal axes of elasticity and damping are typically small and are neglected in the model. Hence, $\boldsymbol{B}_n^s$ and $\boldsymbol{\Lambda}_{\boldsymbol{n}}^s$ are 2×2 matrices describing the damping and elasticity terms of the corresponding mode of the DSG after metallization, which are given as, [123],

$$\boldsymbol{B}_{\boldsymbol{n}}^s = \begin{bmatrix} 2\mu_{xn} & 0 \\ 0 & 2\mu_{yn} \end{bmatrix}, \quad \boldsymbol{\Lambda}_{\boldsymbol{n}}^s = \begin{bmatrix} \omega_{xn}^2 & 0 \\ 0 & \omega_{yn}^2 \end{bmatrix}, \tag{3.2}$$

where μ_{nx} and μ_{ny}, and ω_{nx} and ω_{ny} are the damping coefficients and resonant frequencies along the X- and Y-axis of each mode pair.

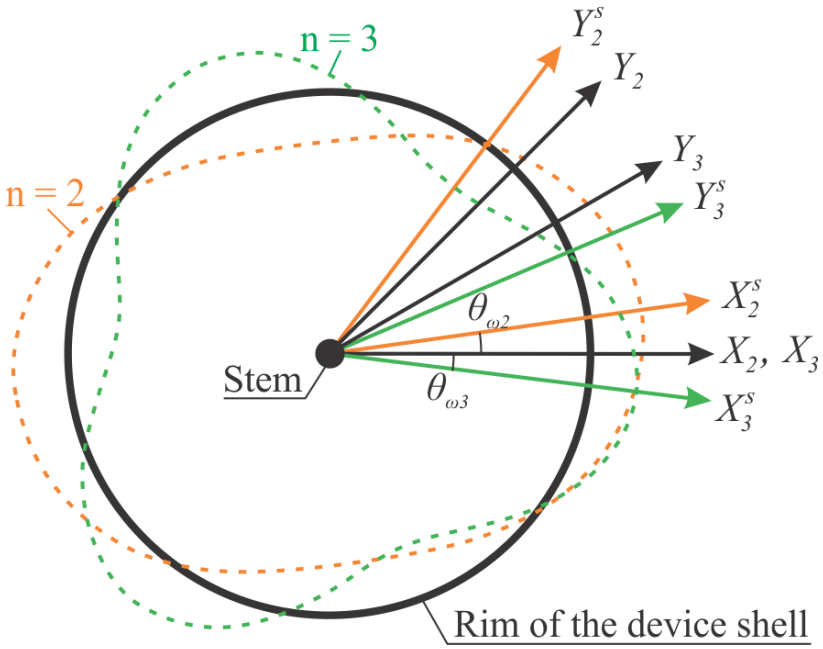

Figure 3.9: Mechanical model of DSG, defining the axes in shell coordinate frame: the principal axes of vibration of n = 2 and n = 3 mode pairs, x_n^s and y_n^s, and the directions of electrostatic forcer and pick-off electrodes applied by the electrode substrate, x_n and y_n.

For the integrated DSG system shown in Fig. 3.10, the main assembly errors include the inclination between the line connecting the base of the resonator and the surface of the substrate, θ; the misalignment between centers of the dual-shell and electrode stage in the x-y plane, Δx and Δy; and φ'_δ, the azimuth angle in the shell's coordinate frame between the point of minimum gap from the shell to the substrate (δ), the center of the shell (x'_0, y'_0), and the defined X-axis of the electrode substrate (X_e). Additionally, $\theta_{\omega 2}$ and $\theta_{\omega 3}$ are the angular misalignments between the principal axes of elasticity of the n = 2 and n = 3 modes with the electrode coordinate frame, X_e and Y_e. In order to capture the assembly errors in the dynamics and include the compensation terms of the integrated DSG, described in Eq. 3.1, it is rewritten in the matrix form as, [115],

$$\begin{bmatrix} \ddot{x}_n \\ \ddot{y}_n \end{bmatrix} + \boldsymbol{B}_n \begin{bmatrix} \dot{x}_n \\ \dot{y}_n \end{bmatrix} + (\boldsymbol{\Lambda_n} - \boldsymbol{\Lambda_{en}}) \begin{bmatrix} x_n \\ y_n \end{bmatrix} = \begin{bmatrix} f_{xn} \\ f_{yn} \end{bmatrix}, \tag{3.3}$$

where $\boldsymbol{B}_n$, $\boldsymbol{\Lambda_n}$, and $\boldsymbol{\Lambda_{en}}$ are 2×2 matrices describing the damping, elasticity, and anisoelas-

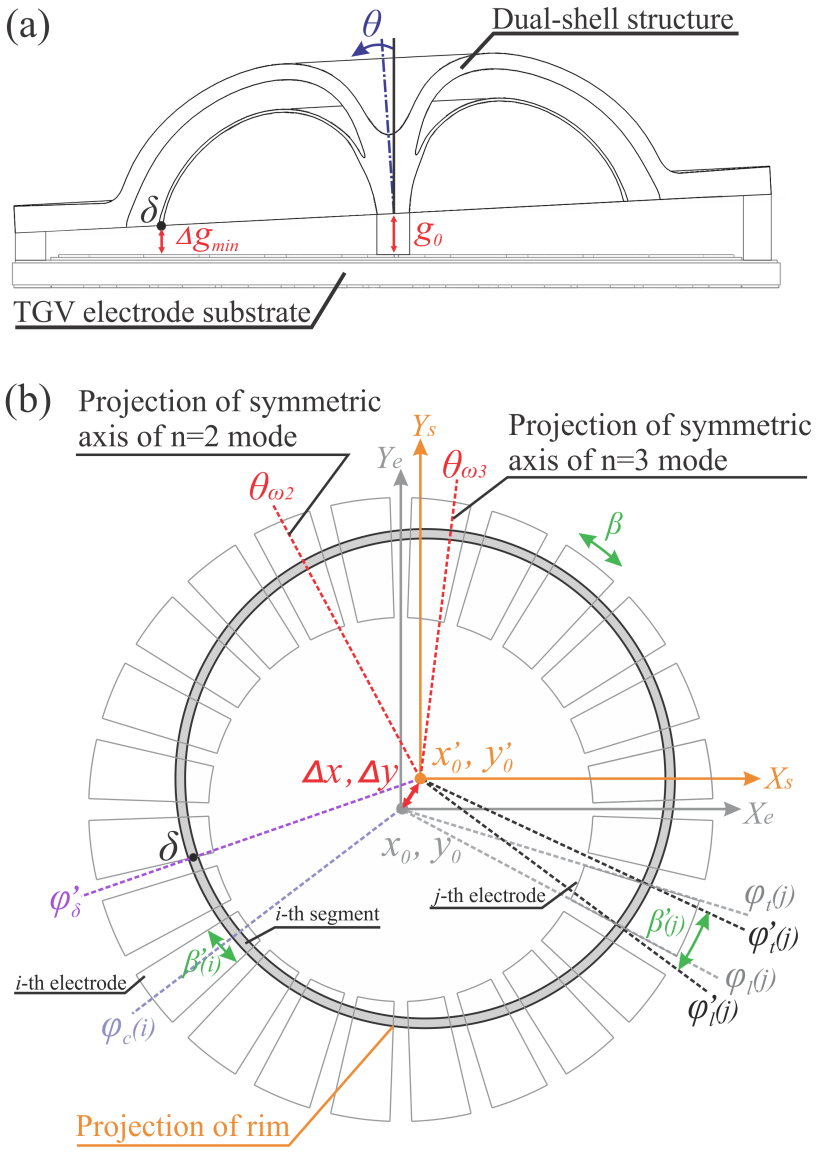

Figure 3.10: The assembly errors of DSG: (a) θ and g_0 are the inclination and vertical offsets; δ is the point where the gap between the shell and the substrate, Δg_{min}, is minimum. (b) $(x_0, y_0), X_e, Y_e$ are the center coordinates and the X- and Y-axis in the substrate frame; $(x'_0, y'_0), X_S, Y_s$ being the equivalence in the shell coordinate frame.

ticity electrostatic compensation terms of the n = 2 or n = 3 mode of the assembled DSG. x_n, y_n, f_{xn}, and f_{yn} are the displacements and forces along the X- and Y-axis, which are determined by directions of their corresponding forcers and pick-offs defined by the electrode coordinate frame, shown in Fig. 3.9.

The matrices $\boldsymbol{B}_n$ and $\boldsymbol{\Lambda}_n$ can be described as, [114],

$$\boldsymbol{B_n} = \begin{bmatrix} 2\mu_{\Sigma n} + 2\mu_{\Delta n}\cos(\phi) & 2\mu_{\Delta n}\sin(\phi) \\ 2\mu_{\Delta n}\sin(\phi) & 2\mu_{\Sigma n} - 2\mu_{\Delta n}\cos(\phi) \end{bmatrix}, \tag{3.4}$$

$$\boldsymbol{\Lambda_n} = \begin{bmatrix} \frac{1}{2}\omega_{\Sigma n}^2 + \frac{1}{2}\omega_{\Delta n}^2\cos(\phi) & \frac{1}{2}\omega_{\Delta n}^2\sin(\phi) \\ \frac{1}{2}\omega_{\Delta n}^2\sin(\phi) & \frac{1}{2}\omega_{\Sigma n}^2 - \frac{1}{2}\omega_{\Delta n}^2\cos(\phi) \end{bmatrix}, \tag{3.5}$$

with $\phi = 2n\theta_{\omega n}$, $\mu_{\Sigma n} = \mu_{xn} + \mu_{yn}$ and $\mu_{\Delta n} = \mu_{xn} - \mu_{yn}$, and $\omega_{\Sigma n}^2 = \omega_{xn}^2 + \omega_{yn}^2$ and $\omega_{\Delta n}^2 = \omega_{xn}^2 - \omega_{yn}^2$.

The electrostatic stiffness matrix per mass, $\boldsymbol{\Lambda_{en}}$, can be derived in terms of the electrical energy stored in the capacitors, U_e, and can be further written in terms of capacitance experienced at each shell segment, [124],

$$\boldsymbol{\Lambda_{en}} = \begin{bmatrix} \frac{\partial^2 U_e}{\partial x_n^2} & \frac{\partial^2 U_e}{\partial x_n \partial y_n} \\ \frac{\partial^2 U_e}{\partial y_n \partial x_n} & \frac{\partial^2 U_e}{\partial y_n^2} \end{bmatrix}, \; U_e = \sum_{j=1}^{24} \frac{v_t^2(j)c(j)}{2m}, \tag{3.6}$$

where $v_t(j)$ is the DC tuning voltage applied on the jth electrode. For each segment $j = 1, ..., 24$, the capacitance accounting for the in-plane misalignment between the dual-shell structure and substrate, $c(j)$, can be calculated as a function of the displacements, x_n and y_n, and by taking the integral along the shell segment from $\varphi_l'(j)$ to $\varphi_t'(j)$, the angles coinciding with the start and end angles of the jth substrate electrode, $\varphi_l(j)$ and $\varphi_t(j)$, [115],

$$c(j) = \int_{\varphi_l'(j)}^{\varphi_t'(j)} \frac{\epsilon R_m w}{g_s(\varphi') - x_n\cos(n\varphi') + y_n\sin(n\varphi')} d\varphi', \tag{3.7}$$

where ϵ is the complex permittivity of air, R_m is the average radius of the sensor shell, and w is the width of rim of the resonator. $g_s(\varphi') = g_0 - \theta R_m\cos(\varphi' - \varphi_\delta')$ is the static electrode gap due to assembly errors, with g_0 being the vertical gap between the central stem and electrode substrate.

The relationship between $(\varphi_l'(j),\ \varphi_t'(j))$ and $(\varphi_l(j),\ \varphi_t(j))$ is given by

$$\tan(\varphi_p(j)) = \frac{\Delta y + R_m \sin(\varphi_p'(j))}{\Delta x + R_m \cos(\varphi_p'(j))},\ p \in \{l, t\}, \tag{3.8}$$

with $\varphi_l(j) = \varphi_c(j) - {}^{\beta}/_{2}$ for the starting angle, $\varphi_t(j) = \varphi_c(j) + {}^{\beta}/_{2}$ being the ending angle, and $\varphi_c(j) = j \times {}^{\pi}/_{12}$ being the angle of the centerline of the jth electrode in the substrate frame. The variable β denotes the width of a single electrode pad. Thus, each of the second partial derivatives in $\boldsymbol{\Lambda_{en}}$ is given by

$$\frac{\partial^2 c(j)}{\partial x_n^2} = \frac{1}{2}\varepsilon R_m w \int_{\varphi_l'(j)}^{\varphi_t'(j)} \frac{2\cos^2(n\varphi')}{g_s(\varphi')^3} d\varphi', \tag{3.9}$$

$$\frac{\partial^2 c(j)}{\partial x_n \partial y_n} = \frac{\partial^2 c(j)}{\partial y_n \partial x_n} = \frac{1}{2}\varepsilon R_m w \int_{\varphi_l'(j)}^{\varphi_t'(j)} \frac{2\cos(n\varphi')\sin(n\varphi')}{g_s(\varphi')^3} d\varphi', \tag{3.10}$$

$$\frac{\partial^2 c(j)}{\partial y_n^2} = \frac{1}{2}\varepsilon R_m w \int_{\varphi_l'(j)}^{\varphi_t'(j)} \frac{2\sin^2(n\varphi')}{g_s(\varphi')^3} d\varphi'. \tag{3.11}$$

The proposed electromechanical model allows for a precise electrostatic tuning of an integrated 3D DSG by defining the appropriate usage of electrodes as well as providing the optimal values of the DC tuning voltages to compensate for both diagonal and off-diagonal terms of the stiffness matrix [111]. As shown in Fig. 3.11(a) and (b), the configurations of electrodes determined by the model are implemented on the TGV electrode substrate of the DSG#1 prototype for flexible excitation, detection, and electrostatic frequency compensation of asynchronous operation using either the n = 2 or n = 3 mode [115]. Fig. 3.11(c) demonstrates the layout for synchronous operation of the DSG in both the n = 2 and n = 3 modes for, potentially, an in-situ gyroscope drift compensation method [125].

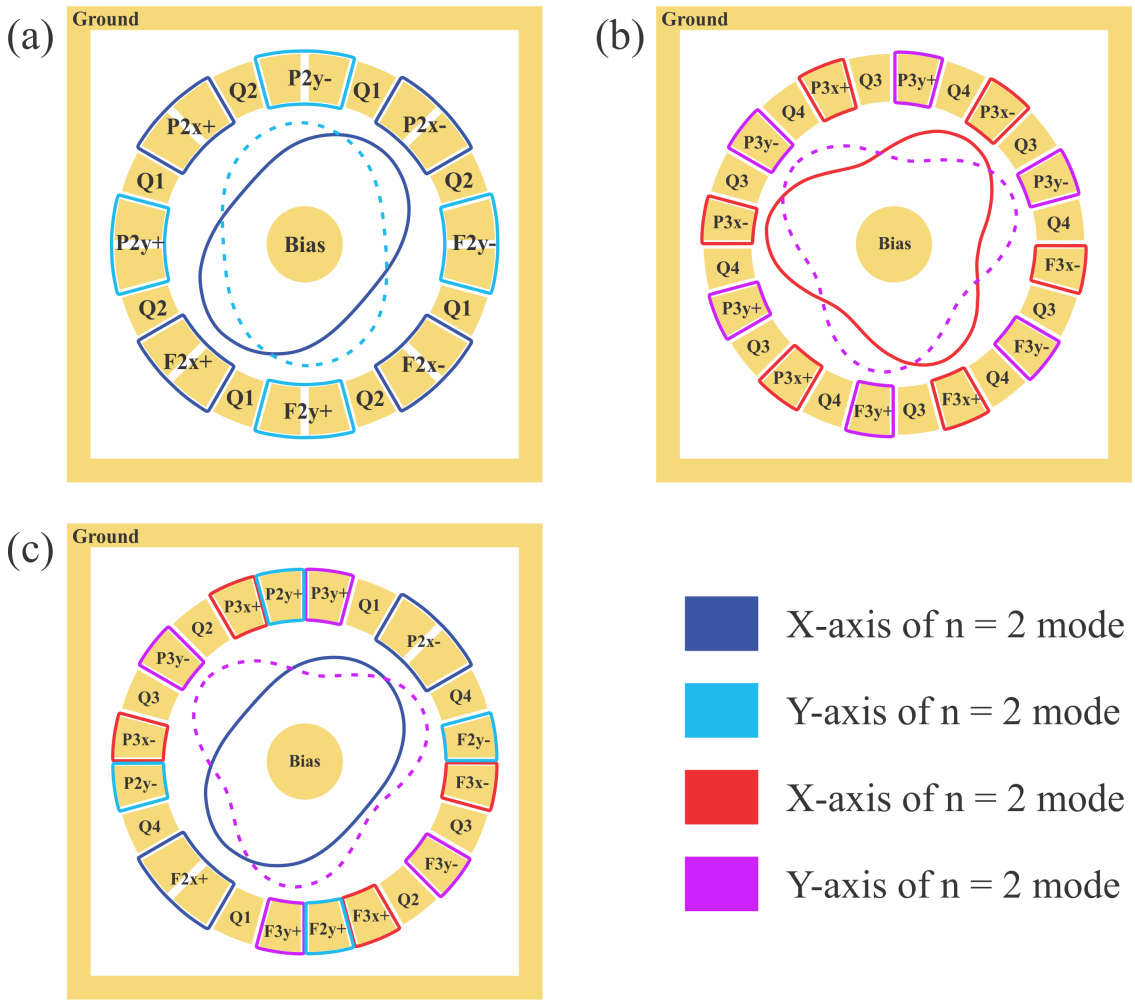

Figure 3.11: The electrode configurations for differential detection and excitation of (a) n = 2 mode, (b) n = 3 mode, and (c) synchronous operation of both modes for angular rate and whole angle measurements. F2x+, F2x-, P2x+, P2x-, F2y+, F2y-, P2y+, P2y-, F3x+, F3x-, P3x+, P3x-, and F3y+, F3y-, P3y+, P3y- indicate differential detection and excitation electrodes for X- and Y-axis of n = 2 and n = 3 modes, respectively. The Q1, Q2, Q3, and Q4 electrodes are for tuning and mode decoupling.

3.5 Assembly Error Identification Method

To enable the electrostatic tuning algorithm for compensating the structural imperfections of an integrated DSG, the assembly errors have to be identified first. However, it is nearly impossible to directly measure the assembly misalignments of a bonded DSG sample. Therefore, an identification method based on static capacitance measurement is presented in this section.

Table 3.2: Parameters and assembly errors used for numerical study of accuracy of the approximate static capacitance model

Parameter	Value	Parameter	Value
Average gap, g_0	10 μm	p_1	1.175 $\times 10^{-12}$
In-plane misalignment, Δx	50 μm	p_2	2.273
In-plane misalignment, Δy	-30 μm	q_0	0.6342
Azimuth angle, φ'_δ	90°	q_1	1.739
Inclination angle, θ	0 to 0.0015 rad	q_2	37.15

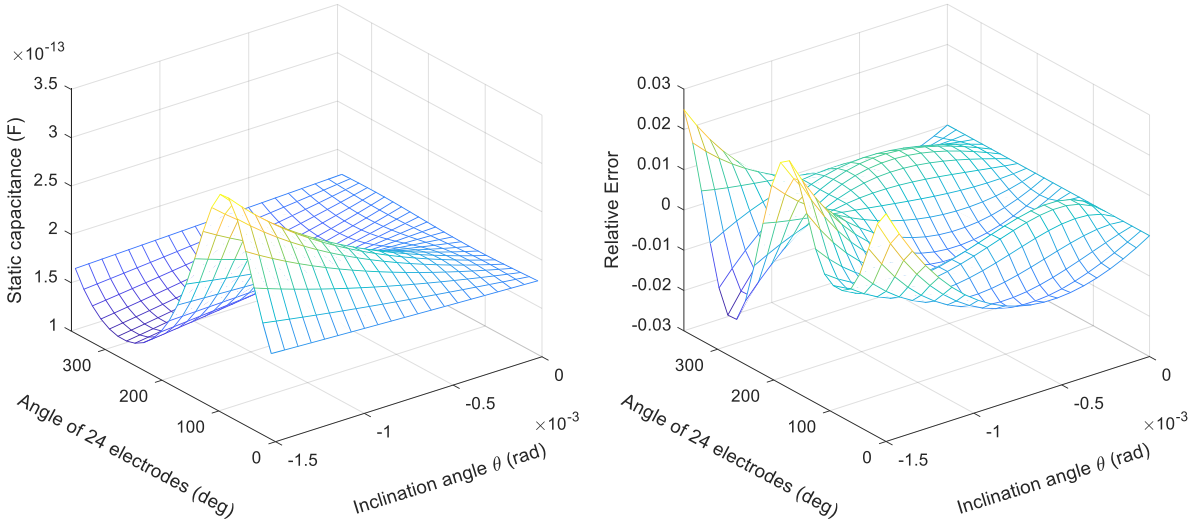

Figure 3.12: (Left) The ideal static capacitances and (right) the relative error of estimated capacitances of the DSG#1 prototype presented as a function of inclination angle, from 0 to 0.0015 rad, simulated using the approximate model and the parameters and assembly errors listed in Table 3.1 and 3.2.

As shown in Fig. 3.10, the static capacitance between the jth segment of the device rim and the jth electrode pad, $c_s(j)$, due to the assembly errors is given by, [114],

$$c_s(j) = \int_{\varphi'_l(j)}^{\varphi'_t(j)} \frac{\epsilon R_m w}{g_0 - \theta R_m \cos(\varphi' - \varphi'_\delta)} d\varphi', \tag{3.12}$$

where $j = 1, ..., 24$. Let $\beta'(j) = \varphi'_t(j) - \varphi'_l(j)$ and $\varphi'_c(j) = \frac{1}{2}(\varphi'_t(j) + \varphi'_l(j))$ represent the span and angle of the centerline of the jth segment in the shell coordinate frame. We assume that the average gap, g_0, is less than 10 μm (defined by the thickness of spacer shims). Thus, based on geometry of the shells in Table 3.1 and 3.2, the maximum inclination angle, θ_{max},

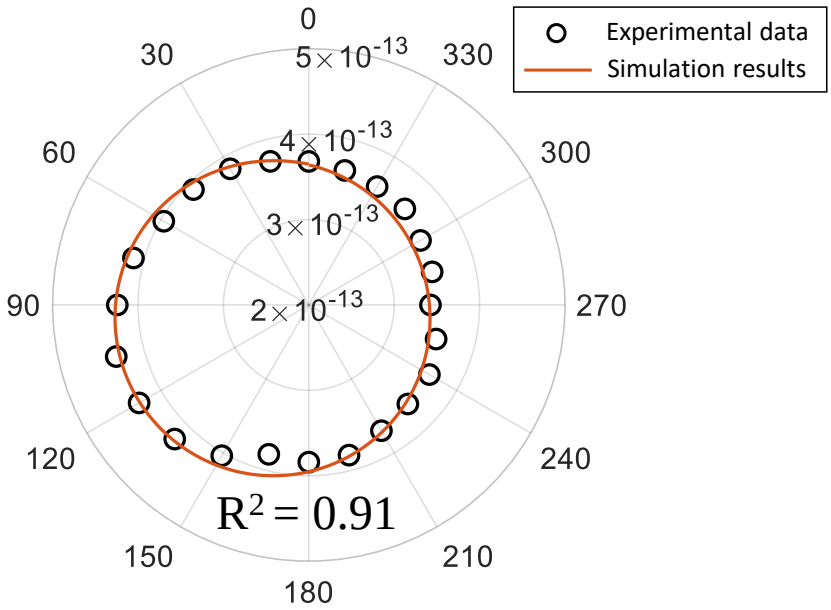

Figure 3.13: Experimental results of the 24 static capacitances of the DSG#1 prototypes, presented in Fig. 3.8(a), with the estimated static capacitances simulated by Eq. 3.14 and 3.15.

will be less than 0.0015 rad. The total static capacitances of the 24 electrodes, c_{tot}, can be approximately written as

$$c_{tot} = \sum_{j=1}^{24} c(j) \approx \frac{\epsilon R_m w}{g_0} \sum_{j=1}^{24} \beta'(j). \tag{3.13}$$

By substituting the in-plane misalignment, Δx and Δy, into Eq. 3.8, the span $\beta'(j)$ can be found, thus, the estimated average gap, $\widehat{g}_0$, is computed as

$$\widehat{g}_0 = \frac{\epsilon R_m w}{c_{tot}} \sum_{j=1}^{24} \beta'(j). \tag{3.14}$$

Based on Eq. 3.12 and 3.14, the approximation of the static capacitance, $c(j)$, can be given as

$$\widehat{c}(j) = \beta'(j) \left\{ P + p_1 \left\{ [1 - Q\cos(\varphi'_c(j) - \varphi'_\delta)]^{p_2\theta} - 1 \right\} \right\}, \tag{3.15}$$

Table 3.3: Identified assembly errors of two DSG prototypes

Errors due to assembly	DSG#1	DSG#2
Vertical gap between stem and substrate, g_0	17μm	14.5μm
In-plane misalignment, Δx, Δy (μm)	26, 14	-28, 34
Azimuth angle of point δ, φ'_δ	112°	78°
Inclination angle between shell and substrate, θ	0.057°	0.034°
Principal axis of elasticity of n = 2 mode, $\theta_{\omega 2}$	5°	11°
Principal axis of elasticity of n = 3 mode, $\theta_{\omega 3}$	-5.3°	4.5°

with

$$P = \frac{\epsilon R_m w}{\widehat{g}_0}, \quad Q = q_0 + q_1\theta + q_2\theta^2, \tag{3.16}$$

where q_0, q_1, q_2, p_1, and p_2 are the approximate parameters that are design dependent.

3.5.1 Accuracy of Approximate Static Capacitance Model

We determined the accuracy of the approximate static capacitance model by comparing the ideal and approximate static capacitances of the DSG#1, estimated using the design and simulation parameters in Table 3.1 and 3.2. The ideal static capacitances of 24 electrodes and the relative error, δc, defined as $\delta c = (\widehat{c}(j) - c(j))/c(j)$, as a function of the inclination angle, are shown in Fig. 3.12. The maximal relative error between the ideal and estimated values of the 24 static capacitances is less than 3% within the misalignment situations listed in Table 3.2, which indicates a good accuracy of the developed identification method.

3.5.2 Identification of Assembly Errors

To identify assembly errors of an integrated DSG using the approximate static capacitance model, Eq. 3.14 and Eq. 3.15, the horizontal offsets of Δx and Δy have to be measured first, and the rest of assembly errors can be then determined by substituting the measured values of static capacitances into the equations.

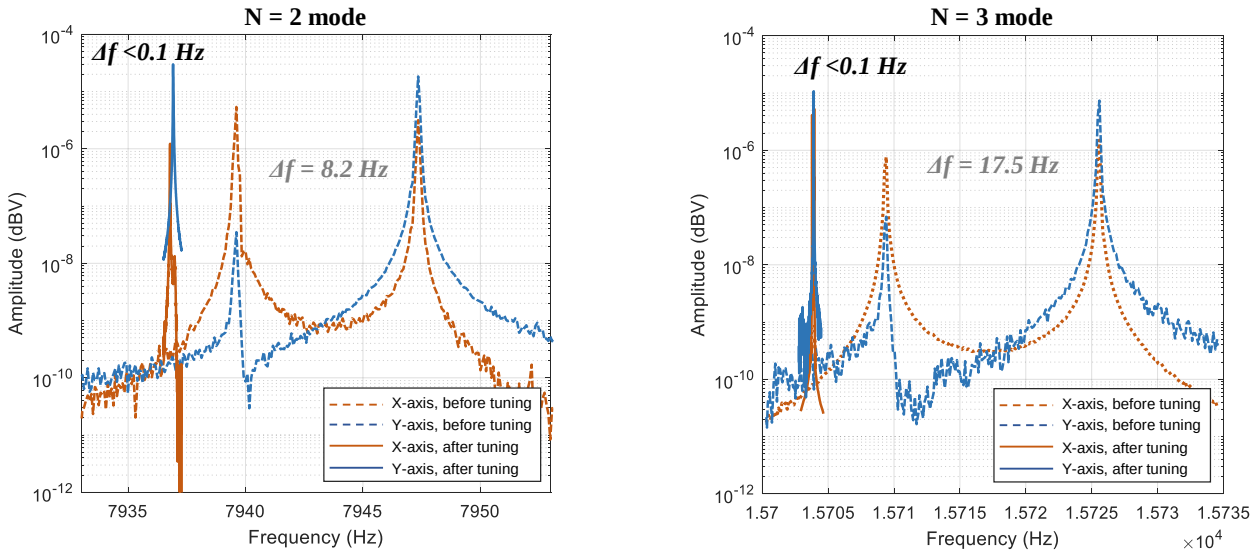

Figure 3.14: Experimentally extracted frequency responses showing electrostatic tuning of the n = 2 (left) and n = 3 (right) modes of the DSG#1 using the electrode configurations shown in Fig. 3.11(a) and (b).

For the DSGs listed in Table 3.1, the in-plane misalignments, Δx and Δy, were measured optically using a Leica DM4 B microscope. Utilizing a MEMS characterization platform (iTMEMS) for static capacitance measurement and the identification method developed in the chapter, the average gap (g_0), inclination angle (θ), and azimuth angle (φ'_δ) were determined and are listed in Table 3.3. The principal axes of elasticity of the n = 2 and n = 3 modes of the DSGs after assembly were experimentally measured using the frequency responses and damping factors, [123], and are also summarized in Table 3.3. Fig. 3.13 presents the experimentally measured static capacitances of the DSG#1. Black markers in Fig. 3.13 are the experimental results, and the solid red line is estimated by Eq. 3.14 and Eq. 3.15, which showed a good agreement between measurements and the analytical model.

3.6 Dual-Shell Gyroscope Operation

In this section, we report results on experimentally implemented electrostatic tuning algorithm and closed-loop Force-to-Re-balance (FRB) control with the DSG architecture. The

DSG#1 with the design parameters and identified assembly errors, reported in Tables 3.1 and 3.3, was tested in a vacuum chamber with a custom-designed Printed Circuit Board (PCB) to apply differential actuation signals to the DSG and measure the motional current through transimpedance amplifiers.

Utilizing the electromechanical tuning algorithm in Section 3.4, the frequency responses of the n = 2 and n = 3 modes of the DSG#1 were simulated, revealing the configurations of electrode, shown in Fig. 3.11(a) and (b). The frequency mismatches of both modes were experimentally tuned to a value on the order of 100 mHz for the near-mode-matched condition, shown in Fig. 3.14, with the following tuning voltages: F_{2y}=40.9V, Q_2=25.1V, F_{3x}=61.3V, and Q_4=40.6V. The closed-loop FRB control was then implemented in the DSG#1 prototype for angular rate measurements using a Zurich HF2Li lock-in amplifier. In all the experiments, the vibration amplitudes along the drive axes (higher resonant frequency mode) of the n = 2 and n = 3 modes were set to 50% of the capacitive gap and were stabilized by the Automatic Gain Control (AGC) and Phase-Locked Loop (PLL) control loops to prevent variations in the amplitude and phase. Quadrature nulling and rate control loops were then implemented on the DSG to suppress motion along the sense axis (lower resonant frequency mode). The noise performances of the DSG operation using either the n = 2 or n = 3 mode are shown in Fig. 3.15, presenting Angle Random Walks of 0.017 and 0.053 deg/rt-hr, and in-run bias instabilities (B. I.) of 0.2 and 0.63 deg/hr, respectively.

The array of 24 planar electrodes with the electrostatic tuning algorithm opens up an opportunity for flexible usage of multiple pairs of modes of DSGs. As a demonstration, the frequency splits of both the n = 2 and n = 3 modes of the DSG prototype were compensated concurrently to the order of 0.6 Hz using the predicted tuning voltages derived by the parameter identification procedure and the tuning algorithm. The following tuning voltages were applied to the electrodes using the configuration shown in Fig. 3.11(c), $F_{2y} = 91V$, $F_{3x} = 96V$, $Q_1 = 12V$, and $Q_2 = 28V$. The frequency responses of the n = 2 and n = 3

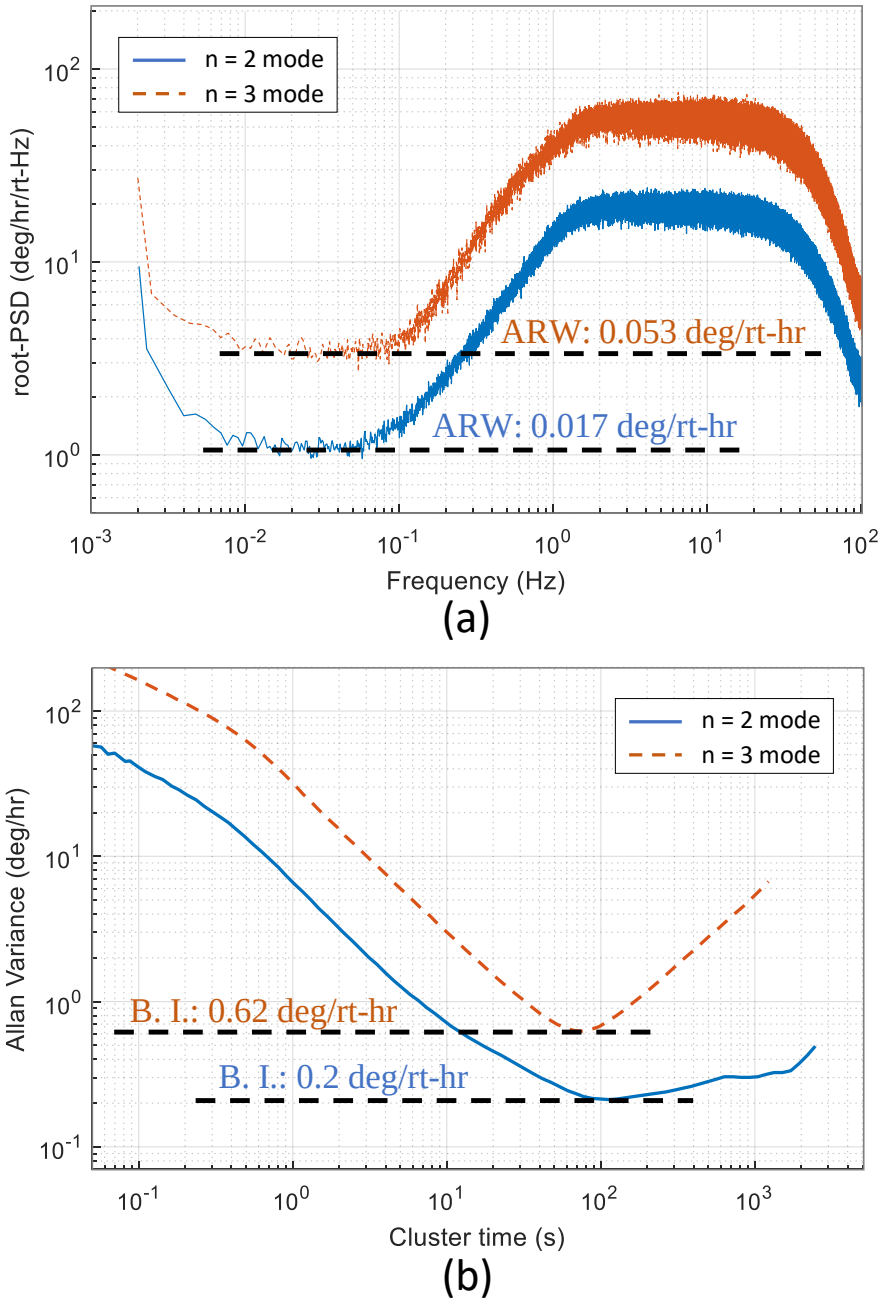

Figure 3.15: (a) The root-PSD and (b) Allan variance characterizations of the DSG's Zero Rate Output using either the n = 2 or n = 3 mode as the operational mode.

modes, before and after tuning, are presented in Fig. 3.16, as the first step towards concurrent operations to obtain two independent measurements of the same angle of rotation for in-situ gyroscope drift compensation [125].

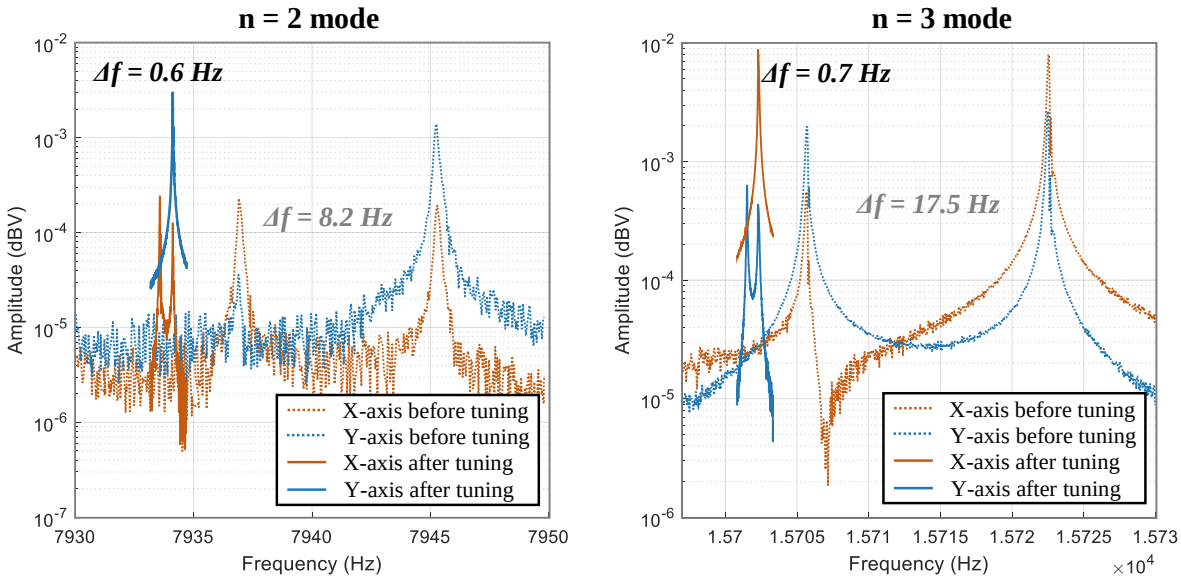

Figure 3.16: Frequency responses of concurrent electrostatic compensation of the n = 2 (left) and n = 3 (right) modes using the electrode configurations shown in Fig. 3.11(c).

3.7 Conclusion

We introduced in this chapter the 3D FS Dual-Shell Gyroscope (DSG) as a paradigm for realization of environmentally robust MEMS CVGs that are capable of providing continuous operation through extreme events of shock and vibrations. The FS DAGs were realized using the triple-stack glassblowing process, and in-plane actuation by out-of-plane electrodes realized using the Thru-Glass-Vias (TGVs) fabrication process. This implementation of Hemispherical Resonator Gyroscopes on micro-scale is reported for the first time. To achieve high-precision gyroscope operation, an identification method based on static capacitance measurements was developed for DSGs to extract assembly errors. In this chapter, we developed an electrostatic tuning algorithms, taking into account the effect of assembly errors to compensate the n = 2 and n = 3 mode pairs, both asynchronously and synchronously. The algorithms permit the use of degenerate modes for high-performance gyroscope operation and also open up an opportunity for flexible usage of a single or multiple pairs of modes of DSGs for in-situ gyroscope drift compensation. We experimentally demonstrated the asynchronous gyroscope operations using either the n = 2 or n = 3 mode of a DSG prototype with an aid

of the proposed identification method and the tuning algorithms, with preliminary results revealing an ARW on the order of 0.017 deg/rt-hr and in-run bias instability of 0.2 deg/hr.

Chapter 4

Effect of Metallization in FS MEMS Resonators

Metallization of Fused Silica (FS) micro-machined capacitive vibratory gyroscopes is necessary to allow for electrostatic actuation and detection of motion. Metal-coating provides electrical conductivity, but reduces the quality factor of resonators and thus impacts the noise characteristics. To achieve high-performance CVG operations, this chapter presents the effect of the metallization material and its thickness on the quality factor and noise characteristics using FS micro-HRGs as test vehicles. In Section 4.1, we first demonstrate the experimental results of the effect of metallization on energy dissipation and electrical resistance and develop an analytical electromechanical model based on the experimentally extracted impacts in Section 4.2. In Section 4.3, a design space for selection of metal coating of FS sensors is investigated. Variations in the noise performance due to metal coating are verified experimentally on in-house developed FS DSGs. We then propose optimal material and thickness of metal coating to optimize the quality factor and increase the gyroscope noise performance. Finally, the chapter is concluded with Section 4.4.

4.1 Effect of Metallization

A thin-film metal coating is needed on the FS sensor shell to electrically bias the proof-mass for capacitive electrostatic actuation and detection. To understand the impact of metallization on gyroscope's noise performance, variations of the Q-factor and electrical resistance due to different materials and thicknesses are studied in this section. The impacts are experimentally validated on in-house developed FS DSG prototypes for demonstration purposes, reported in Chapter 3.

Typically, a few tens of nanometers of the metal layer thin films – or a combination of metals, such as Ir, Cr, Cr/Au, or Ti/Au – are sputter-coated onto the FS resonators, [98, 94]. The type of metals used and their thicknesses have a significant impact on the Q-factor [98] and electrical resistances of the device [117]. Au as one of the most conductive metals and with a great oxidation resistance is commonly used to metalize MEMS sensors. To increase adhesion of Au to a substrate, a thin layer of Cr commonly utilized. Cr is also a highly conductive metal and can be used as a conductive layer by itself, as a low-cost alternative, [126]. Therefore, in this chapter, we consider two types of metal coatings, Cr and Cr/Au with a 1:4 thickness ratio. In all experiments, the thicknesses of Cr/Au metal coatings are reported as the total thicknesses of both Cr and Au layers, unless otherwise specified.

The metal coatings of Cr or Cr/Au with different thicknesses were sputtered onto the inner shells of the two test DSGs. The metal layers were deposited using a Denton DV-502M sputter system with a 20W RF mode and a pressure level of 4.8 mTorr. The deposition rates were 0.3 Å/s for Cr and 0.8 Å/s for Au. Due to curvature of sidewalls of the inner device shells, the actual thicknesses adhered to the curved surfaces were smaller than they would be on a flat surface [127]. An upside-down view of a DSG with a selectively metalized inner vibrating shell using a shadow mask as well as the central and the outer bonding areas forming the anchor are shown in Fig. 4.1. The shadow mask deposition mechanism is

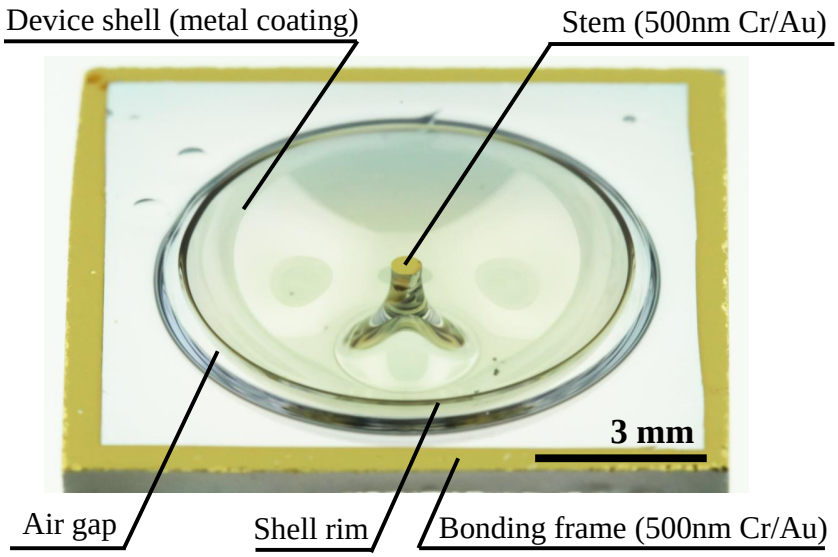

Figure 4.1: An exposed upside-down view of a released dual-shell resonator metal-coated for conductivity and eutectic bonding before its assembly with an electrode substrate. The resonator was sputter-coated with 3/12 nm Cr/Au, while the bonding frame and the central stem were coated with 50/500 nm Cr/Au layer using a shadow mask.

presented in Appendix A.9.

The experimentally measured Q-factors and electrical resistances of the DSG#1 and DSG#2, Fig. 3.8(a) and (b), for the two types of metal coating materials are presented in Fig. 4.2(a) and (b) with thicknesses varying from 5 to 20 nm. The X and Y axes are the principal axis of damping of the device [82]. The Q-factors were characterized in a vacuum chamber under a reduced below atmospheric pressure on the order of 1 μTorr, using a bulk piezo stack for excitation and a Polytech Laser Doppler Vibrometer (LDV) for detection. In all the experiments, the mechanical losses other than surface losses were held constant by controlling the vacuum pressure and contact area between the piezo stack and DSGs. Thus, the surface dissipation due to metallization was the only remaining factor contributing to variations in the Q-factors. The electrical resistances were measured through four-point measurement using a LakeShore FWP6 probe station, with two probes contacting the center stem and two probes contacting the rim of the DSG. Resistivities of sputter-coated Cr and Au layers were experimentally measured, Fig. 4.2(c).

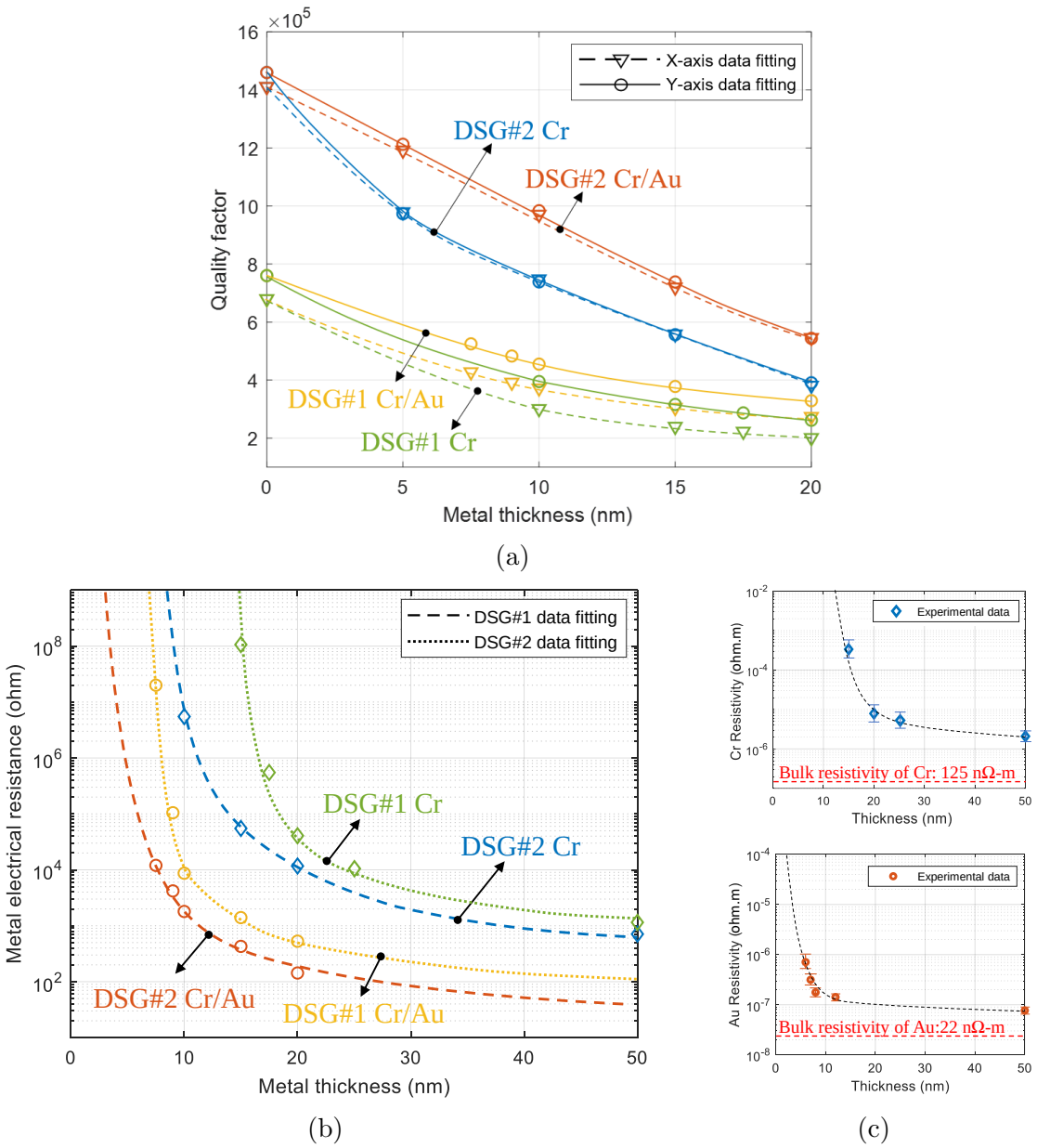

Figure 4.2: Experimental data demonstrating the effects of Cr and Cr/Au metal coatings on (a) quality factor and (b) average metal electrical resistance. The data is presented for two prototypes, DSG#1 and DSG#2. The Q-factors of n = 2 wineglass mode of the DSG#1 and n = 3 mode of the DSG#2 were measured at different thicknesses of coating, from 5 to 20 nm. In (c), the measured resistivities with error bars of the sputter-coated Cr and Au materials are presented. Resistivity values were acquired from flat samples, with thicknesses measured on a flat surface.

As shown in Fig. 4.2, the Q-factors of both the X- and Y-axis of the measured mode pairs of the DSGs decreased with increased metal thicknesses for both prototypes. The

as-fabricated Q-factors of uncoated shells decreased by 55% to 60% when a 20 nm Cr/Au layer was deposited, and the Q-factors decreased by 65% to 71% when a Cr layer of the same thickness was deposited. The most significant electrical resistances of both DSGs were measured when a thin (<10 nm) Cr layer was coated. We concluded, the Cr/Au metal layer is preferred, depicting 100 times less electrical resistance as compared to 20 nm Cr/Au and 20 nm Cr on the DSG#1. The experiments revealed a clear influence of the coating metal materials and thicknesses on the Q-factor and electrical resistance. An increased resistance of ultra thin-film metal coatings can be attributed to an increased resistivity of the sputter-coated metal layers, as demonstrated in Fig. 4.2(c).

Differences in metal electrical resistance and the Q-factor between the two DSGs are primarily due to differences in their 3D geometries. Typically, a poor conductivity of 3D micro-shells is due to a more pronounced shadow effect of the 3D structure during coating. This difference is observed between DSG#1 and DSG#2, where thinner and more uneven metal coatings are found at the near-vertical sidewalls of the rim and the center stem. The metal electrical resistances at different in-plane azimuth angles of the rims for both the DSGs were measured experimentally. Uniformity of each group of resistances was represented by the coefficient of variation (COV), illustrated in Fig. 4.3. Red markers denote the experimental results, $R(\varphi')$, which appeared to be effectively modeled by sinusoidal functions, $R(\varphi') = \alpha \sin(\varphi' + \phi) + R_o$, with respect to the azimuth angle φ' of the rim, shown as solid blue lines in the figure. α, ϕ, and R_o are fitting parameters. A considerable variability of resistances was observed for both DSGs due to an ultra-thin but uneven metal coating, Fig. 4.3.

4.2 Electromechanical Model

The Q-factor significantly impacts the performance of FS micro-HRGs, including sensitivity of motion detection and the gyroscope's noise performance [103, 117]. In addition to

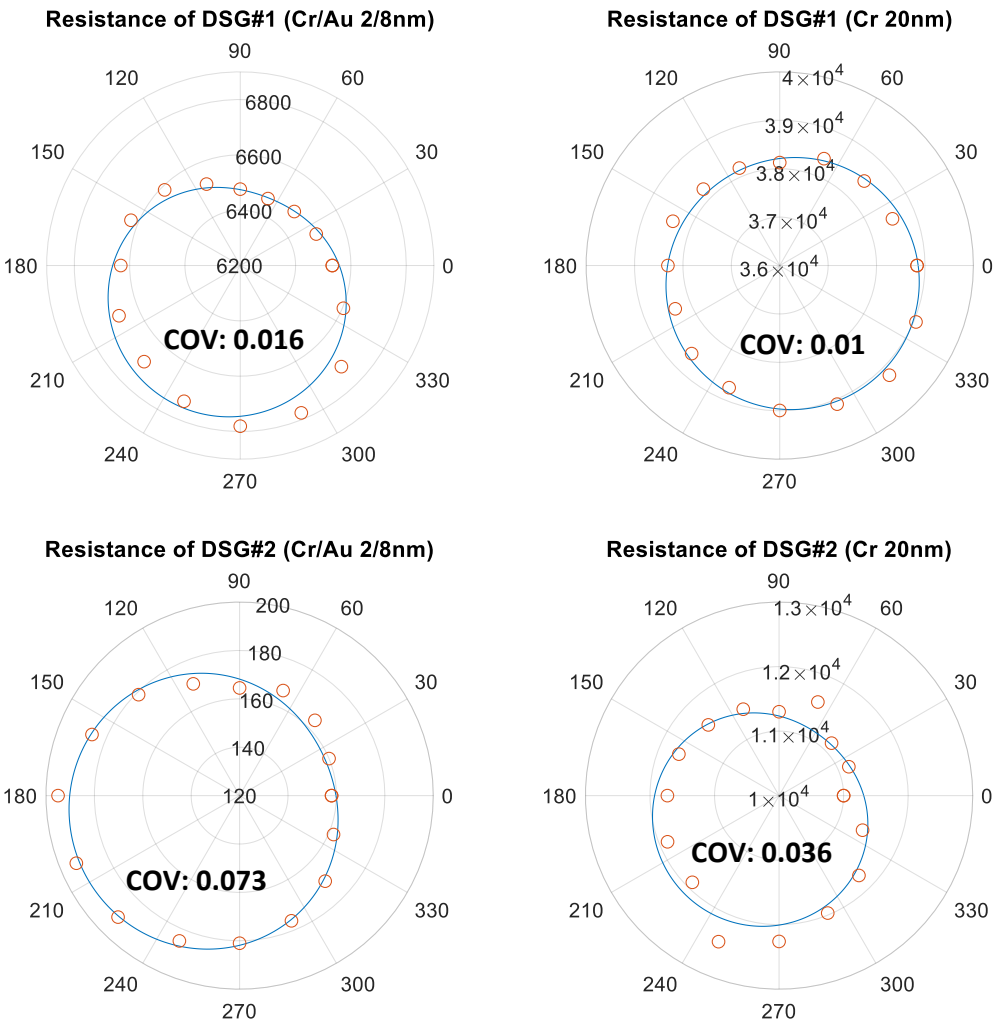

Figure 4.3: Experimental results of the metal electrical resistances of the DSG#1 and DSG#2 prototypes sputter-coated with 10 nm Cr/Au and 20 nm Cr metal layers.

accounting for the effect of metal coating on the Q-factor, it is also necessary to derive a dependence of the electrical resistance due to metallization on the DSG's noise characteristics. An electromechanical model was developed based on experimental observations described in Section 4.1. The model was used to estimate the contribution of electrical resistance of interconnects to the gyroscope's noise performance, followed by an analytical prediction of the overall noise characteristics.

A sketch and simplified electromechanical schematics of DSG integrated with TGV substrate are shown in Fig. 4.4. For our description, we used parameters as defined in [115]. Param-

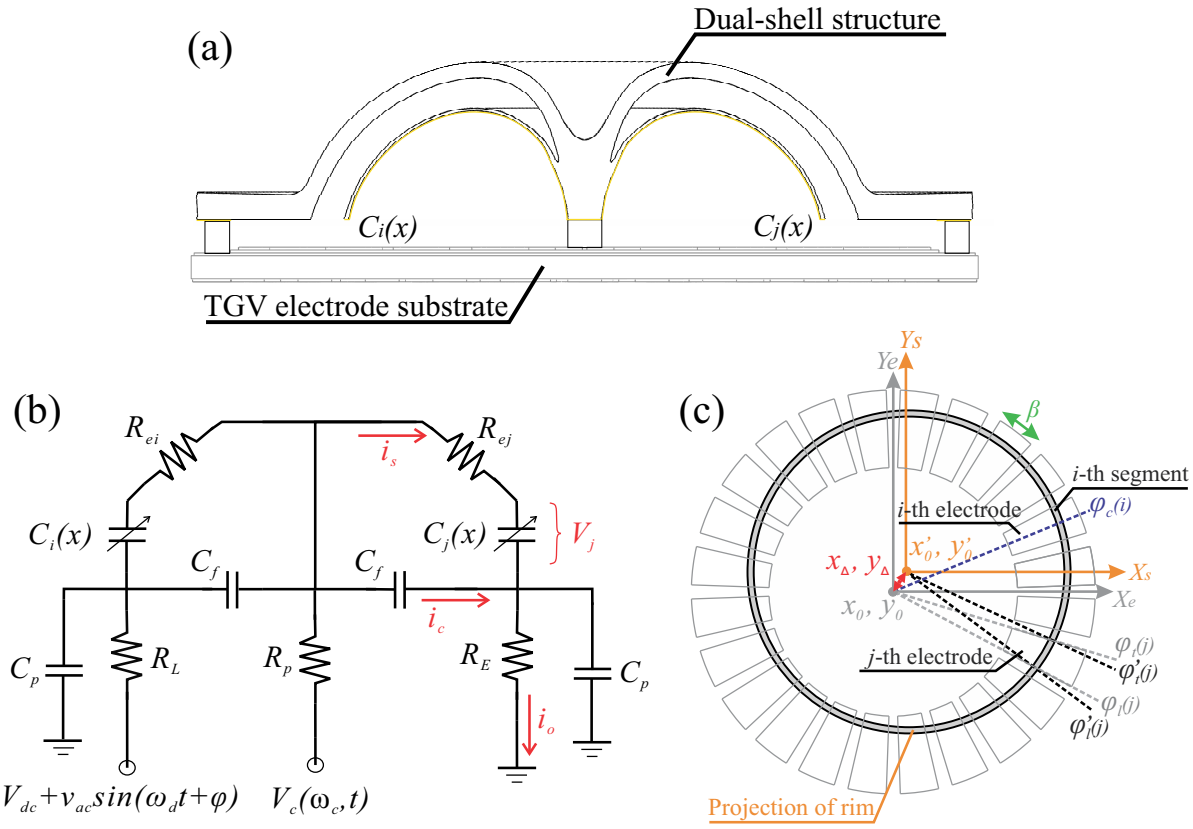

Figure 4.4: (a) Assembled FS Dual-Shell Gyroscope (DSG) and (b) simplified electromechanical schematics, including dynamics of DSG and parasitics introduced by interconnects of the electrode substrate and front-end circuit. (c) In-plane and angular misalignments of DSG is due to assembly errors: (x_0, y_0) are the center coordinates, and X_e and Y_e are the X and Y axes expressed in the substrate coordinate frame; $(x_0', y_0'), X_s$, and Y_s are the center and coordinates of the X and Y axes of the shell coordinate frame.

eters $C_i(x)$ and $C_j(x)$ denote the position-dependent forcer capacitance of the ith electrode and pick-off capacitance of the jth electrode, while R_{ei} and R_{ej} are the effective metal electrical resistances associated with $C_i(x)$ and $C_j(x)$. As illustrated in Fig. 4.4(c), the electrode substrate contains 24 electrode pads. For each segment, $j = 1, ..., 24$, the capacitance, $C_j(x)$, accounts for the in-plane misalignment between the dual-shell structure and substrate, x_Δ and y_Δ, and is calculated by taking the integral along the shell segment from the angle $\varphi_l'(j)$ to $\varphi_t'(j)$, with both angles coinciding with the start and the end angles of the jth electrode of the substrate, $\varphi_l(j)$ and $\varphi_t(j)$.

For electromechanical amplitude modulation of the motional signal, x, an AC bias signal,

$V_c(t) = v_c cos(\omega_c t + \Phi)$, was applied to the proof-mass of DSG though the central stem. Taking into account the effective electrical resistance, R_{ej}, the actual potential difference between movable rim of the shell and anchored jth electrode is $V_j(t)$ at a frequency ω_c. Therefore, the total pick-off current, i_o, and the motion-induced current, i_s, can be expressed as, [117],

$$i_o = i_s + i_c - C_p R_E \frac{d}{dt} i_o, \tag{4.1}$$

$$i_s = \frac{d}{dt}(V_j(t) C_j(x)), \tag{4.2}$$

with

$$i_c = C_f \frac{d}{dt}(i_s R_{ej} + V_j(t)), \tag{4.3}$$

$$V_j(t) = V_c(t) - R_p(i_s + i_c) - i_o R_E - i_s R_{ej}, \tag{4.4}$$

where C_f, C_p, and R_p are the feedthrough capacitance, parasitic capacitance, and parasitic resistance introduced by interconnects of the TGV electrode substrate and the front-end circuit. R_L and R_E are the loading and effective feedback resistances of the pick-off circuit, [120].

To calculate the effective electrical resistance in the electromechanical model, a method of approximation was used. Assuming the jth electrode contains n evenly distributed discrete plates defined by $n+1$ nodes from l to t. The relationship between l and t can be described as $t \equiv l + n$. The nodes l and t are given as $l = \varphi_l'(j)\frac{m}{2\pi}$ and $t = \varphi_t'(j)\frac{m}{2\pi}$, when the total device shell rim is evenly distributed by m nodes. As shown in Appendix B, the effective electrical resistance, R_{ej}, for the C_j electrode can be derived as, [128],

$$R_{ej} = \frac{\sum_{k=l}^{t} \frac{R_k}{M_{k,k}^{-1}} \sum_{i=l}^{t} M_{k,i}^{-1}}{n \sum_{k=l}^{t} \sum_{i=l}^{t} M_{k,i}^{-1}}. \tag{4.5}$$

Parameter $M_{k,i}^{-1}$ is defined as the inverse of the coefficient matrix in Eq. B.3, and can also

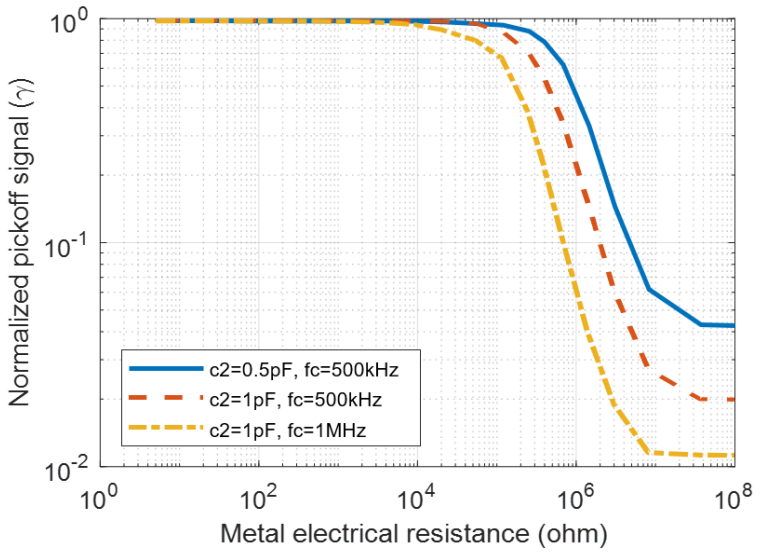

Figure 4.5: Simulation results of the pick-off informational signal as a function of metal electrical resistances for different pick-off capacitances and carrier frequencies, calculated using the electromechanical model in Section 4.2.

be determined using the experimentally acquired resistance, R_k, where $R_k = R(\varphi'|_{2\pi\frac{k}{m}}) = \alpha\sin(2\pi\frac{k}{m}+\phi)+R_o$, as shown in Section 4.1. The details of the calculations can be found in Appendix B.

The pick-off signal was demodulated with $cos(\omega_c t+\omega_d t)$ and $sin(\omega_c t+\omega_d t)$ and then filtered by a low pass filter when a single side-band demodulation technique was used, after which only the $\omega_c+\omega_d$ term would remain. Thus, the amplitude of the $\omega_c+\omega_d$ side-band is the informational signal in the pick-off current and is given by, [129],

$$\|i_{\omega_c+\omega_d}\| \approx \frac{1}{2}C_j(\omega_c+\omega_d)\frac{x_0}{\sqrt{1-x_0^2}}\|V_j\|\,, \tag{4.6}$$

where x_0 is the amplitude of the device shell normalized to the capacitive gap and ω_d is the resonant frequency. Assuming the resonator vibrates with a constant amplitude, the normalized pick-off signals, γ, at different carrier frequencies and pick-off capacitances are modeled in Fig. 4.5. Therefore, the informational signal, $i_{\omega_c+\omega_d}$, was observed to reduce as a function of the electrical resistance, and the effect is more pronounced with a higher carrier

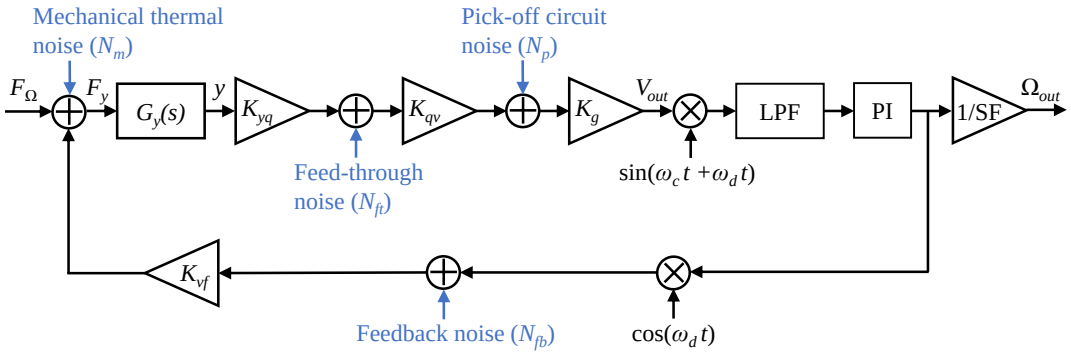

Figure 4.6: Noise model of FRB closed-loop system, including the mechanical thermal noise (N_m), pick-off circuit noise (N_p), feed-through noise (N_{ft}), and feedback circuit noise (N_{fb}).

frequency and a larger pick-off capacitance.

The electrical resistance of the metal film affects the pick-off signals along both the drive and sense modes in a DSG operating under the Force-to-Re-Balance (FRG) mode, especially, when applying a higher carrier frequency to the proof-mass. The large electrical resistance of the ultra-thin metal coating, electrical noise of the pick-off circuits, and weak informational signals would reduce the signal-to-noise ratio (SNR) and further degrade the overall gyroscope noise performance. Although an increase in the metal coating thickness would reduce the electrical resistance and relieve the negative effect of resistance on pick-off signals, a decrease in the Q-factor would affect the mechanical thermal noise and electrical noise in a mode-matched, or near-mode-matched, gyroscope operated in the FRB mode [130].

To further study the conflicting contributions of the metal layer on the Q-factor and electrical resistance on gyroscope's noise performance, an analytical noise model of FRB mode was developed, illustrated in Fig. 4.6. This model takes into account the mechanical thermal noise (N_m), pick-off circuit noise (N_p), feed-through noise (N_{ft}), and feedback circuit noise (N_{fb}). In the model, we assume DC electrostatic tuning voltages were applied to adjust the frequency split and quadrature coupling between the operational modes to achieve a near-mode-matched condition and to eliminate the quadrature-induced noise [19, 111]. The equivalent noise represented by the Angle Random Walk (ARW) was calculated as

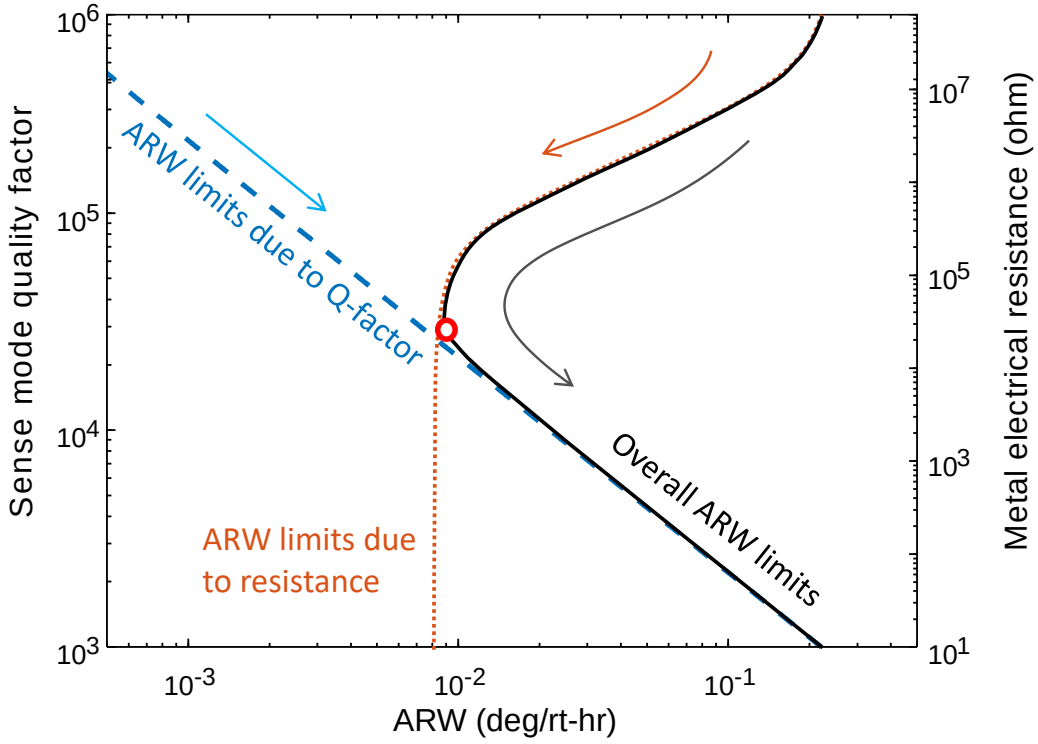

Figure 4.7: The estimated ARW limits of DSG#1 due to quality factor and metal electrical resistance, when device is operated in FRB mode.

$\sqrt{S_{\Omega_n}(\omega)|_{\omega=0}}$, where $S_{\Omega_n}(\omega)$ is the power spectral density (PSD). For a DSG operated in the FRB mode, $S_{\Omega_n}(0)$ is expressed as, [131],

$$S_{\Omega_n}(0) \approx \frac{1}{2m^2\eta^2 A_x^2 \omega_x^2}(S_{N_m} + S_{N_{fb}}K_{vf}^2 + \frac{S_{N_{ft}}K_{qv}^2 + S_{N_p}}{4\gamma^2|G(0)|^2 K_{yq}^2 K_{qv}^2}) \tag{4.7}$$

with

$$G(0) = \frac{1}{2m}\frac{\omega_x\omega_y/Q_y}{(\omega_x^2 - \omega_y^2)^2 + (\omega_x\omega_y/Q_y)^2}, \tag{4.8}$$

where S_{N_m}, S_{N_p}, $S_{N_{ft}}$, and $S_{N_{fb}}$ denote the PSD of N_m, N_p, N_{ft}, and N_{fb}, respectively. ω_x and ω_y are the resonant frequencies along the drive and sense modes. Parameters K_{vf}, K_{yq}, K_{qv}, and K_g are the conversion coefficients from voltage to force, displacement to charge, charge to voltage, and gain of the pick-off differential amplifier in the FRB closed-loop system, respectively. Predictions of ARWs at different Q-factors and resistances were calculated according to the parameters of DSG#1 and the corresponding front-end circuit,

Table 4.1: Parameters of DSG#1 prototype and conversion coefficients of FRB closed-loop system

Parameter	Value	Parameter	Value
Effective mass, m	1.08 $\times 10^{-6}$ kg	K_{vf}	9.6 $\times 10^{-8}$ N/V
Displacement, A_x	6 μm	K_{yq}	1.28$\times 10^{5}$ pC/m
Gap, g	12 μm	K_{qv}	0.65 V/pC
Angular gain, η	0.205	K_g	2$\times 10^{5}$ V/V

Table 3.1 and 4.1.

As shown in Fig. 4.7, the predicted ARW (black line) of the DSG#1 is initially limited by the electrical noise due to a large metal electrical resistance from an ultra-thin metal coating. The arrows in Fig. 4.7 indicate the directions of increase in metal coating thicknesses. The impact of metal electrical resistance on ARW limits was reduced after a certain resistance threshold was reached, which in our case was about 20 kΩ, as predicted by the analytical noise model. The conflicting effects of metallization on the Q-factor and electrical resistance on DSG's noise performance suggest that an optimal metal coating exists for a specific DSG design.

4.3 Noise Characterization

The contribution of metallization material and thickness on gyroscope noise performance in the FRB mode of operation was experimentally quantified using fabricated prototypes of DSG. For illustration purposes, two types of metal layers, Cr and Cr/Au, with thicknesses ranging from 7.5 to 50 nm were sputter-coated on the device shell of the DSG#1 in each experiment. After each metallization, the DSG was temporarily mounted on a Thru-Glass-Via (TGV) substrate of electrical interconnects with an aid of 12 μm spacer shims to control the electrode gap between the rim of the device shell and the electrode pad in all the experiments, as illustrated in Fig. 3.8(a). The assembled DSG was characterized in a vacuum chamber

with a pressure level of around 1 μTorr. An AC carrier signal with an amplitude of 0.5 V and frequency of 500 kHz was applied to the rim of the device shell through the conductive layer and the central stem. The as-fabricated frequency mismatch of 8.2 Hz was electrostatically compensated to a value on the order of 100 mHz for all runs using the tuning algorithm presented in [115]. The vibration amplitudes along the drive axis (higher resonant frequency mode) of the n = 2 mode were set to 50% of the capacitive gap and were stabilized by the AGC and PLL control loops to prevent variations in the amplitude and phase. Quadrature nulling and rate control loops were implemented on the DSG to suppress motion along the sense axis. In this configuration, the gyroscope output in the FRB mode of operation is insensitivity to variations in the frequency split, temperature, electrostatic nonlinearity, and amplitude-frequency coupling [86]. Thus, the impact of metal coating parameters on the Q-factor and electrical resistance were the only two remaining factors contributing to the DSG's noise mechanisms.

Utilizing the closed-loop FRB configuration, as an example, the DSG#1 was instrumented for angular rate measurements. The noise performances represented by ARWs as a function of metal electrical resistances are shown in Fig. 4.8, revealing impact of the metal coating material and its thickness on the DSG's noise performance. The experimentally measured ARWs of the Cr-coated and Cr/Au-coated DSG#1 (marked by circles and diamonds) decreased with increasing metal thicknesses, following the simulation predictions (orange dotted line) until a certain thickness was reached for each metal material, Fig. 4.8. The ARW limits were predicted using the analytical noise model presented in Section 4.2. A reduction in quality factor with increasing film thickness was observed impacting the ARWs, as expected, due to an increased mechanical thermal noise and electrical noise in the near-mode-matched condition.

As shown in Fig. 4.8, the Q-factors of the drive and sense modes were measured to be 372k and 455k, and ARW was measured to be 0.017 deg/rt-hr, when the optimized Cr/Au

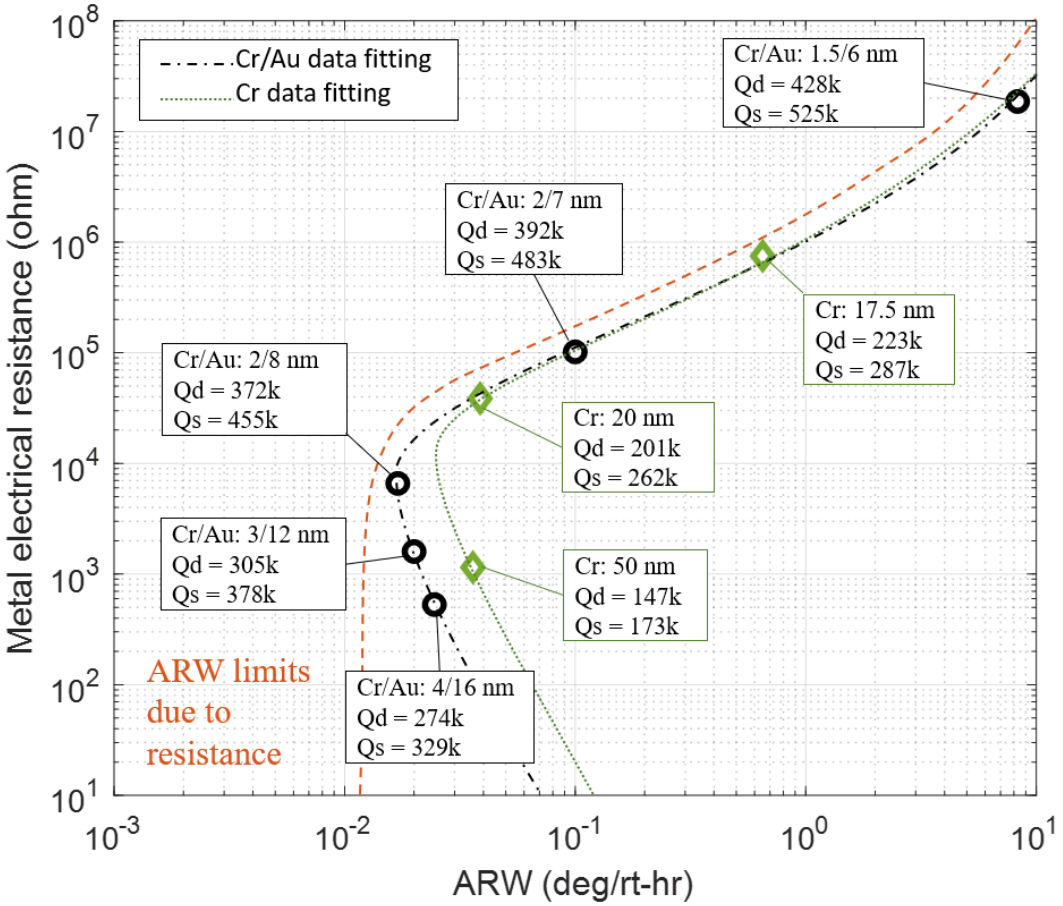

Figure 4.8: The experimentally measured ARWs (marked by circles and diamonds) of the DSG#1 at different thicknesses and materials of metal coating. The estimated ARW limits (orange dotted line) were predicted using the electromechanical model discussed in Section 4.2.

layer with the corresponding thicknesses of 2/8 nm was coated, showing approximately a two times improvement in both the Q-factor and noise performance, when compared to a 20 nm thickness of the Cr layer. In the latter case, the Q-factors of 201k and 262k and an ARW of 0.038 deg/rt-hr were measured. Based on our modeling and experimental results, we can conclude that variations of ARW using different metal coatings are due to changes in the quality factor and electrical resistance of the device shell. An increase in the electrical resistance adversely impacted the SNR, which degraded the DSG's noise performance due to the reduced informational signal. Therefore indeed, improvements in ARW could be achieved by selecting an optimized thickness and metal coating material.

4.4 Conclusion

A thin-film metal coating is needed on Fused Silica (FS) capacitive vibratory resonators to electrically bias the proof-mass for capacitive electrostatic actuation and detection. To demonstrate precision measurement of FS CVGs, a study on the effect of metallization on the quality factor and electrical resistance was presented and supported by experimental results in this chapter. We established a link to the in-run noise performance using the developed electromechanical model. The two types of metal coatings, Cr and Cr/Au, with different thicknesses were studied using in-house developed FS Dual-Shell Gyroscopes (DSGs), a miniaturized version of FS HRGs, for illustration purposes. The developed model aligns well with experimental observations. We observed a clear influence of varying coating materials and thicknesses on the quality factor and electrical resistance, demonstrating an existing trade-off between metallization and Q-factor to achieve the optimal gyroscope's noise performance. We showed that the Cr/Au metal coating is superior to the Cr layer in terms of a lower impact on the quality factor and electrical conductivity. The experimental results reported in this chapter confirmed the impact of metallization on the performance of FS CVGs. The derived conclusions can be applicable to a broad class of FS resonators and are not restricted to a specific design of the DSGs presented in this chapter.

Chapter 5

Effect of EAM on Capacitive MEMS Vibratory Gyroscopes

The Electromechanical Amplitude Modulation (EAM) is frequently used to eliminate feed-through signals between drive and sense in capacitive MEMS resonators, Coriolis Vibratory Gyroscopes (CVGs), and other vibratory sensors for improving signal-to-noise ratio and thus achieving a low noise characteristics. Toward realization of precision gyroscope measurements, there are some undesirable effects of EAM that need to be considered. This chapter investigates the effect of EAM on dissipation of energy and appeared non-linear dynamics in capacitive MEMS CVGs. In Section 5.1, the technology of capacitive detection of motion in MEMS vibratory gyroscopes is first discussed. In Section 5.2, we derive an analytical electro-mechanical model of the EAM scheme for a resonator with parallel-plate capacitive detection. Section 5.3 presents an analysis of factors influencing the electrical dissipation in EAM, including the voltage and frequency of the AC carrier signal and the feedback resistance in the pick-off circuit. The effect of EAM on electrical damping is then experimentally demonstrated on a Dynamically Amplified dual-mass Gyroscope (DAG) for illustration purposes. Utilizing the analytical equations derived from the electro-mechanical

model of Section 5.3, the non-linear electrostatic softening effect of EAM on the amplitude-frequency coupling is presented in Section 5.4. The scale factor nonlinearity, amplitude noise, and frequency noise due to the amplitude-frequency coupling in EAM detection are studied and verified experimentally on the DAG, in Section 5.5 and Section 5.6. The chapter concludes with discussion of the results in Section 5.7.

5.1 Introduction

Capacitive sensing is commonly used in MEMS CVGs for detection of vibratory motion based on measurement of the motion-induced current. Parallel-plates and comb-drives are the two most common configurations of capacitive electrodes. Parallel-plate capacitors, generally, provide higher sensitivity compared to comb-drive capacitors for the same footprint of the device [132]. Due to its advantage in sense density, parallel-plate electrodes have been widely adopted in MEMS resonator designs [70, 133]. However, unlike linear comb-drive capacitors, parallel-plate capacitive electrodes create non-linear capacitance with respect to displacement [134]. Although the non-linear signals limit the use of parallel-plate capacitive detection to operate above a critical amplitude of motion in the open-loop resonators, methods for a stable above-threshold operation were widely reported in recent years, such as their use in differential detection [135] and closed-loop operation [136].

When utilizing the parallel-plate detection of motion in capacitive MEMS CVGs, a predefined bias voltage is required to be applied to the proof-mass, which creates a potential difference on the variable sense capacitor between the movable proof-mass and anchored electrodes. Fig. 5.1 illustrates a typical schematics of the parallel-plate detection, along both the drive and sense modes, using the bias signal, v_b, to extract the motional amplitude of the proof-mass from the pick-off signals in MEMS gyroscopes. The actuation voltage, $v_{ac}(t) + v_{dc}$, is applied to the proof-mass along the drive direction. In such detection scenario, the gyroscope's

output signal due to the Coriolis force caused by the angular rate is detected by the parallel-plate electrodes along the sense direction, which is given by the total motion-induced current along the sense mode, as shown in Fig. 5.1,

$$i_c(t) = \frac{d}{dt}\left[v_b c_s(t) + (v_{ac}(t) + v_{dc}) c_{fxy}(t)\right], \tag{5.1}$$

where c_{fxx} and c_{fxy} are the parasitic feed-through capacitances from the forcer electrode along the drive mode to the pick-off electrodes along the drive and sense modes, respectively, usually induced by the capacitance coupling through the substrate, interconnects, and electrical package of the sensor.

The feed-through driving signal caused by the feed-through capacitance, c_{fxy}, mixes with the output Coriolis signal. The Coriolis force-induced signal is what measured by the gyroscope. An increase in the voltage amplitude of the bias signal in detection of the motional current can theoretically enhance the signal-to-noise ratio (SNR). However, an increase in the bias voltage may affect the quality factor (Q-factor) of MEMS resonators due to an additional non-linear electrostatic force acting on the proof-mass. This phenomenon is known as electrical dissipation [137]. Furthermore, the non-linear electrostatic force induced by the bias voltage in parallel-plate capacitive detection and actuation introduces a non-linear dynamics in CVG, which aggravates the amplitude-frequency coupling [138]. The amplitude-frequency coupling in the gyroscope due to nonlinearity is a dominant source of the frequency noise, degrading gyroscope's sensitivity and in-run noise performance [139].

Typically, a DC voltage is used as the bias electrical signal applied on the proof-mass of a resonator. The feed-through current mixing with the informational signal will disturb the resonance characteristics of the resonator and is difficult to eliminate from the sense signal when a DC bias signal is used. Methods for eliminating the feed-through current could be achieved on the design level, such as utilizing a twin resonator [140] or a complete symmetry

device [141], which is quite challenging, or on the circuit level, such as implementing external trimming capacitors [142] or a gain-tunable feed-through current amplifier [143], which greatly enhances complexity of the circuit and requirements for evaluation hardware and calibration procedures.

Electromechanical Amplitude Modulation (EAM) is a widely used technique in capacitive MEMS CVGs as a mitigation architecture for elimination of feed-through signals. The complexity of technique based on the amplitude modulation of the motional signal by an AC bias (carrier) voltage is simpler than the methods mentioned above for achieving a high level of feed-through rejection. The carrier frequency is often selected to be much higher than the operational frequency of the devices. Therefore, when the frequency demodulation technique is used, the carrier signal modulates the informational signal and shifts the frequency to higher frequencies for subsequent processing in the frequency domain. The technique allows for frequency domain separation between the informational signals and feed-through of the parasitic driving signals [144, 129], hence, reducing the contribution of the feed-through signals in the overall pick-off signal. EAM also avoids interference of the large amplitude and low frequency background noise and thus improves the SNR of the Coriolis signal in MEMS CVGs [112]. The motion-induced current in the EAM scheme is proportional to both the carrier voltage amplitude and frequency [145], which could further reduce the electrical noise and enhance the SNR in gyroscopes. However, it could be a challenge to achieve low power consumption interfaces with wide-bandwidth electronics due to the use of high-frequency carrier signal in the EAM detection.

Conventionally, nonlinearities in a mode-matched or near-mode-matched MEMS CVG are considered to be originating from the suspension geometry, configuration of capacitive electrodes, and non-linear forces in capacitive actuation. In the later case, the electrostatic frequency tuning is used to improve the sensitivity by reducing the frequency split between the drive and sense modes close to the order of the mechanical bandwidth of the gyroscope

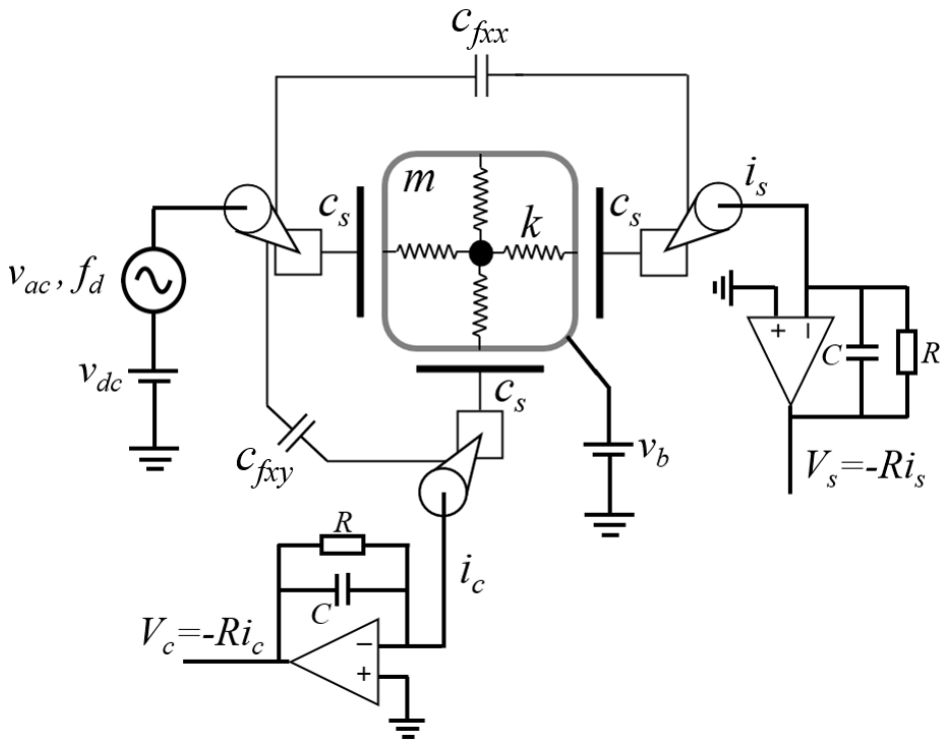

Figure 5.1: Schematics of the parallel-plate detection in a capacitive MEMS CVG.

[146, 147]. For example, the effect of bias voltage on sense electrodes should be also considered as an additional electrostatic force when studying nonlinearities in capacitive CVGs. A DC bias voltage generates the non-linear electrostatic forces affecting both the drive and sense modes. The impact of the DC bias signal on the effective quality factor due to the electrostatic forces has been previously demonstrated and reported in [38]. The induced non-linear electrostatic forces also affect the amplitude-frequency couplings, similar to the effect of electrostatic tuning voltages on non-linear dynamics of the device. Therefore, the previously derived analytical model of the electrostatic tuning voltage in [138] is applicable to study the effect of DC bias voltages.

When the EAM capacitive detection is used, similar to the DC bias signal, an AC carrier potential difference applied to the parallel-plate electrodes induces the non-linear electrostatic forces on a CVG. The AC signal affects the Q-factor through modifying the electrical damping, which was briefly reported in our previous study [148]. The previous study also noticed

variations in gyroscope's output noise due to the frequency and amplitude of the carrier voltage in EAM detection. Nevertheless, the impact and detailed mechanism of non-linear electrostatic forces caused by the EAM parameters on the amplitude-frequency couplings along both the drive and sense modes in CVGs were not covered in the previous study. Consideration of these mechanisms is important due to their effects on the scale factor stability and gyroscope's noise performance through modifying the electromechanical nonlinearity in the sensor. In order to estimate the correlation between the amplitude-frequency coupling due to the EAM parameters and the scale factor stability and gyroscope's in-run noise performance, a model capturing those effects of EAM on MEMS CVGs is developed in this chapter.

5.2 Electro-mechanical Model

Fig. 5.2 depicts an equivalent mass-spring-damper system with capacitive detection and EAM signal processing. This setup is commonly used to describe an ideal drive or sense mode of MEMS CVGs. In the EAM detection scheme, an AC carrier signal, $V_c = v_c cos(\omega_c t + \phi)$, is applied to the proof-mass, m. The equation of motion of a linear 1-DOF electro-mechanical model, in Fig. 5.2, can be presented as

$$m\ddot{x} + b\dot{x} + k_0 x = f_{tm} + f_{e1} + f_{e2}. \tag{5.2}$$

The electrical forces in this model, f_{e1} and f_{e2}, are induced by the corresponding voltages, V_1 and V_2, which are in turn generated by the motion-induced currents, i_1 and i_2. f_{tm} is the force representing the thermo-mechanical noise. The voltages V_1 and V_2, in Fig. 5.2, can be expressed as

$$\frac{V_1}{R_e} + c_{p1}\frac{dV_1}{dt} + \frac{d}{dt}(c_1(x)(V_1 - V_c)) = 0, \tag{5.3}$$

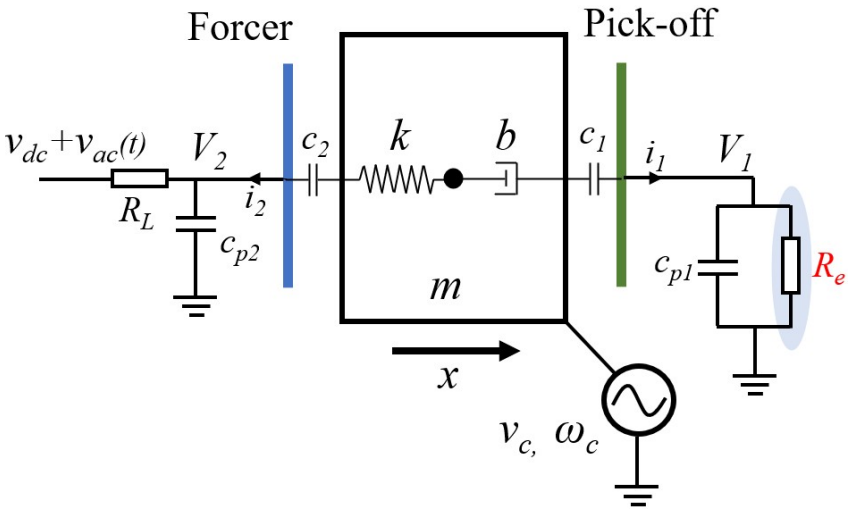

Figure 5.2: Schematics of a parallel-plate capacitive MEMS resonator with actuation on the left side and EAM detection of motion on the right side.

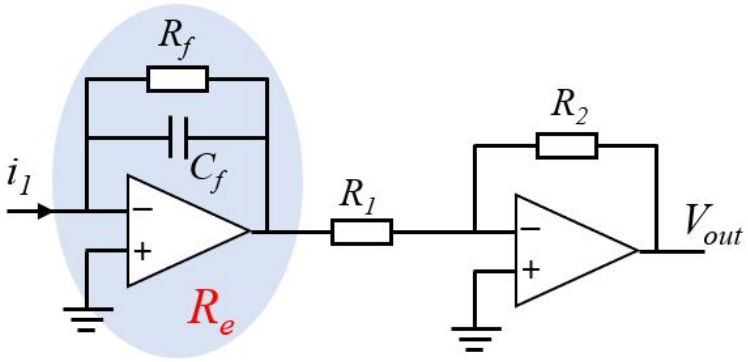

Figure 5.3: Schematics of a two-stage transimpedance amplifier which is often used to measure the motional current. The resistor R_e is an effective equivalent resistance load attached to the sense electrode due to the first stage amplifier.

$$\frac{V_2 - v_{dc}}{R_L} + c_{p2}\frac{dV_2}{dt} + \frac{d}{dt}(c_2(x)(V_2 - V_c)) = 0, \tag{5.4}$$

where c_{p1} and c_{p2} are the parasitic capacitances between the forcer and pick-off electrodes, respectively, and a substrate on which the device is fabricated. Parameters c_1 and c_2 denote the position-dependent forcer and pick-off capacitances given by

$$c_1(x) = \frac{\epsilon A}{g - x}, \quad c_2(x) = \frac{\epsilon A}{g + x}, \tag{5.5}$$

where ϵ is the complex permittivity of air, A is the area of capacitors, and g is the nominal electrode gap between the parallel-plate electrodes of the capacitor. The nominal device capacitance can be expressed as

$$c_n = c_1(x)|_{x=0} = c_2(x)|_{x=0} = \frac{\epsilon A}{g}. \tag{5.6}$$

The actuation voltage, $v_{dc} + v_{ac}(t)$, is applied to the mass via a resistance load, R_L. The resistor R_e denotes the effective equivalent resistance load attached to the sense electrode due to the pick-off circuit. The two-stage sensing circuit diagram is shown in Fig. 5.3, which consists of a low-noise transimpedance amplifier (TIA) with a feedback resistor, R_f, for collecting the motional current from the pick-off electrode. Therefore, the equivalent resistance load R_e is defined as

$$R_e = \frac{1}{\frac{A_{OL}(f)+1}{Z_f} + \frac{1}{Z_{in}}}, \tag{5.7}$$

where $A_{OL}(f)$, Z_f, and Z_{in} are the open-loop gain, feedback impedance, and input impedance of the TIA, respectively. If the resonator is assumed to be a pure oscillator with displacement

$x(t) = x \cdot sin(\omega_d t)$, then solutions of (5.3) and (5.4) are given by, [148],

$$V_1(t) = c_1(t)v_c\{\omega_c[\beta_{\omega_c,1}cos(\omega_c t+\phi) - \alpha_{\omega_c,1}sin(\omega_c t+\phi)] + \frac{x}{2g}\omega_d[\alpha_{\omega_+,1}cos(\omega_+ t+\phi) + \beta_{\omega_+,1}sin(\omega_+ t+\phi) + \alpha_{\omega_-,1}sin(\omega_- t+\phi) + \beta_{\omega_-,1}cos(\omega_- t+\phi)]\}, \quad (5.8)$$

$$V_2(t) = c_2(t)v_c\{\omega_c[\beta_{\omega_c,2}cos(\omega_c t+\phi) - \alpha_{\omega_c,2}sin(\omega_c t+\phi)] - \frac{x}{2g}\omega_d[\alpha_{\omega_+,2}cos(\omega_+ t+\phi) + \beta_{\omega_+,2}sin(\omega_+ t+\phi) + \alpha_{\omega_-,2}sin(\omega_- t+\phi) + \beta_{\omega_-,2}cos(\omega_- t+\phi)]\} + v_{dc} \quad (5.9)$$

with

$$\alpha_{\omega_i,1} = \frac{R_e}{1+R_e^2 c_{t1}^2\omega_i^2}, \quad \alpha_{\omega_i,2} = \frac{R_L}{1+R_L^2 c_{t2}^2\omega_i^2}, \quad (5.10)$$

$$\beta_{\omega_i,1} = \frac{R_e^2 c_{t1}\omega_i}{1+R_e^2 c_{t1}^2\omega_i^2}, \quad \beta_{\omega_i,2} = \frac{R_L^2 c_{t2}\omega_i}{1+R_L^2 c_{t2}^2\omega_i^2}, \quad (5.11)$$

where $c_{t1} = c_{p1} + c_1$ and $c_{t2} = c_{p1} + c_2$. The coefficient ω_i, where "i" can be "c", "+", or "−", denotes the frequencies of ω_c, $\omega_c + \omega_d$, and $\omega_c - \omega_d$, respectively. The derived voltages result in forces applied to the mechanical system via the coupling capacitances. The corresponding forces can be expressed as

$$f_{e1} + f_{e2} = \frac{c_n}{2g}\left[\frac{(V_c - V_1)^2}{(1-x_n)^2} - \frac{(V_c - V_2)^2}{(1+x_n)^2}\right], \quad (5.12)$$

where $x_n = x/g$ is the normalized displacement.

Expanding (5.12) would yield a constant DC force, f_{e0}, and a set of harmonic terms of the applied force that depend on position and velocity. Then, substituting the corresponding equations for forces in (5.2) yields the equation of motion,

$$m\ddot{x} + (b+b_1)\dot{x} + kx - \sum_{n=1}^{\infty} k_{en}x^n = f_{tm} + f_{e0}, \quad (5.13)$$

with the linear and non-linear electrostatic negative stiffness, k_{en}, caused by the harmonics forces, which can be expressed in the form

$$k_{en} = \frac{(n+1)c_n}{g^{n+1}}(v_{dc}^2 + v_c^2) + \frac{(n+2)!c_n^2}{2n!g^{n+1}}(\beta_{\omega_c,1} + \beta_{\omega_c,2})\omega_c v_c^2. \tag{5.14}$$

Here, b_1 is the electrical damping, which is given by

$$b_1 = \frac{1}{2}\Lambda_1 v_c(\alpha_{\omega_+,1} + \alpha_{\omega_-,1}) + \frac{1}{2}\Lambda_2 v_c(\alpha_{\omega_+,2} + \alpha_{\omega_-,2}) \tag{5.15}$$

with

$$\Lambda_1 = \frac{1}{2}\frac{c_n^2}{g^2}v_c, \quad \Lambda_2 = \frac{1}{2}\frac{c_n^2}{g^2}(v_c + v_{dc}). \tag{5.16}$$

The parameters $\alpha_{\omega_+,1}$, $\alpha_{\omega_-,1}$, $\alpha_{\omega_+,2}$, and $\alpha_{\omega_-,2}$ are the coefficients in the solutions that are expressed by (10). The first term ($n = 1$) describes how the electrostatic tuning phenomenon affects characteristics of the resonance frequency. The remained non-linear terms ($n >1$) result in nonlinearity in dynamics of the resonator.

5.3 Electrical Dissipation

The quality factor (Q-factor) is a parameter in MEMS CVGs that is used in optimization of the sensor design. For example, by increasing the quality factor, we can reduce bias instability and Angle Random Walk (ARW) of the gyroscope [68]. Electrical dissipation can be one of the contributing energy dissipation mechanisms affecting the Q-factor in MEMS vibratory devices along with viscous air damping, thermo-elastic damping (TED), anchor loss, and surface loss.

Methods for manipulating electrical dissipation were widely explored in recent years, [149], as a Q-factor tuning method in MEMS resonators. Variations in the amplifier feedback

resistance, DC voltage of bias signal, and parasitic capacitance showed to influence the electrical damping in [38] on a doubly clamped micromechanical beam resonator. Application of DC voltages to CVG systems for reduction of the angle drift caused by the Q-factor mismatch has been already demonstrated in the whole angle gyroscope mode of operation [150].

The quality factor is defined as a ratio of the energy stored, E_S, over the energy dissipated, E_D, per vibration cycle of a resonator, $Q = 2\pi E_S/E_D$. The total dissipated energy per cycle can be expressed as $E_D = \int_0^{\frac{2\pi}{\omega}} (b+b_1)\dot{x}xdt = \pi(b+b_1)\omega x^2$, and defined by energy dissipation sources, including electrical damping, viscous damping, TED, anchor loss, and surface loss. Electrical dissipation b_1 is a function of the voltage and frequency of the carrier signal in the EAM detection and the load resistance, as determined by the model in (5.15). The model suggests that modification of those variables would influence the electrical damping and thus tune the effective Q-factor of a MEMS resonator.

To demonstrate the effect of different factors on the Q-factor in capacitive MEMS CVGs, a Dynamically Amplified dual-mass Gyroscope (DAG), with parameters as defined in [148], was used as a test vehicle, Fig. 5.4. The DAG is a 4-DOF dual-mass spring structure configured to achieve the mechanical amplitude amplification properties, [72, 73, 69, 122], and consists of an inner drive mass, m_1, attached to the central anchor and connected to an outer sense mass, m_2, by concentric ring suspensions, k_1 and k_2. Fig. 5.5 shows an equivalent electro-mechanical system of a DAG illustrating the configuration of the forcer, pick-off, and tuning electrodes. V_{t1} and V_{t2} are the DC tuning voltages representing the electrostatic compensation method used in the operation of the DAG [111].

The device under test is designed to have the first, in-phase translational mode, Fig. 5.6, and the resonance frequency at 4.89 kHz. The DAG was vacuum packaged, using the approach described in [27]. We experimentally measured the quality factors at 180k and 220k along the drive (X) and sense (Y) axes. The structural parameters of the operational mode of

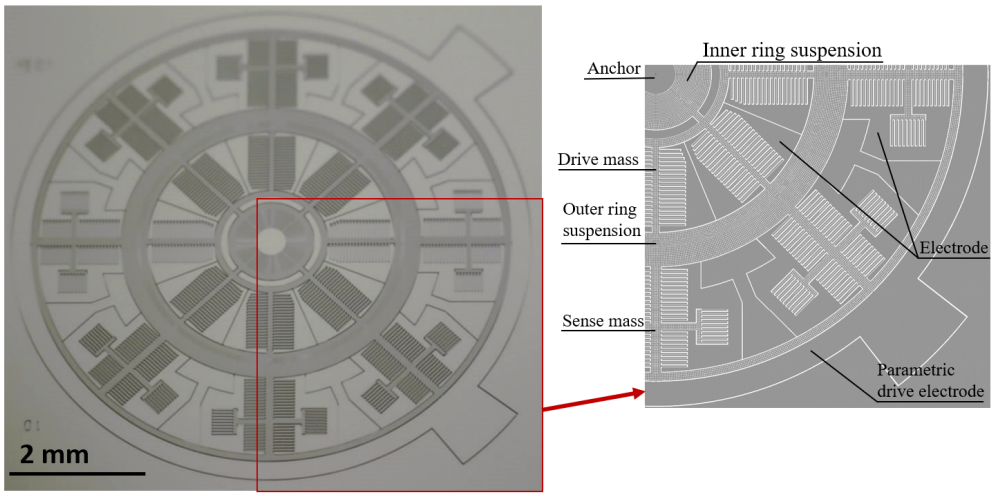

Figure 5.4: An image of Dynamically Amplified dual-mass Gyroscope (DAG) and a close-up view of a quarter of the DAG showing the central anchor, dual-mass architecture, concentric ring suspensions, as well as inner, outer, and parametric electrodes, [72, 73, 69].

the DAG were experimentally identified using the frequency responses and damping factors (Q-factors), [151, 123], and are summarized in Table 5.1. The overall designed capacitances of each inner and outer electrodes and parasitic capacitance are 1.2, 1.64, and 3.3 pF, respectively. The packaged sensor was mounted on a front-end circuit board and tested in a temperature chamber to provide a stable temperature during experiments ($< 0.5°$C fluctuation). The DAG was operated at the resonance frequency controlled by the Phase-Locked Loop (PLL). The drive amplitude during the experiments was set to 1% of the electrode gap for reducing the effect of the anchor loss on the Q-factor measurements [152]. The Q-factor was measured using the ring-down method described in [153].

Fig. 5.7(a) shows the measured quality factors as a function of the feedback resistance, R_{fy}, which was varied from $100k$ to $2M$ in feedback of the transimpedance amplifier along the Y-axis pick-off channel. For all feedback resistor values, a constant carrier signal with the amplitude of 1 V and frequency of 50 kHz was applied to the proof-mass. We observed that increasing the feedback resistances from $100k$ to $2M$ significantly reduced the Q-factor along the Y-axis of the DAG. The experimentally measured values are in agreement with values predicted by the electrical dissipation model in (5.15) based on the device parameters

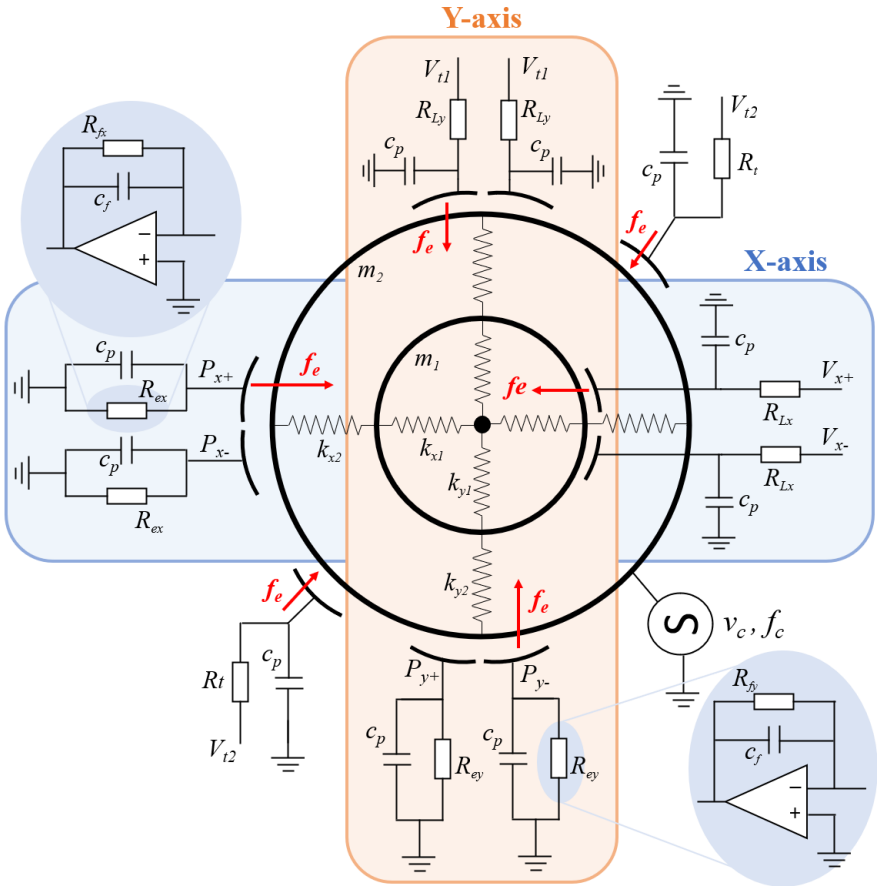

Figure 5.5: The electro-mechanical schematics of DAG. An AC carrier signal with voltage, v_c, and frequency, f_c, is applied to the gyroscope's proof-mass. Two TIAs with feedback resistances, R_{fx} and R_{fy}, are used to collect the motional currents from the pick-off electrodes, P_{x+}, P_{x-}, P_{y+}, and P_{y-}. Parameters R_{ex} and R_{ey} denote the effective equivalent loads caused by the feedback resistances and TIAs. R_t, R_{Lx}, and R_{Ly} are the loading resistances on the corresponding tuning and forcer electrodes.

presented in Table 5.1, where b is equal to $2m\mu_y$.

Fig. 5.7(b) shows the analytical predictions and experimental results on the impact of amplitude and frequency of the carrier signal in EAM on the quality factor. For illustration purposes, a 100 k feedback resistor was used in the TIAs and the response was measured along the Y-axis. From this measurement, we observed a clear influence of the varying carrier amplitudes and frequencies on the Q-factor. The Q-factor was decreasing as a function of the carrier voltage. This behavior is due to increase in electrical damping with increase of the carrier voltage. At the same time, the Q-factor was increasing with increase of the carrier

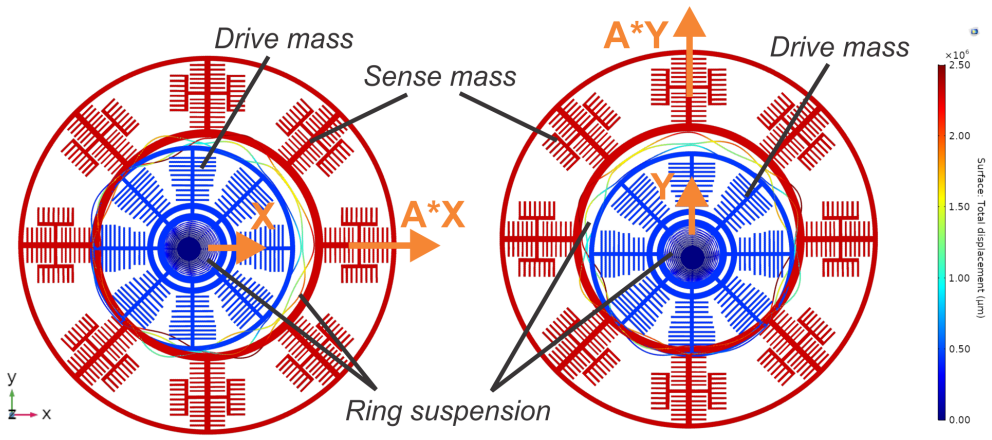

Figure 5.6: FEA model of DAG showing a characteristic motion of inner drive mass and in-phase dynamically amplified motion of outer sense mass along the (a) drive and (b) sense directions with the amplification factor A.

frequency. The observed behavior showed a good agreement with the derived analytical model, discussed in Section 5.2.

We conclude that the quality factor modification arising from the electrical dissipation is strongly dependent on the feedback resistance and the carrier signal in the EAM detection scheme. It raises an important consideration in selection of these parameters in capacitive MEMS CVGs and oscillators.

5.4 Nonlinear Dynamics due to EAM

Variations of the resonant frequency due to electro-mechanical nonlinearities are usually considered as a negative characteristic of MEMS vibratory devices. The non-linear dynamics of a MEMS CVG is mainly caused by the structural suspension nonlinearity and electrostatic stiffness nonlinearity [138]. As a result of non-linear dynamics, the resonant frequency is coupled to the vibration amplitude, known as the amplitude-frequency coupling.

The electrostatic stiffness nonlinearity is used for electrostatic tuning of resonant structures

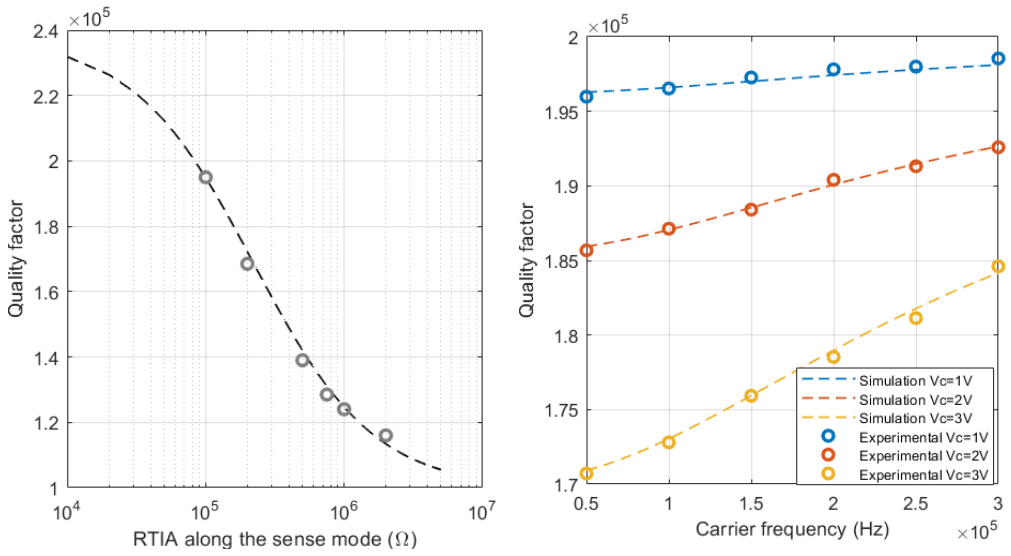

Figure 5.7: (a) Simulation results of the effective Q-factors under different feedback resistances, ranging from 100 k to 2 M, calculated by the electrical dissipation model (black dashed line) and the experimentally measured Q-factors along the Y-axis (circular data points). (b) The simulated Q-factors as a function of the carrier frequency for different peak-to-peak amplitudes of carrier voltages, from 1 to 3 V. The experimental results at different carrier voltages showed a good agreement with simulated trends in the Q-factor as a function of the carrier frequency, confirming the derived analytical model in Section 5.2. The maximum error between the experimental and simulation results for all the data sets is less than 5% of the actual value.

by applying DC tuning voltages across the parallel-plate actuation electrodes and is widely used in resonators and in mode-matched MEMS CVGs. To realize a mode-matched (or degenerate mode) CVG, a higher operational resonant frequency (X-axis, in our case) is matched to the lower resonant frequency (Y-axis) of the same mode by applying the electrostatic tuning voltage along the X-axis, which would subsequently reduce the frequency split between the drive and sense modes and thus improve the angular rate sensitivity. However, the tuning voltage would also result in electrostatic nonlinearity that impacts dynamics along the X-axis, which cannot be ignored. The bias voltage applied to the proof-mass of a capacitive MEMS CVG would lead to a similar effect of electrostatic stiffness nonlinearity, in both the drive and sense modes. In this section, we will discuss the amplitude-frequency coupling in the parallel-plate EAM detection.

For a planar mode-matched MEMS CVG, with a suspension which is usually composed of thin beams and arcs, the flexural displacement is much smaller compared to the geometrical size of the gyroscope's suspension. Conventionally, up to the 5th order components of mechanical non-linear stiffnesses are considered in such systems [146]. Utilizing the X-axis with a higher resonant frequency as the drive mode and the Y-axis as the sense mode, the main nonlinearities in CVGs arise from electrostatic forces due to tuning and bias voltages. The non-linear electrostatic forces can be expanded in a Taylor series and only the odd-order of non-linear stiffnesses remained in the expansion when utilizing a push-pull configuration of the parallel-plate electrodes [138]. Keeping up to the 5th odd-order nonlinearity in the system and ignoring anisoelasticity and anisodamping to simplify the discussion, the non-linear equations of motion along the X- and Y-axis of the gyroscope can be described as

$$\ddot{x} + 2\mu_x\dot{x} + \omega_{nx}^2 x + \eta_3 x^3 + \eta_5 x^5 = f_{ex}, \tag{5.17}$$

$$\ddot{y} + 2\mu_y\dot{y} + \omega_{ny}^2 y + \kappa_3 y^3 + \kappa_5 y^5 = f_{ey}, \tag{5.18}$$

where μ_x, μ_y, ω_{nx}, and ω_{ny} denote the damping coefficients and resonant frequencies along the drive and sense modes, respectively. The odd-order of non-linear stiffnesses, the geometric Duffing nonlinearity (3rd order) terms, η_3 and κ_3, and quintic nonlinearity (5th order) terms, η_5 and κ_5, along the drive and sense modes are included in (5.17) and (5.18).

Based on the analytical equation, (5.12), in the parallel-plate EAM detection with a push-pull configuration, the electrostatic forces per resonator mass along the X- and Y-axis, f_{ex} and f_{ey}, can be expressed as

$$f_{ex} = \frac{c_x}{2mg}\left[\frac{(V_1(c_x, x) - V_c)^2}{(1 - x_n)^2} - \frac{(V_2(c_x, x) - V_c)^2}{(1 + x_n)^2}\right], \tag{5.19}$$

$$f_{ey} = \frac{c_y}{2mg}\left[\frac{(V_1(c_y, y) - V_c)^2}{(1 - y_n)^2} - \frac{(V_2(c_y, y) - V_c)^2}{(1 + y_n)^2}\right], \tag{5.20}$$

where m, c_x and c_y, x_n and y_n are the resonator mass, nominal capacitances, and normalized

displacements along the X- and Y-axis, respectively. Parameters V_1 and V_2 are the equivalent voltages applied to the push-pull electrodes along the X- and Y-axis, which were derived in (5.8) and (5.9). The actuation voltage, $v_{dc}+v_{ac}$, is included in the voltage $V_2(c_x, x)$. The v_{dc} along the X-axis also serves as an electrostatic tuning voltage. V_c is the AC carrier voltage in the EAM scheme with the amplitude v_c and frequency f_c.

Utilizing the derived equations in the electro-mechanical model in Section 5.2, the nonlinear electrostatic stiffnesses capturing the frequency variations and up to the 5th odd-order nonlinearity terms can be expanded and then substituted in (5.17) and (5.18) as

$$\ddot{x} + 2\mu_x\dot{x} + \omega_{0x}^2 x + \eta_3' x^3 + \eta_5' x^5 = f_x, \tag{5.21}$$

$$\ddot{y} + 2\mu_y\dot{y} + \omega_{0y}^2 y + \kappa_3' y^3 + \kappa_5' y^5 = 0, \tag{5.22}$$

with

$$\begin{aligned}
&\omega_{0x}^2 = \omega_{nx}^2 - \frac{k_{e1}}{m}, \quad \omega_{0y}^2 = \omega_{ny}^2 - \frac{k_{e1}|_{v_{dc}=0}}{m}, \\
&\eta_3' = \eta_3 - \frac{k_{e3}}{m}, \qquad \eta_5' = \eta_5 - \frac{k_{e5}}{m}, \\
&\kappa_3' = \kappa_3 - \frac{k_{e3}|_{v_{dc}=0}}{m}, \quad \kappa_5' = \kappa_5 - \frac{k_{e5}|_{v_{dc}=0}}{m}.
\end{aligned}$$

Due to relatively slow-varying amplitude and phase during the ring down response [146], the amplitude of vibrations and amplitude-frequency couplings along the X- and Y-axis are given by, [154],

$$a_x(t) = a_{0x}e^{-\mu_x t},\ a_y(t) = a_{0y}e^{-\mu_y t}, \tag{5.23}$$

$$\omega_x(t) = \omega_{0x} + \sum_{n=3}^{2k+1} \frac{n(n-1)\eta_n'}{2^{n+1}\omega_{0x}} a_x^{n-1}(t), \tag{5.24}$$

$$\omega_y(t) = \omega_{0y} + \sum_{n=3}^{2k+1} \frac{n(n-1)\kappa_n'}{2^{n+1}\omega_{0y}} a_y^{n-1}(t), \tag{5.25}$$

where a_{0x} and a_{0y} are the original vibration amplitudes during the ring down response. η'_n and κ'_n denote the non-linear electro-mechanical stiffness terms in the drive and sense modes. The amplitude-frequency relationships derived in (5.24) and (5.25) are represented as a function of the DC tuning voltage as well as the amplitude and frequency of the AC carrier signal in EAM.

To study the amplitude-frequency coupling due to the EAM parameters in MEMS CVGs, nonlinearity in the Dynamically Amplified dual-mass Gyroscope (DAG) was experimentally characterized. In the electrode configuration of the DAG, illustrated in Fig. 5.4, the drive and sense modes are all excited using the inner differential electrodes while the electrostatic tuning voltages are applied to two separated outer electrodes relative to ground. The electrode configuration is presented in Fig. 5.8 and the electrostatic compensation method of DAGs was presented in our previous publications, [111]. The 4-DOF dual-mass system of the DAG in EAM detection could be restructured to a reduced-order model. An equivalent 2-DOF electro-mechanical system, utilizing the approximation method presented in our recent work, [74], captured an accurate dynamics of the DAG at the operational mode. Therefore, the derived electrostatic non-linear stiffnesses in (5.14), (5.24), and (5.25) are applicable to our 4-DOF system. The experimentally derived parameters of the equivalent DAG model and electrical component values of the front-end circuit are summarized in Table 5.1.

Variations in resonant frequencies in the ring-down measurements as functions of the normalized amplitude of vibrations along the drive (X) and sense (Y) modes in the DAG were measured using a PLL control loop, shown in Fig. 5.9. The experimental results of the

Table 5.1: Experimentally Extracted parameters for the equivalent model of DAG and the component values of front-end circuit

ω_{0x} (rad/s)	ω_{0y} (rad/s)	μ_{0x} $(1/s)$	μ_{0y} $(1/s)$
$3.0964e^4$	$3.0758e^4$	0.103	0.085
$Mass$ (kg)	c_n (pF)	c_p (pF)	R_L (k)
$1.17e^{-6}$	1.64	3.3	100

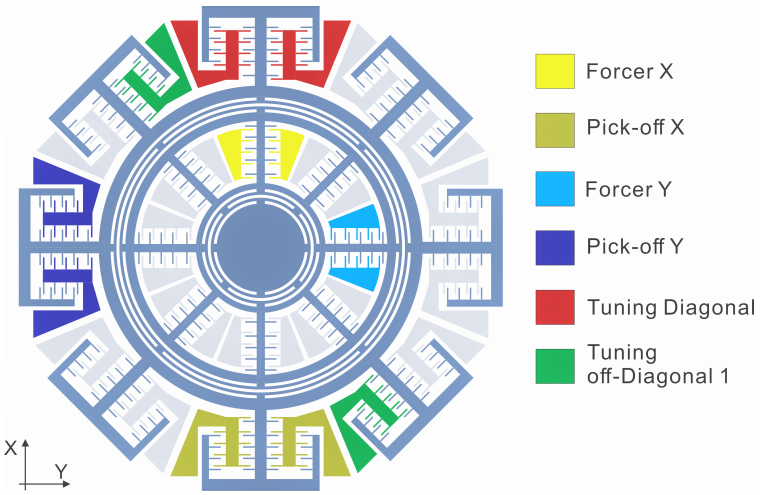

Figure 5.8: Configuration of forcer, pick-off, and tuning electrodes in the Dynamically Amplified dual-mass Gyroscope (DAG).

amplitude-frequency couplings along the X- and Y-axis are demonstrated at different carrier voltages and frequencies. The extracted parameters of the 3rd order non-linear stiffnesses from measurements are shown in Fig. 5.10(a) and (b), and simulation results in Fig. 5.10 are derived using the analytical models presented by (5.24) and (5.25) with the experimentally obtained parameters. Fig. 5.10(c) illustrates the simulated frequency responses of the DAG along the X-axis at different EAM parameters, which showed a good agreement with the experimental measurements. Fig. 5.9 and Fig. 5.10 demonstrate the aggravated amplitude-frequency couplings along both the drive and sense modes in the DAG due to increase in electrostatic nonlinearity caused by both the carrier voltages and frequencies in EAM detection.

5.5 Scale Factor Nonlinearity due to EAM

The non-linear dynamics due to electro-mechanical non-linear stiffnesses in MEMS CVGs would generally degrade sensors' performance. For example, in the open-loop rate mode of operation of MEMS CVGs, the X-axis with a higher resonant frequency can be used as

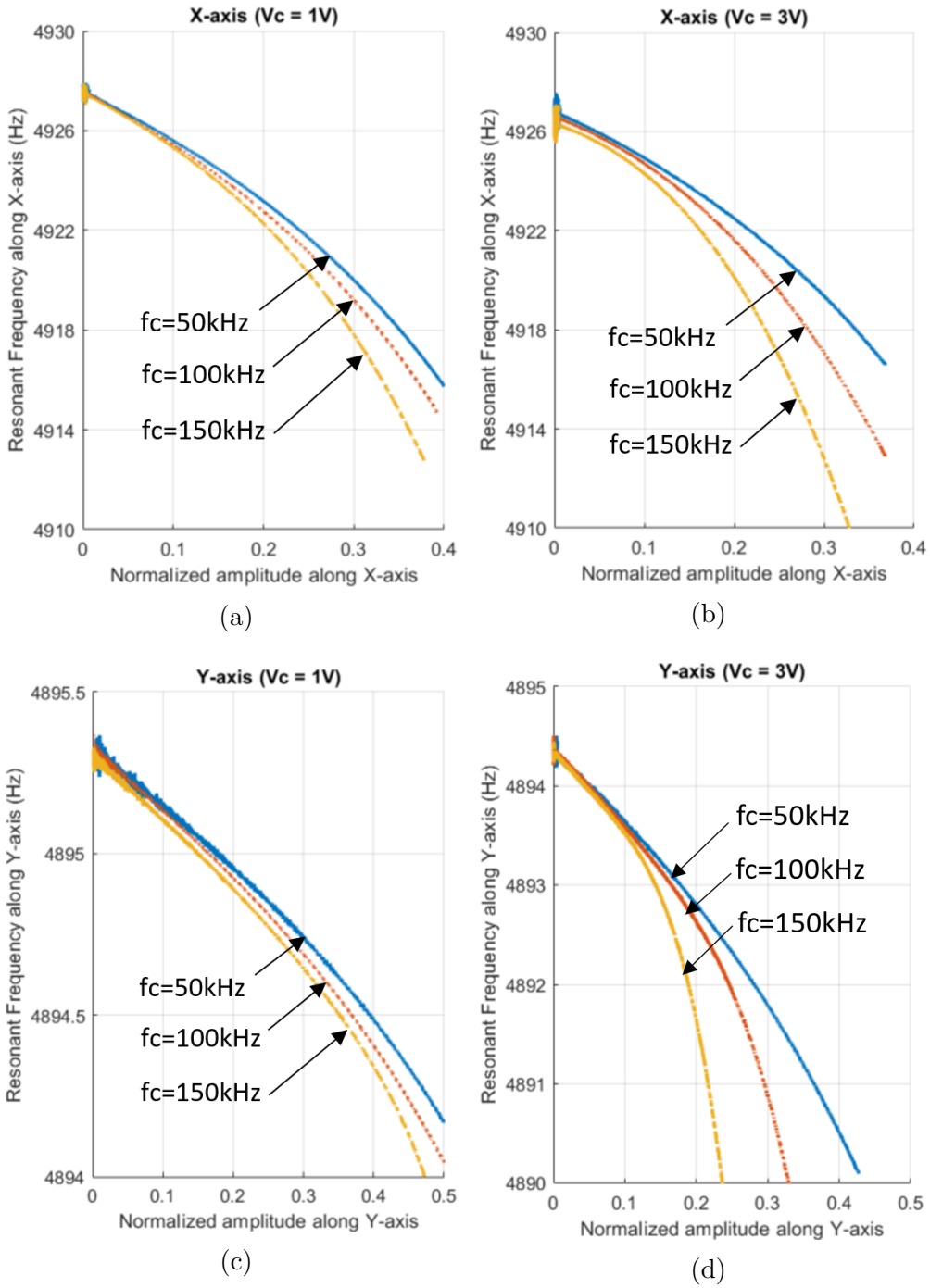

Figure 5.9: The ring-down responses along the drive axis, (a) and (b), and the sense axis, (c) and (d), at different carrier voltages, 1 or 3 Vpp, and frequencies, from 50 to 150 kHz.

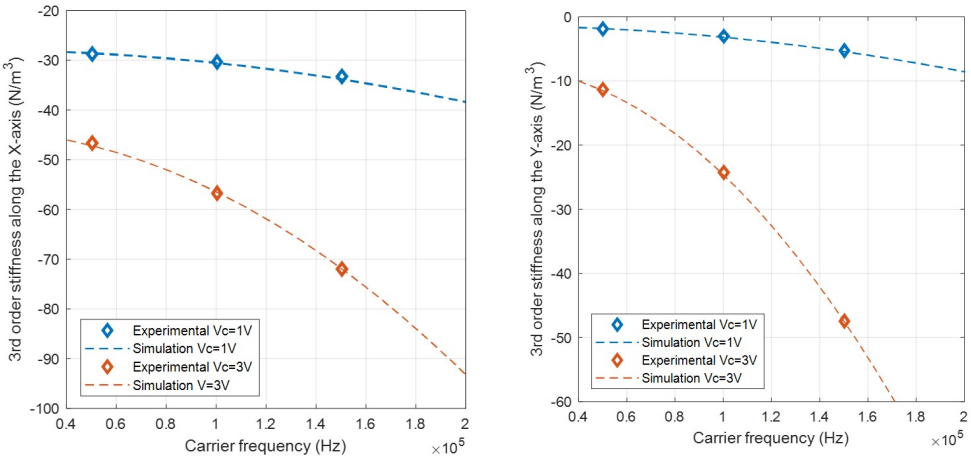

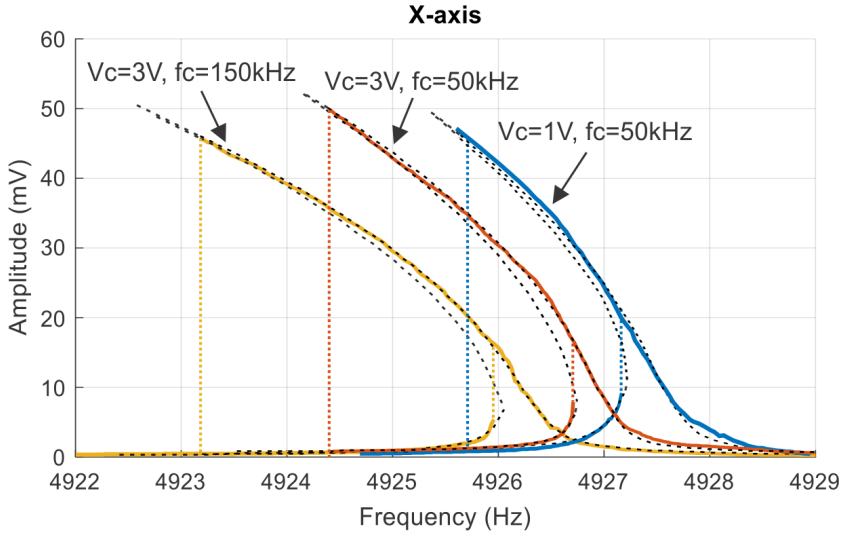

Figure 5.10: The 3rd order stiffnesses of the DAG along (a) the drive and (b) the sense modes extracted from experimental data and superimposed with simulations using the analytical model at different carrier voltages and frequencies. The maximum difference between the measured and predicted 3rd order stiffnesses for all the data sets is less than 7% of the actual value. (c) The experimentally measured and simulated frequency responses along the drive mode at different carrier voltages, 1 or 3 Vpp, and frequencies, 50 or 150 kHz.

either the drive mode or sense mode. By utilizing the X-axis as the sense mode, which is required to be electrostatically tuned to reduce the resonant frequency, that is to match the resonant frequency, along the Y-axis in a near-mode-matched (low frequency split) or mode-matched gyroscope, the non-linear dynamics due to the electrostatic tuning will cause a large amplitude-frequency coupling along the sense axis, which results in mode-matching

limitation, gyroscope scale-factor nonlinearity, and instability in the sense mode resonant frequency [86]. On the contrary, utilizing the X-axis as the drive mode of the gyroscope, even though the configuration avoids a large nonlinearity in the sense mode due to the eliminated need for electrostatic tuning, the contribution of EAM to the electrostatic nonlinear stiffensses still remains in the gyroscope's sense mode, which would subsequently result in nonlinearity of the gyroscope's scale factor and affect the in-run noise performance.

The scale factor nonlinearity in the open-loop rate mode of operation is mainly caused by nonlinear dynamics in gyroscope's sense mode, including nonlinearity of suspension geometry, parallel-plate capacitance, electrostatic stiffnesses due to the tuning voltage [147] and the EAM carrier signal, derived in Section 5.4, as well as the phenomena of the mode coupling between the drive and sense modes.

In order to identify the effect of the EAM parameters on the scale factor nonlinearity, it is necessary to study and quantify each nonlinearity mechanism separately by first isolating the contribution of EAM from the rest of the contributing factors.

The geometric nonlinearity of both the drive and sense modes in MEMS CVGs could be identified using the ring-down responses, derived in Section 5.4. Linearization of the nonlinear pick-off signal due to parallel-plate detection can be achieved utilizing the Side Band Ratio (SBR) method demonstrated in [129].

Utilizing the X-axis (a higher frequency mode, in our case) as the drive axis of MEMS CVGs in the open-loop rate mode of operation, the X-axis is electrostatically tuned and locked by PLL and AGC controllers to prevent variations in the amplitude and phase. Therefore, the nonlinearity due to the electrostatic tuning will only affect the dynamics along the drive mode. In this configuration of mode-matched or near-mode-matched CVGs, the effects of EAM parameters and the mode coupling will be the only two remaining factors contributing to the scale factor nonlinearity.

The scale factor in mode-matched gyroscopes is strongly dependent on the frequency split and quadrature coupling between the drive and sense modes. Due to the amplitude-frequency coupling along the sense axis, the resonant frequency of the sense mode would reduce with increase in the sense amplitude, which is caused by the large input angular rate, and thus the scale factor of the sensor would behave non-linearly. The analytical equations describing the impact of mode coupling on scale factor nonlinearity in the open-loop rate mode of operation were presented in [138]. Quadrature coupling due to fabrication imperfection in MEMS CVGs as an error can be decoupled from the angular rate signal using a phase delay in the demodulation process.

Using the non-linear electrostatic stiffness models presented in Section 5.2 and Section 5.4, the effect of EAM on non-linear dynamics of the scale factor can be estimated through the steady-state response of the equations of motion, (B.13) and (5.22), and the vibration amplitude along the sense direction due to the input rotation can be calculated as

$$Y = \frac{2X_a\omega_{0x}\Omega}{\sqrt{({\omega'_y}^2 - \omega_{0x}^2)^2 + (2\mu_y\omega_{0x})^2}} \tag{5.26}$$

with

$$\omega'_y = \omega_{0y} + \sum_{n=3}^{2k+1} \frac{n(n-1)\kappa'_n}{2^{n+1}\omega_{0y}} Y^{n-1},$$

where X_a is the vibration amplitude along the X-axis (drive axis) and Ω is the measured angular velocity. Parameter ω'_y is the resonance frequency along the Y-axis described by the amplitude-frequency coupling in (5.25).

The contribution of EAM parameters on the scale factor nonlinearity in the open-loop rate mode of operation was experimentally quantified using the DAG architecture. In our experiments, a higher resonant frequency mode (X-axis) was stabilized with a constant vibration amplitude at 20% of the capacitance gap. The electrostatic tuning voltages were applied along the X-axis to achieve the frequency split (Δf) on the order of 1 Hz for improving

gyroscope sensitivity and reaching a near-mode-matched condition of all the experiments. The scale factor nonlinearity due to the mode coupling at $\Delta f = 1Hz$ was simulated and illustrated by the solid black line in Fig. 5.11.

Fig. 5.11 presented the normalized scale factors extracted along the Y-axis, which was measured using the SBR method with the rotation rate of up to 270 deg per second. The data were obtained for different EAM parameters used for signal processing. Our results showed a good agreement between the experimental results and the analytical results predicted by the model in (5.26). The experiments demonstrated a clear influence of the selected carrier voltages and frequencies on the scale factor nonlinearity. We believe the mechanism is through modification of the amplitude-frequency coupling along the sense axis, suggesting that the EAM parameters play an important role in determining the scale factor while operating a MEMS CVG in the open-loop rate mode mechanization under the mode-matching or near-mode-matched conditions.

5.6 Noise Characterization in EAM Detection

In capacitive MEMS CVGs, a bias voltage is applied on the proof-mass to extract its motional amplitude and both DC and AC bias voltages generate the electrostatic non-linear stiffnesses along the drive and sense modes. In the EAM detection scheme, the pick-off signal along the sense axis (or Y-axis) of an open-loop rate mode CVG can be simplified as, [129],

$$V_{ele} \approx \frac{1}{2} R \frac{c_{ny}}{g} v_c \omega_c (y + \epsilon_y) + V_N, \tag{5.27}$$

where V_{ele}, R, c_{ny}, y, and V_N are the pick-off signal, feedback resistance, nominal capacitance of pick-off electrodes, amplitude along the sense axis, and equivalent electrical noise, respectively. Parameters v_c and ω_c are the amplitude and frequency of the carrier signal

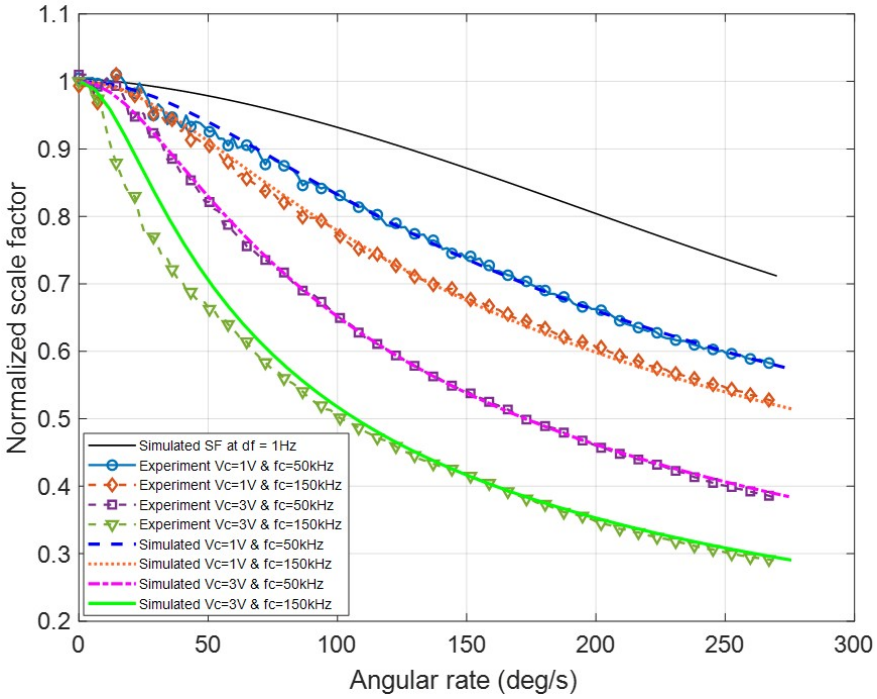

Figure 5.11: The experimentally measured and simulated scale factor nonlinearity of the DAG at different carrier voltages and frequencies of EAM. The simulated scale factors at 1 Hz frequency split in the open-loop rate mode of operation were modeled using the method presented in [138]. The maximum error between the measured and simulated gyroscope angular rates up to 270 deg per second for all the data sets is less than 8%.

in the EAM detection scheme. The pick-off signal is proportional to the EAM parameters, which affects the SNR between the Coriolis signal and electrical noise. EAM detection also holds the benefit of reducing the contribution of feed-through noise by shifting the informational signal to higher frequencies, which allows a further improvement of SNR of the Coriolis signal and reduction of flicker noise (or 1/f noise) in CVGs. At the same time, the carrier voltage, and the frequency of EAM specifically, impacts the electrical noise from the TIA of the front-end circuit [155]. Therefore, it is necessary to study the effect of the EAM parameters on noise performance and determine the optimized EAM configuration to achieve the desired noise performance of a gyroscope.

In order to derive the correlation between the EAM parameters and noise performance in a gyroscope, an accurate model predicting the contribution of non-linear dynamics to the

gyroscope's noise contributions is necessary. A gyroscope noise model was derived in our previous publications, [148], which captured the most dominant sources of noise in capacitive MEMS CVGs in EAM detection, including the mechanical–thermal noise (MTN), flicker noise (FN), electronic-thermal noise (ETN), and operational amplifier noise (OAN). Next, an additional source of noise in capacitive MEMS CVGs, frequency noise, will be discussed.

The frequency noise due to the amplitude-frequency coupling along the drive mode is considered as a dominant noise in MEMS CVGs. The frequency noise coupled with the quadrature-induced noise along the sense mode would degrade the gyroscope's noise performance. The amplitude-frequency coupling along the drive mode is mainly caused by electro-mechanical nonlinearities due to electrostatic tuning voltage and bias voltage, especially, while using a higher resonant frequency mode as the drive axis in mode-matched CVGs. The effect of both the carrier voltage amplitude and frequency in the EAM detection on the amplitude-frequency coupling along the drive mode was presented in Section 5.4, (5.24). Due to the coupling, the frequency noise can be quantified using the vibration amplitude noise along the drive mode.

The resonant frequency along the drive mode due to the electrostatic non-linear stiffnesses can be calculated by solving the non-linear equation of motion, (5.17),

$$\omega_x = \sqrt{\omega_{x0}^2 - \frac{k_{ex}}{g}} \approx \omega_{x0} - \frac{k_{ex}}{2g\omega_{x0}}, \tag{5.28}$$

where k_{ex} is electrostatic stiffness along the drive mode acquired by the electrostatic force per mass, f_{ex}, (5.19), which can be rewritten in the form of $f_{ex}(t) = k_{ex}x_a(t)$. Utilizing the Euler's formula and Newton's binomial theorem, the electrostatic stiffness due to the tuning voltage, v_{dc}, and EAM parameters is derived as

$$k_{ex} = \frac{c_{nx}}{mg}(v_{dc}^2 + \frac{1}{2}v_c^2)\sum_{n=1}^{2k+1}\frac{(n+1)!}{2^{n-1}(\frac{n-1}{2})!(\frac{n+1}{2})!}x_a^{n-1} + \frac{c_{nx}^2}{mg}v_c^2\omega_c^2\beta\sum_{n=1}^{2k+1}\frac{(n+2)!}{2^n(\frac{n-1}{2})!(\frac{n+1}{2})!}x_a^{n-1}, \tag{5.29}$$

with

$$\beta = \frac{R^2 c_{tx}}{1 + R^2 c_{tx}^2 \omega_c^2} + \frac{R_L^2 c_{tx}}{1 + R_L^2 c_{tx}^2 \omega_c^2}, \quad c_{tx} = c_{nx} + c_p,$$

where c_{nx}, c_p, R_L denote the nominal capacitance along the drive mode, parasitic capacitance associated with the capacitance between the electrode and substrate, and loading resistance, respectively.

The drive axis amplitude is stabilized by PLL/AGC control loops in the open-loop rate mode of operation, therefore, the vibration amplitude, x_a, can be presented in the form of $x_a = \bar{x}_a + \epsilon_x$, where $\bar{x}_a$ is the steady-state response and ϵ_x is the amplitude noise. Then, substituting (5.29) into (5.28), the correlation between the amplitude noise and frequency noise, ϵ_{ω_x}, due to the amplitude-frequency coupling in EAM detection is estimated as

$$\frac{\epsilon_{\omega_x}}{\epsilon_x} = -\frac{c_{nx}(v_{dc}^2 + \frac{1}{2}v_c^2)}{2mg^2\omega_{x0}} \sum_{n=3}^{2k+1} \frac{(n-1)(n+1)!}{2^{n-1}(\frac{n-1}{2})!(\frac{n+1}{2})!} \bar{x}_a^{n-2} - \frac{c_{nx}^2 v_c^2 \omega_c^2}{2mg^2\omega_{x0}} \beta \sum_{n=3}^{2k+1} \frac{(n-1)(n+2)!}{2^n(\frac{n-1}{2})!(\frac{n+1}{2})!} \bar{x}_a^{n-2}. \tag{5.30}$$

It should be noted that the frequency noise is proportional to the amplitude noise along the drive axis due to the amplitude-frequency coupling, which is impacted by the EAM parameters based on the derived equation, (5.24). An increase in the voltage and frequency of the carrier signal would result in a large amplitude-frequency coupling and an increased frequency noise along the drive mode based on (5.30), which is later discussed to lead to increase in quadrature-induced noise along the sense mode and consequently would affect the gyroscope's noise performance. The correlation between the quadrature-induced noise and frequency noise was discussed in [19].

To demonstrate the contribution of EAM parameters on the gyroscope's noise performance, the DAG was experimentally characterized and the gyroscope's equivalent noise represented by the Angle Random Walk (ARW) is illustrated in Fig. 5.12. The gyroscope was operated in the open-loop rate mode and the drive amplitude was locked at 20% of the capacitance

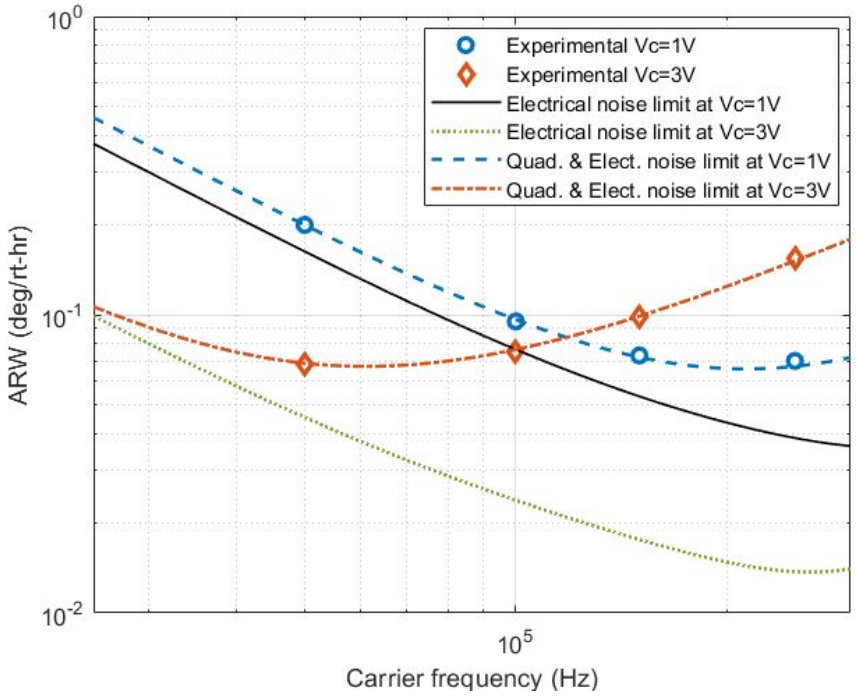

Figure 5.12: The experimentally measured ARWs (marked by circles and diamonds) of the DAG at different carrier voltages and frequencies. The estimated ARWs were predicted using the noise model discussed in Section 5.6. The maximum error of 5% between the measured and predicted ARWs of the DAG is presented. The model included the MTN, FN, ETN, OAN, and quadrature-induced noise.

gap by using the PLL/AGC control loops for all the experiments. The electrostatic tuning voltages were applied along the higher resonant frequency mode to achieve the frequency split on the order of 1 Hz. The experimentally measured and estimated ARWs of the DAG were performed as a function of the carrier frequency from 50 to 300 kHz at different carrier voltages.

Without considering the frequency noise due to non-linear dynamics, the predicted ARWs of the DAG using the noise model in the two cases, $v_c = 1$ and 3 Vpp, were limited by the electrical noise, shown in Fig. 5.12, black solid and green dotted lines. In both cases, the predicted ARWs limits are reduced as a function of the carrier frequency due to increase in the SNR. However, the experimentally measured ARWs (marked by circles and diamonds) followed the trends in Fig. 5.12, which were predicted using the noise model, including the

quadrature-induced noise derived in (5.30). It was demonstrated that the noise performance of the DAG was mainly limited by the quadrature-induced noise generated by the amplitude-frequency coupling along the drive mode in a near-mode-matched condition. Due to the constant contribution of the quadrature-induced noise caused by the geometric nonlinearity at a certain drive amplitude (20% of electrode gap in both cases), we can conclude that the variation of ARWs at different carrier voltages and frequencies is due to changes in the quadrature-induced noise caused by the electrostatic nonlinearity. Increase in the EAM parameters impacted the electrostatic nonlinearity and aggravated the amplitude-frequency coupling, which resulted in degrading the DAG's noise performance due to the large frequency noise. Considering the improvements in the SNR caused by the EAM parameters, the experiments also suggested how improvements in ARW could be achieved by incorporating the optimized EAM configuration in the sensor's detection architecture.

It should be understood that a standard configuration of the EAM scheme may be underutilized the benefits of SNR and sensitivity improvements of the EAM detection; for example, the carrier frequency is usually about five to ten times more than the resonance frequency of a sensor with a carrier voltage on the level of 0.5 to 1 V. In our case of the DAG characterization, the carrier voltage with the amplitude of 1 V and frequency of 50 kHz used as the nominal parameters of the EAM detection resulted in a sensitivity of 1.83 mV/deg/s and ARW of 0.2 deg/rt-hr, which is about three times worse than the sensitivity of 5.64 mV/deg/s and ARW of 0.07 deg/rt-hr using the optimized EAM configuration, 1 V and 150 kHz, in Fig. 5.12. On the contrary, misusing the benefits of the EAM scheme for improvement of SNR and sensitivity by using a large carrier voltage and frequency may lead to an aggravated amplitude-frequency coupling and result in degrading scale factor stability and noise performance of a gyroscope. In our experiments, using a 3 V amplitude of the carrier signal with a frequency of more than 100 kHz could be considered as the abused EAM configuration with a significantly degraded ARW and non-linear scale factor of the DAG, presented in Fig. 5.11 and Fig. 5.12.

5.7 Conclusion

The Electromechanical Amplitude Modulation (EAM) is an important and commonly used approach for elimination of feed-through signals between forcer and pick-off electrodes in capacitive MEMS resonators, CVGs, and other vibratory sensors. However, there are some undesirable effects of EAM impacting structural symmetry and energy dissipation in MEMS resonator's performance that need to be considered. In this chapter, we presented a comprehensive work, supported by analytical and experimental analysis, on the effect of the carrier voltage and frequency in EAM detection scheme on electrical dissipation, scale factor instability, and in-run noise performance of a CVG with parallel-plate capacitors used for detection of motion. We predicted analytically and observed experimentally, that the AC bias signal in the parallel-plate electrodes would induce a set of non-linear harmonic forces applied to the gyroscope as a result of the front-end circuit. We confirmed that these forces generate the electrical damping, therefore, affecting the quality factor of the sensor. An analytical model was derived for studying the effect. The carrier voltage amplitude and frequency, as well as the feedback resistance of the transimpedance amplifier, were experimentally demonstrated to introduce the electrical damping in the electro-mechanical model and thus modify the quality factor of the CVG. In this chapter, we used the Dynamically Amplified dual-mass Gyroscope (DAG) for illustration purposes, however, the phenomenon is expected to present in other designs of vibratory gyroscopes.

We confirmed that non-linear electrostatic forces also impact the electrostatic negative stiffnesses, which results in the aggravated amplitude-frequency couplings along both the drive and sense modes in the CVGs. Changes in the 3rd and 5th order of the non-linear electrostatic stiffnesses were captured by our analytical equations and the effect of these higher-order terms where in-line with experimental observations. The experimental results and the analytical models showed how the EAM parameters influence the scale factor nonlinearity of the system.

When the EAM scheme of feed-through reduction was used, we also found a correlation between the quadrature noise and frequency noise due to the amplitude-frequency coupling along the drive mode. The correlation was theoretically predicted and experimentally verified using the DAG as a demonstration vehicle. Even though we recognized that an increase in the carrier voltage and frequency of EAM would amplify the output pick-off signals to improve the SNR and to reduce the impact of the external electrical noise, our experimental data and the simulation results suggested that the large amplitude-frequency coupling along the drive mode of the DAG due to the increased carrier voltage and frequency would lead to a larger frequency noise and quadrature noise. Thus, bluntly increasing the carrier voltage and frequency of EAM to separate the operational signal from the feed-through noise and electrical noise is not justifiable and would effectively limit the gyroscope's noise performance in the open-loop rate mode of operation. Therefore, our conclusion is that it is always necessary to carefully determine the optimized parameters in the EAM detection scheme to achieve a desired noise performance of the sensor. The optimization is device-specific. We derived the effect of EAM parameters on noise performance for the DAG architecture with parameters discussed in this chapter. Following the same approach, an optimization in selection of EAM parameters can be achieved for other designs of MEMS CVGs.

Chapter 6

Conclusions

This dissertation presents our research efforts on development and realization of MEMS Coriolis Vibratory Gyroscopes for environmentally robust and precision measurement of absolute rotations. Toward this goal, two different paradigms were investigated in this thesis. A shock survival mechanism was designed for high-performance low-frequency MEMS CVGs to improve environmental survivability by immobilizing the proof-mass of the device during the event of shock and vibration. The mechanism was enabled by the developed fabrication process. Parallel development of a solution utilizing the inherent structural robustness of Fused Silica Dual-shell Gyroscope (DSG) for continuous gyroscope operation in adverse environments was also studied. To achieve precision gyroscope operations, efforts to address the challenges associated with imperfection-induced errors as well as the realization of mode-matched gyroscope operation were presented in this thesis. Factors, including metallization and Electromechanical Amplitude Modulation, that impact the structural symmetry and energy dissipation mechanisms in MEMS resonators were also analyzed and implemented to improve gyroscope performance in realization of both paradigms. Specific contributions of this work are summarized below.

6.1 Contributions of the Dissertation

- A shock survival mechanism, Trap-and-Hold (TAH) concept, was developed to increase the environmental immunity of the gyroscope to mechanical shocks and vibrations. The proposed method utilizes out-of-plane electrodes to electrostatically trap and keep the gyroscope's proof-mass locked to the substrate during the events of shocks to prevent mechanical fracture of the structure while recovering its noise characteristics and high sensitivity operation upon releasing the proof-mass after the shock. To demonstrate the TAH concept, a design of MEMS Dynamically Amplified dual-mass Gyroscope (DAG) as the test vehicle was implemented. The design optimization and mode-ordering with respect to geometric parameters were studied using finite element analysis, and a design of the dual-mass gyroscope was developed to achieve high quality factors and low noise through design optimization. The high sensitivity angular rate measurement with low noise characteristics was demonstrated on the DAGs, revealing ARW of 0.007 deg/rt-hr and in-run bias instability of 0.08 deg/hr. Two fabrication processes using the through-wafer-interconnect techniques to form the TAH out-of-plane electrodes were developed to realize the TAH add-on mechanism, supported by the experimental demonstrations. Fundamental characteristics of the device were validated before and after shocks.

- Toward realization of precision operation-through-shock, the developments of Fused Silica (FS) Dual-Shell Gyroscopes (DSGs) were presented. Fabrication processes were developed that realized the capacitive detection and actuation of a FS DSG through integrating with a Thru-Glass-Vias (TGVs) planar electrode substrate. To achieve the mode-matched gyroscope operation for high angular rate measurements, we developed an electromechanical model for electrostatic compensation of the structural asymmetry. The asymmetry is caused by non-uniform temperature during glassblowing, misaligned lapping of DSGs, and assembly errors caused by the misalignment of the integration

step. We proposed an identification method of the assembly errors based on static capacitance measurements. Compensation algorithms for both asynchronous and synchronous tuning of the n = 2 and n = 3 mode pairs were then theoretically derived and experimentally demonstrated on a DSG prototype. As a result, a near-mode-matched gyroscope operation was demonstrated using the proposed tuning method, revealing ARW on the order of 0.017 deg/rt-hr and in-run bias instability of 0.2 deg/hr.

- A study on the effect of metallization on the quality factor and electrical resistance of FS micro-machined resonators was presented and supported by experimental results. An analytical model was developed to simulate the impact and link it to the in-run noise performance. The developed model aligns well with experimental observations. The two types of metal coatings, Cr and Cr/Au, with different thicknesses were studied. We observed a clear influence of varying coating materials and thicknesses on the quality factor and electrical resistance, demonstrating an existing trade-off between metallization and Q-factor to achieve the optimal gyroscope's noise performance. Two FS DSGs with different geometries were used to demonstrate the impact of metallization on gyroscope performance, allowing to generalize our conclusions. We concluded that it is always necessary to carefully determine the optimized parameters in metallization to achieve an optimal noise performance of FS sensors.

- Developments of evaluation electronics and analysis of non-linear dynamics of MEMS capacitive CVGs were studied to further improve gyroscope performance. An analytical model based on the Electromechanical Amplitude Modulation (EAM) technique was investigated, capturing the effect of bias signal on electrical dissipation, amplitude-frequency coupling, scale factor instability, and in-run noise performance of gyroscopes, followed by the experimental demonstrations. This study concludes the necessity to optimize EAM parameters of MEMS CVGs to achieve optimal gyroscope noise characteristics.

6.2 Future Research Directions

6.2.1 On-chip Ovenization of 3D Encapsulated MEMS Sensors for Temperature Compensation and Vacuum Packaging

In Chapter 2, the process of Through-Glass-Vias (TGVs) utilizing glass re-flow technique for encapsulating planar MEMS resonators was proposed and explored on MEMS dynamically amplified dual-mass gyroscopes. The additional feature was introduced to improve structural robustness against mechanical shock and vibrations. Both the in-plane and out-of-plane electrodes were implemented on the cap stage using TGVs. However, temperature compensation has not been explored. The developed glass re-flow technique is not only capable of forming a cap stage for vacuum packaging and in-plane and out-of-plane sensor operations, but it is also possible to create micro-heaters and thermal sensors for on-chip ovenization and temperature stabilization to reduce the temperature-induced long-term bias and scale-factor drifts.

Besides, improvement of vacuum encapsulation might be demonstrated by modifying the cap wafer fabrication process and wafer-level bonding process. For example, to increase the tolerance of misalignment between the cap and device wafers, especially for tilt misalignment, a low temperature and low-pressure bonding method using Au-to-Au eutectic bonding might be used [27]. The low temperature and pressure could eliminate the undesired diffusion between the bonding Au and Si devices and electrodes and reduce the stress-induced errors in MEMS resonators. To implement the bonding method, a modified fabrication process with micro-heaters and thermal sensors, as an example, is illustrated in Fig. 6.1. The isolation trenches should be created in the SOI device wafer, from Step (i) to (iV), for preventing the overflow of Au/Sn eutectic alloy during the bonding process as illustrated in Step (2). This modified process might simplify the demands of the fabrication process and could potentially

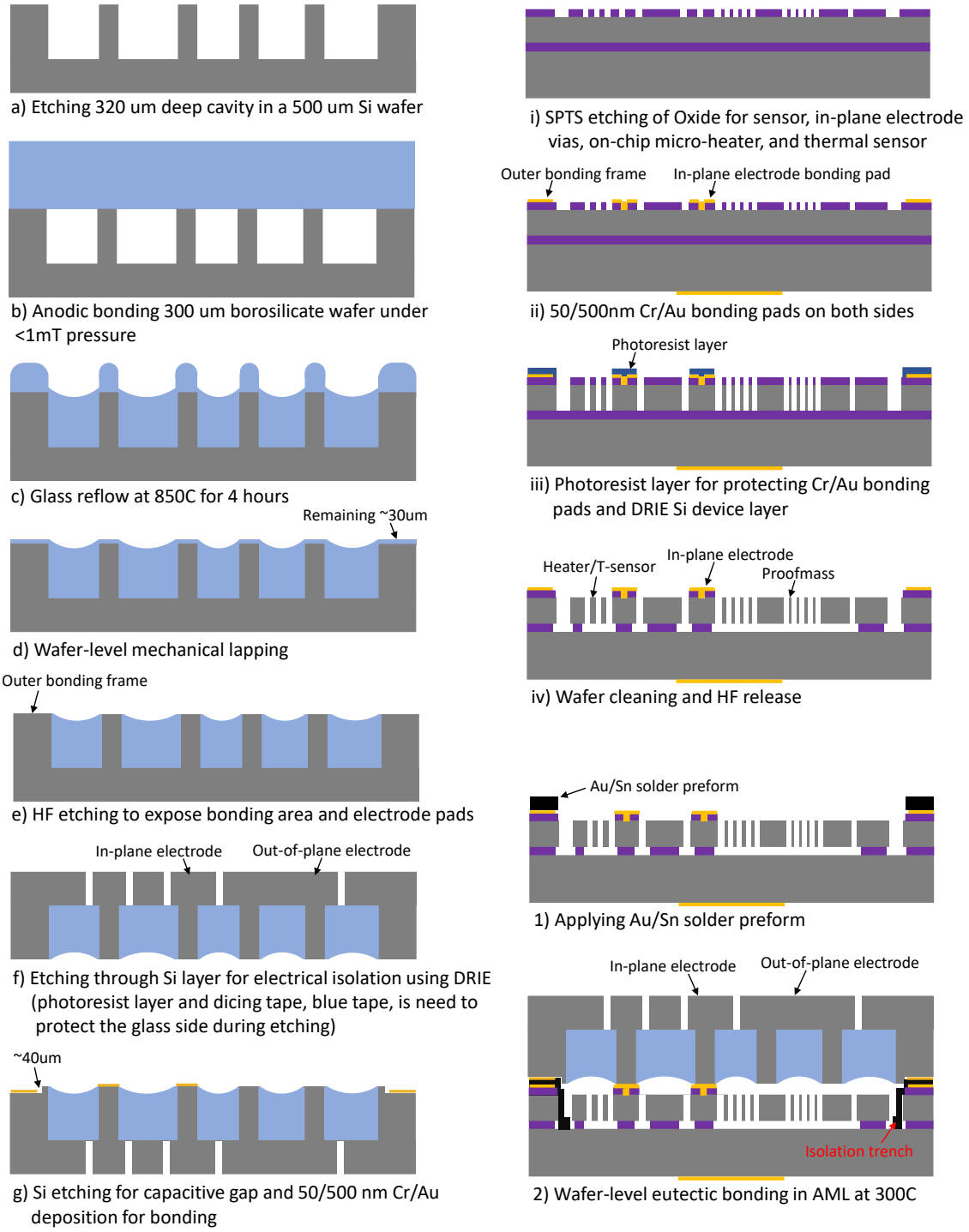

Figure 6.1: Wafer-level fabrication and encapsulation process of planar MEMS SOI devices with on-chip micro-heater and temperature sensor (T-sensor).

improve the yield of vacuum packaging.

6.2.2 Laser Trimming Compensation of Structural Asymmetry

Electrostatic compensation of frequency mismatch due to fabrication imperfection is an active compensation technique widely used in mode-matching gyroscope operation. In Chapter 3, such a technique was successfully employed for tuning a Fused Silica (FS) dual-shell gyroscope (DSG) and taking into account the assembly errors. However, electrostatic tuning of DSG often requires high amplitudes of the tuning voltage due to large capacitive gaps, which results in a degraded noise performance and scale factor nonlinearity caused by non-linear electrostatic forces introduced by the high tuning voltages. In addition, the miniaturized sensors might not have enough tuning capability to provide the demanded amplitude of tuning voltages to compensate for large frequency splits electrostatically. Therefore, the mechanical trimming modification of DSGs might be preferable to reduce large as-fabricated frequency splits, followed by a relatively low tuning voltage for high accuracy electrostatic tuning. Methods of mechanical trimming techniques, such as laser ablation, chemical etching, directional lapping, and selective deposition, have demonstrated the reduction of the frequency split in many different implementations of micro-machined HRGs. However, the disturbance of the surface roughness and shell structure caused by those trimming methods might affect the quality factor of the devices.

Femtosecond laser-induced Chemical etching (FLICE) of Fused Silica materials is a promising technique for mechanical trimming of structural asymmetry of micro-shell resonators. The low thermal-induced disruption and high selectivity etching of FLICE make it an attractive solution for frequency compensation of FS HRGs, which has not yet been demonstrated.

6.2.3 FLICE Release of Micro-Shell Resonators

In addition to FLICE laser trimming of structural asymmetry of FS HRGs, the laser-associated micro-shell release might also be performed by using the FLICE process. The

FLICE laser-writing and chemical etching with an ultra-high laser-induced etching selectivity on the order of 855:1 and a high aspect ratio on the order of 55:1 are ideal for micro-HRGs release to eliminate micro-cracks and control capacitive gaps compared with mechanical lapping and chemical–mechanical polishing [96], especially for thermo-elastic "blowing" micro-HRGs, demonstrated in [51, 91]. Using the FLICE release method, the fabrication process might be simplified due to eliminating the integration step between the sensor and electrode substrate. Two process flows, for illustration purposes, are designed for both micro-glassblowen hemispherical shell resonators and dual-shell resonators based on the FLICE release method, and shown in Fig. 6.2 and Fig. 6.3. By using the processes, the electrostatic sensor operation might be achieved by the co-fabricated electrodes with a capacitive gap as small as a single beam-width of the femtosecond laser.

6.2.4 Cylindrical Shell Vibration Gyroscope

The FLICE-associated process might enable the 3D fabrication of FS Cylindrical shell Vibration Gyroscopes on the micro-scale with a diameter on the order of a few millimeters. A dual cylindrical shell structure might be also created using the FLICE process. The proposed implementation is similar to the FS dual-shell gyroscope. The outer cap cylindrical shell might contain the in-plane electrode pads with the capability to in-situ vacuum packaging of the inner sensing element. An example of the fabrication process is illustrated in Fig. 6.4. The co-fabricated electrodes on the cap cylindrical shell might achieve the uniform capacitive gaps. The process is also compatible with the high vacuum encapsulation using the passive getter pumping technique.

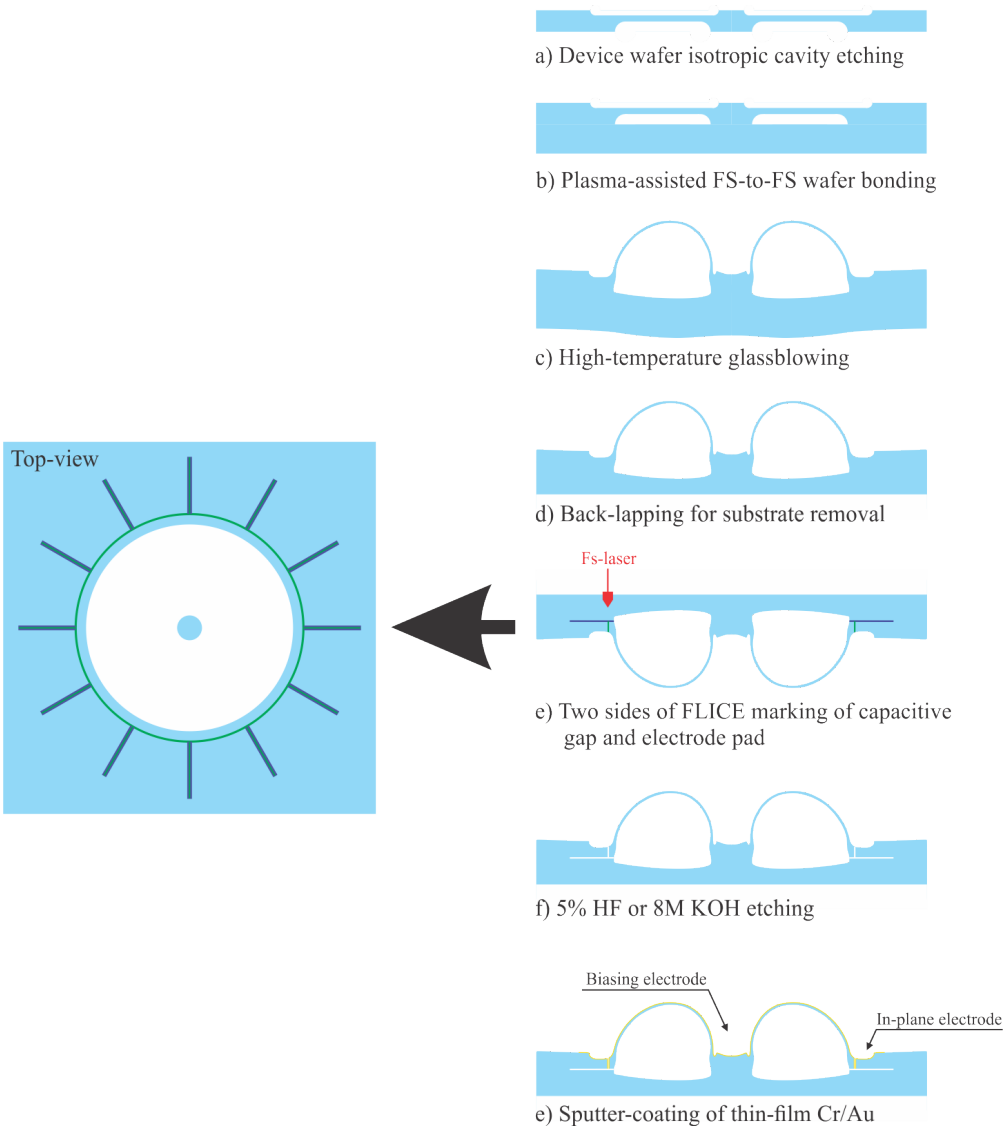

Figure 6.2: Process flow for FS thermo-elastic "blowing" micro-HRG using a developed laser-associated release.

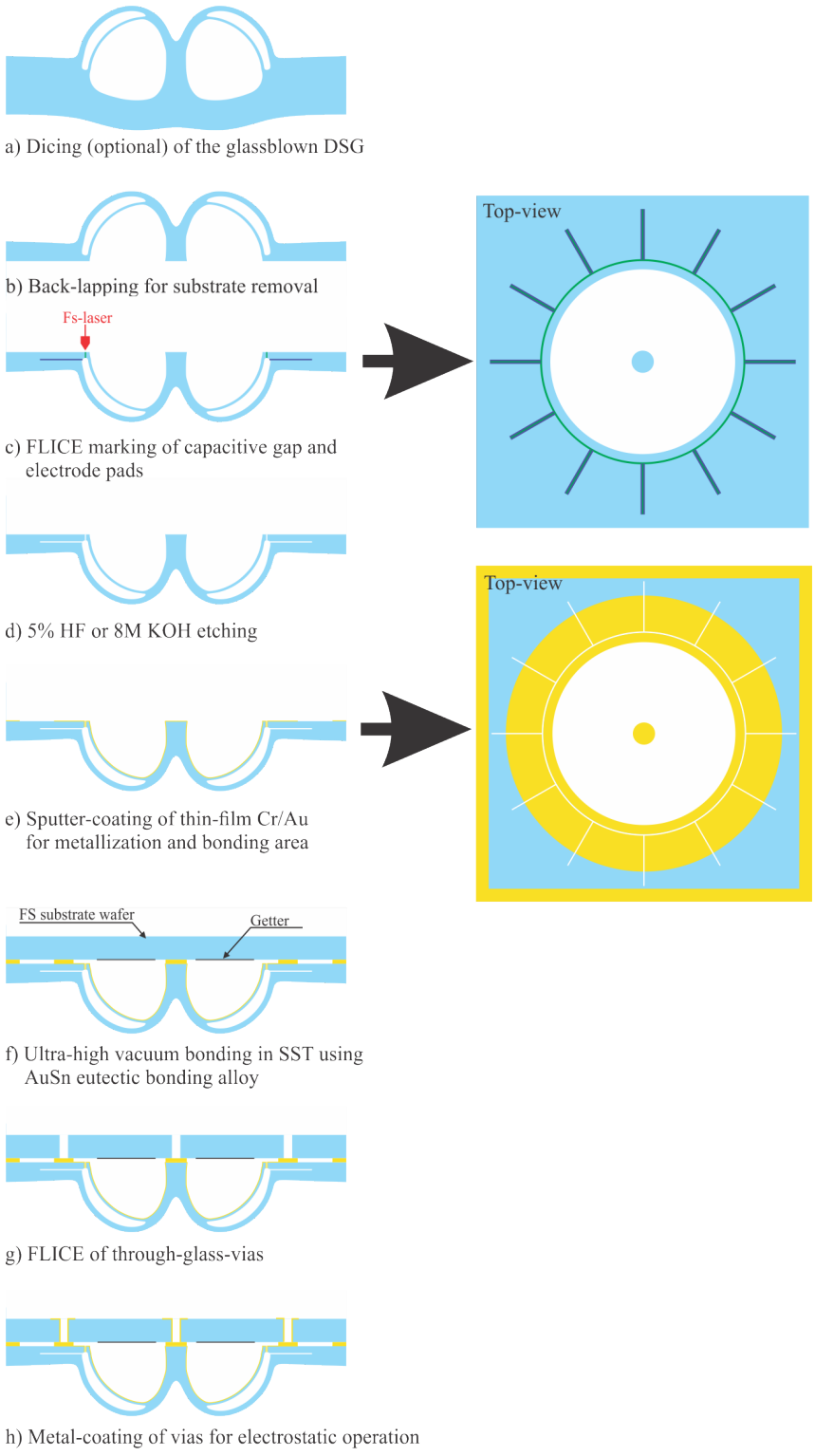

Figure 6.3: Process flow for FS glass-blown Dual-shell gyroscope using a developed laser-associated release. The process is compatible with the high vacuum in-situ encapsulation and passive getter pumping technique. The details of the fabrication process of the electrode substrate are illustrated in Fig. 6.5.

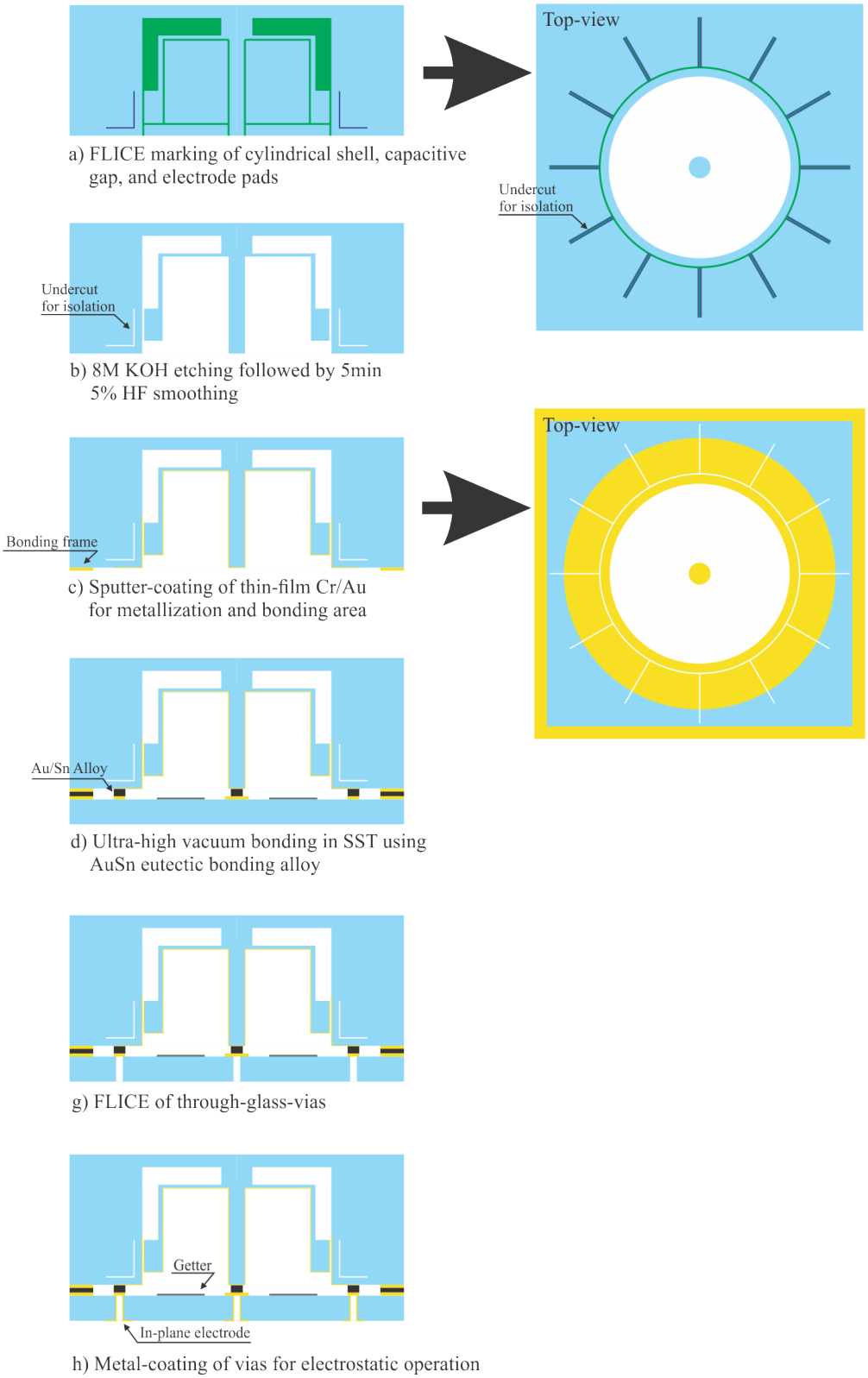

Figure 6.4: Process flow for FLICE-associated fabrication process of MEMS dual cylindrical shell gyroscope. The process is also compatible with the piezo actuation and tuning techniques.

6.2.5 In-situ Compensation of Drift with Multi-Mode Operation

The angular rate drifts of the n = 2 and n = 3 mode pairs of a disk resonator showed a strong correlation which had been demonstrated as an in-situ gyroscope drift compensation method in [125]. Similarly, both the n = 2 and n = 3 mode pairs in a DSG are configured to yield measurements of angular rate. After the development of the electrostatic compensation algorithm of simultaneous tuning of both mode pairs of DSGs in Chapter 3, a concurrent gyroscope operation of both modes might be implemented to extract simultaneous angular rate measurements from the same DSG to compensate for the long-term thermal-induced drift.

6.2.6 In-situ Vacuum Encapsulation of Dual-Shell Gyroscope

The eutectic bonding process of FS dual-shell gyroscopes for assembly with vacuum encapsulation was proposed in our recent work [94]. The electrode substrate with both the center and outer bonding frame was fabricated using the glass-in-silicon re-flow process. However, due to the mismatch of the thermal expansion coefficients between the FS dual-shell and Si electrode substrate, the thermal-induced stress would result in frequency shifts and increased energy dissipations. A modified in-situ vacuum encapsulation fabrication process, illustrated in Fig. 6.5, might ease the issue, simplify the process, and increase the imperfection tolerance. The bonding is based on AuSn eutectic alloy with a low re-flow temperature of around 278 °C. The process is compatible with the passive getter pumping technique for achieving a long-term ultra-high vacuum. The in-plane and out-of-plane electrodes would be fabricated using a laser-associated through-glass-vias technique after the bonding process.

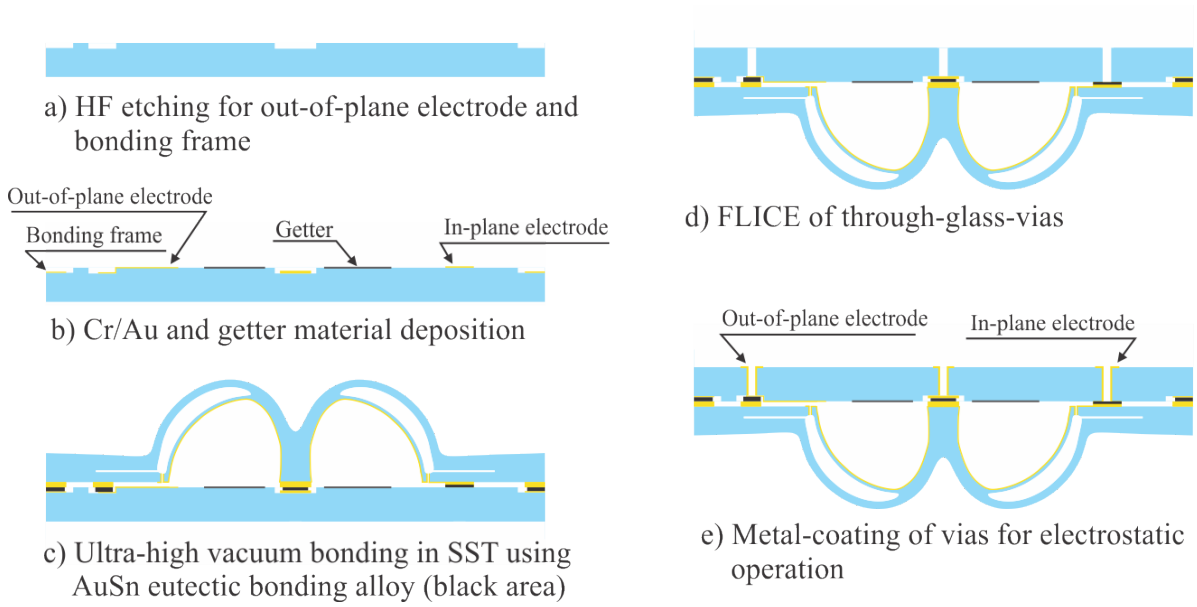

Figure 6.5: Process flow of FS electrode substrate for integrating with FS DSGs using laser-patterned Through-Glass-Vias. The out-of-plane capacitive gap and bonding areas (about 40 μm) were wet etched in HF solution. The proposed electrode substrate enables both the in-plane and out-of-plane electrodes, in-situ vacuum packaging, and the getter pumping technique.

6.2.7 MEMS "Crystal-Ball" IMU

Laser-patterned Through-Glass-Vias fabrication is an integral part of the 3D MEMS Inertial Measurement Unit (IMU). The process proposed in Section 6.2.6 allows for electrical connection between the front and the back sides of the FS substrate and in-situ vacuum packaging of FS Dual-Shell Gyroscopes. Hence, a multi-gyroscope unit or IMU with 3-axis gyroscopes and accelerometers might be formed by assembling the sensors on a 3D backbone frame, as illustrated in Fig. 6.6. Once "Crystal-Ball" IMU is formed into a 3D configuration, thru-wafer interconnects of the device substrates and 3D backbone enable a path for electrical signals from inertial sensors on each surface of the "Crystal-Ball" to the network of metal traces inside of the 3D frame. This creates an opportunity for efficient usage of the "Crystal-Ball" IMU inner volume by integrating with Application-Specific Integrated Circuits (ASICs) on the inner side of the IMU structure.

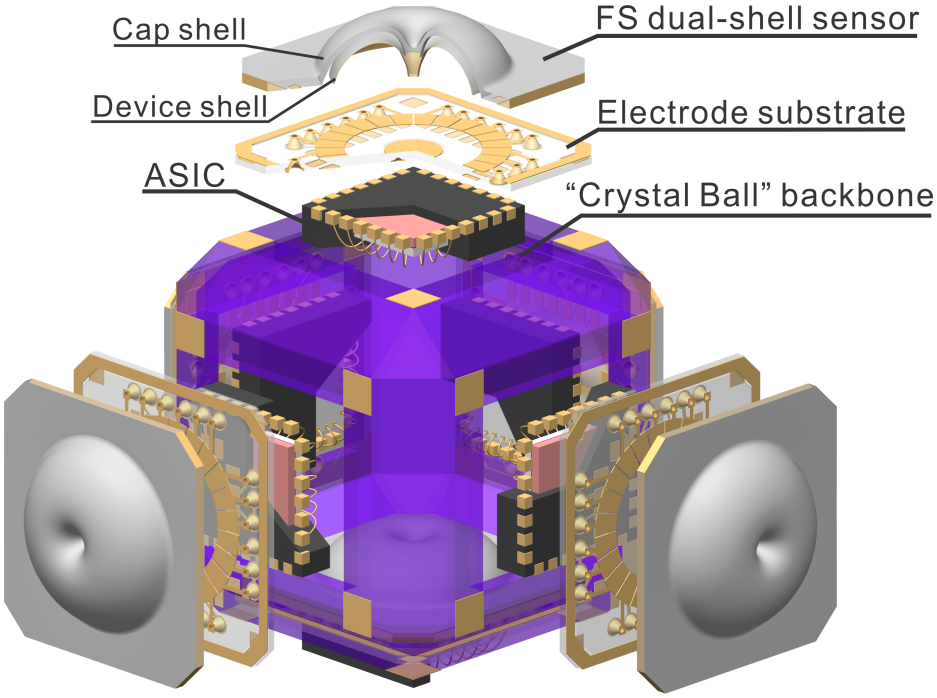

Figure 6.6: Illustration of Micro “Crystal-Ball” IMU. Double-sided fabrication process and laser-patterned Through-Glass-Vias enable efficient utilization of the IMU inner volume for integrating with ASICs and in-situ vacuum packaging of individual inertial sensors.

6.2.8 Thru-Wafer Interconnects for Double-Sided Fabrication Process

The design structure of DAG is presented in Chapter 2. The geometrical parameter optimization was explored in order to reduce anchor loss through the central stem to achieve the high quality factor of the devices. However, due to the unbalanced oscillatory motion of the in-plane translational mode, improvement of the quality factor is limited. Thanks to the development of Thru-wafer interconnect techniques in Chapter 2 and Section 6.2.1 and 6.2.6, fabrication of a double-ended sensor design seems to be a choice to eliminate the unbalanced motion applied on the substrate. The double-ended sensor consists of two identical sensors fabricated on both sides of a substrate wafer, as illustrated in Fig. 6.7. The two sensors could be fabricated separately and then bonded together as the process shown in Fig. 6.8(a) or marked onto both sides of a single FS wafer utilizing the developed FLICE-associated

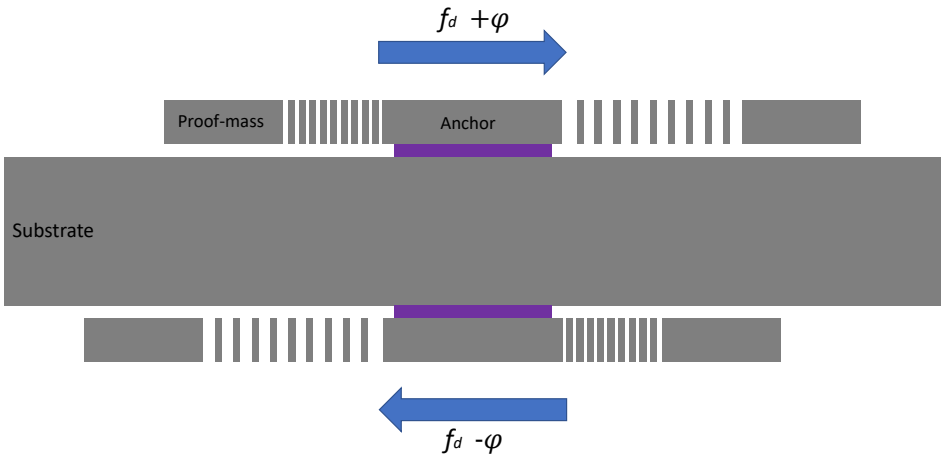

Figure 6.7: Illustration of dynamically balanced double-ended sensor concept.

process as shown in Fig. 6.8(b). The central anchors should be aligned, and the two identical sensors would be actuated using the anti-phase signals with the same frequency in order to achieve the concept of dynamical balance to effectively preserve the energy loss through the substrate. Besides, the two processes proposed in Fig. 6.8(a) and (b) are compatible with in-situ vacuum package, passive getter pumping technique, and in- and out-of-plane electrodes.

6.2.9 High Shock Resilient of FS Dual-Shell Gyroscopes

Due to its inherent structural robustness, FS Dual-Shell Gyroscope was proposed as a mitigation approach for continuous high-precision gyroscope operation through mechanical shocks and vibrations. The sensor design and implementation were also developed in Chapter 3. However, the shock resilience and operation-through-shock have not been experimentally demonstrated.

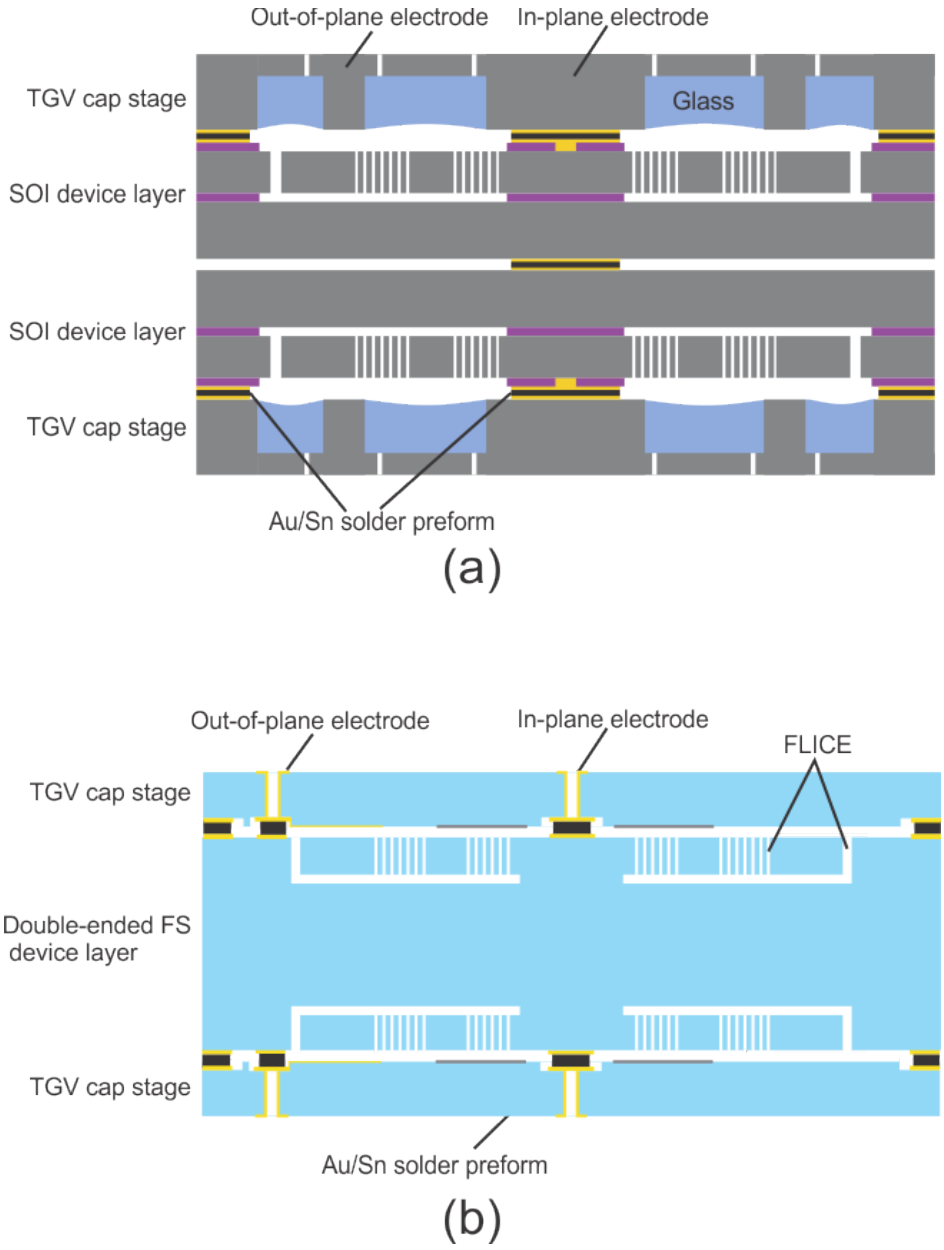

Figure 6.8: Process flows of double-sided fabrication utilizing (a) Silicon-in-Glass vias formed by glass re-flow technique presented in Fig. 6.1 and (b) FLICE-patterned Through-Glass-Vias technique presented in Fig. 6.5.

Bibliography

[1] Masakatsu Kourogi, Nobuchika Sakata, Takashi Okuma, and Takeshi Kurata. Indoor/outdoor pedestrian navigation with an embedded GPS/RFID/self-contained sensor system. In *International Conference on Artificial Reality and Telexistence*, Hangzhou, China, Nov. 29 – Dec. 1, 2006.

[2] Yusheng Wang, Chi-Shih Jao, and Andrei M Shkel. Scenario-dependent ZUPT-aided pedestrian inertial navigation with sensor fusion. *Gyroscopy and Navigation*, 12(1):1–16, 2021.

[3] Neil Barbour and George Schmidt. Inertial sensor technology trends. *IEEE Sensors Journal*, 1(4):332–339, 2001.

[4] Safran PRIMUS 400 Datasheet. https://www.safran-electronics-defense.com/security/navigation-systems.

[5] Honeywell HG9900 Datasheet. https://aerospace.honeywell.com/en//media/aerospace/files/brochures/n61-1638-000-000-hg9900inertialmeasurementunit-bro.pdf.

[6] Michael Perlmutter and Laurent Robin. High-performance, low cost inertial MEMS: A market in motion. In *IEEE/ION Position, Location and Navigation Symposium*, Myrtle Beach, SC, USA, Apr. 23–26, 2012.

[7] Vittorio Passaro, Antonello Cuccovillo, Lorenzo Vaiani, Martino De Carlo, and Carlo Edoardo Campanella. Gyroscope technology and applications: A review in the industrial perspective. *Sensors*, 17(10):2284, 2017.

[8] Navid Yazdi, Farrokh Ayazi, and Khalil Najafi. Micromachined inertial sensors. *Proceedings of the IEEE*, 86(8):1640–1659, 1998.

[9] Euan J Boyd, Li Li, Robert Blue, and Deepak Uttamchandani. Measurement of the temperature coefficient of Young's modulus of single crystal silicon and 3C silicon carbide below 273 K using micro-cantilevers. *Sensors and Actuators A: Physical*, 198:75–80, 2013.

[10] Sang Won Yoon. *Vibration Isolation and Shock Protection for MEMS.* PhD thesis, University of Michigan, 2009.

[11] Chihwan Jeong, Seonho Seok, Byeungleul Lee, Hyeonched Kim, and Kukjin Chun. A study on resonant frequency and Q-factor tunings for MEMS vibratory gyroscopes. *Journal of Micromechanics and Microengineering*, 14(11):1530, 2004.

[12] Sungjin Yoon, Usung Park, Jaewook Rhim, and Sang Sik Yang. Tactical grade MEMS vibrating ring gyroscope with high shock reliability. *Microelectronic Engineering*, 142:22–29, 2015.

[13] Yann Meyer, Thierry Verdot, Manuel Collet, J Baborowski, and P Muralt. Active isolation of electronic micro-components with piezoelectrically transduced silicon MEMS devices. *Journal of Smart Materials and Structures*, 16(1):128–134, 2007.

[14] Sang Won Yoon, Navid Yazdi, Noel C Perkins, and Khalil Najafi. Micromachined integrated shock protection for MEMS. *Sensors and Actuators A: Physical*, 130:166–175, 2006.

[15] Sina Askari, Mohammad H Asadian, and Andrei M Shkel. Retrospective correction of angular gain by virtual carouseling in MEMS gyroscopes. In *IEEE International Symposium on Inertial Sensors and Systems (INERTIAL)*, Naples, FL, USA, April 1–5, 2019.

[16] David M Rozelle. The hemispherical resonator gyro: From wineglass to the planets. In *AAS/AIAA Space Flight Mechanics Meeting*, Savannah, GA, USA, Feb. 8–12, 2009.

[17] Andrei M Shkel. Type I and type II micromachined vibratory gyroscopes. In *IEEE/ION Position, Location and Navigation Symposium (PLANS)*, San Diego, CA, USA, April 25-27, 2006.

[18] David D. Lynch. MRIG frequency mismatch and quadrature control. In *IEEE International Symposium on Inertial Sensors and Systems (INERTIAL)*, Laguna Beach, CA, USA, Feb. 25–26, 2014.

[19] Daryosh Vatanparvar and Andrei M Shkel. Quadrature-induced noise in Coriolis vibratory gyroscopes. In *IEEE International Symposium on Inertial Sensors and Systems (INERTIAL)*, Virtual Symposium, Mar. 23–26, 2020.

[20] Robert P Leland. Mechanical-thermal noise in MEMS gyroscopes. *IEEE Sensors Journal*, 5(3):493–500, 2005.

[21] David D. Lynch. Vibratory gyro analysis by the method of averaging. In *Int. Conf. Gyroscopic Technol. Navigat.*, St. Petersburg, Russia, May 1995.

[22] Marc Weinberg, Rob Candler, Saurabh Chandorkar, Jonathan Varsanik, Thomas Kenny, and Amy Duwel. Energy loss in MEMS resonators and the impact on inertial and RF devices. In *IEEE International Solid-State Sens., Actuators Microsyst. (TRANSDUCERS)*, Denver, CO, USA, June 21–25, 2009.

[23] Shirin Ghaffari, Saurabh A Chandorkar, Shasha Wang, Eldwin J Ng, Chae H Ahn, Vu Hong, Yushi Yang, and Thomas W Kenny. Quantum limit of quality factor in silicon micro and nano mechanical resonators. *Scientific Reports*, 3(1):1–7, 2013.

[24] Wei Guan, Danmeng Wang, Mohammad H Asadian, Yusheng Wang, and Andrei M Shkel. Effect of geometry on energy losses in fused silica dual-shell gyroscopes. In *IEEE International Symposium on Inertial Sensors and Systems (INERTIAL)*, Avignon, France, May 8–11, 2022.

[25] Joab J Blech. On isothermal squeeze films. *Journal of Lubrication Technology*, 105(4):615–620, 1983.

[26] Young-Ho Cho, Albert P Pisano, and Roger T Howe. Viscous damping model for laterally oscillating microstructures. *IEEE Journal of Microelectromechanical Systems*, 3(2):81–87, 1994.

[27] Mohammad H Asadian, Sina Askari, and Andrei M Shkel. An ultrahigh vacuum packaging process demonstrating over 2 million Q-factor in MEMS vibratory gyroscopes. *IEEE Sensors Letters*, 1(6):1–4, 2017.

[28] Clarence Zener. Internal friction in solids. I. Theory of internal friction in reeds. *Physical Review*, 52(3):230, 1937.

[29] Clarence Zener. Internal friction in solids II. General theory of thermoelastic internal friction. *Physical Review*, 53(1):90, 1938.

[30] Yusheng Wang, Yu-Wei Lin, Janna Glaze, Gabrielle Davis Vukasin, Dongsuk D Shin, Hyun-Keun Kwon, David B Heinz, Yunhan Chen, Dustin D Gerrard, Thomas W Kenny, and Andrei M Shkel. Quantification of energy dissipation mechanisms in toroidal ring gyroscope. *IEEE Journal of Microelectromechanical Systems*, 30(2):193–202, 2021.

[31] Ron Lifshitz and Michael L Roukes. Thermoelastic damping in micro-and nanomechanical systems. *Physical Review B*, 61(8):5600, 2000.

[32] Dustin D Gerrard, Yunhan Chen, Saurabh A Chandorkar, Guo Yu, Janna Rodriguez, Ian B Flader, Dongsuk D Shin, Carl D Meinhart, Ole Sigmund, and Thomas W Kenny. Topology optimization for reduction of thermo-elastic dissipation in MEMS resonators. In *IEEE International Solid-State Sens., Actuators Microsyst. (TRANSDUCERS)*, Kaohsiung, Taiwan, June 18-22, 2017.

[33] Rob N Candler, Amy Duwel, Mathew Varghese, Saurabh A Chandorkar, Matthew A Hopcroft, Woo-Tae Park, Bongsang Kim, Gary Yama, Aaron Partridge, Markus Lutz, et al. Impact of geometry on thermoelastic dissipation in micromechanical resonant beams. *IEEE Journal of Microelectromechanical Systems*, 15(4):927–934, 2006.

[34] Tal Nagourney, Jae Yoong Cho, Behrouz Shiari, Ali Darvishian, and Khalil Najafi. 259 second ring-down time and 4.45 million quality factor in 5.5 khz fused silica bird-bath shell resonator. In *IEEE International Solid-State Sens., Actuators Microsyst. (TRANSDUCERS)*, Kaohsiung, Taiwan, June 18-22, 2017.

[35] Yan Xie, Hao-Chieh Hsieh, Pradeep Pai, Hanseup Kim, Massood Tabib-Azar, and Carlos H Mastrangelo. Precision curved micro hemispherical resonator shells fabricated by poached-egg micro-molding. In *IEEE Sensors Conference*, Taipei, Taiwan, Oct. 28-31, 2012.

[36] Jinling Yang, Takahito Ono, and Masayoshi Esashi. Surface effects and high quality factors in ultrathin single-crystal silicon cantilevers. *Applied Physics Letters*, 77(23):3860–3862, 2000.

[37] Steven D Penn, Gregory M Harry, Andri M Gretarsson, Scott E Kittelberger, Peter R Saulson, John J Schiller, Joshua R Smith, and Sol O Swords. High quality factor measured in fused silica. *Review of Scientific Instruments*, 72(9):3670–3673, 2001.

[38] Nicholas E Bousse, James ML Miller, Hyun-Keun Kwon, Gabrielle D Vukasin, and Thomas W Kenny. Quality factor tuning of micromechanical resonators via electrical dissipation. *Applied Physics Letters*, 116(2):Jan. 2020, Art, no. 023506.

[39] Kenji Numata, Shigemi Otsuka, Masaki Ando, and Kimio Tsubono. Intrinsic losses in various kinds of fused silica. *Classical and Quantum Gravity*, 19(7):1697, 2002.

[40] Daryosh Vatanparvar and Andrei M Shkel. Effect of fabrication imperfections on energy loss through mechanical mode coupling in MEMS. In *IEEE International Symposium on Inertial Sensors and Systems (INERTIAL)*, Lake Como, Italy, Mar. 26–29, 2018.

[41] Saurabh A Chandorkar, Manu Agarwal, Renata Melamud, Robert N Candler, Kenneth E Goodson, and Thomas W Kenny. Limits of quality factor in bulk-mode micromechanical resonators. In *IEEE International Conference on Micro Electro Mechanical Systems (MEMS)*, Wuhan, China, Jan 13-17, 2008.

[42] T Gordon Brown. Harsh military environments and microelectromechanical (MEMS) devices. In *IEEE SENSORS*, Toronto, ON, Canada, Oct. 22–24, 2003.

[43] Herbert R Shea. Reliability of MEMS for space applications. In *Proc. SPIE*, volume SPIE-6111, pages 84–93, 2006.

[44] Sajal Singh, Ali Darvishian, Jae Yoong Cho, Behrouz Shiari, and Khalil Najafi. High-Q 3D micro-shell resonator with high shock immunity and low frequency mismatch for MEMS gyroscopes. In *IEEE International Conference on Micro Electro Mechanical Systems (MEMS)*, Seoul, Korea, Jan. 27-31, 2019.

[45] Mehran Mehregany, Christian A Zorman, Narayanan Rajan, and Chien Hung Wu. Silicon carbide MEMS for harsh environments. *Proceedings of the IEEE*, 86(8):1594–1609, 1998.

[46] Cenk Acar and Andrei M Shkel. Inherently robust micromachined gyroscopes with 2-DOF sense-mode oscillator. *IEEE Journal of Microelectromechanical Systems*, 15(2):380–387, 2006.

[47] Korhan Sahin, Emre Sahin, Said Emre Alper, and Tayfun Akin. A wide-bandwidth and high-sensitivity robust microgyroscope. *Journal of Micromechanics and Microengineering*, 19 (7): 074004, 2009.

[48] Cenk Acar and Andrei M Shkel. *MEMS vibratory gyroscopes: structural approaches to improve robustness*. MEMS Reference Shelf Series. New York: Springer, 2009, ISBN: 978–0–387–09535–6, 2008.

[49] Mohammad H Asadian, Yusheng Wang, and Andrei M Shkel. Development of 3D fused quartz hemi-toroidal shells for high-Q resonators and gyroscopes. *IEEE Journal of Microelectromechanical Systems*, 28(6):954–964, 2019.

[50] Sajal Singh, Ali Darvishian, Jae Yoong Cho, Behrouz Shiari, and Khalil Najafi. High-Q 3D micro-shell resonator with high shock immunity and low frequency mismatch for MEMS gyroscopes. In *IEEE International Conference on Micro Electro Mechanical Systems (MEMS)*, Seoul, Korea, Jan. 27–31, 2019.

[51] Mohammad H Asadian and Andrei M Shkel. Fused quartz dual shell resonator. In *IEEE International Symposium on Inertial Sensors and Systems (INERTIAL)*, Naples, FL, USA, April 1–5, 2019.

[52] Mohammad H Asadian, Danmeng Wang, Yusheng Wang, and Andrei M Shkel. 3D dual-shell micro-resonators for harsh environments. In *IEEE/ION Position, Location and Navigation Symposium (PLANS)*, Portland, Oregon, USA, April 20–23, 2020.

[53] Andrei M. Shkel, Mohammad H. Asadian Ardakani, and Yusheng Wang. Fused quartz dual shell resonator and method of fabrication. US Patent App. 16/836,387.

[54] Said Emre Alper, Kivanc Azgin, and Tayfun Akin. A high-performance silicon-on-insulator MEMS gyroscope operating at atmospheric pressure. *Sensors and Actuators A: Physical*, 135(1):34–42, 2007.

[55] Marco Del Sarto, Simone Sassolini, Lorenzo Baldo, Mauro Marchi, and Martin J McCaslin. Batch-fabricated silicon electrostatic micropositioner for dual-stage actuation. In *Micromachining and Microfabrication Process Technology VIII*, San Jose, CA, USA, Jan. 27-29, 2003.

[56] Kun Zhang, Wei Jiang, and Xinxin Li. Wafer-level sandwiched packaging for high-yield fabrication of high-performance MEMS inertial sensors. In *IEEE International Conference on Micro Electro Mechanical Systems (MEMS)*, Wuhan, China, Jan. 28, 2008.

[57] Atsushi Kazama, Takanori Aono, and Ryoji Okada. High shock-resistant design for wafer-level-packaged three-axis accelerometer with ring-shaped beam. *IEEE Journal of Microelectromechanical Systems*, 27(2):355–364, 2018.

[58] Alexandra Efimovskaya, Yu-Wei Lin, and Andrei M Shkel. Double-sided process for MEMS SOI sensors with deep vertical thru-wafer interconnects. *IEEE Journal of Microelectromechanical Systems*, 27(2):239–249, 2018.

[59] Andreas C Fischer, Simon J Bleiker, Tommy Haraldsson, Niclas Roxhed, Göran Stemme, and Frank Niklaus. Very high aspect ratio through-silicon vias (TSVs) fabricated using automated magnetic assembly of nickel wires. *Journal of Micromechanics and Microengineering*, 22(10):105001, 2012.

[60] Li Wenyin, Wu Xuezhong, Xiao Dingbang, Hou Zhanqiang, Chen Zhihua, Wang Xinghua, and Zhou Jian. Characterization of signal transfer performance of a through glass via (TGV) substrate with silicon vertical feedthroughs. *Microelectronic Engineering*, 165:52–56, 2016.

[61] Aric B Shorey and Rachel Lu. Progress and application of through glass via (TGV) technology. In *Pan Pacific Microelectronics Symposium (Pan Pacific)*, Big Island, HI, USA, Jan. 25–28, 2016.

[62] Igor P Prikhodko, Alexander A Trusov, and Andrei M Shkel. Compensation of drifts in high-Q MEMS gyroscopes using temperature self-sensing. *Sensors and Actuators A: Physical*, 201:517–524, 2013.

[63] Chae Hyuck Ahn, Vu A Hong, W Park, Yushi Yang, Yunhan Chen, Eldwin J Ng, J Huynh, AD Challoner, Kenneth E Goodson, and Thomas W Kenny. On-chip ovenization of encapsulated disk resonator gyroscope (DRG). In *IEEE International Solid-State Sens., Actuators Microsyst. (TRANSDUCERS)*, Anchorage, AK, USA, June 21–25, 2015.

[64] Igor P Prikhodko, Alexander A Trusov, and Andrei M Shkel. Achieving long-term bias stability in high-Q inertial MEMS by temperature self-sensing with a 0.5 millicelcius precision. Hilton Head, SC, USA, June 3-7, 2012.

[65] Jonathan J Bernstein and Marc S Weinberg. Comb drive micromechanical tuning fork gyro fabrication method. March 5 1996. US Patent 5,496,436.

[66] Michael W Putty and David S Eddy. Microstructure for vibratory gyroscope, September 19 1995. US Patent 5,450,751.

[67] Mohammad H Asadian, Sina Askari, Yusheng Wang, and Andrei M Shkel. Characterization of energy dissipation mechanisms in dual foucault pendulum gyroscopes. In *IEEE International Symposium on Inertial Sensors and Systems (INERTIAL)*, Naples, FL, USA, April 1–5, 2019.

[68] Alexander A. Trusov, Grant Atikyan, David M. Rozelle, Andrew D. Meyer, Sergei A. Zotov, Brent R. Simon, and Andrei M. Shkel. Flat is not dead: Current and future performance of Si-MEMS quad mass gyro (QMG) system. In *IEEE/ION Position, Location and Navigation Symposium (PLANS)*, Monterey, CA, USA, May 5–8, 2014.

[69] Danmeng Wang, Alexandra Efimovskaya, and Andrei M. Shkel. Amplitude amplified dual-mass gyroscope: Design architecture and noise mitigation strategies. In *IEEE International Symposium on Inertial Sensors and Systems (INERTIAL)*, Naples, FL, USA, April 1–5, 2019.

[70] Doruk Senkal, Alexandra Efimovskaya, and Andrei M. Shkel. Dual foucault pendulum gyroscope. In *IEEE International Solid-State Sens., Actuators Microsyst. (TRANSDUCERS)*, Anchorage, AK, USA, June 21–25, 2015.

[71] Sina Askari, Mohammad H Asadian, Kasra Kakavand, and Andrei M Shkel. Vacuum sealed and getter activated MEMS quad mass gyroscope demonstrating better than 1.2 million quality factor. In *IEEE International Symposium on Inertial Sensors and Systems (INERTIAL)*, Laguna Beach, CA, USA, Feb. 22–25, 2016.

[72] Christopher C Painter and Andrei M. Shkel. Dynamically amplified rate integrating gyroscope, August 16 2005. US Patent 6,928,874.

[73] Danmeng Wang, Mohammad H Asadian, Alexandra Efimovskaya, and Andrei M Shkel. A comparative study of conventional single-mass and amplitude amplified dual-mass MEMS Vibratory Gyroscopes. In *IEEE International Symposium on Inertial Sensors and Systems (INERTIAL)*, Kauai, HI, USA, Mar. 27–30, 2017.

[74] Daryosh Vatanparvar, Danmeng Wang, and Andrei M. Shkel. Direct angle measurement using dynamically-amplified gyroscope. *IEEE Sensors Journal*, 22(7):6336–6344, 2022.

[75] Doruk Senkal, Mohammed J Ahamed, Alexander A Trusov, and Andrei M Shkel. Achieving sub-Hz frequency symmetry in micro-glassblown wineglass resonators. *IEEE Journal of Microelectromechanical Systems*, 23(1):30–38, 2013.

[76] Doruk Senkal, Mohammed J Ahamed, Mohammad H Asadian, Sina Askari, and Andrei M Shkel. Out-of-plane electrode architecture for fused silica micro-glassblown 3-D wineglass resonators. In *IEEE Sensors Conference*, Valencia, Spain, Nov. 2–4, 2014.

[77] Jae Yoong Cho, Jialiang Yan, Jeffrey A Gregory, Harald Eberhart, Rebecca L Peterson, and Khalil Najafi. High-Q fused silica birdbath and hemispherical 3-D resonators made by blow torch molding. In *IEEE International Conference on Micro Electro Mechanical Systems (MEMS)*, Taipei, Taiwan, Jan. 20-24, 2013.

[78] Jong-Kwan Woo, Jae Yoong Cho, Christopher Boyd, and Khalil Najafi. Whole-angle-mode micromachined fused-silica birdbath resonator gyroscope (WA-BRG). In *IEEE International Conference on Micro Electro Mechanical Systems (MEMS)*, San Francisco, CA, USA, Jan. 26-30, 2014.

[79] Yusheng Wang, Mohammad H Asadian, and Andrei M Shkel. Modeling the effect of imperfections in glassblown micro-wineglass fused quartz resonators. *Journal of Vibration and Acoustics*, 139(4), 2017.

[80] Wei Li, Xiang Xi, Kun Lu, Yan Shi, Zhanqiang Hou, Yulie Wu, Xuezhong Wu, and Dingbang Xiao. A novel micro shell resonator gyroscope with sixteen T-shape masses. In *International Conference on Solid-State Sensors, Actuators and Microsystems & Eurosensors XXXIII (TRANSDUCERS & EUROSENSORS XXXIII)*, Berlin, Germany, June 23-27, 2019.

[81] Wei Li, Xiang Xi, Kun Lu, Yan Shi, Zhanqiang Hou, Yulie Wu, Xuezhong Wu, and Dingbang Xiao. A novel high transduction efficiency micro shell resonator gyroscope with 16 T-shape masses using out-of-plane electrodes. *IEEE Sensors Journal*, 19(13):4820–4828, 2019.

[82] Yusheng Wang, Mohammad H Asadian, and Andrei M Shkel. Compensation of frequency split by directional lapping in fused quartz micro wineglass resonators. *Journal of Micromechanics and Microengineering*, 28(9):095001, 2018.

[83] Anthony D Challoner, H Ge Howard, and John Y Liu. Boeing disc resonator gyroscope. In *IEEE/ION Position, Location and Navigation Symposium (PLANS)*, Monterey, CA, USA, May 5-8, 2014.

[84] Peng Shao, Curtis L Mayberry, Xin Gao, Vahid Tavassoli, and Farrokh Ayazi. A polysilicon microhemispherical resonating gyroscope. *IEEE Journal of Microelectromechanical Systems*, 23(4):762–764, 2014.

[85] Parsa Taheri-Tehrani, T Su, A Heidari, G Jaramillo, C Yang, S Akhbari, H Najar, S Nitzan, D Saito, L Lin, et al. Micro-scale diamond hemispherical resonator gyroscope. In *Solid-State Sensors, Actuators, Microsyst.*, Hilton Head, SC, USA, June 8-12, 2014.

[86] Daryosh Vatanparvar and Andrei M Shkel. Effect of electrostatic nonlinearity on force-to-rebalance mode of operation in CVG. In *DGON Inertial Sensors and Systems - Symposium Gyro Technology (ISS)*, Virtual Symposium, Sept. 15–16, 2020.

[87] Anupam Viswanath, Tao Li, and Yogesh Gianchandani. High resolution micro ultrasonic machining for trimming 3D microstructures. *Journal of Micromechanics and Microengineering*, 24(6):065017, 2014.

[88] H. Xiaodong, L. Junkang, Y. Bo, Z. Qiang, L. Ke, and L Ting. Application of ion beam in the mass balancing of hemispherical resonator. In *the Fifth Chinese Society of Inertial Technology Annual Conference*, Guilin, China, Oct. 2003.

[89] Yuting Wang, Yao Pan, Tianliang Qu, Yonglei Jia, Kaiyong Yang, and Hui Luo. Decreasing frequency splits of hemispherical resonators by chemical etching. *Sensors*, 18(11):3772, 2018.

[90] Sina Askari, Mohammad H. Asadian, Kasra Kakavand, and Andrei M. Shkel. Near-navigation grade quad mass gyroscope with Q-factor limited by thermo-elastic damping. In *Solid-State Sensors, Actuators, Microsyst.*, Hilton Head, SC, USA, June 5–9, 2016.

[91] Doruk Senkal, Mohammed J Ahamed, Mohammad H Asadian Ardakani, Sina Askari, and Andrei M Shkel. Demonstration of 1 million Q-factor on microglassblown wineglass resonators with out-of-plane electrostatic transduction. *IEEE Journal of Microelectromechanical Systems*, 24(1):29–37, 2014.

[92] Libin Zeng, Yao Pan, Yiming Luo, Pengbo Xiao, Jianping Liu, Zhongqi Tan, Kaiyong Yang, and Hui Luo. Fused silica cylindrical shell resonators with 25 million Q-factors. *Journal of Physics D: Applied Physics*, 54(49):495104, 2021.

[93] P. E Miller, T. I Suratwala, L. L Wong, M. D Feit, J. A Menapace, P. J Davis, and W. A Steele. The distribution of subsurface damage in fused silica. In *Boulder Damage Symposium XXXVII: Annual Symposium on Optical Materials for High Power Lasers*, Boulder, CO, USA, Sep. 19-21, 2005.

[94] Mohammad H Asadian, Danmeng Wang, and Andrei M Shkel. Fused quartz dual-shell resonator gyroscope. *IEEE Journal of Microelectromechanical Systems*, accepted.

[95] Jae Yoong Cho, Jialiang Yan, Jeffrey A Gregory, Harald W Eberhart, Rebecca L Peterson, and Khalil Najafi. 3-dimensional blow torch-molding of fused silica microstructures. *IEEE Journal of Microelectromechanical Systems*, 22(6):1276–1284, 2013.

[96] Daryosh Vatanparvar, Doreen Hii, and Andrei M Shkel. Fabrication process and structural characterization of fused silica-on-silicon toroidal ring gyroscope. In *IEEE Sensors*, Sydney, Australia, Oct. 31 - Nov. 3, 2021.

[97] T. H Gilani and Dian Rabchuk. Electrical resistivity of gold thin film as a function of film thickness. *Canadian Journal of Physics*, 96(3):272–274, 2018.

[98] Tal Nagourney, Jae Yoong Cho, Ali Darvishian, Behrouz Shiari, and Khalil Najafi. Effect of metal annealing on the Q-factor of metal-coated fused silica micro shell resonators. In *IEEE International Symposium on Inertial Sensors and Systems (INERTIAL)*, Hapuna Beach, HI, USA, Mar. 23–26, 2015.

[99] Jao Yoong Cho, Tal Nagourney, Ali Darvishian, and Khalil Najafi. Ultra conformal high aspect-ratio small-gap capacitive electrode formation technology for 3D micro shell resonators. In *IEEE International Conference on Micro Electro Mechanical Systems (MEMS)*, Las Vegas, NV, USA, Jan. 22–26, 2017.

[100] Lu Xu, Bin Luo, Jintang Shang, Zhaoxi Su, Shouyu Han, and Yinghui Zhang. Study on the effect of assembly errors on the electrostatic tuning ability in micro umbrella shell resonators. In *International Conference on Electronic Packaging Technology (ICEPT)*. IEEE, Xiamen, China, Sept. 14-17, 2021.

[101] Jiangkun Sun, Sheng Yu, Yongmeng Zhang, Yan Shi, Kun Lu, Xiang Xi, Xuezhong Wu, and Dingbang Xiao. Characterization and compensation of detection electrode errors for whole-angle micro-shell resonator gyroscope. *IEEE Journal of Microelectromechanical Systems*, 31(1):19 – 28, 2021.

[102] Zhihu Ruan, Xukai Ding, Zhengcheng Qin, Jia Jia, and Hongsheng Li. Modeling and compensation of assembly inclination error of micro hemispherical resonator gyroscope under force-to-rebalance mode. *IEEE Sensors Journal*, 21(13):14726 – 14738, 2021.

[103] Jae Yoong Cho, Sajal Singh, Jong-Kwan Woo, Guohong He, and Khalil Najafi. 0.00016 deg/rt-hr angle random walk (ARW) and 0.0014 deg/hr bias instability (BI) from a 5.2 MQ and 1-cm precision shell integrating (PSI) gyroscope. In *IEEE International Symposium on Inertial Sensors and Systems (INERTIAL)*, Virtual Symposium, Mar. 23–26, 2020.

[104] Mohammad H Asadian, Yusheng Wang, Sina Askari, and Andrei Shkel. Controlled capacitive gaps for electrostatic actuation and tuning of 3D fused quartz micro wineglass resonator gyroscope. In *IEEE International Symposium on Inertial Sensors and Systems (INERTIAL)*, Kauai, HI, USA, Mar. 27–30, 2017.

[105] Doruk Senkal, MJ Ahamed, AA Trusov, and AM Shkel. Electrostatic and mechanical characterization of 3-D micro-wineglass resonators. *Sensors and Actuators A: Physical*, 215:150–154, 2014.

[106] Khalil Najafi and Jae Yoong Cho. Assembly processes for three-dimensional microstructures, April 7 2020. US Patent 10,612,925.

[107] David B Heinz, Vu A Hong, Yushi Yang, Chae-Hyuck Ahn, and Thomas W Kenny. High-g ($>$ 20,000 g) inertial shock survivability of epitaxially encapsulated silicon MEMS devices. In *IEEE International Conference on Micro Electro Mechanical Systems (MEMS)*, Las Vegas, NV, USA, Jan. 22–26, 2017.

[108] Christopher W. Dyck, Jamse J. Allen, and Robert J. Huber. Microelectromechanical dual-mass resonator structure, May 28 2002. US Patent 6,393,913.

[109] Jasmina Casals-Terre and Andrei M. Shkel. Dynamic analysis of a snap-action micromechanism. In *IEEE Sensors Conference*, Vienna, Austria, Oct. 24–27, 2004.

[110] Erdinc Tatar, Said Emre Alper, and Tayfun Akin. Quadrature-error compensation and corresponding effects on the performance of fully decoupled MEMS gyroscopes. *IEEE Journal of Microelectromechanical Systems*, 21(3):656–667, 2012.

[111] Alexandra Efimovskaya, Danmeng Wang, Yu-Wei Lin, and Andrei M. Shkel. Electrostatic compensation of structural imperfections in dynamically amplified dual-mass gyroscope. *Sensors and Actuators A: Physical*, 275:99–108, 2018.

[112] Huiliang Cao, Hongsheng Li, Jun Liu, Yunbo Shi, Jun Tang, and Chong Shen. An improved interface and noise analysis of a turning fork microgyroscope structure. *Mechanical Systems and Signal Processing*, 70:1209–1220, 2016.

[113] Jae Yoong Cho, J-K Woo, Guohong He, Donguk Yang, Christopher Boyd, Sajal Singh, Ali Darvishian, Behrouz Shiari, and Khalil Najafi. 1.5-million Q-factor vacuum-packaged birdbath resonator gyroscope (BRG). In *IEEE International Conference on Micro Electro Mechanical Systems (MEMS)*, Seoul, Korea, Jan. 27–31, 2019.

[114] Zhennan Wei, Guoxing Yi, Yan Huo, Ziyang Qi, and Zeyuan Xu. The synthesis model of flat-electrode hemispherical resonator gyro. *Sensors*, 19(7):1690, 2019.

[115] Danmeng Wang, Mohammad H. Asadian, Doreen Hii, and Andrei M. Shkel. Fused silica dual-shell gyroscope with in-plane actuation by out-of-plane electrodes realized using glassblowing and thru-glass-vias fabrication. In *IEEE International Conference on Micro Electro Mechanical Systems (MEMS)*, Tokyo, Japan, Jan. 10–14, 2022.

[116] Zeyuan Xu, Guoxing Yi, Meng Joo Er, and Chao Huang. Effect of uneven electrostatic forces on the dynamic characteristics of capacitive hemispherical resonator gyroscopes. *Sensors*, 19(6):1291, 2019.

[117] Danmeng Wang, Wei Guan, Mohammad H Asadian, Doreen Hii, and Andrei M Shkel. Effect of metallization on metal-coated fused silica dual-shell gyroscopes. In *IEEE International Symposium on Inertial Sensors and Systems (INERTIAL)*, Avignon, France, May 8–11, 2022.

[118] Danmeng Wang, Mohammad H. Asadian, Wei Guan, Doreen Hii, Austin R. Parrish, and Andrei M. Shkel. Effect of metallization on quality factor and noise characteristics in fused silica dual-shell gyroscopes. *IEEE Journal of Microelectromechanical Systems*, Accepted.

[119] Kun Lu, Xiang Xi, Wei Li, Yan Shi, Zhanqiang Hou, Ming Zhuo, Xuezhong Wu, Yulie Wu, and Dingbang Xiao. Research on precise mechanical trimming of a micro shell resonator with t-shape masses using femtosecond laser ablation. *Sensors and Actuators A: Physical*, 290:228–238, 2019.

[120] Danmeng Wang and Andrei M Shkel. Effect of EAM on capacitive detection of motion in MEMS vibratory gyroscopes. *IEEE Sensors Journal*, 22(3):2271 – 2281, 2022.

[121] Andrei M. Shkel and Doruk Senkal. Environmentally robust micro-wineglass gyroscope. US Patent 9,429,428.

[122] Danmeng Wang, Radwan M Noor, and Andrei M Shkel. Dynamically amplified dual-mass gyroscopes with in-situ shock survival mechanism. In *IEEE International Symposium on Inertial Sensors and Systems (INERTIAL)*, Virtual Symposium, Mar. 23–26, 2020.

[123] Srikantha Phani and Ashwin A Seshia. Identification of anisoelasticity and nonproportional damping in MEMS gyroscopes. In *NSTI-Nanotech*, volume 2, pages 343–346, 2004.

[124] Haoran Wen, Anosh Daruwalla, and Farrokh Ayazi. Resonant pitch and roll silicon gyroscopes with sub-micron-gap slanted electrodes: Breaking the barrier toward high-performance monolithic inertial measurement units. *Microsystems & Nanoengineering*, 3(1):1–9, 2017.

[125] Howard H Ge, Amir H Behbahani, and Robert T M'Closkey. MEMS gyro drift compensation using multiple rate measurements derived from a single resonator. In *IEEE/ION Position, Location and Navigation Symposium (PLANS)*, Monterey, CA, USA, April 23–26, 2018.

[126] Daryosh Vatanparvar, Doreen Hii, and Andrei M Shkel. Fabrication process and structural characterization of fused silica-on-silicon toroidal ring gyroscope. In *IEEE Sensors Conference*, Sydney, Australia, Oct. 31 - Nov. 3, 2021.

[127] Nathan Bishop, Julian Walker, Casey T DeRoo, Tianning Liu, Mohit Tendulkar, Vincenzo Cotroneo, Edward N Hertz, Vladimir Kradinov, Eric D Schwartz, Paul B Reid, Thomas N. Jackson, and Susan Trolier-McKinstry. Thickness distribution of sputtered films on curved substrates for adjustable X-ray optics. *Journal of Astronomical Telescopes, Instruments, and Systems*, 5(2):021005, 2019.

[128] Victor F. Zhuravlev and David D. Lynch. Electric model of a hemispherical resonator gyro. *Mechanics of Solids*, 30(5):10 – 21, 1995.

[129] Alexander A. Trusov and Andrei M. Shkel. A novel capacitive detection scheme with inherent self-calibration. *IEEE Journal of Microelectromechanical Systems*, 16(6):1324–1333, 2007.

[130] Xukai Ding, Jia Jia, Yang Gao, and Hongsheng Li. Mechanical and electrical noise in sense channel of MEMS vibratory gyroscopes. *Sensors*, 17(10):2306, 2017.

[131] Feng Bu, Xi Wang, Bo Fan, Shuwen Guo, Dacheng Xu, Xiang Xu, and Heming Zhao. Noise model considering electrical feed-through under force rebalance closed-loop detection of MEMS gyroscope. *Journal of Micromechanics and Microengineering*, 30(5):055007, 2020.

[132] Cenk Acar and Andrei M. Shkel. Structurally decoupled micromachined gyroscopes with post-release capacitance enhancement. *Journal of Micromechanics and Microengineering*, 15(5):1092, 2005.

[133] Sang Won Yoon, Sang Woo Lee, NC Perkins, and Khalil Najafi. Vibration sensitivity of MEMS tuning fork gyroscopes. In *IEEE Sensors*, Atlanta, GA, USA, Oct. 28–31, 2007.

[134] William C Tang, Tu-Cuong H Nguyen, and Roger T Howe. Laterally driven polysilicon resonant microstructures. *Sensors and Actuators A: Physical*, 20(1-2):25–32, 1989.

[135] Parsa Taheri-Tehrani, Martial Defoort, and David A Horsley. Operation of a high quality-factor gyroscope in electromechanical nonlinearities regime. *Journal of Micromechanics and Microengineering*, 27(7):075015, 2017.

[136] Hyung Kyu Lee, Renata Melamud, Saurabh Chandorkar, James Salvia, Shingo Yoneoka, and Thomas W Kenny. Stable operation of MEMS oscillators far above the critical vibration amplitude in the nonlinear regime. *IEEE Journal of Microelectromechanical Systems*, 20(6):1228–1230, 2011.

[137] Jianbing Xie, Yongcun Hao, and Weizheng Yuan. Energy loss in a MEMS disk resonator gyroscope. *Micromachines*, 10(8):493, 2019.

[138] Daryosh Vatanparvar and Andrei M Shkel. Instabilities due to electrostatic tuning of frequency-split in Coriolis vibratory gyroscopes. In *IEEE Sensors*, Virtual Symposium, Oct. 25–28, 2020.

[139] Hyung K Lee, Paul A Ward, Amy E Duwel, James C Salvia, Yu Q Qu, Renata Melamud, Saurabh A Chandorkar, Matthew A Hopcroft, Bongsang Kim, and Thomas W Kenny. Verification of the phase-noise model for MEMS oscillators operating in the nonlinear regime. In *IEEE International Solid-State Sens., Actuators Microsyst. (TRANSDUCERS)*, Beijing, China, June 5–9, 2011.

[140] Joshua E-Y Lee and Ashwin A Seshia. Parasitic feedthrough cancellation techniques for enhanced electrical characterization of electrostatic microresonators. *Sensors and Actuators A: Physical*, 156(1):36–42, 2009.

[141] Hao Kang, Jing Yang, and Honglong Chang. A closed-loop accelerometer based on three degree-of-freedom weakly coupled resonator with self-elimination of feedthrough signal. *IEEE Sensors Journal*, 18(10):3960–3967, 2018.

[142] Joan Giner and Kazuo Ono. Adaptive feedthrough cancellation in mems gyroscopes in reconfigurable IC+ FPGA platform. In *IEEE International Symposium on Inertial Sensors and Systems (INERTIAL)*, Lake Como, Italy, Mar. 26–29, 2018.

[143] Hemin Zhang, Weizheng Yuan, Yongcun Hao, and Honglong Chang. Influences of the feedthrough capacitance on the frequency synchronization of the weakly coupled resonators. *IEEE Sensors Journal*, 15(11):6081–6088, 2015.

[144] Jun Cao and Clark T.-C. Nguyen. Drive amplitude dependence of micromechanical resonator series motional resistance. In *IEEE International Solid-State Sens., Actuators Microsyst. (TRANSDUCERS)*, Sendai, Japan, June 7–10, 1999.

[145] Alexander A. Trusov and Andrei M. Shkel. Capacitive detection in resonant MEMS with arbitrary amplitude of motion. *Journal of Micromechanics and Microengineering*, 17(8):1583, 2007.

[146] Pavel M Polunin, Yushi Yang, Mark I Dykman, Thomas W Kenny, and Steven W Shaw. Characterization of MEMS resonator nonlinearities using the ringdown response. *IEEE Journal of Microelectromechanical Systems*, 25(2):297–303, 2016.

[147] Daryosh Vatanparvar, Mohammad H Asadian, Sina Askari, and Andrei M Shkel. Characterization of scale factor nonlinearities in Coriolis vibratory gyroscopes. In *IEEE International Symposium on Inertial Sensors and Systems (INERTIAL)*, Naples, FL, USA, April 1–4, 2019.

[148] Danmeng Wang and Andrei M. Shkel. Effect of EAM on quality factor and noise in MEMS vibratory gyroscopes. In *IEEE International Symposium on Inertial Sensors and Systems (INERTIAL)*, Virtual Symposium, Mar. 22–25, 2021.

[149] Guillaume Jourdan, Gauthier Torricelli, Joël Chevrier, and Fabio Comin. Tuning the effective coupling of an AFM lever to a thermal bath. *Nanotechnology*, 18, 475502, 2007.

[150] Ryunosuke Gando, Shunta Maeda, Kei Masunishi, Yasushi Tomizawa, Etsuji Ogawa, Yohei Hatakeyama, Tetsuro Itakura, and Tamio Ikehashi. A MEMS rate integrating gyroscope based on catch-and-release mechanism for low-noise continuous angle measurement. In *IEEE International Conference on Micro Electro Mechanical Systems (MEMS)*, Belfast, Ireland, Jan. 21–25, 2018.

[151] Claus-Peter Fritzen. Identification of mass, damping, and stiffness matrices of mechanical systems. *Transactions of ASME, Journal of Vibration, Acoustics, Stress, and Reliability in Design*, 108(9):9–16, 1986.

[152] Sergei A. Zotov, Brent R. Simon, Gunjana Sharma, Jie Han, Igor P. Prikhodko, Alexander A Trusov, and Andrei M. Shkel. Investigation of energy dissipation in low frequency vibratory MEMS demonstrating a resonator with 25 minutes time constant. In *Solid-State Sensors, Actuators, Microsyst.*, Hilton Head, SC, USA, June 8–12, 2014.

[153] James M Lehto Miller, Azadeh Ansari, David B Heinz, Yunhan Chen, Ian B Flader, Dongsuk D Shin, L Guillermo Villanueva, and Thomas W Kenny. Effective quality factor tuning mechanisms in micromechanical resonators. *Applied Physics Reviews*, 5(4):041307, 2018.

[154] Nikolay N. Bogolyubov and Yu A Mitropolskii. Asymptotic methods in the theory of nonlinear oscillations. Nauka, Moscow, Russia, 1974.

[155] Igor P. Prikhodko, Sergei A. Zotov, Alexander A. Trusov, and Andrei M. Shkel. What is MEMS gyrocompassing? comparative analysis of maytagging and carouseling. *IEEE Journal of Microelectromechanical Systems*, 22(6):1257–1266, 2013.

Appendix A

Lab Procedures

The procedures developed to fabricate SOI resonators, FS Dual-shell Gyroscopes (DSGs), as well as the Thru-Glass-Vias (TGVs) for both the cap stage of SOI sensors, and the electrode substrates of DSGs are listed in this section. Please acquire training and access of all the required equipment involved in the whole process first.

A.1 Lithography Recipes and Protocols

A.1.1 Purpose

This process is used in the fabrication of photoresist (PR) hard masks for Si DRIE. Different recipes would result in various thicknesses of PR layers. Recipes were demonstrated for two types of photoresists, Shipley1827 and AZ4620, and were optimized for 10W power on MA6 equipment. Shipley1827 typically forms a PR coating with a thickness of around 2 to 4 μm for high-resolution feature patterning, such as SOI MEMS devices. AZ4620 PR coating, on the other hand, usually results in a thicker layer with a thickness of around 5 to 12 μm for

low-resolution and long duration Si etching.

A.1.2 Process

A.1.2.1 Wafer Cleaning

Wafer cleaning is critical for the subsequent process. The PR coating is extremely sensitive to dust, PR residues, or any contaminants on the surface from previous fabrication steps, (leftover contaminants are common in SOI MEMS fabrication). Even a small speck on the proof-mass would destroy the particular SOI sensor on the wafer. Conducting the following cleaning steps for any re-used wafer to completely remove all possible residue on the Oxide surface. If the wafer was coated by PR and needed to be recycled or re-conducted, Step 1(a) and (b) are interchangeable with Step 2(a) and (b) are interchangeable. Otherwise, use Step 1(a) and Step 2(a).

1(a). Solvent clean the wafer with Acetone and IPA followed by DI water rinsing and wafer blow dry. Blow dry it.

1(b). Use an AZ 400T photoresist stripper bath and rinse under running DI water. Blow dry it.

2(a). Piranha cleaning. After cleaning, blow dry the wafer and dehydrate the wafer in a clean dehydration furnace at 120°C for >45 minutes before continuing with subsequent lithography process.

2(b). Place the wafer in a Plasma-Therm 790 and load a process named "O2ASH200" for 30 mins. Unload the wafer when the process is done and directly conduct the following lithography processes.

Do not clean a brand new SOI wafer before lithography process. Directly remove the SOI wafer out of the wafer box and dehydrate it in a clean dehydration furnace at 120°C for >45

minutes. You can never clean an SOI wafer as well as the vendors did. This is also true for Si wafers purchased from a reliable vendor.

A.1.2.2 Spin Coating of Hexamethyldisilizane (HMDS)

If the wafer is covered with an Oxide layer, such as a SOI wafer, conduct the following steps.

1. Use Acetone and cleanroom wipes to clean a Laurell spinner before using it.
2. Apply a clean aluminum foil on a hotplate and heat it to 150°C as preparation.
3. Load the wafer onto the spinner and center it. Turn on the spinner vacuum.
4. Set the recipe of the spinner: (Step 1) 500rpm at an acceleration of 3 for 10s and (Step 2) 2000rpm at 5 acceleration for 30s.
5. Blow the wafer using a Ni gun to remove particles. Pour enough HMDS to cover at least half of the wafer. Close the lid and start the spinner immediately.
6. Bake the wafer for 5 minutes at the prepared hotplate immediately when Step 5 is completed.
7. Transfer the wafer to a clean wipe to cool it down.
8. Use cleanroom wipes to clean the spinner after using it.

A.1.2.3 Spin Coating of Shipley1827

1. Use Acetone and cleanroom wipes to clean a Laurell spinner before using it.
2. Program the spinner recipe as follows: (Step 1) 500rpm at 3 acceleration for 10s and (Step 2) 4500rpm at 5 acceleration for 30s. Typically, the parameters of Step 1 of recipes are kept the same. The parameters of Step 2 would determine the thicknesses and properties of the PR coating. Several recipes with their exposure and development parameters are summarized in Table A.1.

3. Load the wafer onto the spinner and center it. Turn on the spinner vacuum.

4. Blow the wafer using a Ni gun to remove particles. Pour Shipley 1827 directly onto the center of the wafer to cover 1/3 of the wafer. Close the lid and start the spinner immediately.

5. Open the lid quickly when spinning is done. Cover the wafer with your hand as you open the lid to prevent PR from dripping onto it.

6. Pick up the wafer with your hand, only contacting the rim. Do not use tweezer as it leaves a mark into wet PR.

7. Soft bake the wafer in 90°C oven for 20 mins or using a hotplate at 110°C for 5 mins.

8. Use Acetone and cleanroom wipes to clean the spinner after using it.

A.1.2.4 Spin Coating of AZ4620

1. Use Acetone and cleanroom wipes to clean a Laurell spinner before using it.

2. Program the spinner recipe as follows: (Step 1) 500rpm at 3 acceleration for 10s and (Step 2) 2000rpm at 5 acceleration for 30s. More recipes with theirs exposure and development parameters are summarized in Table A.1.

3. Load the wafer onto the spinner and center it. Turn on spinner vacuum.

4. Blow the wafer using a Ni gun to remove particles. Directly pour AZ4620 onto the center of the wafer to cover 2/3 of the wafer. Close the lid and start the spinner.

5. Open the lid quickly when spinning is done. Cover the wafer with your hand as you open the lid to prevent PR from dripping onto it.

6. Pick up the wafer with your hand, only contacting the rim. Do not use tweezer as it leaves a mark into wet PR.

7. Soft bake the wafer in 90°C oven for 30 mins or using a hotplate at 110°C for 10 mins.

8. Use Acetone and cleanroom wipes to clean the spinner after using it.

Table A.1: Process parameters for Shipley1827 and AZ4620 lithography

Photoresist	Thickness	Spinning coating parameters	Exposure	Development
Shipley1827	3μm	4500 rpm, accl 5, and 30 secs	20s	20s
Shipley1827	3.5μm	3500 rpm, accl 5, and 30 secs	25s	30s
Shipley1827	4μm	2500 rpm, accl 5, and 30 secs	30s	40s
AZ4620	6μm	2500 rpm, accl 5, and 40 secs	40s	60s
AZ4620	8μm	2000 rpm, accl 5, and 40 secs	55s	90s
AZ4620	10μm	1500 rpm, accl 5, and 40 secs	70s	120s

A.1.2.5 Exposure

1. (Optional) Rest the wafer at room temperature with humidity of 40% for 30 mins to rehydrate the AZ4620 PR. This step is useful for thick PR development. Insufficient PR film rehydration will need a higher exposure dose and longer development time, or worse, complete development may not be achieved.

2. Load mask in the Karl Suss MA6 Mask Aligner. Turn on vacuum hold, blow Ni, and insert mask (protect the mask use your hands during this step). If a plastic mask is used, stick mask onto an empty glass mask and proceed as usual.

3. Do lamp test for Ch2 until the power stabilizes at 10W. Repeat this step several times.

4. Edit exposure time as listed in Table A.1 and set the contact gap to 25 μm. If using vacuum contact, set the parameters to 8s, 4s, and 8s. Hard contact can be used for AZ4620. For Shipley1827, only soft contact can be used.

5. Insert the wafer and blow Ni. Align the mask and wafer using either top-side or back-side alignment. It is recommended to at least perform a rough alignment before exposure.

6. Start the exposure process. Do not look directly at the UV light. Oversee the output power during the exposure.

7. Unload the wafer and mask when the process is done.

A.1.2.6 Developing

1. (Optional) Rest the wafer at room temperature with humidity of 40% for 30 mins to rehydrate the AZ4620 photoresist again.
2. For AZ4620, prepare a diluted AZ400K developer bath using the water-to-developer ratio of 4:1 and mix the solution well with a tweezer. For Shipley1827, prepare a pure MF319 developer bath.
3. Prepare a DI water bath.
4. Place the wafer into the developer bath, time the process as listed in Table A.1.
5. When all exposed PR cleared up (especially the center area), quickly remove the wafer from the developer bath and dip it into the DI water bath. Rinse it under running water.
6. Blow dry the wafer and check complete development under a microscope. The exposed region should be cleared up without light slash marks, allowing the underlying Si or Oxide substrate to be seen. Repeat Steps 3 - 6 until the PR is fully developed, especially for a thick PR coating (>10μm).
7. (Optional) Hard bake the wafer after developing at 120°C for 20 mins would round the edges of the PR features and improve the resistance during DRIE.

A.1.3 Remarks

1. The PR layer's thickness varies from center to fringes. The center part is always thicker than the fringes.
2. The thicker PR coating would result in edge-bead on the fringe area. It can be removed using a razor blade or AZ EBR solvent.
3. Several imperfections of PR coating are shown in Fig. A.1. Fig. A.1(a) shows an off-centered spinning coating and an off-centered exposure. Fig. A.1(b) causes by over-exposure or failure to use soft contact mode for Shipley1827. The line marks from the center to fringes

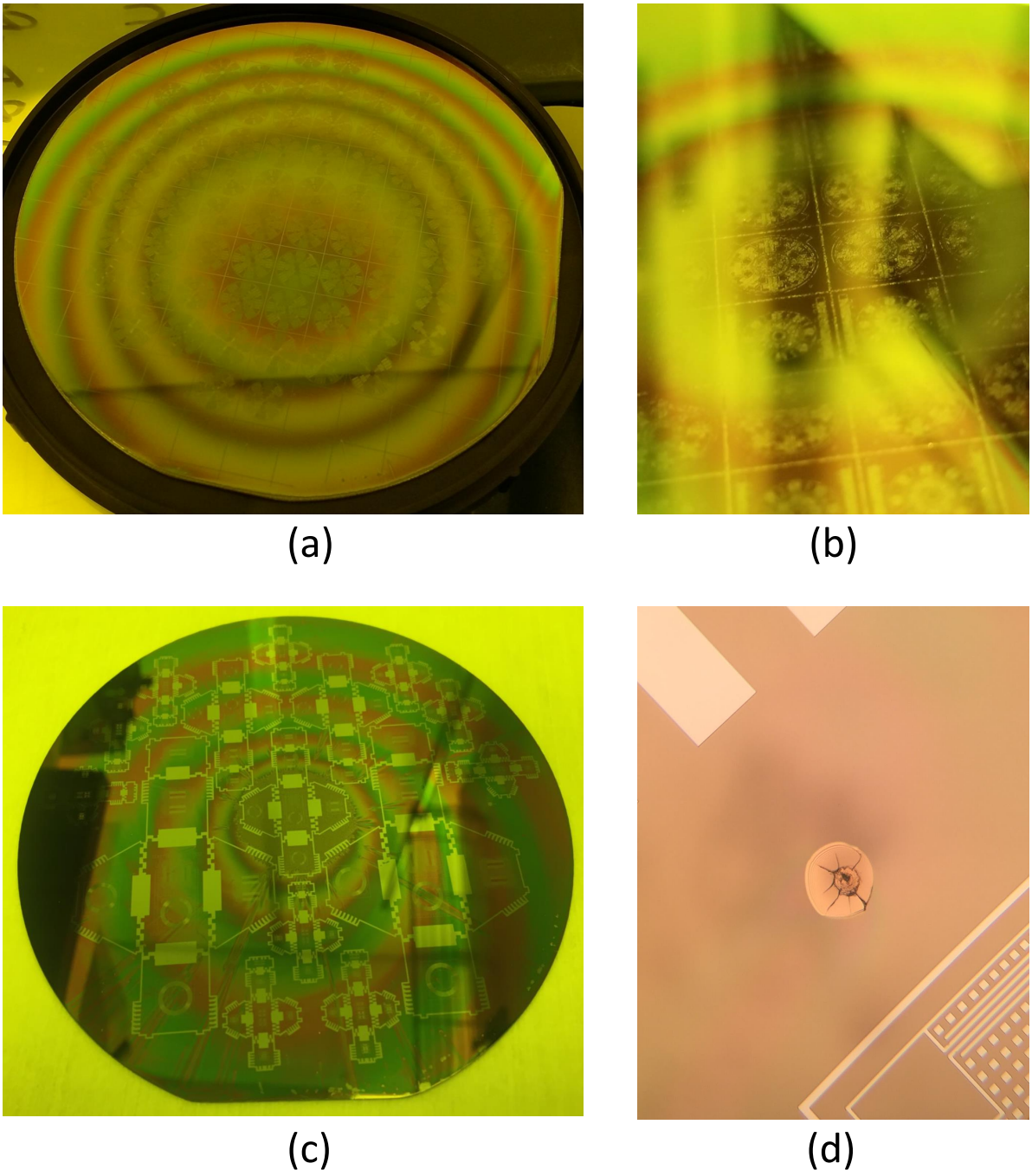

Figure A.1: Pictures of the imperfections of photoresist coating.

of the wafer in Fig. A.1(c) are due to over-pouring of Shipley1827. A circular or irregular mark on the PR coating is typically caused by the residue, dust, or contamination on the surface of the wafer before applying the PR or due to the air bubbles inside the PR liquid. An example is shown in Fig. A.1(d).

4. Over-developing or under-developing is easy to happen if the wafer is immersed for slightly longer or shorter than needed. It is always better to be conservative and check several times for optimal PR coating under a microscope. Typically, an over-red developer bath after developing would indicate the over-developing. On the contrary, a clean developer bath after developing would indicate the under-developing.
5. It is hard to control the developer time if an old developer bath is used. Do not over-used the developer bath.

A.2 Standard SOI Sensor Fabrication Process

A.2.1 Purpose

This process is used in the fabrication of SOI inertial devices, which includes the metallization, lithography, hard mask patterning, DRIE of device layer, dicing, cleaning, and HF vapor release. Please acquire training and access for all the required equipment involved in the entire process first.

A.2.2 Process

A.2.2.1 Metallization

A 50/500 nm Ti/Au or Cr/Au layer is required on the backside for a SOI sensor in order to allow for LCC vacuum packaging. The metal coating could be preformed using an E-beam Evaporator. Load the SOI wafers upside down so that the metal layer would attach to the Si side of the wafers. Allow the wafers fully cooling down before venting and unloading. Use a

photoresist layer to define the backside bonding pads and alignment marks. The lithography process is described in Section A.1. After wet etching of the metal layers, the photoresist layer needs to be removed using Acetone and IPA method or AZ 400T stripper method as described in Section A.1. A wafer-level Piranha cleaning is optional at this point, described in Section A.3.

A.2.2.2 Oxide Hard Mask Etching

The process starts with lithography of the Oxide hard mask. The photoresist mask is spin coated onto the SOI wafer using the 2μm Shipley1827 recipe and following the processes described in Section A.1. Backside alignment is required during the exposure step using MA6.

1. Clean the SPTS APS PM chamber using "O2 Clean" recipe for 30 mins before loading the SOI wafer.

2. Wipe the backside of the SOI wafer (if needed) before place the wafer in SPTS chamber. Etch for about 8 mins using the "UCI SiO2 PR" recipe until the unprotected Oxide layer is removed completely.

3. Remove the photoresist hard mask using Acetone and IPA method or AZ 400T stripper method as described in Section A.1, followed by a wafer-level wet cleaning using Piranha solution, described in Section A.3.

A.2.2.3 DRIE of Device Layer

1. Clean STS DRIE chamber using "O2 Clean" recipe for 30 mins before loading the SOI wafer.

2. Place wafer into STS, gently blow N2 to remove dust particles. Etch using the "Procesam"

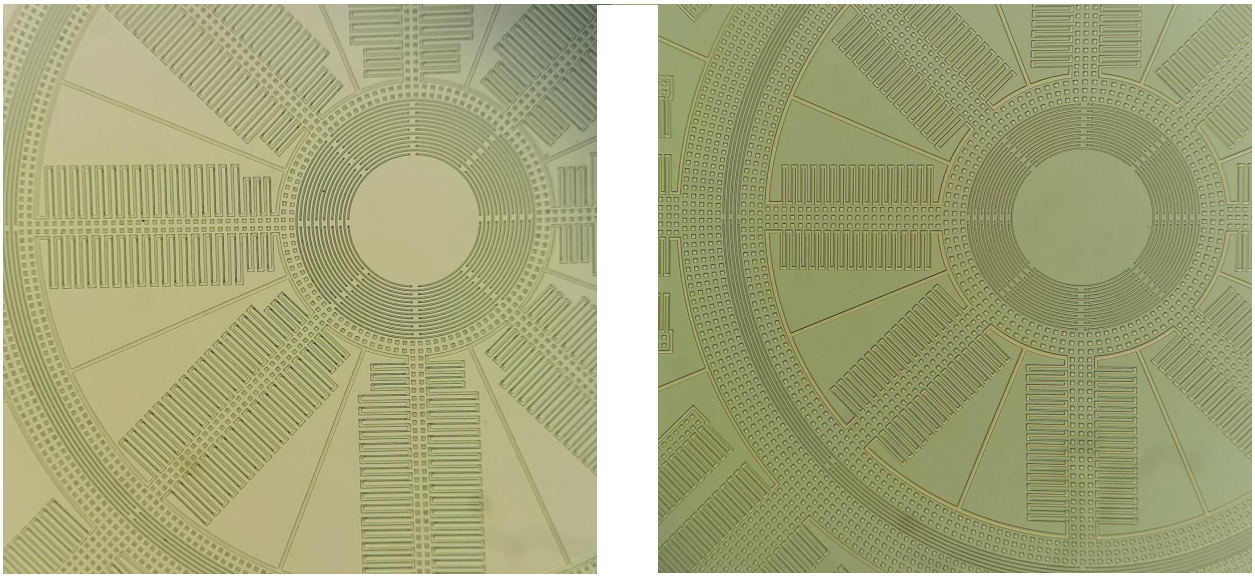

Figure A.2: Examples of (a) an under-etched SOI resonator with black marks in its capacitive gaps and (b) a fully-etched SOI sensor. The images were taken by a Leica DM4 B microscope using 5X lens.

recipe.

3. Time to etch 100 μm Silicon layer using "Procesam" recipe is approximately 45 mins, but actual value changes over time and depends on the sensors features. Run only 40 mins of "Procesam" recipe first and unload wafer to observe the gaps. If the etching wasn't complete, add 1 or 2 mins DRIE based on the observation, as shown in Fig. A.2, until all the gaps are clean and fully etched. Time to etch 50 μm Silicon layer using "Procesam" recipe is approximately 22 mins. Run only 18 mins of "Procesam" recipe for the first time and unload wafer to observe the gaps. If the etching wasn't complete, add 0.5 or 1 mins DRIE based on the observation until all the gaps are clean and fully etched.

A.2.2.4 Wafer Dicing

Wafer dicing in UCI using DISCO DAD3220 requires a protective layer on top of the device features. This can be conducted by attaching the device layer onto the dicing tape and dic-

ing from the bottom side, covering the device surface using a layer of dicing tape and dicing from the upper side, or spin-coating a photoresist layer onto the device surface. If a dicing tape is attached to the device layer, use an Acetone bath to remove the tape and followed by IPA and water baths. **Do Not** rip off the tape directly. It would damage the structures. However, using a photoresist layer as protection would be preferable for SOI inertial sensors.

1. Dehydrate the SOI wafer in the clean dehydration furnace at 120°C for >45 minutes.

2. Use aluminum foils to build a storage area with a cover. Use aluminum foil to form a stand to hold the wafer from center point so that the fringes would hang in the Step 8.

3. Apply HMDS as described in Section A.1.

4. Program the spinner recipe as follows: (Step 1) 400rpm at 3 acceleration for 10s and (Step 2) 400rpm at 3 acceleration for 10s.

5. Load the wafer onto the spinner and center it. Turn on the spinner vacuum.

6. Directly pour Shipley1827 onto the center of the wafer to cover all surface of the wafer. Close the lid and start the spinner.

7. Open the lid quickly when spinning is done. Pick up the wafer with your hand, only contacting the rim.

8. Place the wafer onto the aluminum foil stand made in Step 2 and cover it. Let the wafer stay in the storage overnight so that all the gaps on the device layer would fill with photoresist.

9. Soft bake the wafer in 60°C for 20 mins using a hotplate, increase the temperature to 80°C for 20 mins, and then increase the temperature again to 90°C to fully dry the photoresist before dicing.

A.2.2.5 Die-Level Cleaning and HF Vapor Release

After dicing of the SOI wafer, an individual die-level wet cleaning has to be conducted. If a photoresist layer was used as the protection during dicing, use AZ 400T photoresist stripper bath to fully remove all photoresist first. Place the sensor dies into the **new** AZ 400T bath and cover the container. Heat it up to 100°C to speed up the process. It may take about 1 hour of the process. Place the sensors into several DI water baths to clean AZ 400T. Conduct the die-level Piranha cleaning of the devices as the process described in Section A.3. Place the cleaned devices into new petri dishes. It is optional to perform a 20 mins "O2ASH200" using a Plasma-Therm 790 RIE followed by another run of Piranha cleaning. This step might hypothetically improve quality factor by cleaning polymer residues caused by the DRIE step.

The oscillatory structure of SOI devices will be then released using a HF Vapor Phase Etcher. Program the vapor etcher to 49°C and place the sensors onto the sample holder. Place the holder onto the HF container. Time to release 5 μm Oxide layer is approximately 90 mins. Add more time if it is necessary. Use IR Microscope to make sure that the moving structures are fully released. Two examples are shown in Fig. A.3. **Do not** over-release the anchors and electrodes. It might lead to damage the structures during wire-bonding.

A.2.3 Remarks

1. Oxide etching in SPTS would burn the photoresist hard mask if you etch longer at a time. The 1.5 μm Oxide layer should be fully etched in 30 mins. However, the etching program may fail due to bad condition of the SPTS.
2. For DRIE of Si device layer, "Process b" recipe can also be used. It has a faster etch rate compared with "Processan" but results in a worse uniformity and surface roughness.
3. Typically, over-etching of DRIE would lead to a large frequency mismatch of sensors, and

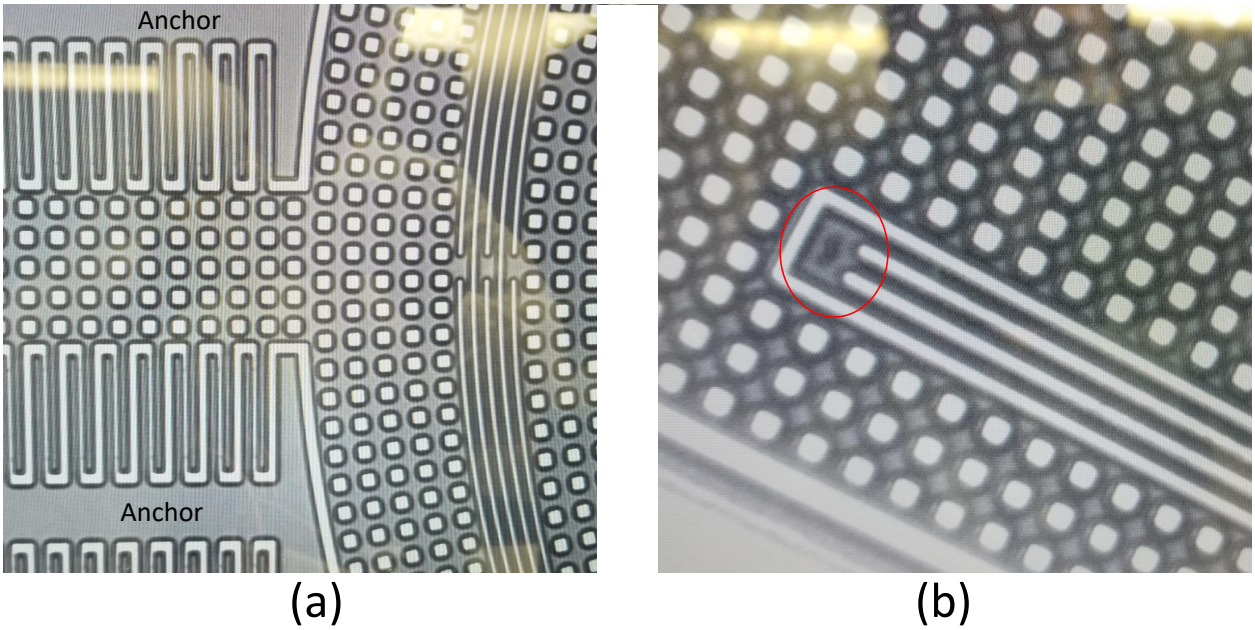

Figure A.3: (a) Example of a SOI sensor after 30 min HF release. There is no difference between the two anchors and sensor's proofmass. (b) A under-released device after 80 mins HF release with the remained Oxide substrate that high lights in a red box.

under-etching would short the testing circuit and no oscillatory behavior may be observed.

4. During STS DRIE, the machine would leave a circular mark on the backside of the wafer. A handle wafer or blue tape would prevent the mark. If a blue tape is attached onto the wafer, it is necessary to cut the tape to the size of the wafer size so that DRIE would not attack the tape during etching.

A.3 Wafer-level and Die-level Wet Cleaning Recipes and Protocols

A.3.1 Purpose

Wet cleaning of Wafers and dies is a critical step in inertial sensor fabrication process. Piranha cleaning and RCA-1 cleaning are the two most common processes that can be concluded for both wafer-level and die-level. Piranha cleaning is typically stronger compared to RCA-1 and is able to remove dust, photoresist residues, polymer, Cu, and any contaminants on the surface from previous fabrication steps. RCA-1 cleaning, on the other hand, is required for some specific surface treatments. Aqua Regia cleaning is even stronger than Piranha solution and can attack gold. Please acquire training and access for all the required equipment involved in the whole process first.

A.3.2 Process

Wet cleaning containers and tools are located in a cleanroom box as shown in Fig. A.6(a). **Only** use those containers to conclude wet cleaning process.

1. Place several cleanroom wipes on a wet cleaning bench and rinse the container that would use in the process. After rinsing them, place the containers upside down on a new wipe before using them.

2. Prepare a hot-plate and change aluminum foil.

A.3.2.1 Mixing Solutions

For Piranha cleaning, add 1 to 2 parts of 98% Sulfuric Acid (Orange cap) into a 5 inches container. Then **slowly** pour in 1 part of 30% Hydrogen peroxide (in a cleanroom refrigerator) into the container. Place the container onto the hot-plate and heat up the solution to about 120°C. The samples, wafers or dies to be cleaned can be placed in the solution anytime after the solution has been mixed. The cleaning period is about 15 mins. **Only** use metal tweezers in Piranha solution. **Do not** boil the solution. The portion of Hydrogen peroxide **can not** be more than Sulfuric Acid.

For RCA-1 cleaning, add 5 parts of DI water into a 5 inches container. Then add 1 part of 27% Ammonium Hydroxide (green cap) into the container. Place the container onto the hot-plate and heat up the solution to 70 to 75°C. Then add 1 part of 30% Hydrogen peroxide (in a cleanroom refrigerator) into the container. Place the samples, wafers or dies to be cleaned, in the solution and keep the solution around 70 to 75°C during the cleaning. The cleaning period is about 15 mins.

For Aqua Regia cleaning, add 3 parts of 98% Hydrochloric Acid (blue cap) into a 5 inches container. Then **slowly** pour in 1 part of Nitric acid into the container. Place the container onto the hot-plate and heat up the solution to about 100°C. The under-cleaning samples can be placed in the solution anytime after the solution has been mixed. The cleaning period is about 15 mins until no yellow gas is observed. Noted that the Aqua Regia solution is very strong and dangerous. **Only** use metal tweezers in Aqua Regia solution. **Do not** boil the solution.

A.3.2.2 Solution Cleaning

1. After the cleaning step is completed, slowly take the samples out of the solution. Immediately place the samples into a DI water bath.
2(a). For wafer-level cleaning, rinse the wafer individually under running DI water and then place the wafer into another new DI water bath. Rinse the tweezer. Change the water for the first bath and rinse the water container. Take out the same wafer from the second DI water bath and then rinse it under running water again. Place it into the new water bath and rinse the tweezer. This cleaning cycle has to be repeated at least twice before blow drying the wafer. Two methods can be used to blow dry wafers, as shown in Fig. A.4. Place the wafers into a wafer holder in a clean dehydration oven at 120°C for 20 mins.
2(b). For die-level cleaning, use a plastic tweezer to transfer the samples to the second DI water bath for 5 mins. Rinse the tweezer. Change the water for the first bath and rinse the water container. Place the samples into the new water bath for 5 mins. Repeat this step at least twice. Prepare a clean container and a lid. Change gloves and use clean aluminum foil to cover the inner surface of the container and lid. Place the wet samples into the container and bake them into a clean dehydration oven at 120°C for 20 mins.

A.3.3 Remarks

1. During the wet cleaning of die-level, the samples would move and bump into each other. Figure A.5 shows two dippers that can be used to clean small samples to prevent the issue.
2. Figure A.6 shows an example of wafer-level cleaning. A wafer holder made out of Teflon can be used, as shown in Fig. A.6(c). The wafer and holder should be placed in to solution as shown in Fig. A.6(d). Typically, leave the very bottom level empty and insert wafers starting from the second slot.

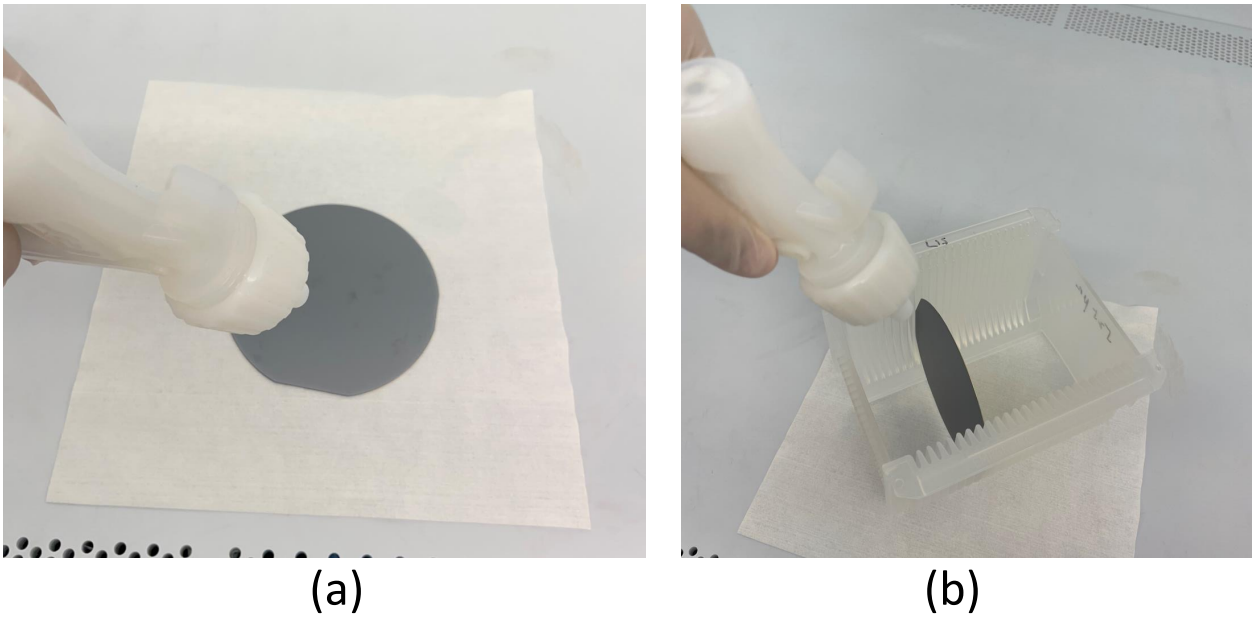

Figure A.4: Methods of wafer-level blow drying.

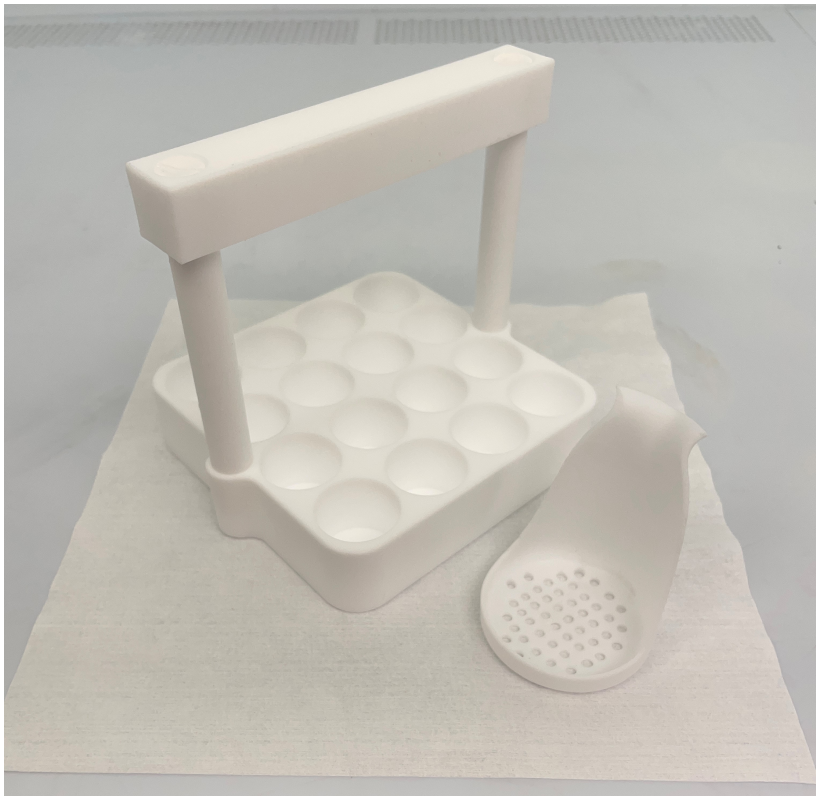

Figure A.5: Teflon dippers for small samples wet cleaning.

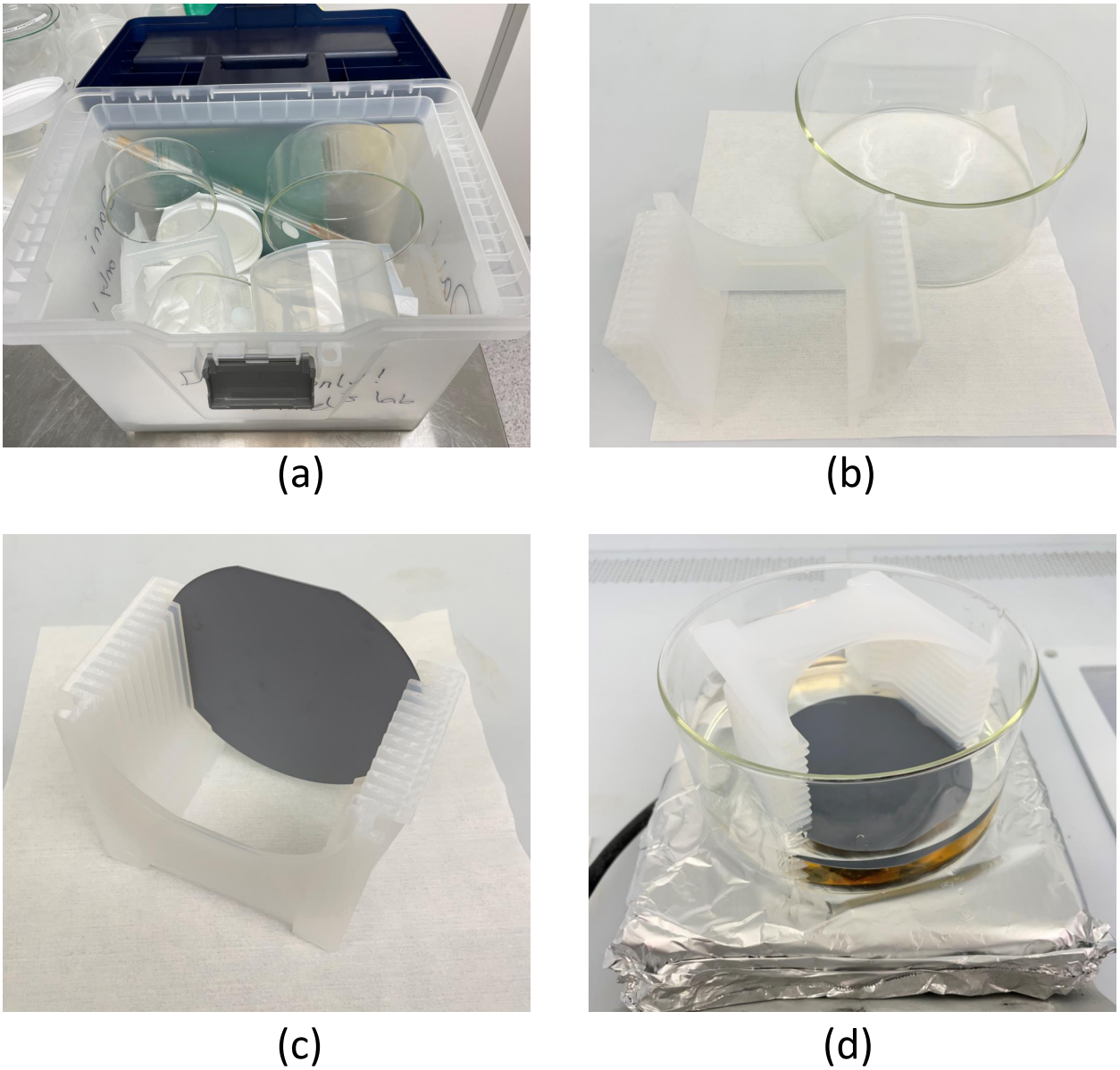

Figure A.6: Illustration of wafer-level wet cleaning.

A.4 Fused Silica Sensor Annealing

A.4.1 Purpose

This process is used in the fabrication of Fused Silica (FS) micro-shell resonators for the improvement of quality factors. Due to a non-isothermal and rapid cooling of the glass-blowing process in the fabrication, significant thermal stresses would result in an increase in

mechanical energy loss. Appropriate thermal annealing would reduce the internal stresses. Please acquire training and access for the annealing tube furnace used in the process first.

A.4.2 Process

The glassblown shell resonators can be thermally annealed in a Thermco 3000 annealing tube furnace with controlled heating and cooling rates. Sample cleaning is critical before this annealing process. Remove all metal coating and other residues first. Piranha cleaning should then be conducted.

1. Load micro-shell resonators on the sample holder. Two methods could be used as illustrated in Fig. A.7(a) and (b). The advantage of the second method is to prevent contamination from the tube by adding a cap wafer on the top of the holders.
2. Load the holder at the middle of the annealing tube.
3. Set the ramp to 950°C with 3°C/min heating rate.
4. Set the annealing at 950°C for 9 hours under continuous N2 flow.
5. Set the cooling rate to 400°C at 0.1°C/min.
6. Turn off the controlled cooling and cool down to room temperature before unloading the holder.

A.4.3 Remarks

1. Cover the sample holder using aluminum foil to keep it clean. A dirty holder would contaminate both the annealing tube and the samples.
2. The annealing tube needs to be cleaned regularly. Please contact the staff to conduct this step if required.

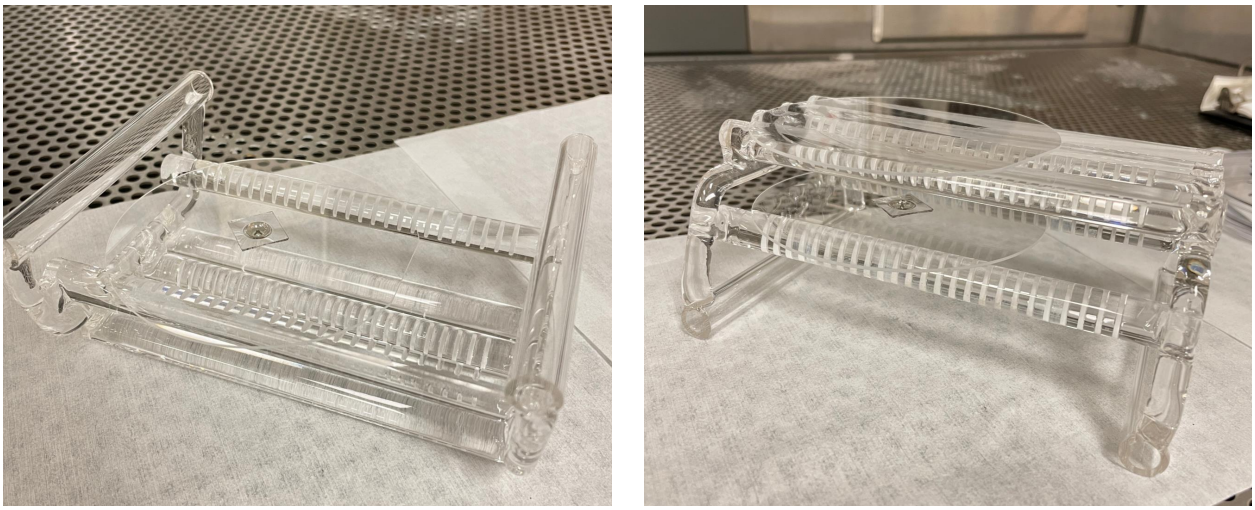

Figure A.7: Illustration of the setup and sample holder of micro-shell resonators used in the annealing process.

A.5 Silicon-in-Glass Re-flow Process

A.5.1 Purpose

This process is used in the fabrication of through-glass-vias stages for 3D encapsulation of FS dual-shell resonators and SOI planar sensors. It is a reverse process of high-temperature glassblowing. It takes advantage of the drop in viscosity of glass material and the low-pressure condition or vacuum in the pre-etched cavity to form Silicon-in-Glass vias at high temperature. Please acquire training and access for all the required equipment involved in the whole process first.

A.5.2 Process

A.5.2.1 Deep Etching of Si wafer

The process starts with a double-side polished 500 μm Si wafer with ultra-low resistivity.

1. Attach a handle wafer using a layer of photoresist or thermal oil to the Si wafer. A >6μm layer of Photoresist layer can be used in this step. Using a drop of thermal oil would be preferable. Set a hotplate to 110°C and place the handle wafer on top of it. Apply a drop of the oil at the center of the handle wafer. Place the Si wafer on top of the handle wafer and bake the stack for 5 mins.

2. Apply a layer of photoresist as the hard mask for the Si wafer. The photoresist layer with at least 15 μm thick would be sufficient to etch about 350 μm in depth for Si wafers. A double-layer AZ4620 photoresist can be spin coated onto the Si wafer with a short soft-bake period in between. The photoresist mask is then defined using lithography with a double-exposure duration described in Section A.1.

3. Load the Si stack into STS DRIE and etch using the "Process B" recipe.

4. Measure the etch depth in the middle and at the edge of the Si wafer using DEKTAK until the desired etch depth is achieved. The remaining thickness of the Si wafer should be greater than 120 μm.

5. Remove the handle wafer by placing the wafer stack on top of a hotplate with a temperature of 110°C for about 5 mins. Gently twist the Si wafer to separate the two wafers.

6. Remove the photoresist hard mask using an AZ 400T photoresist stripper bath and rinse the wafer under running DI water before blow drying it.

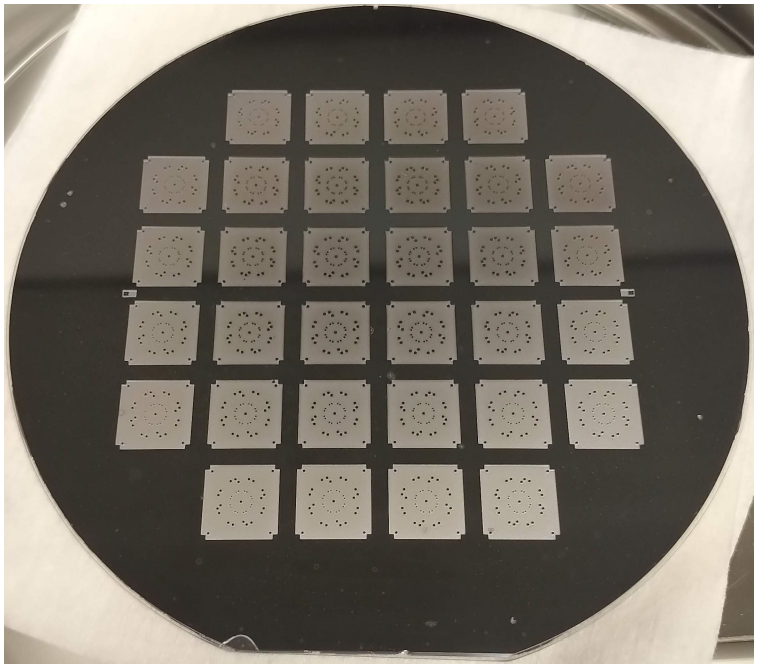

Figure A.8: A picture of the Glass-Si wafer created by the anodic bonding process.

A.5.2.2 Anodic Bonding

1. The Borofloat 33 glass and etched Si Wafers must be thoroughly cleaned before they are bonded. Piranha cleaning and RCA-1 cleaning should be conducted in sequence. After cleaning, blow dry the glass wafer and use the dehydration oven to dry the Si wafer.

2. Place the two wafers into two fresh (new) 5 inches petri dishes and load them inside an AML-AWB wafer bonder. The glass wafer should be loaded on the upper platen.

3. Perform the anodic bonding at vacuum condition and set the contact force to 500N. Gradually increase the bonding voltage and temperature to 600V and 370°C.

4. Turn off the heaters and voltage supply when the bonding process is completed. The total charge during bonding is linearly dependent on the contacted area. The total charge of 4 inches wafers bonding should be around 1500 to 2000 mC.

5. Unload the bonded wafer stack when the temperature is back to room temperature. An example of a bonded Glass-Si wafer is shown in Fig. A.8.

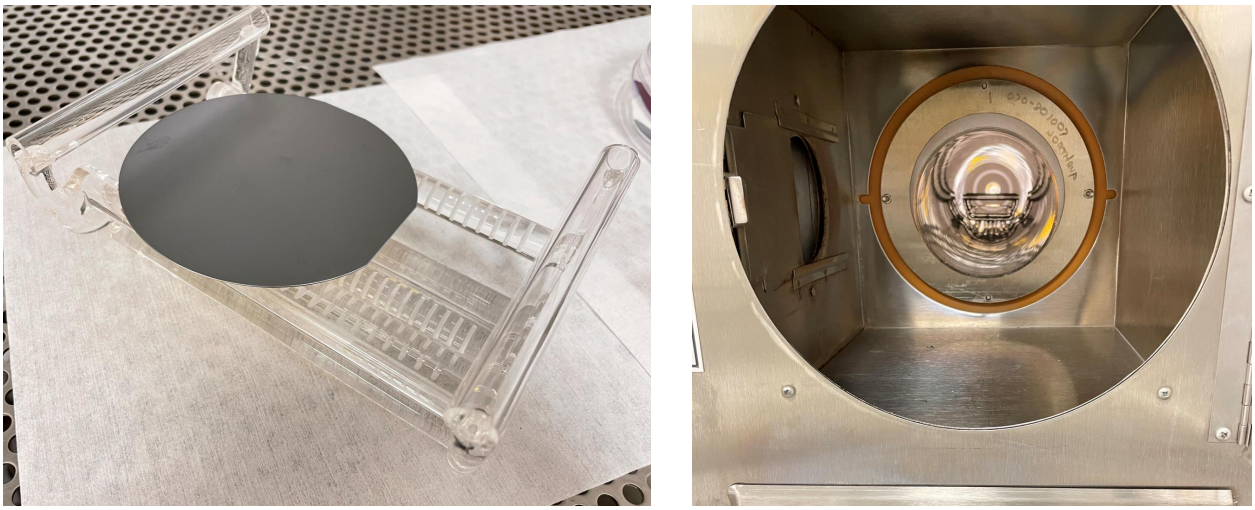

Figure A.9: Illustration of the setup and sample holder used in the glass re-flow process.

A.5.2.3 High Temperature Glass Re-flow Process

1. Place the bonded stack on the holder with the glass side face-up, as shown in Fig. A.9(a).
2. Load the holder with the stack to the middle of the annealing tube, as shown in FigA.9(b). The reverse holding method can be used in this step too, as shown in Fig. A.7(b).
3. Control the tube temperature as the program shown in Fig. A.10.
4. Turn off the temperature control when the temperature is below 400°C.
5. Unload the wafer when the temperature reaches room temperature.

A.5.2.4 Wafer-level Lapping

1. Spin coat a layer of photoresist on the Si-side of the bonded stack after glass re-flow.
2. Place the stack onto a 4-inch wafer holder and let the photoresist layer attach to the holder, as shown in Fig. A.11(b).
3. Press down the stack with a lightweight and soft-bake the holder on a hotplate at 150°C.
4. Calibrate the Allied High Tech Lapping machine before any wafer-level lapping.

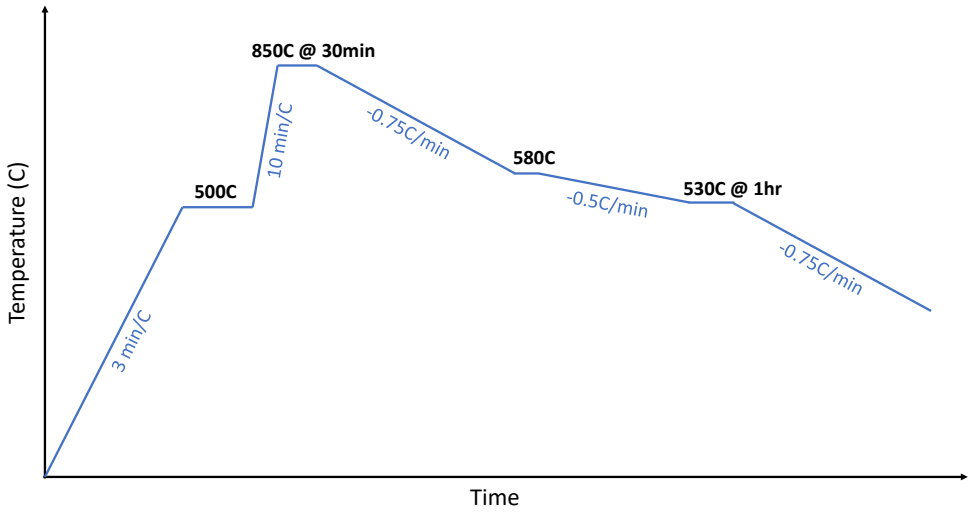

Figure A.10: The temperature profile of the annealing tube for glass re-flow.

5. Lap the wafer using a 30 μm diamond lapping film (green) until the Si surface is exposed. This step may take about a few hours. Do not press down the lapping holder too much. It may lead to detach the wafer from the holder.

6. Place the cloth lapping pad on the machine and apply 3 μm diamond slurry on the lapping pad. Continue lapping the wafer until an obvious change in the surface quality is observed.

7. Use 0.5 μm diamond slurry to perform a fine polish on the wafer.

8. Place the holder in an Acetone bath until the wafer is separated from the holder.

9. Do solvent clean (Acetone and IPA) of the wafer and rinse it under DI water.

A.5.3 Remarks

1. It is key to cool down the tube correctly. Failure to do so would lead to the following results, as shown in Fig. A.11. The issue shown in Fig. A.11(a) is due to leakage. For Fig. A.11(b) and (d), the incorrect cool-down step was performed. An annealing step (>30 mins) is needed to be executed around 530°C with a slow cooling rate around 580 to 530°C. Besides, unloading the wafer too early (>60°C) would result in a broken wafer, as shown in Fig. A.11(c). An appropriate glass re-flow process would result in a wafer shown in Fig.

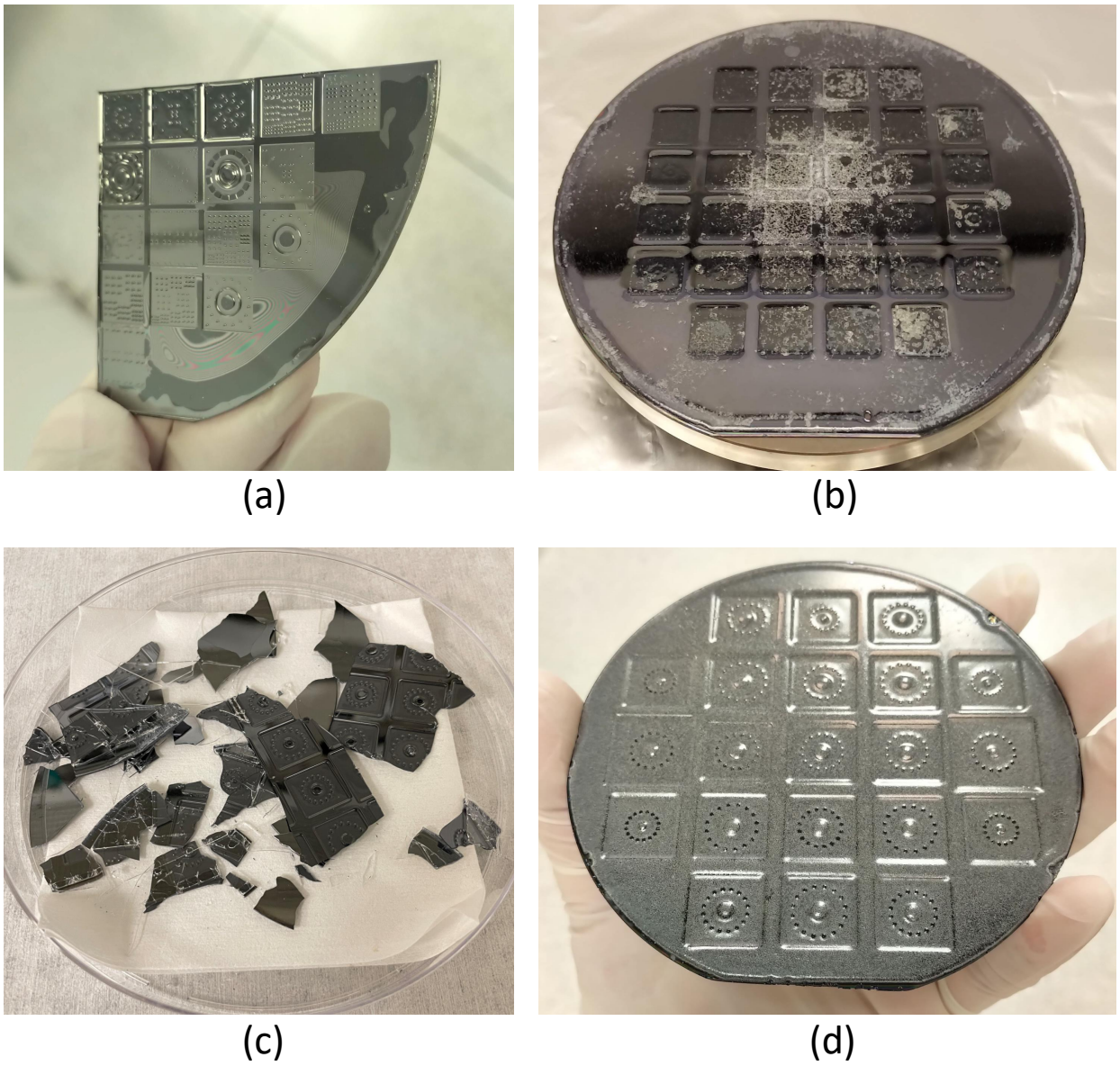

Figure A.11: Pictures of the failures of the glass re-flowed wafers.

A.12.

2. Do not use a diamond lapping film with <30 μm diamond size to lap the wafer. It would detach the wafer from the holder.

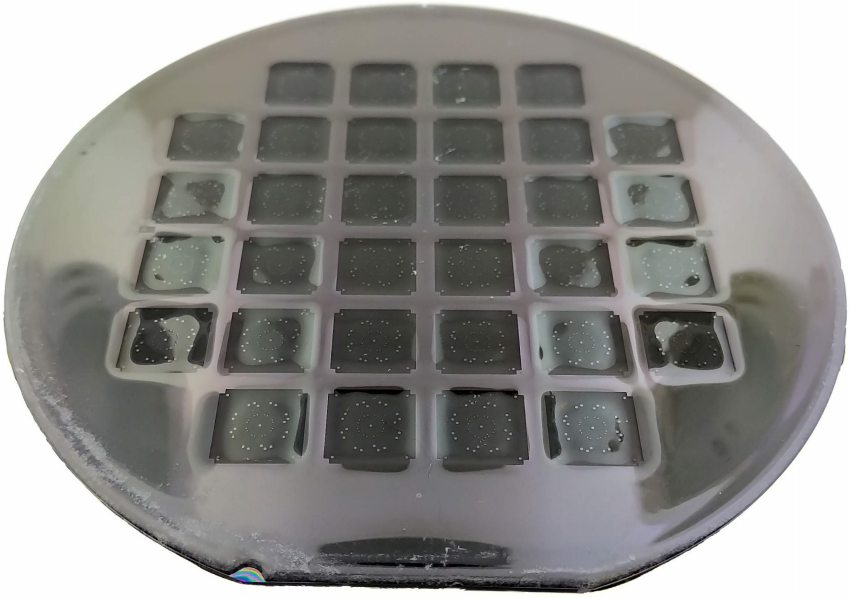

Figure A.12: A picture of the Silicon-in-Glass wafer formed by the proposed glass re-flow process.

A.6 Wet Etching of Glass Wafer

A.6.1 Purpose

This process is used to wet etch glass wafers to create vias or cavities for through-glass-vias. Please acquire training and access for all the required equipment involved in the whole process first.

A.6.2 Process

A.6.2.1 Preparation

For Borofloat or Pyrex wafer, a Cr/Au or Ti/Au metal layer with a thickness of 100/100 nm is sufficient as a hard mask for a fast and shallow wet etching process. The features on the hard mask could be patterned using a photoresist layer and metal etchant.

Table A.2: Process parameters of BOE and HF wet etching of glass

Solution Parameters	Etching Rate (μm/hr)
BOE 10 mL + HCL 20mL + DI water 170 mL	2.667
BOE 35 mL + HCL 70mL + DI water 170 mL	7.5
2% HF 200 mL + HCL 50mL	10.5
5% HF 200 mL + HCL 70mL	12
6% HF 200 mL + HCL 70mL	25.5
9% HF 200 mL + HCL 90mL	40

A.6.2.2 Wet Etching

A Pyrex container can perform the wet etching of Borofloat or Pyrex wafer using the thin-film metal hard mask. Both BOE and diluted HF solution can be used in this process. It is necessary to work with fresh HF or BOE solutions. The recycled solution will result in a reduction in the etching rate. Few example recipes are listed in the Table A.2. Adding HCL solution would help with the uniformity of wafer-level etching. Covering the container with a lid during the etching could prevent evaporation. **DO NOT** directly rinse the wafer under running DI wafer if the wet-etching process wasn't completed. The running water would damage the hard mask due to isotropic wet etching. Placing the wafer gently into several DI water baths could clean the residues of HF solution. **DO NOT** blow dry the wafer. It would also break the metal hard mask. Use the dehydration oven to dry the wafers (10 mins should be sufficient).

A.6.2.3 Hard Mask Removal

1. Dip the wafer into the metal etchant to completely remove all the metal hard masks.
2. Place the wafer into a DI water bath and rinse under DI water.
3. Use the dehydration oven to dry the wafer.

A.6.3 Remarks

1. Using a metal hard mask would result in micro-trenches and could peel off easily during a long etching process.
2. The etch rate varies over time.
3. Placing the container onto a shaker during the etching could improve the etching uniformity.

A.7 Wet Etching of Fused Silica Wafer

A.7.1 Purpose

This process is used to wet etch Fused Silica (FS) wafers to create cavities for high-temperature glass-blowing. This is the first step in the fabrication of FS dual-shell wineglass resonators. Please acquire training and access for all the required equipment involved in the whole process first.

A.7.2 Process

A.7.2.1 Poly-Si Hard Mask

Poly-Si hard masks for wet etching of FS wafer are required. A layer of 2 μm undoped Poly-Si should be sufficient as a hard mask. The features could be defined using a photoresist layer and followed by RIE Si etching in a Plasma-Therm 790. The unprotected 2 μm Poly-Si region can be removed by running 3 mins of the process named "SF6O2SH". Be very careful with the Poly-Si hard mask during the entry process. Any damage to the mask would be

transferred to the FS wafer during the wet etching process. After etching of Poly-Si layer, the wafer needs to be cleaned, and the photoresist residue has to be removed. Using AZ 400T photoresist stripper bath would be preferable, followed by DI water rinsing. The alternative method is to use solvent cleaning (Acetone and IPA).

A.7.2.2 Wet Etching

1. Pour 300 mL 49% HF into the Teflon container about half-full. The solution should be fresh. Be very careful during the process and Open the DI water valve to keep water running in case of a splash.
2. It is necessary to protect the back side, mask one side of the FS wafer using one-sided dicing tape (blue tape). Peel off the blue tape and touch it at one edge of the wafer. Slowly work your way to the other edge till the whole wafer is covered with blue tape. (If bubbles form, you can peel back the blue tape a little bit and stick it again to remove the bubbles. Removing the air bubbles is not necessary. Removal of the blue tape could potentially damage the Poly-Si hard mask.) Once the blue tape sticks to the wafer nicely, take a razor blade to trim the tape to the edges.
3. Place the wafer into HF bath. Put the lid on the container and gently transfer the whole setup into a second container.
4. Etch for required duration. The typical etch rate is about 1.07 μm/min.
5. Remove the wafer gently and place it into several DI water baths.
6. Rinse the wafer under running DI water.
7. If a blue tape protects the wafer, place the wafer into an Acetone bath, and the blue tape will peel off by itself without damaging the hard mask, followed by IPA and water baths.
8. Blow dry the wafer or use the dehydration oven to dry the wafer.
9. If the etching process has to be suspended, gently remove the wafer and place it into several DI water baths. **DO NOT** directly rinse the wafer under running DI wafer and blow

dry the wafer. Use the dehydration oven to dry the wafers. If a blue tape protects the wafer, remove the tape first as described in Step 7 before drying it.

10. Measure the etch depth in the middle and at the edge using DEKTAK before the hard mask removal.

A.7.2.3 Poly-Si Removal

1. Prepare 400 mL 45% pre-mixed KOH solution.

2. Fill 200 mL KOH into each Pyrex container and mark the containers as #1 and #2. Put plastic meshes into each glass container, and these will lift the wafer so that the back side can be etched.

3. Place the containers onto a hotplate and wait for the solution to reach equilibrium temperature at 80 °C.

4. Perform solvent cleaning (Acetone and IPA) on the wafer and rinse it under DI water. Place the wafer into the #1 KOH bath. Do not mix solvents and KOH. Ensure that the wafer is thoroughly rinsed with DI water after the solvent clean.

5. For 2 μm Poly-Si layer, it takes approximately 6 minutes to visibly remove (making the wafer transparent). Wait for an extra 60 seconds until no dark spots is left on the wafer and take the wafer out.

6. Prepare the following setup before removing the wafer from the KOH solution: two DI water baths, an Acetone bath, and an IPA bath.

7. Once the wafer is removed from the first KOH bath, quickly do the following: Dump it into the DI water baths, rinse under running water, and do solvent clean (Acetone and IPA). Rinse it under running water and finally place it into KOH #2 bath.

8. Replace all the baths in Step 6.

9. Wait for 5 minutes and remove the wafer out of the KOH bath #2.

10. Repeat the rinsing and solvent cleaning in Step 7.

11. Blow dry the wafer and place it into a fresh (new) 5 inches petri dish.

A.7.3 Remarks

1. Measuring the etch depth using DEKTAK can damage the Poly-Si thin film. Make sure you take the measurement from the same point to minimize the damage.
2. The variation of etching depth in the whole wafer is usually as low as 0.1 μm. If you are seeing significantly higher variation, that means that the amount of HF solution used is not enough.
3. There are usually broken pieces of Poly-Si thin film inside the containers after this process. Try to remove them using cleanroom wipes, as they can contaminate future process.es
4. Keep the bonding side faced up during the entry process. Do not flip the wafer over and contact the cleanroom wipe.
5. If the FS wafers would be followed by plasma-associated bonding in the subsequent process, add 18 μm in depth during the etching since polishing would remove about 18 μm thickness from the surface.

A.8 Triple-stack Plasma-Aided Glass-to-Glass Wafer Bonding

A.8.1 Purpose

This process is used to bond three Fused Silica (FS) wafers to form triple-wafer stacks. This is a critical step in the fabrication of FS dual-shell wineglass resonators. The advantage of plasma-associated bonding is that no intermediate material is needed as the bonding interface. Thus, the triple wafer stack can survive under high temperatures. Please acquire

training and access for all the required equipment involved in the whole process first.

A.8.2 Process

A.8.2.1 Wafer Cleaning

Wafer cleaning is critical in this bonding process since the process is super sensitive to dust, Poly-Si residues, photoresist, or any contamination on the surface from previous fabrication steps. The bonding surfaces of the FS wafer must be polished and then thoroughly cleaned before they are bonded. The polishing step should be completed by the wafer vendor. Send the wafer back to the vendor for fine polishing. Executing the following cleaning steps in sequence to completely remove all possible residue on the bonding surface.

1. Solvent cleaning (Acetone and IPA)
2. Piranha cleaning
3. RCA-1 cleaning
4. After cleaning, store the wafers separately in clean Teflon wafer holders with DI water.

A.8.2.2 Surface Activation

1. Wipe the bench with Acetone and IPA thoroughly before operating and change gloves.
2. Blow dry one FS wafer by placing it on a clean wipe on the bench. Prepare a clean (new) petri dish with a cleanroom wipe folded inside the container to prevent stiction. Also, blow dry the tweezers before transferring the wafer inside the petri dish. Repeat the process for the second wafer. If it is the second bonding, use the dehydration oven to dry the stack.
3. Place two FS wafers into the chamber of a Plasma-Therm 790 RIE. Load the process named "O2SHKEL" for 3 minutes. Transfer the wafers back to the Petri dishes after the process is finished.

4. Rinse one of the wafers under running DI water for 1 minute in the bench. Then blow dry it as in Step 2. Place the wafer back into the Petri dish to avoid any dust contaminating the bonding surface. Repeat the process for the second wafer.

A.8.2.3 Wafer Bonding

1. Change gloves and place one wafer (preferably the thinner one) on a piece of clean wipe with the bonding surface faced up.
2. Take out the other wafer and flip it so that the bonding surface (activated surface) is at the bottom.
3. Gently place the second one on top of the first wafer.
4. Press the center of the top wafer with your hand. The bonding area will spread from the center to the fringes if the surfaces are clean. Work with the bubbles (unbonded area), and you can press the stack to squeeze and drive the air bubbles into a nearby cavity to improve the yield of the bonding area.

A.8.2.4 Wafer Bonding with Alignment

The surface activation is valid for about 30 minutes. The bonding step would be performed in an AML-AWB wafer bonder. Complete the loading, alignment, and bonding as fast as possible would improve the yield of the bonding process.

1. Change gloves and load two FS wafers in the AML bonder (preferably the thinner one on the upper platen). Both the bonding surfaces of the two wafers are faced up.
2. Set the height of the spring pin on the upper platen to about 100 μm so that the center of the upper wafer would contact the bottom wafer first.

3. Close the lid and align the upper and lower wafers.

4. After alignment, contact wafers and set the force to 100N. Then, switch to the "controlling manually" button.

5. Set the force to 500N and press the "controlling force" button. Then press the "controlling manually" button. Keep the wafers under this condition for 1 minute.

6. Unload the bonded wafers from the AML bonder. Noted that the bonding process is not complete yet.

7. Keep pressing the stack to squeeze the unbonded area manually to improve the yield.

A.8.2.5 Wafer Annealing

1. Place the stack at room temperature for at least one day before annealing.

2. Load the stack on a hotplate or AML wafer bonder. Set the temperature for annealing to 400°C with a ramp-up rate of 50°C/h. It is optional to use the AML wafer bonder for the first annealing of the triple-stack, but it is recommended to execute the second annealing process in the AML wafer bonder under the "controlling force" mode with 500N force.

3. Anneal the bonded stack for >1 day before removing it from the heat plate.

A.8.3 Remarks

1. If cavities were formed on the cap and substrate wafers, execute the bonding between the cap and device wafers first and then bond the stack to the substrate wafer. Otherwise, the bonding order does not matter.

2. Before surface activation, clean the chamber of the Plasma-Therm 790 using the process "O2ASH200" for at least one hour.

3. If the yield of bonding is lower than 80% for the first bonding and 40% for the second

bonding, it is an option to separate the two wafers and bond them again.

4. Perform the entire bonding cycle from wafer cleaning to annealing for the first bonding and then execute the circle again for the second bonding.

A.9 Selective Metallization of FS DSGs

A.9.1 Purpose

This process is to assemble a shadow mask to a FS dual-shell gyroscope for selective metallization. Please acquire training and access for all the required equipment involved in the whole process first.

A.9.2 Process

A.9.2.1 Shadow Mask Assembly

The details of the shadow mask assembly are shown in Fig. A.13.

1. Prepare the setup as shown in Fig. A.13(a). The vacuum-compatible tape is required.

2. Cut the dicing tape into two small rectangular shapes and attach them to the edges of the FS dual-shell resonator, as shown in Fig. A.13(b) and (c).

3. Match the size of the shadow masks to the device shell and place the shadow mask on top of the dual-shell sample.

4. Tape them together using vacuum-compatible tape. The final result is shown in Fig. A.13(d).

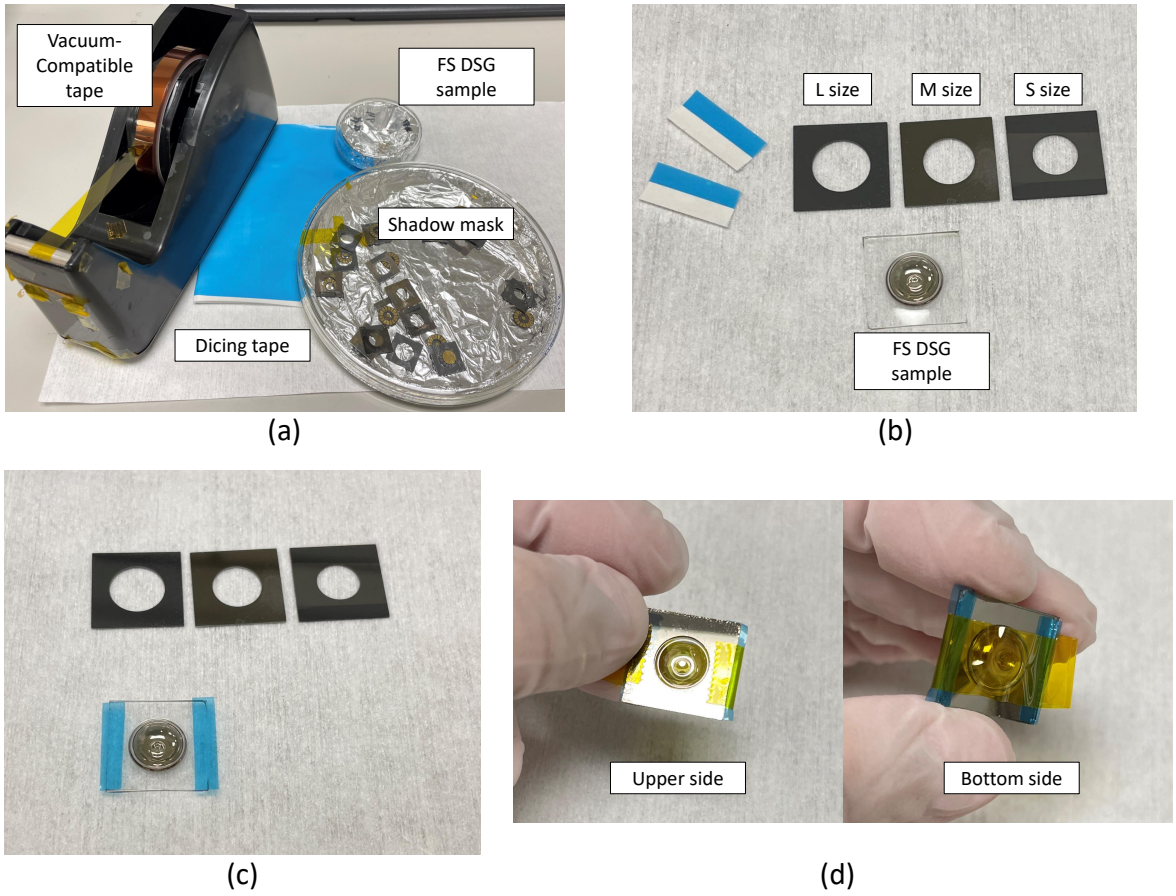

Figure A.13: Details of the shadow mask assembly.

A.9.2.2 Metal Deposition

The 3D metal coating can be performed using a sputter-coater or Angstrom evaporator. After the assembly between the shadow mask and dual-shell sample, the bonded stack would be loaded inside the deposition chamber, as illustrated in Fig. A.14. The vacuum-compatible tape is required during the process. Reverse the assembly steps to remove the shadow mask.

A.9.3 Remarks

1. After loading the samples in the sputter-coater or Angstrom evaporator before depositing of each metal layer, a long pre-deposition step is recommended due to oxidized layer and

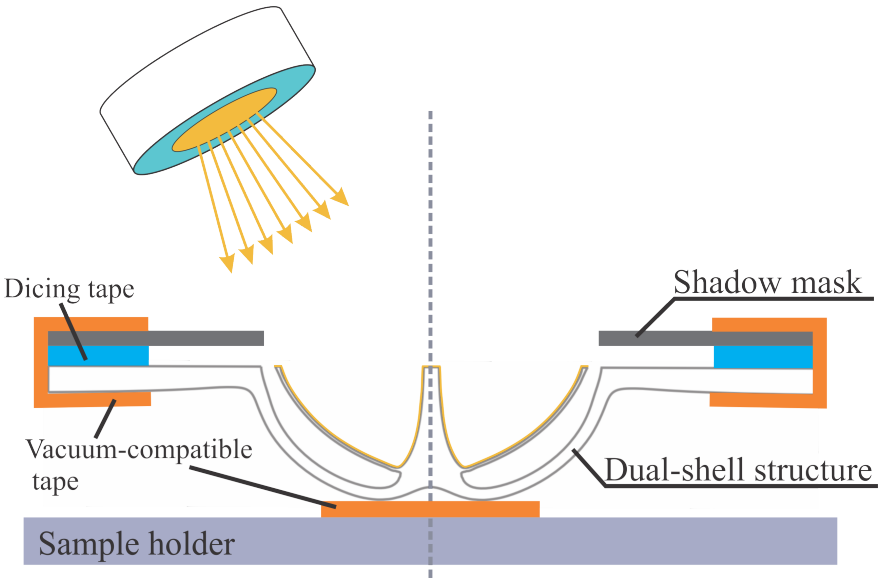

Figure A.14: Illustration of selective metallization of FS dual-shell gyroscopes in a 3D sputter-coater.

dust attached on each metal source which could contaminate the samples and might lead to delamination.

2. Allow a sufficient cooling period before venting and unloading the samples. Fast ramping down of the temperature would lead to delamination of the metal coating too.

3. Using the 20W RF mode recipe in the sputter coater would result in deposition rates of 0.3 Å/s for Cr and 0.8 Å/s for Au.

4. The deposition recipes of Ti, Cr, and Au are located in the folder named "Danmeng Wang" in the Angstrom evaporator.

Appendix B

Discrete Electrical Model of Hemispherical Resonator Gyroscopes

To represent the metal electrical resistance between the stem and the rim of DSGs during the four-point measurement described in Section 4.2, a discrete electric model of the dual-shell resonator can be used, illustrated in Fig. B.1(a), [128]. The rim of the device shell is evenly distributed as m nodes from the 1st to the mth node, where the node $m+1$ is equivalent to the 1st node due to the curvature of the device, that is as $m+1 \equiv 1$. A voltage of E_k with current, I_k, is directly applied to the kth node by one of the probes during the resistance measurement. Therefore, the equivalent electrical resistance between the kth node and the ground (central stem) is defined as $R_k = E_k/I_k$.

A fragment of the electric circuit of the discrete electric model is illustrated in Fig. B.1(b). The currents induced by the voltage E_k through the distributed resistances ρ_i and r_i are

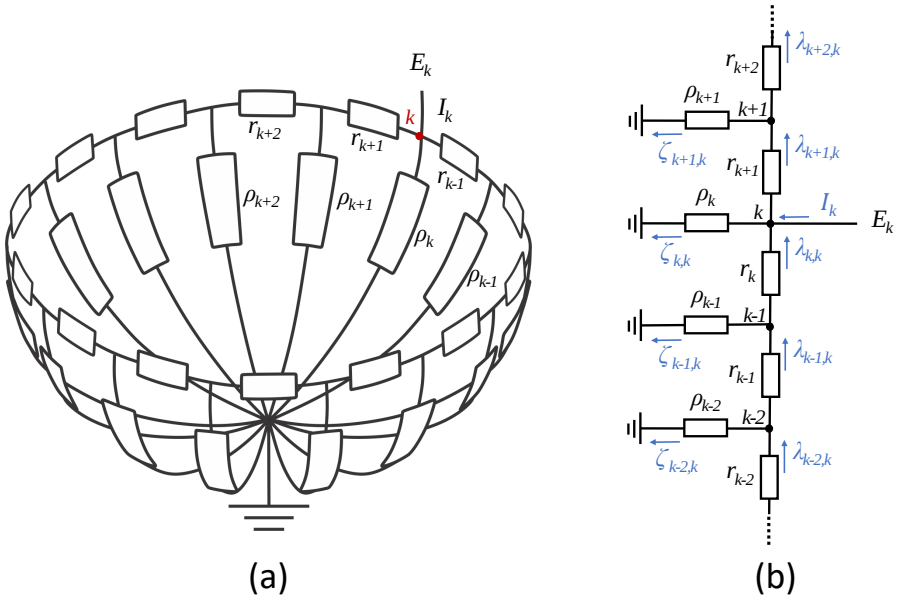

Figure B.1: (a) Schematics of the discrete resistance model of a metallized DSG structure with (b) a fragment of the electric circuit model. A voltage applied on the kth node representing the resistance measurement in Section 4.2.

defined as $\zeta_{i,k}$ and $\lambda_{i,k}$. Utilizing Kirchhoff's current law, the circuit has the form of

$$-\frac{\rho_{i-1}}{r_{i-1}}\zeta_{i-1,k}+\eta_i\zeta_{i,k}-\frac{\rho_{i+1}}{r_i}\zeta_{i+1,k}=\begin{cases}0 & \text{if } i\neq k\\ I_k & \text{if } i=k\end{cases} \tag{B.1}$$

with

$$\eta_i=1+\frac{\rho_i}{r_{i-1}}+\frac{\rho_i}{r_i}. \tag{B.2}$$

Based on measurements of electrical resistance, R_k, in Section 4.1, we assumed that R_k and ρ_k are sine functions as $R_k=\alpha\sin(2\pi\frac{k}{m}+\phi)+R_o$ and $\rho_k=\beta\sin(2\pi\frac{k}{m}+\phi)+\rho_o$, and $r_k=\gamma$ is evenly discrete. The discrete electric model can then be described by a linear algebraic system in the form of

$$M_{m\times m}*\zeta_{m\times m}=I_{m\times 1}, \tag{B.3}$$

where

$$M = \begin{bmatrix} \eta_1 & -\frac{\rho_2}{\gamma} & 0 & 0 & \cdots & 0 & -\frac{\rho_m}{\gamma} \\ -\frac{\rho_1}{\gamma} & \eta_2 & -\frac{\rho_3}{\gamma} & 0 & \cdots & 0 & 0 \\ 0 & & \ddots & & & & 0 \\ \vdots & 0 & -\frac{\rho_{k-1}}{\gamma} & \eta_k & -\frac{\rho_{k+1}}{\gamma} & 0 & \vdots \\ 0 & & & & \ddots & & 0 \\ 0 & 0 & \cdots & 0 & -\frac{\rho_{m-2}}{\gamma} & \eta_{m-1} & -\frac{\rho_m}{\gamma} \\ -\frac{\rho_1}{\gamma} & 0 & \cdots & 0 & 0 & -\frac{\rho_{m-1}}{\gamma} & \eta_m \end{bmatrix}, \tag{B.4}$$

$$\zeta_{m\times m} = \begin{bmatrix} 0 & \cdots & 0 & \zeta_{0,k} & 0 & \cdots & 0 \\ \vdots & \ddots & & \vdots & & \ddots & \vdots \\ 0 & \cdots & 0 & \zeta_{k,k} & 0 & \cdots & 0 \\ \vdots & \ddots & & \vdots & & \ddots & \vdots \\ 0 & \cdots & 0 & \zeta_{m-1,k} & 0 & \cdots & 0 \end{bmatrix}, I_{m\times 1} = \begin{bmatrix} 0 \\ \vdots \\ I_k \\ \vdots \\ 0 \end{bmatrix}. \tag{B.5}$$

Using the inverse of the coefficient matrix in Eq. B.3, the current, $\zeta_{i,k}$ is derived as

$$\zeta_{i,k} = M_{i,k}^{-1} I_k \tag{B.6}$$

Therefore, the distributed resistance ρ_k can be expressed as

$$\rho_k = \frac{E_k}{\zeta_{k,k}} = \frac{R_k I_k}{\zeta_{k,k}} = \frac{R_k}{M_{k,k}^{-1}}. \tag{B.7}$$

For an assembled dual-shell system with 24 electrode pads overlapped with the rim of the device shell, the effective electrical resistance of the jth electrode, R_{ej}, can be derived by an electric model presented in Fig. B.2(a). The jth electrode from the start and end angles, $\varphi_l'(j)$ to $\varphi_t'(j)$, is assumed to be evenly distributed by n plates, from the lth to tth node, where $l \equiv \varphi_l'(j)\frac{m}{2\pi}$, $t \equiv \varphi_t'(j)\frac{m}{2\pi}$, and $t \equiv l + n$.

To simplify the discussion, the voltage, V, current, I, loading resistance, R, and total charge

of the C_j capacitance, Q_j, are also evenly distributed for n plates. The relationship of these parameters is given by

$$R\dot{Q}_j + \frac{Q_j}{C_j} + R_{ej}I = V. \tag{B.8}$$

From the fragment of the electric circuit illustrated in Fig. B.2(b), the voltages, loading resistances, charges, and capacitances for the kth plates are defined as

$$V_k = V,\ R_k = nR,\ Q_j = \sum_{k=l}^{t} q_k = nq_k,\ C_j = \sum_{k=l}^{t} c_k = nc_k, \tag{B.9}$$

where $k = l, l+1, ..., t$. The currents through the distributed resistances ρ_k and r_k inducted by the voltage V are defined as i_k and j_k. Utilizing Kirchhoff's laws, the circuit shown in Fig. B.2(b) has the form

$$nR\dot{q}_k + \frac{q_k}{c_k} + \rho_k i_k = V_k, \tag{B.10}$$

$$\rho_k i_k - \rho_{k+1} i_{k+1} - r_k j_k = 0, \tag{B.11}$$

$$i_k + j_k - j_{k-1} = \dot{q}_k. \tag{B.12}$$

From Eq. B.10 – B.12, we find

$$j_k = \frac{1}{r_k}(\rho_k i_k - \rho_{k+1} i_{k+1}),\ \sum_{k=1}^{m} r_k i_k = 0,\ I = \sum_{k=l}^{t} i_k. \tag{B.13}$$

Substituting Eq. B.10 and Eq. B.13 into Eq. B.8 and matching each current term, the Eq. B.8 can be rewritten in the form of

$$R\sum_{k=l}^{t} \dot{q}_k + \frac{1}{n}\sum_{k=l}^{t} \frac{q_k}{c_k} + \frac{1}{n}\sum_{k=l}^{t} \rho_k i_k = V. \tag{B.14}$$

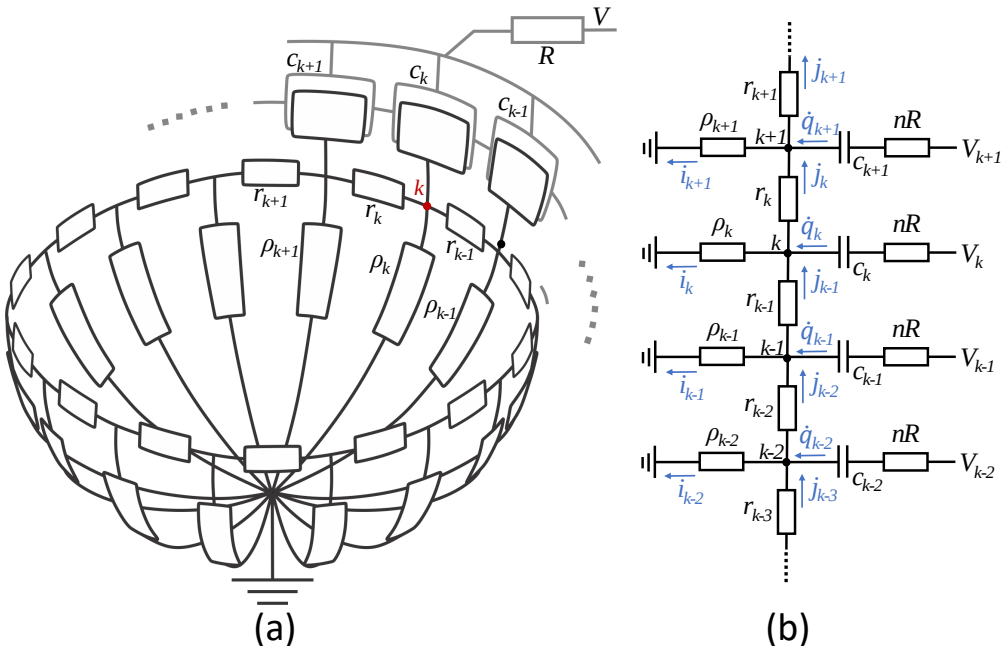

Figure B.2: (a) Schematics of the discrete resistance model of an assembled DSG structure with a voltage of V applied to the jth electrode. The model can be represented by (b) a fragment of the electric circuit model.

Therefore, the effective electrical resistance of the jth capacitance is derived as

$$R_{ej} = \frac{\sum_{k=l}^{t} \rho_k i_k}{nI} = \frac{\sum_{k=l}^{t} \rho_k i_k}{n \sum_{k=l}^{t} i_k}, \tag{B.15}$$

By matching the discrete electric models in Fig. B.1 and Fig. B.2, the equivalent relationships can be found as

$$i_k = \sum_{i=l}^{t} \zeta_{k,i} = \sum_{i=l}^{t} M_{k,i}^{-1} I_i = \sum_{i=l}^{t} M_{k,i}^{-1} \dot{q}_i. \tag{B.16}$$

By substituting Eq. B.7 and Eq. B.16 into Eq. B.15, the effective electrical resistance of the jth capacitance is found as

$$R_{ej} = \frac{\sum_{k=l}^{t} \frac{R_k}{M_{k,k}^{-1}} \sum_{i=l}^{t} M_{k,i}^{-1}}{n \sum_{k=l}^{t} \sum_{i=l}^{t} M_{k,i}^{-1}}. \tag{B.17}$$

Appendix C

List of Vendors

Airgas

Location: Santa Ana, CA 92704, USA

Phone: 855-625-5285

Email: wecanhelp@airgas.com

Airgas is a local supplier of laboratory gas equipment.

Allied High Tech Products, Inc.

Location: Rancho Dominguez, CA, USA

Phone: 800-675-1118

Email: info@alliedhightech.com

Allied High Tech Products, Inc. provides the die-level and wafer-level lapping and publishing instruments for release of Fused Silica shell resonators and all lapping related products, such as lapping films, slurry, lubricants, and lapping fixtures. Maintenance and repair of the Multiprep Polishing System are also available in the vendor.

Angstrom Engineering, Inc.

Location: Southern Ontario, Canada

Phone: 800-695-8270

Email: sales@angstromengineering.com

Angstrom Engineering, Inc. specializes in material deposition equipment and supplies, including Physical Vapor Deposition (PVD), Chemical Vapor Deposition (CVD), and evaporation. Relative supplies for Angstrom Engineering EvoVac Glovebox Evaporator at Irvine Materials Research Institute (IMRI), including crucibles, metal targets, are available from Angstrom Engineering, Inc.

Coining Inc.

Location: Montvale, NJ, USA

Phone: 201-791-4020

Email: coining.sales@ametek.com

Coining, Inc. provides solder preforms for Au-Sn eutectic bonding.

CAD/Art Services Inc.

Location: Bandon, Or 97411, USA

Phone: 541-347-5315

Email: cas@outputcity.com

CAD/Art Services Inc. provides low-price plastic laser-marked photomask with maximum resolution up to 25400 DPI (1μm).

Electro Tech Machining Location: Long Beach, CA, USA

Phone: 562-436-9281

Email: etm@etm-lb.com

Electro Tech Machining manufactures customized graphite parts. Possible applications include die-attachment, shell assembly, vacuum packaging, and shadow mask for deposition.

Front Range Photomask Co. LLC Location: Lake Havasu City, AZ, USA

Phone: 928-733-6217

Email: masks@frontrange-photomask.com

Front Range Photomask Co. LLC provides glass photomask fabrication service with accuracy ranging from 0.2μm to 1μm.

Kurt J. Lesker

Location: Jefferson Hills, PA 15025, USA

Phone: 800-245-1656

Website: https://www.lesker.com/

Kurt J. Lesker provides supplies for Physical Vapor Deposition (PVD) including deposition materials, such as Au, Cr, and Ti, and supplies for vacuum chambers and pumps.

Marvell Nanofabrication Laboratory Location: Berkeley, CA, USA

Phone: 510-809-8600

Email: rhemp@berkeley.edu

Marvell Nanofabrication Laboratory at UC Berkeley is a cleanroom facility providing microfabrication services. Specifically, double-side 2μm doped Poly-Si LPCVD is necessary as the hard mask during HF wet etching of the Fused Silica wafers. The thickness of the wafers can be as high as 2mm using the "Old recepit".

Mark Optics, Inc.

Location: Santa Ana, CA, USA

Phone: 714-545-6684

Email: quote@markoptics.com

Mark Optics, Inc. is a custom optics provider that specializes in glass wafers. Available materials include Pyrex, Fused Quartz, Borosilicate Glass (BSG), and Ultra Low Expansion Titania Silicate Glass (ULE TSG). Wafer polishing service for etched wafers is also available at Mark Optics, Inc.

Photo-sciences Inc.

Location: Torrance, CA, 90505, USA

Phone: 310-634-1500

Email: JDaniel@plastronics.com

Photo-sciences Inc. offers high-quality glass photomasks with high accuracy features of 2μm +/-0.25μm. Masks are typically used in lithography of inertial sensors fabrication.

Plastronics sockets & connectors

Location: Irving, TX 75062, USA

Phone: 972-258-2580

Email: JDaniel@plastronics.com

Plastronics offers complete, reliable burn-in test socket solutions for all the latest packaged devices, including LCC and PLCC packages. The material is compatible with vacuum condition. For LCC 44 packages, the socket part number is P2044S-B-AU.

Sierra Assembly Technology Inc.

Location: Fontana, CA 92337, USA

Phone: 909-355-5400

Website: https://www.protoexpress.com

Sierra Assembly Technology, Inc. offers high-quality and specialized PCBs. The ENIG surface finish of pads are wire-bondable. Arlon 85N is a polyimide and lamination prepreg system that provides excellent stability and low out-gassing for ultra-high vacuum applications.

SST Vcauum Reflow Systems

Location: Downey, CA, 90242, USA

Phone: 562-803-3361

Email: info@sstinternational.com

SST Vacuum Reflow Systems is now part of Palomar Technologies and the manufacturer of vacuum sealing furnace and supplier of the consumables. Maintenance and repair of the SST

vacuum sealing System are also available in the vendor.

Ultrasil LLC

Location: Hayward, CA 94545, USA

Phone: 510-266-3700

Email: rduque@ultrasil.com

Ultrasil LLC offers standard silicon wafers SSP and DSP silicon wafers, prime silicon wafers, SOI (Silicon on Insulator) wafers, and SOI Wafers with Ion implants and coatings. Typically, each order takes about more than 6 months to arrive.

University Wafer

Location: South Boston, MA 0217, USA

Phone: 800-713-9375

Email: chris@universitywafers.com

University Wafer, Inc. offers highest-quality silicon wafers and other semiconductor substrates and services including thermal oxide, nitride, thin films, dicing and more.